

AD-A252 602



1992

~~THESIS~~ DISSERTATION

①

Development of Two-Dimensional Parametric Radar Signal
Modeling and Estimation Techniques with Application to
Target Identification

Joseph J. Sacchini, Captain

AFIT Student Attending: Ohio State University

AFIT/CI/CIA-92-004D

AFIT/CI
Wright-Patterson AFB OH 45433-6583

Approved for Public Release IAW 190-1
Distributed Unlimited
ERNEST A. HAYGOOD, Captain, USAF
Executive Officer

DTIC
ELECTE
S B D
JUL 9 1992

DISTRIBUTION STATEMENT A
Approved for public release;
Distribution Unlimited

92 7 09 013

92-18004



DEVELOPMENT OF TWO-DIMENSIONAL
PARAMETRIC RADAR SIGNAL MODELING AND
ESTIMATION TECHNIQUES WITH
APPLICATION TO TARGET IDENTIFICATION

A Dissertation

Presented in Partial Fulfillment of the Requirements for
the Degree Doctor of Philosophy in the
Graduate School of The Ohio State University

by

Joseph J. Sacchini, M.S.E.E., B.E.

* * * * *

The Ohio State University

1992

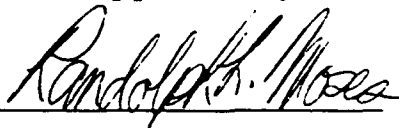
Dissertation Committee:

Randolph L. Moses

Ashok K. Krishnamurthy

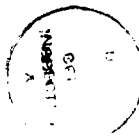
Ri-Chee Chou

Approved by


Adviser

Department of Electrical
Engineering

To my Father and Mother



ii

Accession For	
NTIS GRA&I	<input checked="checked" type="checkbox"/>
DTIC TAB	<input type="checkbox"/>
Unannounced	<input type="checkbox"/>
Justification	
By _____	
Distribution/	
Availability Codes	
Dist	Avail and/or Special
A-1	

ACKNOWLEDGMENTS

My sincere thanks go to my advisor, Prof. Randolph Moses, who, despite a very heavy student load, found the time to guide me through each phase of this work. His expertise in signal processing and Radar Target Identification were invaluable to this work and my understanding of these topics. I also wish to thank Profs. Ashok Krishnamurthy, Ri-Chee Chou and Lee Potter who took interest in this work and provided many helpful comments, and Dr. Ronald Marhefka for providing insight on The Geometrical Theory of Diffraction and electromagnetic scattering.

Several graduate students were very helpful during the completion of this work. Bill Steedly provided many helpful discussions on Prony modeling and estimation procedures. Also, Mr. Steedly's Master's Thesis served as a 1-D starting point for the 2-D polarimetric modeling. Ron Dilsavor provided insight on radar imaging and target detection. Jondae Ying was also helpful in discussing the Prony modeling and estimation procedures. Mark Hanes was invaluable in answering my many questions concerning the computer systems here.

I am grateful to the United States Air Force for supporting my graduate education here at The Ohio State University. Finally, I would like to thank my mother, Mary Jane, and father, Joseph, for their love and support throughout this work and all of my graduate studies.

VITA

October 20, 1962 Born—Cleveland, Ohio, U. S. A.

June 16, 1984 B. E. Electrical Engineering,
summa cum laude
Youngstown State University
Youngstown, Ohio, U. S. A.

September 21, 1984 Commissioned as Second Lieutenant
United States Air Force
San Antonio, Texas, U. S. A.

October 1984 - September 1986 Avionics Systems Engineer
Aeronautical Systems Division
Wright-Patterson AFB, Ohio, U. S. A.

September 21, 1986 Promoted to First Lieutenant
United States Air Force
Wright-Patterson AFB, Ohio, U. S. A.

September 1986 - September 1988 SR-71 Electronic Warfare Engineer
Aeronautical Systems Division
Wright-Patterson AFB, Ohio, U. S. A.

April 13, 1988 M. S. E. E. Electrical Engineering,
The University of Dayton
Dayton, Ohio, U. S. A.

September 21, 1988 Promoted to Captain
United States Air Force
Wright-Patterson AFB, Ohio, U. S. A.

September 16, 1991 Licensed as a Professional Engineer,
The State of Ohio
Columbus, Ohio, U. S. A.

PUBLICATIONS

"Currents Induced on Dielectric Coated Wires," M.S.E.E. Thesis, The University of Dayton, Dayton, Ohio, U. S. A., April 1988.

FIELDS OF STUDY

Major Field: Electrical Engineering

Studies in Communications:

Professors R. L. Moses,
A. K. Krishnamurthy,
L. C. Potter, F. D. Garber

Studies in Electromagnetics:

Professors R. G. Kouyoumjian,
R. C. Chou

Studies in Mathematics:

Professor U. Gerlach

TABLE OF CONTENTS

DEDICATION	ii
ACKNOWLEDGMENTS	iii
VITA	iv
LIST OF FIGURES	ix
LIST OF TABLES	xxi
ABSTRACT	xxiii
CHAPTER	PAGE
I Introduction	1
1.1 Background	1
1.2 Description of Study	2
1.3 Previous Work in Radar Target Identification	4
1.4 Summary of Chapters	9
II Target Scattering Fundamentals	12
2.1 Background and Introduction	12
2.2 Electromagnetic Fundamentals	12
2.3 Scattering Matrix Formulation	15
2.4 Summary	20
III Electromagnetic Behavior of Canonical Scattering Centers	21
3.1 Background and Introduction	21
3.2 Electromagnetic Analysis	23

3.2.1	Point Scatterer	23
3.2.2	Sphere	23
3.2.3	Edge and Corner	26
3.2.4	Dihedral	34
3.2.5	Trihedral	45
3.2.6	Flat Plate	46
3.2.7	Cylinder	50
3.3	Summary of Scattering Characteristics for Canonical Scattering Centers	50
3.4	Scattering Model for a Complicated Target	54
3.5	Damped Exponential Modeling of Scattering Behavior of Canonical Scattering Centers	55
3.6	Summary	65
IV	Signal Processing Fundamentals	67
4.1	Background and Introduction	67
4.2	One-Dimensional Techniques	68
4.3	Two-Dimensional Techniques	75
4.4	Summary	91
V	The Two-Dimensional TLS-Prony Technique	94
5.1	Introduction	94
5.2	Basic Technique Description	94
5.2.1	Background and Introduction	94
5.2.2	Data Model	95
5.2.3	Estimation Algorithms	97
5.2.4	Examples	113
5.3	Full-Polarization Extension of TLS-Prony Technique	122
5.3.1	Background and Introduction	122
5.3.2	Data Model	126
5.3.3	Estimation Algorithms	131
5.3.4	Examples	139
5.4	Summary	147
VI	Simulations Utilizing GTD Flat Plate Data	148
6.1	Introduction	148

6.2	Description of Data	151
6.3	Single-Polarization Analysis of Plate	153
6.3.1	Single Polarization Analysis of Fifteen Degree Polar Swaths of Data	156
6.3.2	Single Polarization Analysis of Fifteen Degree Polar Swaths of Data with Larger Model Orders Chosen	176
6.3.3	Single Polarization Analysis of Square Grids of Data Inter- polated from Fifteen Degree Polar Swaths of Data	187
6.3.4	Single Polarization Analysis of Three Degree Polar Swaths of Data	207
6.4	Full-Polarization Analysis of Plate	230
6.4.1	Full-Polarization Analysis of Fifteen Degree Polar Swaths of Data	231
6.4.2	Full-Polarization Analysis of Fifteen Degree Polar Swaths of Data with Higher Model Orders	237
6.4.3	Full-Polarization Analysis of Square Grids of Data Interpo- lated from Fifteen Degree Polar Swaths of Data	240
6.4.4	Full-Polarization Analysis of Three Degree Polar Swaths of Data	244
6.5	Analysis of Individual Scattering Centers on Plate	255
6.6	Summary	257
VII	Summary and Conclusions	263
7.1	Summary of Work and Conclusions	263
7.2	Areas for Future Research	269
	REFERENCES	273

LIST OF FIGURES

FIGURE	PAGE
1 Radar Target Identification Process.	1
2 Radar Target orientation.	18
3 Standard spherical coordinate system.	24
4 Impulse response approximation for a conducting sphere, taken from [1].	25
5 Frequency domain response for a conducting sphere, taken from [2]. .	26
6 Definition of a corner and an edge.	27
7 MM impulse response estimation for a 0.5m square inclined flat plate.	30
8 MM frequency response estimation for the leading edge of the plate shown in Figure 7.	31
9 GTD impulse response estimation for the leading edge of the plate shown in Figure 7.	33
10 GTD frequency response estimation for the leading right corner of the plate shown in Figure 7.	35
11 MM frequency response estimation for the leading right corner of the plate shown in Figure 7.	36
12 GTD azimuthal angular response estimation for the leading left corner of a 0.5m flat plate.	37
13 GTD elevation angular response estimation for the leading left corner of a 0.5m flat plate.	38

14	GTD azimuthal angular response estimation for the leading edge of a 0.5m flat plate.	39
15	Sketch of a typical dihedral.	40
16	GTD frequency and time domain response estimates for the scattering from a rectangular dihedral taken from [3].	41
17	MM time domain response estimate for the scattering from a dihedral.	42
18	MM frequency response estimate for the scattering from a dihedral. .	43
19	MM angular response estimate for the scattering from a dihedral. . .	44
20	Definition of a trihedral.	46
21	MM frequency domain response estimate for the scattering from a trihedral.	47
22	MM angular response estimate for the scattering from a trihedral. . .	48
23	Broadside angle of incidence off of a flat plate.	49
24	GTD frequency domain response estimate for the scattering from a flat plate.	50
25	Sketch of a right circular cylinder.	52
26	Damped exponential modeling for frequency dependencies of scattering centers with types $t = -1$ and $t = -0.5$	59
27	Damped exponential modeling for frequency dependencies of scattering centers with types $t = 0$ and $t = 0.5$	60
28	Damped exponential modeling for frequency dependence of scattering center with type $t = 1$	61
29	Damped exponential modeling for scattering center angular dependencies of a constant and $U(\psi)$	64
30	Damped exponential modeling for scattering center angular dependence of $\delta(\psi)$	65
31	Impulse response estimation for an inclined flat plate from ESL data.	71

32	Impulse response estimation for an inclined flat plate from ESL data.	72
33	Impulse response estimation for an inclined flat plate from ESL data for limited bandwidth.	76
34	Impulse response estimation for an inclined flat plate from ESL data for limited bandwidth using SVD-Prony method.	77
35	Radar-target geometry for 2-D imaging.	78
36	2-D frequency domain data set for full angular coverage.	81
37	2-D frequency domain data set for limited angular coverage.	82
38	Image of a plate, in the flat plate orientation, generated by direct numerical integration of Equation 4.24 for full angular coverage data (<i>hh</i> -polarization).	84
39	Image of a plate (inclined plate orientation) generated by direct nu- merical integration of Equation 4.24 for full angular coverage data (<i>hh</i> -polarization).	86
40	Desired point on rectangular grid between data points on polar grid. .	87
41	Image of a flat plate generated by interpolation to a square grid fol- lowed by the 2-D IFFT for full angular coverage data (<i>hh</i> -polarization). 88	
42	Image of an inclined plate generated by interpolation to a square grid followed by the 2-D IFFT for full angular coverage data (<i>hh</i> - polarization).	89
43	Image of an inclined plate generated for limited angular coverage data (<i>hh</i> -polarization) for off corner incidence.	90
44	Image of an inclined plate generated for limited angular coverage data (<i>hh</i> -polarization) for off edge incidence.	92
45	2-D frequency locations for Example 1.	115
46	Example 1. $10\log_{10}(1/\text{Variance})$ versus total SNR in dB for <i>x</i> -pole and <i>y</i> -pole frequencies using Algorithm One.	116

47	Example 1. $10\log_{10}(1/\text{Variance})$ versus total SNR in dB for x -pole and y -pole magnitudes using Algorithm One.	118
48	Example 1. $10\log_{10}(1/\text{Variance})$ versus total SNR in dB for x -pole and y -pole frequencies using Algorithm Two.	120
49	Example 1. $10\log_{10}(1/\text{Variance})$ versus total SNR in dB for x -pole and y -pole magnitudes using Algorithm Two.	121
50	Example 2. $10\log_{10}(1/\text{Variance})$ versus total SNR in dB for x -pole and y -pole frequencies using Algorithm Two.	123
51	Example 2. $10\log_{10}(1/\text{Variance})$ versus total SNR in dB for x -pole and y -pole magnitudes using Algorithm Two.	124
52	Polarization ellipse of scattering center consistent with IEEE standard.	129
53	Polarization ellipse of scattering center as viewed traveling toward the radar (observer). All of the ellipses plotted in this dissertation follow this convention.	130
54	Polarization ellipses for Example FP1.	141
55	Example FP1. $10\log_{10}(1/\text{Variance})$ versus total SNR in dB for x -pole and y -pole frequencies using FPA2.	142
56	Example FP1. $10\log_{10}(1/\text{Variance})$ versus total SNR in dB for x -pole and y -pole magnitudes using FPA2.	143
57	Example FP2. $10\log_{10}(1/\text{Variance})$ versus total SNR in dB for x -pole and y -pole frequencies using Algorithm FPA2.	145
58	Example FP2. $10\log_{10}(1/\text{Variance})$ versus total SNR in dB for x -pole and y -pole magnitudes using Algorithm Two.	146
59	Thin metal perfectly conducting square plate analyzed.	148
60	Geometry for scattering measurements from plate.	154
61	2-D frequency plane plot of scattering data collected by radar.	155
62	Contour image of plate for $\phi = 45^\circ$ generated from a 15° polar swath of hh -polarization data.	156

63	Single polarization inclined plate example for a 15° swath of polar data centered around 0°. Model orders were $Q, K, R, L = 10, 2, 10, 2$. .	159
64	Single polarization inclined plate example for a 15° swath of polar data centered around 0° and 7.5°. Model orders were $Q, K, R, L = 10, 2, 10, 2$ for 0° and $Q, K, R, L = 10, 4, 10, 2$ for 7.5°.	160
65	Single polarization inclined plate example for a 15° swath of polar data centered around 7.5°. Model orders were $Q, K, R, L = 10, 4, 10, 2$.	161
66	Single polarization inclined plate example for a 15° swath of polar data centered around 15°. Model orders were $Q, K, R, L = 10, 4, 10, 1$.	162
67	Single polarization inclined plate example for a 15° swath of polar data centered around 15° and 30°. Model orders were $Q, K, R, L = 10, 4, 10, 1$ for 15° and 30°.	163
68	Single polarization inclined plate example for a 15° swath of polar data centered around 30°. Model orders were $Q, K, R, L = 10, 4, 10, 1$.	164
69	Single polarization inclined plate example for a 15° swath of polar data centered around 45°. Model orders were $Q, K, R, L = 10, 4, 10, 1$.	165
70	Single polarization inclined plate example for a 15° swath of polar data centered around 45° and 60°. Model orders were $Q, K, R, L = 10, 4, 10, 1$ for 45° and 60°.	166
71	Single polarization inclined plate example for a 15° swath of polar data centered around 60°. Model orders were $Q, K, R, L = 10, 4, 10, 1$.	167
72	Single polarization inclined plate example for a 15° swath of polar data centered around 75°. Model orders were $Q, K, R, L = 10, 4, 10, 1$.	168
73	Single polarization inclined plate example for a 15° swath of polar data centered around 75° and 82.5°. Model orders were $Q, K, R, L = 10, 4, 10, 1$ for 75° and $Q, K, R, L = 10, 4, 10, 2$ for 82.5°.	169
74	Single polarization inclined plate example for a 15° swath of polar data centered around 82.5°. Model orders were $Q, K, R, L = 10, 4, 10, 2$.	170
75	Single polarization inclined plate example for a 15° swath of polar data centered around 90°. Model orders were $Q, K, R, L = 10, 2, 10, 2$.	171

76	Single polarization inclined plate example for a 15° swath of polar data centered around 90° . Model orders were $Q, K, R, L = 10, 2, 10, 2$. The polarization is vv	172
77	RE versus SNR for noise added to the GTD data of the plate. All three polarizations are shown for $\phi = 0^\circ$ and $\phi = 45^\circ$. The model orders were $Q, K, R, L = 10, 2, 10, 2$ for the $\phi = 0^\circ$ plots and $Q, K, R, L = 10, 4, 10, 1$ for the $\phi = 45^\circ$ plots. The data is a 15° swath of polar data.	175
78	Single polarization inclined plate example for a 15° swath of polar data centered around 0° . Model orders were $Q, K, R, L = 10, 4, 10, 4$. .	177
79	Single polarization inclined plate example for a 15° swath of polar data centered around 7.5° . Model orders were $Q, K, R, L = 10, 6, 10, 4$.	178
80	Single polarization inclined plate example for a 15° swath of polar data centered around 15° . Model orders were $Q, K, R, L = 10, 6, 10, 4$.	179
81	Single polarization inclined plate example for a 15° swath of polar data centered around 30° . Model orders were $Q, K, R, L = 10, 6, 10, 4$.	180
82	Single polarization inclined plate example for a 15° swath of polar data centered around 45° . Model orders were $Q, K, R, L = 10, 6, 10, 4$.	181
83	Single polarization inclined plate example for a 15° swath of polar data centered around 60° . Model orders were $Q, K, R, L = 10, 6, 10, 4$.	182
84	Single polarization inclined plate example for a 15° swath of polar data centered around 75° . Model orders were $Q, K, R, L = 10, 6, 10, 4$.	183
85	Single polarization inclined plate example for a 15° swath of polar data centered around 82.5° . Model orders were $Q, K, R, L = 10, 6, 10, 4$.	184
86	Single polarization inclined plate example for a 15° swath of polar data centered around 90° . Model orders were $Q, K, R, L = 10, 4, 10, 4$.	185
87	RE versus SNR for noise added to the GTD data of the plate. All three polarizations are shown for $\phi = 0^\circ$ and $\phi = 45^\circ$. The model orders were $Q, K, R, L = 10, 4, 10, 4$ for the $\phi = 0^\circ$ plots and $Q, K, R, L = 10, 6, 10, 4$ for the $\phi = 45^\circ$ plots. The data is a 15° swath of polar data.	188

88	Single polarization inclined plate example for a square grid (from 15° polar) of data centered around 0°. Model orders were $Q, K, R, L = 10, 2, 10, 2$	191
89	Single polarization inclined plate example for a square grid (from 15° polar) of data centered around 0° and 7.5°. Model orders were $Q, K, R, L = 10, 2, 10, 2$ for 0° and $Q, K, R, L = 10, 4, 10, 2$ for 7.5°. . . .	192
90	Single polarization inclined plate example for a square grid (from 15° polar) of data centered around 7.5°. Model orders were $Q, K, R, L = 10, 4, 10, 2$	193
91	Single polarization inclined plate example for a square grid (from 15° polar) of data centered around 15°. Model orders were $Q, K, R, L = 10, 4, 10, 1$	194
92	Single polarization inclined plate example for a square grid (from 15° polar) of data centered around 15° and 30°. Model orders were $Q, K, R, L = 10, 4, 10, 1$ for 15° and 30°.	195
93	Single polarization inclined plate example for a square grid (from 15° polar) of data centered around 30°. Model orders were $Q, K, R, L = 10, 4, 10, 1$	196
94	Single polarization inclined plate example for a square grid (from 15° polar) of data centered around 45°. Model orders were $Q, K, R, L = 10, 4, 10, 1$	197
95	Single polarization inclined plate example for a square grid (from 15° polar) of data centered around 45° and 60°. Model orders were $Q, K, R, L = 10, 4, 10, 1$ for 45° and 60°.	198
96	Single polarization inclined plate example for a square grid (from 15° polar) of data centered around 60°. Model orders were $Q, K, R, L = 10, 4, 10, 1$	199
97	Single polarization inclined plate example for a square grid (from 15° polar) of data centered around 75°. Model orders were $Q, K, R, L = 10, 4, 10, 1$	200

98	Single polarization inclined plate example for a square grid (from 15° polar) of data centered around 75° and 82.5°. Model orders were $Q, K, R, L = 10, 4, 10, 1$ for 75° and $Q, K, R, L = 10, 4, 10, 2$ for 82.5°.	201
99	Single polarization inclined plate example for a square grid (from 15° polar) of data centered around 82.5°. Model orders were $Q, K, R, L = 10, 4, 10, 2$	202
100	Single polarization inclined plate example for a square grid (from 15° polar) of data centered around 90°. Model orders were $Q, K, R, L = 10, 2, 10, 2$	203
101	Single polarization inclined plate example for a square grid (from 15° polar) of data centered around 90°. Model orders were $Q, K, R, L = 10, 2, 10, 2$. The polarization is vv	204
102	RE versus SNR for noise added to the GTD data of the plate. All three polarizations are shown for $\phi = 0^\circ$ and $\phi = 45^\circ$. The model orders were $Q, K, R, L = 10, 2, 10, 2$ for the $\phi = 0^\circ$ plots and $Q, K, R, L = 10, 4, 10, 1$ for the $\phi = 45^\circ$ plots. The data lies on a square grid interpolated from a 15° swath of polar data.	206
103	Single polarization inclined plate example for a 3° polar swath of data centered around 0°. Model orders were $Q, K, R, L = 10, 2, 10, 2$	209
104	Single polarization inclined plate example for a 3° polar swath of data centered around 0° and 7.5°. Model orders were $Q, K, R, L = 10, 2, 10, 2$ for 0° and $Q, K, R, L = 10, 4, 10, 2$ for 7.5°.	210
105	Single polarization inclined plate example for a 3° polar swath of data centered around 7.5°. Model orders were $Q, K, R, L = 10, 4, 10, 2$	211
106	Single polarization inclined plate example for a 3° polar swath of data centered around 15°. Model orders were $Q, K, R, L = 10, 4, 10, 1$	212
107	Single polarization inclined plate example for a 3° polar swath of data centered around 15° and 30°. Model orders were $Q, K, R, L = 10, 4, 10, 1$ for 15° and 30°.	213
108	Single polarization inclined plate example for a 3° polar swath of data centered around 30°. Model orders were $Q, K, R, L = 10, 4, 10, 1$	214

109	Single polarization inclined plate example for a 3° polar swath of data centered around 45° . Model orders were $Q, K, R, L = 10, 4, 10, 1$	215
110	Single polarization inclined plate example for a 3° polar swath of data centered around 45° and 60° . Model orders were $Q, K, R, L = 10, 4, 10, 1$ for 45° and 60°	216
111	Single polarization inclined plate example for a 3° polar swath of data centered around 60° . Model orders were $Q, K, R, L = 10, 4, 10, 1$	217
112	Single polarization inclined plate example for a 3° polar swath of data centered around 75° . Model orders were $Q, K, R, L = 10, 4, 10, 1$	218
113	Single polarization inclined plate example for a 3° polar swath of data centered around 75° and 82.5° . Model orders were $Q, K, R, L = 10, 4, 10, 1$ for 75° and $Q, K, R, L = 10, 4, 10, 2$ for 82.5°	219
114	Single polarization inclined plate example for a 3° polar swath of data centered around 82.5° . Model orders were $Q, K, R, L = 10, 4, 10, 2$	220
115	Single polarization inclined plate example for a 3° polar swath of data centered around 90° . Model orders were $Q, K, R, L = 10, 2, 10, 2$	221
116	Single polarization inclined plate example for a 3° polar swath of data centered around 90° . Model orders were $Q, K, R, L = 10, 2, 10, 2$. The polarization is vv	222
117	RE versus SNR for noise added to the GTD data of the plate. All three polarizations are shown for $\phi = 0^\circ$ and $\phi = 45^\circ$. The model orders were $Q, K, R, L = 10, 2, 10, 2$ for the $\phi = 0^\circ$ plots and $Q, K, R, L = 10, 4, 10, 1$ for the $\phi = 45^\circ$ plots. The data is a 3° swath of polar data.	223
118	RE versus SNR for noise added to the GTD data of the plate. All three polarizations are shown for $\phi = 30^\circ$. The model orders are $Q, K, R, L = 10, 4, 10, 1$. The data is a 3° swath of polar data.	224
119	Estimated pole locations for noise corrupted GTD data. The GTD data is a 3° polar swath with hh -polarization centered around $\phi = 45^\circ$. The model orders were $Q, K, R, L = 10, 4, 10, 1$	227

120	Estimated pole locations for noise corrupted GTD data. The GTD data is a 3° polar swath with hh -polarization centered around $\phi = 45^\circ$. The model orders were $Q, K, R, L = 10, 4, 10, 2$	228
121	Full polarization flat plate example for a 15° polar swath of data centered around $0^\circ, 7.5^\circ, 15^\circ$ and 30°	232
122	Full polarization flat plate example for a 15° polar swath of data centered around $45^\circ, 60^\circ, 75^\circ$ and 82.5°	233
123	Full polarization flat plate example for a 15° polar swath of data centered around 90°	234
124	RE versus SNR for noise added to the GTD data of the plate. Full polarization results are shown for $\phi = 0^\circ$ and $\phi = 45^\circ$. The model orders were $Q, K, R, L = 10, 2, 10, 2$ for the $\phi = 0^\circ$ plot and $Q, K, R, L = 10, 4, 10, 1$ for the $\phi = 45^\circ$ plot. The data is a 15° swath of polar data.	235
125	Full polarization flat plate example for a 15° polar swath of data centered around $0^\circ, 7.5^\circ, 15^\circ$ and 30° with higher model orders chosen.	238
126	Full polarization flat plate example for a 15° polar swath of data centered around $45^\circ, 60^\circ, 75^\circ$ and 82.5° with higher model orders chosen.	239
127	Full polarization flat plate example for a 15° polar swath of data centered around 90° with higher model orders chosen.	240
128	RE versus SNR for noise added to the GTD data of the plate. Full polarization results are shown for $\phi = 0^\circ$ and $\phi = 45^\circ$. The model orders were $Q, K, R, L = 10, 4, 10, 4$ for the $\phi = 0^\circ$ plot and $Q, K, R, L = 10, 6, 10, 4$ for the $\phi = 45^\circ$ plot. The data is a 15° swath of polar data.	241
129	Full polarization flat plate example for a square grid of data interpolated from a 15° polar swath of data centered around $0^\circ, 7.5^\circ, 15^\circ$ and 30°	242
130	Full polarization flat plate example for a square grid of data interpolated from a 15° polar swath of data centered around $45^\circ, 60^\circ, 75^\circ$ and 82.5°	243

131	Full polarization flat plate example for a square grid of data interpolated from a 15° polar swath of data centered around 90°	245
132	RE versus SNR for noise added to the GTD data of the plate. Full polarization results are shown for $\phi = 0^\circ$ and $\phi = 45^\circ$. The model orders were $Q, K, R, L = 10, 2, 10, 2$ for the $\phi = 0^\circ$ plot and $Q, K, R, L = 10, 4, 10, 1$ for the $\phi = 45^\circ$ plot. The data lies on a square grid which was interpolated from a 15° swath of polar data.	247
133	Full polarization flat plate example for a 3° polar swath of data centered around $0^\circ, 7.5^\circ, 15^\circ$ and 30°	248
134	Full polarization flat plate example for a 3° polar swath of data centered around $45^\circ, 60^\circ, 75^\circ$ and 82.5°	249
135	Full polarization flat plate example for a 3° polar swath of data centered around 90°	250
136	RE versus SNR for noise added to the GTD data of the plate. Full polarization results are shown for $\phi = 0^\circ, \phi = 30^\circ$, and $\phi = 45^\circ$. The model orders were $Q, K, R, L = 10, 2, 10, 2$ for the $\phi = 0^\circ$ plot and $Q, K, R, L = 10, 4, 10, 1$ for the $\phi = 30^\circ$ and $\phi = 45^\circ$ plots. The data is a 3° swath of polar data.	251
137	Estimated ellipses for noise corrupted GTD data. The GTD data is a full-polarization 3° polar swath. The model orders were $Q, K, R, L = 10, 4, 10, 1$ for all of the plots.	252
138	Estimated ellipses for noise corrupted GTD data. The GTD data is a full-polarization 3° polar swath. The model orders were $Q, K, R, L = 10, 4, 10, 2$ for all of the plots.	253
139	Frequency response comparisons for parameter estimates from a square grid of data generated from a 15° polar swath of data centered around $\phi = 45^\circ$	258
140	Angular response comparisons for parameter estimates from a square grid of data generated from a 15° polar swath of data centered around $\phi = 45^\circ$	259
141	Frequency response comparisons for parameter estimates from a 3° polar swath of data centered around $\phi = 45^\circ$	260

142	Angular response comparisons for parameter estimates from a 3° polar swath of data centered around $\phi = 45^\circ$	261
-----	---	-----

LIST OF TABLES

TABLE		PAGE
1	Approximate Frequency and Angle characteristics of canonical scattering centers.	53
2	Correspondence between terms in damped exponential scattering model and electromagnetically based scattering model.	57
3	Summary of amplitude coefficients and poles for 1-D frequency domain scattering from canonical scattering centers.	62
4	Summary of amplitude coefficients and poles for 1-D angular domain scattering from canonical scattering centers.	63
5	Summary of steps performed in Algorithm One.	106
6	Summary of steps performed in Algorithm Two.	109
7	Summary of steps performed in FPA1.	137
8	Summary of steps performed in FPA2.	139
9	Model orders and relative errors for single polarization results for the scattering from an inclined plate. The data is a 15° polar swath. . . .	158
10	Model orders and relative errors for single polarization results for the scattering from an inclined plate with model orders larger than the model orders in Table 9. The data is a 15° polar swath.	187
11	Model orders and relative errors for single polarization results for the scattering from an inclined plate. The data lies on a square grid (from 15° polar swath).	205
12	Model orders and relative errors for single polarization results for the scattering from an inclined plate. The data is a 3° polar swath. . . .	225

13	Model orders and relative errors for full-polarization results for the scattering from an inclined plate. The data is a 15° angular swath of polar data.	236
14	Model orders and relative errors for full-polarization results for the scattering from an inclined plate. The model orders for these examples were chosen higher than the model orders in Table 13. The data is a 15° angular swath of polar data.	244
15	Model orders and relative errors for full-polarization results for the scattering from an inclined plate. The data lies on a square grid and was interpolated from a 15° polar swath of data.	246
16	Model orders and relative errors for full-polarization results for the scattering from an inclined plate. The data is a 3° angular swath of polar data.	254

ABSTRACT

This dissertation develops one and two-dimensional signal processing models and algorithms which are utilized in the Radar Target Identification Problem. A basic assumption of this work is that the high-frequency scattering from a radar target, such as an aircraft, land-based vehicle, or ship, is comprised of the sum of the scattering from a finite number of canonical scattering centers, each with a specific location and identity. By high-frequency it is meant that the overall size of the target is at least one wavelength. The scattering center assumption is more valid as the individual scattering centers become more electrically isolated. If two individual scattering centers are electrically close, then their combined response is, in general, not the sum of their individual responses.

First, this dissertation investigates the electromagnetic scattering characteristics of canonical scattering centers. Canonical scattering centers are scattering centers on a target which account for the vast majority of the scattering from that target in the high-frequency case. Some of the targets of interest in this work are aircraft, tanks, trucks, automobiles and ships. Predominant scattering centers on these targets include corners, edges, plates, dihedrals, trihedrals, and cylinders. The scattering centers are described by their scattering characteristics as functions of angle, frequency, and polarization.

Second, this dissertation develops a two-dimensional (2-D) signal processing technique for locating and characterizing scattering centers from radar data. The radar gathers scattering data of a target at both multiple frequencies and multiple angles. This type of data is gathered (in raw form) by both Synthetic Aperture Radars and Inverse Synthetic Aperture Radars. The 2-D signal processing technique developed here is based on a 2-D extension of a total least squares (TLS) solution to a Prony Model and is called the 2-D TLS-Prony Technique. This technique can use single or multiple-polarization data. With full-polarization data, polarimetric characteristics of the scattering centers are found using the transient polarization response concept. This concept uses an ellipse to characterize the polarimetric characteristics of each scattering center. The abilities of the 2-D TLS-Prony Technique are demonstrated utilizing simulated 2-D radar data.

CHAPTER I

Introduction

1.1 Background

Non-cooperative target recognition (NCTR) utilizing radar has been of interest for many years. The term "non-cooperative" implies that the target neither hinders (*e.g.* by jamming) nor helps (*e.g.* by identifying itself) the illuminating radar. The process of recognition is accomplished since the target "changes" the transmitted radar signal, and since how the target changes this signal is, in some way, characteristic of the target. NCTR accomplished through radar is designated Radar Target Identification (RTI).

The overall process of RTI is shown in Figure 1. The raw data is obtained from the radar, and in many cases this data must be processed to compensate

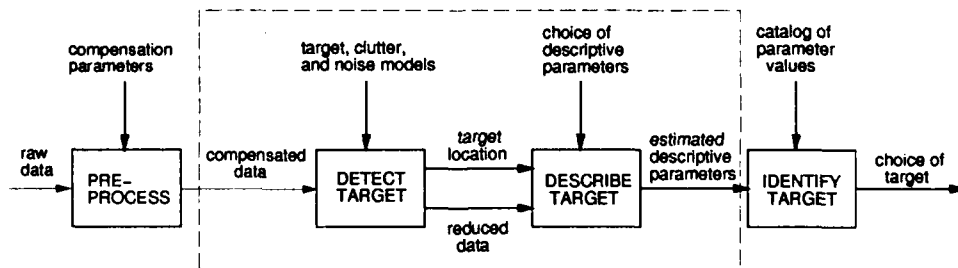


Figure 1: Radar Target Identification Process.

for factors such as radar target velocity, radar target orientation, radar antenna characteristics, path of radar relative to target and radar target range. Once the data has been preprocessed, it is ready to be used by the target detection algorithm. The purpose of the target detection algorithm is to detect the presence of and estimate the location of a target. Also, this algorithm may reduce the data set to yield another smaller data set that still contains the important target descriptive information. The target location and the reduced data set are passed onto the target description algorithm. This algorithm takes the target location and the reduced data set and forms an estimated descriptive parameter set which describes the target of interest. This descriptive parameter set is sent to a target identification algorithm and compared with idealized parameter sets, and a classification of the target is made.

1.2 Description of Study

This dissertation focuses on and develops one-dimensional (1-D) and two-dimensional (2-D) signal processing models and algorithms which are utilized in the target detection and target description stages of the RTI process. A basic assumption of this work is that the high-frequency scattering from a complicated target such as an aircraft, land-based vehicle, or tank is comprised as the sum of the scattering from a finite number of canonical scattering centers, each with a specific location and identity (*e.g.* corner, edge, dihedral, etc.). This assumption is more valid as the individual scattering centers become more electrically isolated (electrical isolation between two scattering centers implies that the physical distance between

the two scattering centers is several or more wavelengths, where the wavelength is the wavelength of the electromagnetic wave illuminated by the radar). If two individual scattering centers are electrically close (physically, less than or around one wavelength apart), then their combined response is, in general, not the simple sum of their individual responses. Also, if the overall target size is less than one wavelength, then the phenomena of resonance will dominate the scattering from the object, and the scattering center assumption fails. Thus, the scattering center assumption is considered high-frequency, which implies that the size of the overall target is a wavelength or greater.

First, this dissertation investigates the electromagnetic characteristics of canonical scattering centers. Canonical scattering centers are scattering centers on a target which account for the vast majority of the scattering from that target in the high-frequency case. Some of the targets of interest in this work are aircraft, tanks, trucks, automobiles, and ships. Predominant scattering centers on these targets include corners, edges, plates, dihedrals, trihedrals, and cylinders. The scattering centers are described by their scattering characteristics as functions of angle, frequency, and polarization. The scattering centers in this work are assumed to be perfect conductors.

Second, this dissertation develops a 2-D signal processing technique for locating and characterizing scattering centers from radar data. By 2-D, it is meant that the radar gathers data on a target at multiple frequencies and multiple angles. It is assumed that both the magnitude and phase of the received signal are known. This

type of data is gathered (in raw form) by both Synthetic Aperture Radars (SARs) and Inverse Synthetic Aperture Radars (ISARs). The 2-D signal processing technique developed here is based on a 2-D extension of a total least squares (TLS) solution to a Prony Model and is called the 2-D TLS-Prony Technique. This technique can use single or multiple-polarization data. With full-polarization data, polarimetric characteristics of the scattering centers are found using the transient polarization response (TPR) concept [4]. This concept uses an ellipse to characterize the polarimetric characteristics of each scattering center.

1.3 Previous Work in Radar Target Identification

The techniques developed in this dissertation are useful for determining the identity of a target from its structure. The determination of the physical characteristics of a target from the scattering behavior of that target is, in general, an inverse scattering problem. The general problem of inverse scattering is ill-posed [5]. Thus, some assumptions must be made in order to make the RTI problem solvable.

The idea of approximating the impulse response of a target was described by Kennaugh and Cosgriff in 1958 [6] and later by Kennaugh and Moffatt in 1965 [1]. Kennaugh and Moffatt also looked at other transient responses such as step responses and ramp responses. In 1981, techniques were developed by Moffatt and others [7] to utilize the impulse and other transient responses for target identification purposes. These techniques all used the range (or time) domain responses which exploited the geometrical characteristics of the targets. All of these techniques assumed a single polarization and a single radar-target orientation.

Assuming that the scattering from a complicated target is made up of the sum of the scattering from a finite number of scattering centers, the first step in analyzing the scattering data from a target is to determine the presence and location of the canonical scattering centers. Fourier techniques have been used successfully [4] by taking the local maxima of the range domain waveform. Parametric techniques [8, 9] have been used to determine the locations of the scattering centers for the 1-D problem. The parametric techniques have been shown to have superior resolution capabilities than the Fourier techniques [10]. A 1-D canonical scattering center algorithm was developed by Carrière and Moses [11]. This algorithm takes 1-D data and returns the types (*e.g.* corner, edge), locations, and amplitudes of the canonical scattering centers which comprise the target at that aspect angle.

This dissertation develops a new method for estimating 2-D frequencies and amplitude coefficients from a 2-D data set. This method is applied to radar data in this dissertation, but it can also be applied in other areas such as sonar, geophysics, radio astronomy, radio communications, and medical imaging. The estimation of 2-D frequencies and amplitude coefficients from a 2-D data set has been investigated utilizing many different approaches [12]–[18] such as Fourier-based methods, data extension, maximum likelihood method (MLM), maximum entropy method (MEM), autoregressive (AR) models, and linear prediction (LP) models [19]–[25].

Fourier-based methods are currently used in tomography to generate an image of an object [13]–[17]. The properties of these techniques have been well studied [13]. However, these techniques are limited by Fourier resolution capabilities. Also, these

techniques do not directly estimate 2-D frequencies. Thresholding along with a peak detection scheme must be used in the 2-D frequency domain to determine the 2-D frequencies.

Other methods include the MLM of spectral estimation which was proposed as an m -dimensional (m -D) technique for array processing [19]. This technique has also been applied to the tomography problem in [24]. The MEM of spectral estimation has also been applied to the 2-D problem [21, 22, 25]. This method also provides high resolution, but does not exist for all data sets [26]. Two-dimensional AR modeling and algorithms exist [10, 20, 23], but these are computationally expensive. State space methods [27] and a matrix pencil method [28] have also been used. Prony's method coupled with total least squares (TLS) techniques in one-dimension (1-D) has been used successfully to estimate frequencies in the presence of noise [29]. This dissertation extends Prony's model to 2-D.

A related method 2-D method, developed by Hua [28], also estimates 2-D frequencies. In Hua's method, two estimation steps are performed to separately estimate the x -components and y -components of the 2-D frequencies. Then, a matching step is performed to find the correct x -component and y -component frequency pairings. The matrix pencil method is employed for noise cleaning purposes in Hua's method.

The polarimetric characteristics of radar targets have been investigated for many years. In the late 1940's and early 1950's Kennaugh [30] developed the concept of an 'optimal polarization' for a target. This optimal polarization is found by

determining the eigenvalues of the monostatic, monochromatic scattering matrix. The eigenvector corresponding to the largest eigenvalue yields the transmit and receive polarization which yields the maximum received power of any polarization. Also related to this is the 'null polarization' concept, which is the transmit and receive polarization which provides zero received power.

Huynen developed a phenomenological theory of radar targets in [31] which extended the work of Kennaugh. Huynen characterized a target by a 3×3 set of parameters based upon power quantities. This set of parameters closely resembles the 4×4 Stokes reflection matrix [32]. The Huynen parameters relate to the physical characteristics of the target. The Huynen approach is monochromatic. Boerner used Kennaugh's optimal polarization concept and Huynen's work to analyze the wideband scattering of radar targets [33]. The polarimetric properties of scattering centers on the target are isolated by gating the response of the scattering center of interest in the time domain. The Huynen parameters of the a scattering center on the object are calculated for the center frequency of the wideband data. This work confirmed the assumption that the high-frequency scattering from a complicated radar target consists of the sum of the scattering from a finite number of scattering centers.

Another polarimetric-based method, developed by Cameroon [34], used the polarimetric behavior of several canonical shapes. The scattering matrix for each scattering center is decomposed into parts corresponding to non-reciprocal, asymmetric, and symmetric scatterers. The decomposition proceeds further into specific scatter-

ing types which fit into one of the above three classes. Classification is accomplished by determining the specific identity of each scattering center.

Chamberlin [4] introduced the transient polarization response concept (TPR). In the TPR concept, the target is illuminated with an impulse of a circularly polarized electromagnetic wave and as the wave interacts with each scattering center on the target, each scattering center will reflect back a wave with a polarization which is determined by the polarimetric characteristics of that scattering center. This concept has been investigated in 1-D utilizing nonparametric [4, 35, 36] and parametric [37, 38] techniques. This dissertation extends the parametric-based TPR method of Steedly [37, 38] to the 2-D case.

Classification work has been done utilizing the scattering center approach. Sands in [39] used a data base of known targets and compared a candidate target to the known targets. In this work, each target is described by a set of scattering centers; only the scattering center location is important, and its identity is not used. The data-base target that has the best "match" to the candidate target is declared the winner. Other classification work, using statistical techniques such as the nearest neighbor method, is reported in [40].

Much of the above work assumes that the scattering centers are of the point scatterer variety; that is, the models only allow for undamped exponentials in one or two-dimensions. This dissertation allows for 2-D damped exponentials. This is important in modeling scattering centers which are not point scatterers, and thus do not have scattering characteristics that are constant as a function of frequency

or angle.

1.4 Summary of Chapters

Chapter II defines the scattering matrix and how the scattering data is collected. This is a background chapter which outlines the assumptions concerning the form and content of the scattering matrix and how the scattering coefficients are related to the radar data. Also, the conversion of the scattering matrix from one polarization basis to another is outlined.

Chapter III investigates the scattering characteristics of canonical scattering centers. Techniques such as The Method of Moments (MM) and The Geometrical Theory of Diffraction (GTD) are used to determine the scattering characteristics of structures such as the edge, corner, dihedral, trihedral and cylinder. The scattering characteristics of each canonical shape are estimated as a function of frequency, radar-target orientation, and polarization. The high-frequency scattering model for a complicated radar target is defined, which is the sum of the scattering responses from a finite number of canonical scattering centers. Finally, the ability of a damped exponential model to accurately model the scattering characteristics of the canonical scattering centers is discussed.

Chapter IV is a background signal processing chapter which is needed to introduce 1-D and 2-D signal processing techniques. Non-parametric techniques such as the 1-D and 2-D IFFTs are introduced and examples are shown on how these techniques produce a down-range profile and an image of a target, respectively. The 1-D TLS-Prony Technique is described, which is a 1-D parametric signal processing

technique. Prony's model (in 1-D) is introduced, which is the 1-D damped exponential model used by the 1-D TLS-Prony Technique. The estimation algorithm used by this technique is described, and examples are shown which illustrate this 1-D technique. Several 2-D IFFT based image generation techniques are also described. Images generated by the various techniques are also shown.

Chapter V develops the 2-D TLS-Prony Technique. This is a new technique for estimating two-dimensional (2-D) poles and amplitude coefficients in a 2-D Prony-based model. The fundamental estimation algorithm involves two parts, each utilizing a 1-D singular value decomposition-based technique. This 2-D technique is capable of locating frequencies anywhere in the 2-D frequency plane. The basic algorithm is first developed for a single 2-D data set, such as a set of radar measurements with a single transmit and receive polarization. Simulations are shown which demonstrate the performance of the algorithm for various noise levels. Then, the algorithm is extended to the multiple data set case, which applies when full-polarization 2-D measurements of a target are available. Simulations are shown which demonstrate the performance of this algorithm for the multiple data set case for various noise levels.

Chapter VI discusses examples of the 2-D TLS-Prony Technique applied to simulated radar data. The scattering from an inclined thin metal plate is generated using the Geometrical Theory of Diffraction (GTD). This data is used by both the single-polarization and the full-polarization 2-D TLS Prony Techniques to estimate the locations and the polarimetric characteristics of the scattering centers on the

plate. Issues involving 2-D angular and frequency bandwidths, model order selection, effects of noise on parameter estimates, and the form of the data set on the 2-D frequency plane are addressed. Also, the validity of the damped exponential to model the scattering from the canonical scattering centers is addressed.

Finally, Chapter VII provides a summary and draws conclusions based upon the work presented in the dissertation. Also, areas for future research are discussed.

CHAPTER II

Target Scattering Fundamentals

2.1 Background and Introduction

This chapter describes how target-scattering information is acquired by a radar. A target's scattering characteristics in the far field are contained in its scattering matrix. The scattering matrix contains multiple polarization information for a given object at a given orientation relative to the radar at a specific frequency. In its most general form, the scattering matrix for a target is a function of frequency of illumination, target orientation, and transmit and receive polarizations. It is possible for a target to have both monostatic and bistatic scattering matrices. For this research, only the monostatic case is investigated.

2.2 Electromagnetic Fundamentals

It is assumed that the target is in the far-field of the radar antenna. Thus, a locally plane wave is assumed to impinge upon the target. A plane wave is the solution to the homogeneous wave equation. Consider Maxwell's Equations in their time domain point form:

$$\nabla \times \vec{\mathcal{E}}(\mathfrak{R}, t) = -\frac{\partial \vec{\mathcal{B}}(\mathfrak{R}, t)}{\partial t}$$

$$\begin{aligned}
\nabla \times \vec{\mathcal{H}}(\mathfrak{R}, t) &= \vec{\mathcal{J}}_v(\mathfrak{R}, t) + \frac{\partial \vec{\mathcal{D}}(\mathfrak{R}, t)}{\partial t} \\
\nabla \cdot \vec{\mathcal{D}}(\mathfrak{R}, t) &= \rho_v(\mathfrak{R}, t) \\
\nabla \cdot \vec{\mathcal{B}}(\mathfrak{R}, t) &= 0.
\end{aligned} \tag{2.1}$$

The spatial position of the field quantities is denoted by \mathfrak{R} (\mathfrak{R} would be x, y, z for the standard rectangular coordinate system) and t denotes time in Equation 2.1. Note that the field quantities above are vectors. In this chapter, vectors are designated by an arrow over the vector quantity (*e.g.* $\vec{\mathbf{E}}$) and complex numbers are designated by boldface quantities (*e.g.* \mathbf{E}). It is assumed that the media of propagation between the radar and target is ideal free space, which is linear, time-invariant, homogeneous, isotropic, dispersionless, and lossless. With the use of the Fourier Transform, to convert from the (\mathfrak{R}, t) domain to the (\mathfrak{R}, ω) domain, Maxwell's Equations can be expressed in the frequency domain point form as

$$\begin{aligned}
\nabla \times \vec{\mathbf{E}}(\mathfrak{R}, \omega) &= -j\omega \vec{\mathbf{B}}(\mathfrak{R}, \omega) \\
\nabla \times \vec{\mathbf{H}}(\mathfrak{R}, \omega) &= \vec{\mathbf{J}}_v(\mathfrak{R}, \omega) + j\omega \vec{\mathbf{D}}(\mathfrak{R}, \omega) \\
\nabla \cdot \vec{\mathbf{D}}(\mathfrak{R}, \omega) &= \rho_v(\mathfrak{R}, \omega) \\
\nabla \cdot \vec{\mathbf{B}}(\mathfrak{R}, \omega) &= 0
\end{aligned} \tag{2.2}$$

where ω denotes the radian frequency. It will be assumed that all of the above field terms (in Equations 2.2) are time-harmonic [41], and thus contain an implicit $e^{j\omega t}$ term. This term is suppressed for the remainder of this work. The constitutive relations for free space are

$$\vec{\mathbf{D}} = \epsilon_o \vec{\mathbf{E}} \tag{2.3}$$

$$\vec{\mathbf{B}} = \mu_o \vec{\mathbf{H}}. \quad (2.4)$$

It is well known that the field due to a point source of current is proportional to $\frac{e^{-jk_o r}}{r}$ where r is the distance from the point source to the observation point and $k_o = \frac{2\pi}{\lambda_o}$ where λ_o is the wavelength of the electromagnetic wave in free space. This is the mathematical representation for a spherically expanding wave. However, for this research, it is assumed that the target is in the far field of the radar antenna. Thus, it is assumed that the incident electromagnetic field is “locally-plane” around the target. An expression for a plane wave is found by solving Maxwell’s Equations in a source-free region (source-free means that $\mathbf{J}_v(\mathfrak{R}, \omega) \equiv 0$ and $\rho_v(t) \equiv 0$). With some manipulation of Equations 2.2–2.4 the free space wave-equation is found and given by

$$\nabla^2 \vec{\mathbf{E}} - k_o^2 \vec{\mathbf{E}} = 0, \quad (2.5)$$

where

$$k_o = \omega \sqrt{\mu_o \epsilon_o} = \frac{2\pi}{\lambda_o}. \quad (2.6)$$

A solution to this wave-equation is a plane wave and is given by

$$\vec{\mathbf{E}}(\mathfrak{R}, \omega) = \mathbf{E}(\mathfrak{R}, \omega) \hat{\mathbf{p}}, \quad (2.7)$$

where

$$\mathbf{E}(\mathfrak{R}, \omega) = E_o e^{j\phi_o} e^{-jk_o r}, \quad (2.8)$$

and

$$E_o = |\mathbf{E}(\mathfrak{R}, \omega)|. \quad (2.9)$$

The absolute value signs take the magnitude of the complex scalar $\mathbf{E}(\mathfrak{R}, \omega)$. The term $\hat{\mathbf{p}}$ is a complex unit vector which expresses the direction (or polarization) of the electric field. The terms E_o and ϕ_o are the arbitrary magnitude and phases of the electric field, respectively. This wave is traveling in the positive r direction. The term $\hat{\mathbf{p}}$ has the properties

$$\hat{\mathbf{p}} \cdot \hat{\mathbf{p}}^* = 1, \quad (2.10)$$

$$\hat{\mathbf{p}} \cdot \hat{\mathbf{p}}_{\perp}^* = \hat{\mathbf{p}}^* \cdot \hat{\mathbf{p}}_{\perp} = 0, \quad (2.11)$$

where $*$ denotes complex conjugate. The unit vector $\hat{\mathbf{p}}_{\perp}$ is defined to be orthogonal to the unit vector $\hat{\mathbf{p}}$. Using linear combinations of these vectors, it is possible to construct any desired polarization.

2.3 Scattering Matrix Formulation

As stated before, the scattering matrix relates the transmitted electric field to the scattered electric field. The transmitted electric field will be expressed as the linear combination of a horizontally polarized component and a vertically polarized component. Thus,

$$\vec{\mathbf{E}}^t = \mathbf{E}_h^t \hat{\mathbf{p}}_h + \mathbf{E}_v^t \hat{\mathbf{p}}_v. \quad (2.12)$$

The transmitted electric field is a function of range from the radar (or transmitter). The electric field incident upon the target at a range r_o from the radar is given by

$$\vec{\mathbf{E}}^i = \vec{\mathbf{E}}^t(r_o). \quad (2.13)$$

Of course, most targets have physical size and are not located at a single point. It is assumed that the magnitude of the incident field is constant in the vicinity of the

target, but the phase of the incident field is not. The incident electric field at a distance r_i from the reference point r_o is given by

$$\mathbf{E}^i(r_i) = E_o e^{j(\phi_o - 2\pi \frac{r_i}{\lambda_o})}, \quad (2.14)$$

where

$$E_o = |\mathbf{E}^t(r_o)|, \quad (2.15)$$

and ϕ_o is an arbitrary phase constant. The point r_o on the target will be called the phase reference point on the target.

The scattered electric field, $\vec{\mathbf{E}}^s$, is a function of range from the target (the reference point on the target, designated r_o for the incident electric field, is considered the origin for the scattered electric field). Thus, the incident electric field and the scattered electric field can be expressed in the following matrix relationship as

$$\begin{bmatrix} \mathbf{E}_h^s(\omega) \\ \mathbf{E}_v^s(\omega) \end{bmatrix} = \begin{bmatrix} a_{hh}(\omega) & a_{hv}(\omega) \\ a_{vh}(\omega) & a_{vv}(\omega) \end{bmatrix} \begin{bmatrix} \mathbf{E}_h^i(\omega) \\ \mathbf{E}_v^i(\omega) \end{bmatrix} \quad (2.16)$$

where the incident field value is measured at the point r_o and the scattered field is measured back at the radar. Equation 2.16 shows how the polarization of the scattered field may be different than the polarization of the incident field, and thus, the target "changes" the polarization of the electromagnetic wave. Since the scattered field is measured at the radar, and it is known that the scattered field will expand spherically in the far field, the $\frac{e^{-jk_o r}}{r}$ term, where r is the distance from the phase reference point on the target to the radar, can be taken out of the scattering matrix. This is a more convenient way to express the scattering matrix. The a coefficients

can be written as

$$\mathbf{a}_{XY} = \mathbf{s}_{XY} \frac{e^{-jk_0 r}}{r} \quad XY \in [hh, hv, vh, vv]. \quad (2.17)$$

Using Equations 2.17 and 2.16, the incident and scattered electric fields are now related by

$$\begin{bmatrix} \mathbf{E}_h^s(\omega) \\ \mathbf{E}_v^s(\omega) \end{bmatrix} = \begin{bmatrix} s_{hh}(\omega) & s_{hv}(\omega) \\ s_{vh}(\omega) & s_{vv}(\omega) \end{bmatrix} \begin{bmatrix} \mathbf{E}_h^i(\omega) \\ \mathbf{E}_v^i(\omega) \end{bmatrix} \left(\frac{e^{-jk_0 r}}{r} \right) \quad (2.18)$$

where the four s_{XY} elements form the scattering matrix. The scattering matrix above is a function of frequency only (and not range). This is true as long as the radar and target are fixed in space relative to one another. As the radar-target orientation changes (in aspect angle), the scattering matrix changes. It is assumed in this research that the range between the radar and the designated phase center on the target remains fixed. If this is not the case, then corrections can be made to the data to achieve this situation [42]. Thus, the s_{XY} elements, denoted the scattering coefficients, are a function of radar-target orientation. For the purposes of the scattering matrix, only one set of angles, (θ, ϕ) , is required to designate the radar-target orientation.

In SAR, the radar moves while the target remains fixed, whereas in ISAR, the radar remains fixed while the target moves. The scattering coefficients are identical for either scenario. It is assumed that the scattering coefficients correspond to the scenario where there is no relative velocity between the target and the radar. If this is not the case, then the measurements can be corrected to simulate this situation [42]. Figure 2 shows the radar-target orientation. This is a target fixed coordinate system;

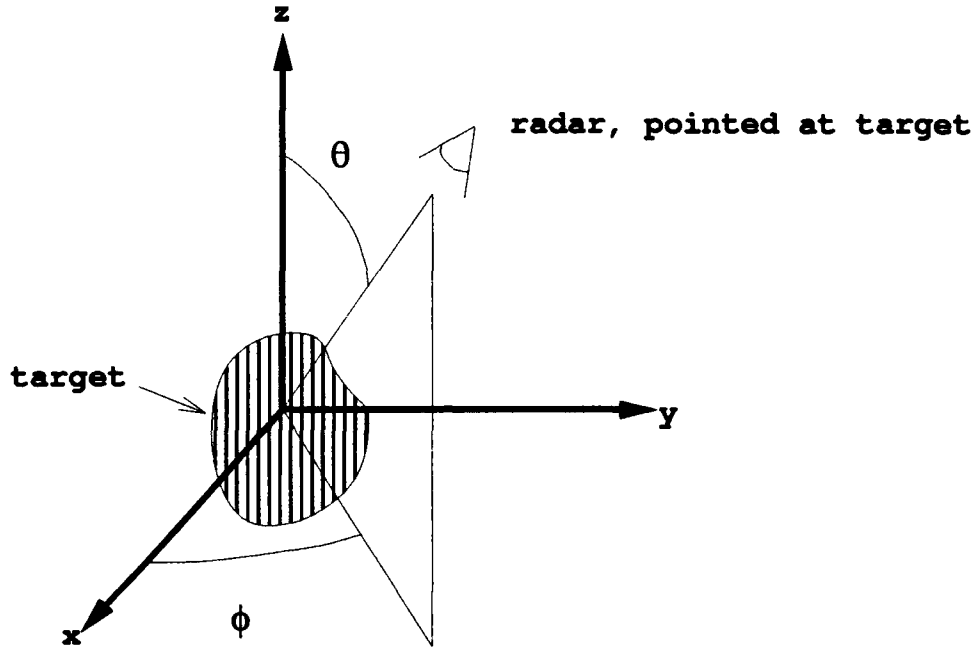


Figure 2: Radar Target orientation.

that is, the target does not move relative to the coordinate system, and only the radar moves. Thus, the more general form of Equation 2.18 is given by

$$\begin{bmatrix} \mathbf{E}_h^s(\omega, \theta, \phi) \\ \mathbf{E}_v^s(\omega, \theta, \phi) \end{bmatrix} = \begin{bmatrix} s_{hh}(\omega, \theta, \phi) & s_{hv}(\omega, \theta, \phi) \\ s_{vh}(\omega, \theta, \phi) & s_{vv}(\omega, \theta, \phi) \end{bmatrix} \begin{bmatrix} \mathbf{E}_h^i(\omega, \theta, \phi) \\ \mathbf{E}_v^i(\omega, \theta, \phi) \end{bmatrix} \left(\frac{e^{-jk_0 r}}{r} \right) \quad (2.19)$$

where the coordinates θ and ϕ , as defined in Figure 2, are the standard spherical coordinate angles. The scattering matrix is formally defined as

$$\mathbf{S}_{hv: hv}(\omega, \theta, \phi) = \begin{bmatrix} s_{hh}(\omega, \theta, \phi) & s_{hv}(\omega, \theta, \phi) \\ s_{vh}(\omega, \theta, \phi) & s_{vv}(\omega, \theta, \phi) \end{bmatrix} \quad (2.20)$$

where the $hv : hv$ notation on $\mathbf{S}_{hv: hv}$ denotes that the scattering matrix is based upon an incident field (first hv term) expressed in the horizontal and vertical polarization basis and a scattered field (second hv term) expressed in the horizontal and vertical

polarization basis.

The radar cross section (RCS) of an object can be determined from the scattering coefficients. The RCS of an object is defined as

$$\sigma_{XY}(\omega, \theta, \phi) = \lim_{r \rightarrow \infty} \left(4\pi r^2 \frac{|E_s(\omega, \theta, \phi, r)|^2}{|E_i(\omega, \theta, \phi, r)|^2} \right) \quad (2.21)$$

Comparing Equations 2.19 and 2.21, it is observed that

$$\sigma_{XY} = 4\pi |s_{XY}|^2. \quad (2.22)$$

The choice of a horizontal and vertical polarization basis was arbitrary and any two linearly independent bases could be chosen [31]. Usually, orthogonal bases such as left circular-right circular or horizontal-vertical are used. The scattering matrix will change when different polarization bases are chosen. However, the scattering matrix contains all of the inherent target information.

The conversion of the scattering matrix from one polarization basis to another is easily accomplished. This is outlined by Chamberlin in [43], Section 4.2. For example, the conversion from the horizontal-vertical polarization basis to the right circular-left circular polarization basis is given by

$$\begin{bmatrix} s_{rr}(\omega, \theta, \phi) & s_{rl}(\omega, \theta, \phi) \\ s_{lr}(\omega, \theta, \phi) & s_{rr}(\omega, \theta, \phi) \end{bmatrix} = \mathbf{U}_{rl:hv}^T \begin{bmatrix} s_{hh}(\omega, \theta, \phi) & s_{hv}(\omega, \theta, \phi) \\ s_{vh}(\omega, \theta, \phi) & s_{vv}(\omega, \theta, \phi) \end{bmatrix} \mathbf{U}_{rl:hv} \quad (2.23)$$

or

$$\mathbf{S}_{rl:rl} = \mathbf{U}_{rl:hv}^T \mathbf{S}_{hv:hv} \mathbf{U}_{rl:hv} \quad (2.24)$$

where

$$\mathbf{U}_{rl:hv} = \frac{1}{\sqrt{2}} \begin{bmatrix} 1 & \pm 1 \\ j & \pm j \end{bmatrix} \quad (2.25)$$

and where the choice of sign is a matter of convention and T denotes transpose. Choosing the second column of $\mathbf{U}_{rl:hv}$ to be $\frac{1}{\sqrt{2}} [1, j]^T$, the receive wave polarizations for transmit left-circular polarization and transmit right-circular polarization are equal at $\omega t = 0$ (assuming the scattering matrix is unitary). With the second column of $\mathbf{U}_{rl:hv}$ set at $\frac{1}{\sqrt{2}} [1, j]^T$, Equation 2.23 reduces to

$$\begin{bmatrix} s_{rr} & s_{rl} \\ s_{lr} & s_{rr} \end{bmatrix} = \begin{bmatrix} s_{hh} + js_{hv} + js_{vh} - s_{vv} & s_{hh} - js_{hv} + js_{vh} + s_{vv} \\ s_{hh} + js_{hv} - js_{vh} + s_{vv} & s_{hh} - js_{hv} - js_{vh} - s_{vv} \end{bmatrix} \quad (2.26)$$

where the (ω, θ, ϕ) notation has been dropped for convenience. Assuming that $s_{hv} = s_{vh}$ (valid assumption for free space, which is the assumed media of propagation between the radar and the target), Equation 2.26 reduces to

$$\begin{bmatrix} s_{rr} & s_{rl} \\ s_{lr} & s_{rr} \end{bmatrix} = \begin{bmatrix} s_{hh} + 2js_{hv} - s_{vv} & s_{hh} + s_{vv} \\ s_{hh} + s_{vv} & s_{hh} - 2js_{hv} - s_{vv} \end{bmatrix}. \quad (2.27)$$

Conversions to other polarization bases are accomplished using different $\mathbf{U}_{AB:CD}$ matrices (where AB and CD are arbitrary polarization bases), as outlined in [43].

2.4 Summary

In this chapter the scattering matrix and the data collection geometry were defined. It was shown that the scattering matrix contains all of the inherent target information. This is a background chapter which outlines the assumptions concerning the form and content of the scattering matrix and how the scattering coefficients are related to the radar data. It was also stated here that the assumed media of propagation is free space. The concept of polarization bases was also introduced.

CHAPTER III

Electromagnetic Behavior of Canonical Scattering Centers

3.1 Background and Introduction

Before a target can be broken down into its primary scattering centers, the scattering characteristics of the canonical scattering centers must be estimated and modeled. The scattering characteristics consist of, for this research, the monostatic scattering as a function of frequency of illumination, angle of incidence, and transmit and receive polarization. A great deal of work has been done in the area of plane wave scattering prediction for simple shapes [44, 45]. Exact analytical scattering solutions exist for only a few simple shapes, such as a sphere and an infinite right circular cylinder.

Approximate methods are available to estimate the scattering from other shapes. For example, the Method of Moments (MM) [46] is a numerical technique which, theoretically, can estimate the scattering from any physical structure. It has been implemented in a computer code [47] for flat plate type structures, which can be used to predict the scattering from simple thin rectangular plates and combinations of these plates. Shapes such as dihedrals, trihedrals and cubes can be constructed from combinations of these shapes. The Geometrical Theory of Diffraction (GTD) [48],

which has been implemented in a computer code [49] for limited scenarios, can also be used to predict the scattering from these shapes. The GTD is an asymptotic high-frequency scattering estimate; that is, the GTD estimate becomes more and more accurate as the frequency increases. The MM is an accurate estimate at all frequencies, but as the frequency increases so does the required amount of computations. The CPU time goes up as frequency to the fourth power for two dimensional objects such as a flat plate. Along with exact and approximate theoretical methods of scattering prediction, experimental scattering results exist for several simple shapes such as a thin metal plate and a sphere-capped cylinder. This data is multiple frequency, angle, and polarization.

A goal of this chapter is to develop a list of canonical scattering centers which are commonly found on the radar targets of interest. This list must be based upon knowledge of what basic scattering mechanisms are present on radar targets. Eight canonical scattering centers are analyzed here. They are the point scatterer, sphere, flat plate, corner, edge, dihedral, trihedral, and cylinder. This group is not all inclusive for all potential radar targets, but contains scattering centers found on many radar targets. The scattering characteristics of each will be analyzed in this chapter. Also, models for the scattering behavior of each of the canonical scattering centers are determined. These models must be simple enough for use in inverse scattering algorithms but be as accurate as possible from an electromagnetic sense. These models are listed in Table 1 at the end of the next section.

Next, the scattering from a complicated target is modeled by the sum of the

scattering responses from a finite number of canonical scattering centers. In Chapter V, the scattering from the canonical scattering centers is modeled by damped exponentials. The validity of this model is discussed at the end of Chapter III.

3.2 Electromagnetic Analysis

In this section, the scattering behavior of each of the scattering centers are investigated as functions of angle and frequency. The point scatterer, the sphere and the infinite circular cylinder have exact analytical solutions. The remaining scatterers in Table 1 have no exact solutions and are analyzed utilizing the MM and the GTD. The standard spherical coordinate system is used in the following sections and is sketched in Figure 3. It also must be pointed out that this analysis concentrates on the high-frequency scattering of a structure. As stated before, high-frequency implies that the overall size of an object is near or over one wavelength.

3.2.1 Point Scatterer

The point scatterer, by definition, scatters identically for all frequencies, angles, and polarizations. Thus the model for this scattering center, which is a constant for both frequency and angular dependencies, is simple and accurate.

3.2.2 Sphere

There is a theoretical solution for the scattering from the sphere [45]. This solution is an infinite series which gives the backscattered field for one frequency of illumination. The impulse response of the sphere is shown in Figure 4, taken from [1].

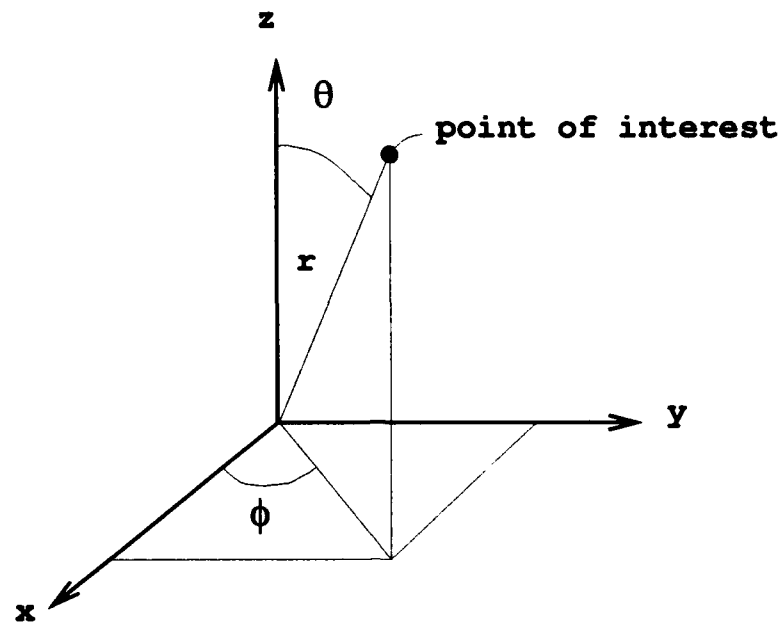


Figure 3: Standard spherical coordinate system.

This plot has three curves. The solid line is an approximation using 475 discrete frequency solutions found using the exact theoretical solution. Fortunately, the series solution to the scattering from the sphere converges quickly and an accurate result is available using just a small number of terms (usually around 25 terms). A simple Inverse Fast Fourier Transform (IFFT) is used to determine the time-domain waveform. The dotted curve in Figure 4 is found using the Physical Optics (PO) scattering approximation. This approximation assumes that the object has a 'lit' side and a 'dark' side. The lit side corresponds to the surface of the object that is directly illuminated by the incident field and the dark side is the remaining surface of the object. The PO approximation assumes an equivalent current induced by

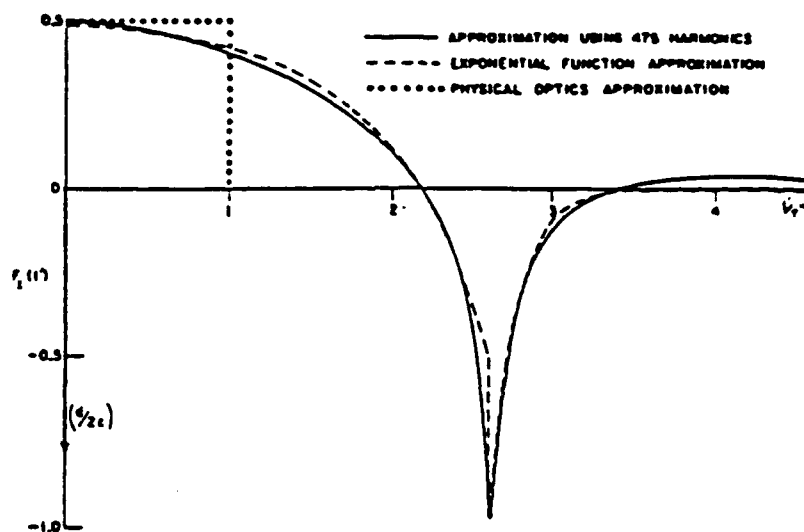


Figure 4: Impulse response approximation for a conducting sphere, taken from [1].

the incident fields on the lit side and the scattered fields are found from this current. The final curve on the plot, the exponential function approximation, is the PO approximation along with two exponential functions which are added in to correct for some of the phenomena that the PO approximation misses such as the creeping wave. The solid line in Figure 4 is based upon the exact electromagnetic solution to the sphere and therefore is assumed to be the most accurate model of the sphere. Note that there is an impulse function (whose energy is directly proportional to the diameter of the sphere) associated with this impulse response at time $t' = 0$.

The RCS of a sphere of radius a as a function of wavelength is shown in Figure 5 taken from [2]. This plot was generated by calculating the infinite series at a number

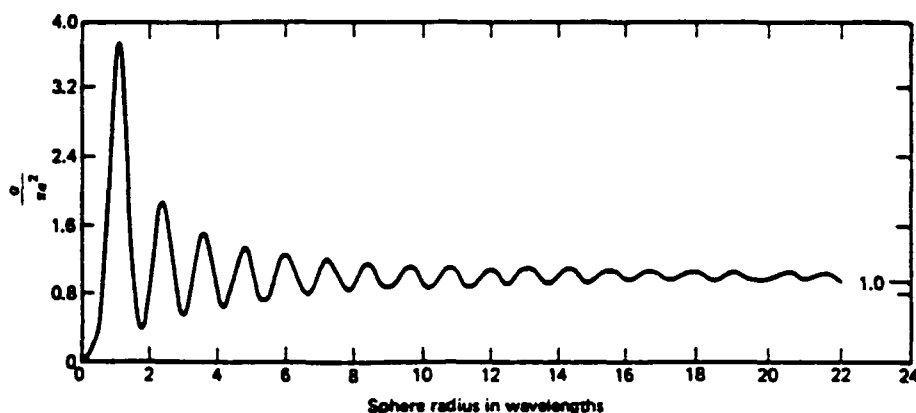


Figure 5: Frequency domain response for a conducting sphere, taken from [2]. The sphere radius is a , while σ is the RCS of the sphere.

of frequencies. The x -axis of this plot is the sphere radius, in wavelengths. As the sphere radius increases in relation to the wavelength, it can be seen that the RCS of the sphere, σ , begins to converge to its high-frequency value of πa^2 . Recall that the RCS of an object is related to the field scattered by the object by Equation 2.21. The frequency model for a sphere is chosen to be a constant, which is a high-frequency approximation to the actual scattering from a sphere. Thus, this only models the impulse function in Figure 4. The angular behavior for a sphere is constant as a function of angle and polarization due to the physical symmetry of the sphere. Thus, the angular model for a sphere is that of a constant.

3.2.3 Edge and Corner

Since the methods of determining the scattering from edges and corners are identical, the procedure for determining the scattering from each will be described con-

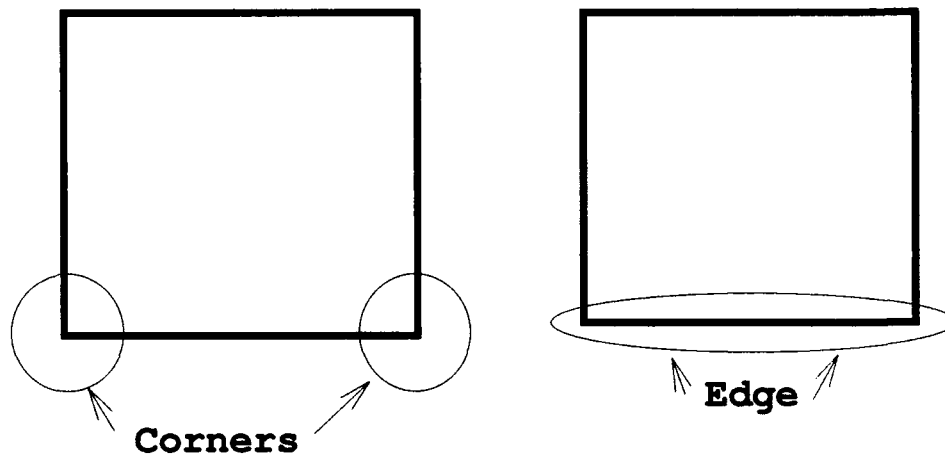


Figure 6: Definition of a corner and an edge.

currently. The scattering by the edge and corner are approximated by taking the scattering results for a flat plate using the MM and time-gating out an edge or corner. For the purposes of this research, a corner is defined as any point on the perimeter of a thin polygonal structure (such as a square plate) where the angle between the two rays extending out from the point is not 180° . An edge is defined as the knife-edge structure between two corners on the thin polygonal structure. Figure 6 shows the definition of an edge and a corner for the thin square plate structure.

The two methods used to estimate the scattering from edges and corners are the MM and the GTD. Historically, the MM has always been considered a 'more accurate' estimate since it is a numerical approximation to the actual integral equation that arises in the scattering problem. The GTD is based on asymptotic evaluations of the same integral equations and also the assumption that the scattering centers

on a structure are electrically independent.

The impulse response of a thin plate shows that the predominant scattering centers occur at edges and corners which are physical discontinuities. This confirms a basic assumption of this research, that the scattering from objects occurs at isolated scattering centers such as the corners and edges of thin plates. This behavior can be exploited to determine just how an edge alone scatters. Note that the GTD prediction of the scattering from an edge is simply the sum of the GTD scattering predictions of the two corners that are at the ends of the edge.

A MM solution for the scattering from a flat plate can be found using the code described in [47]. Data for a 0.5 meter square flat perfectly conducting thin plate was obtained from 50 MHz to 3.2 GHz in 50 MHz steps. Due to computer time limitations, 3.2 GHz was the upper bound on the frequency for this structure. The plate was viewed at many angles. However full spherical coverage was not obtained once again due to computer limitations. Figure 7 shows the truncated impulse response of the 0.5 meter square plate oriented as shown. Note that the units of the scattering magnitude are in volts per meter. These magnitude values correspond to the scattered electric field, E_X^s , measured one kilometer from the plate for an incident field, E_Y^i , of one volt per meter. Many of the scattering plots in this chapter follow this convention. The conversion from these scattered field values to the values of the scattering coefficients is accomplished by multiplying the scattered field values by 1000 square meters per volt to yield the scattering coefficient values.

To determine the scattering from an edge or corner, the IFFT was used to convert

the frequency domain data to the time domain and then a rectangular bandpass filter was used in the time domain to isolate the scattering center of interest. The Fast Fourier Transform (FFT) was then used to convert back to the frequency domain. Figure 8 shows the frequency response of the leading edge of the plate found by the procedure outlined above. Note that the width of the bandpass window in the time (or range) domain is 0.5 meters. The x -axis of Figure 8 is in meters. The conversion between time, t , and down-range distance, $d_{\text{down-range}}$, is given by

$$d_{\text{down-range}} = \frac{ct}{2} \quad (3.1)$$

where c is the propagation velocity of the electromagnetic wave in free space.

The procedure of gating out the scattering centers on the flat plate enables the MM to yield scattering estimates for the corner and the edge. In a 1-D sense, this procedure can only be used for limited aspect angles as resolution problems arise for certain aspect angles when the corners become close in down-range distance. In 2-D, a 2-D window can be used on an image to isolate scattering centers of interest.

Two of the factors which determine the quality of the scattering estimates for the corner and the edge using the MM are Gibb's phenomena and the Fourier resolution limit. Gibb's phenomena is present in each step of the conversion from one domain to another [50]. The Fourier resolution limit is a factor in separating the responses from the various corners of the plate since only 64 data points were available for each aspect angle. However, even with these limitations, the MM still yields valuable data for many aspect angles and is a much needed tool in this analysis.

The GTD was also used to analyze the scattering response from the corner and

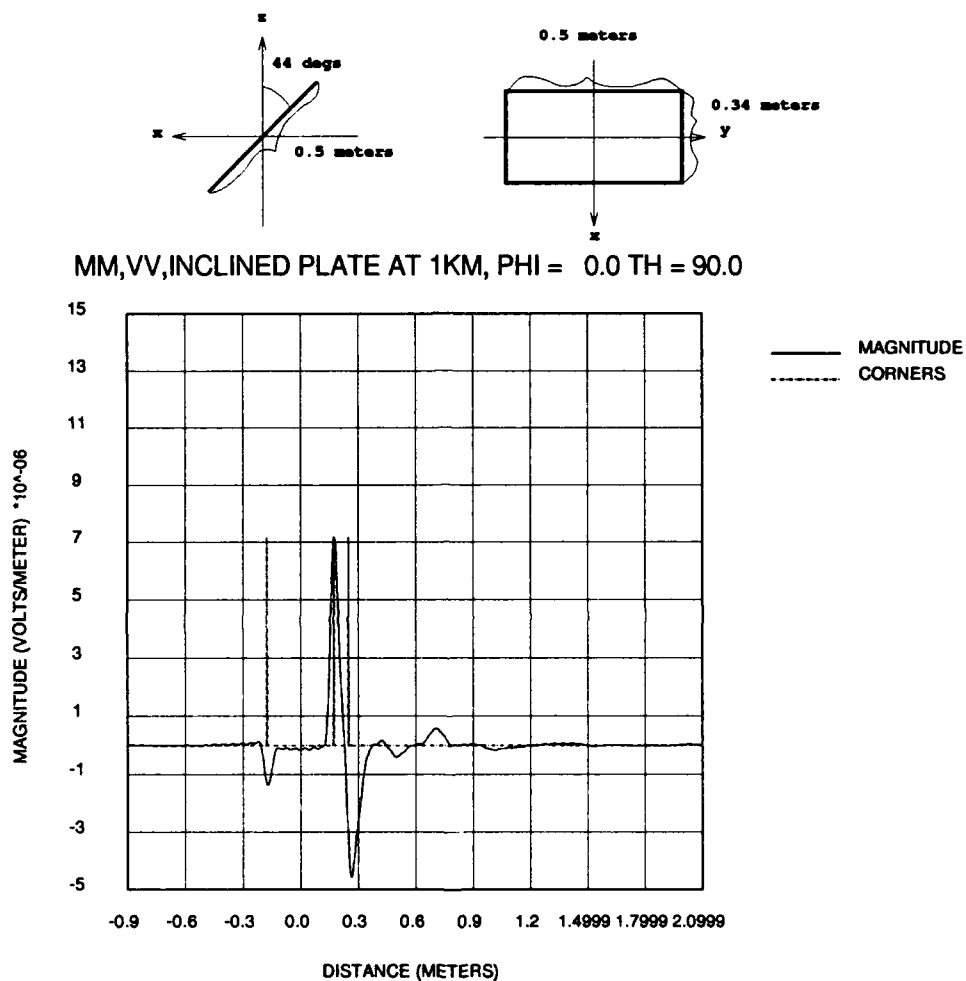


Figure 7: MM impulse response estimation for a 0.5m square inclined flat plate. Frequency samples from 50 MHz to 3.2 GHz in 50 MHz steps were used. Monostatic scattering results for $\theta = 90^\circ$ and $\phi = 0^\circ$ in the standard spherical coordinate system. The dashed lines on the plots show the locations of the leading edge, trailing edge and surface wave scattering locations for the plate.

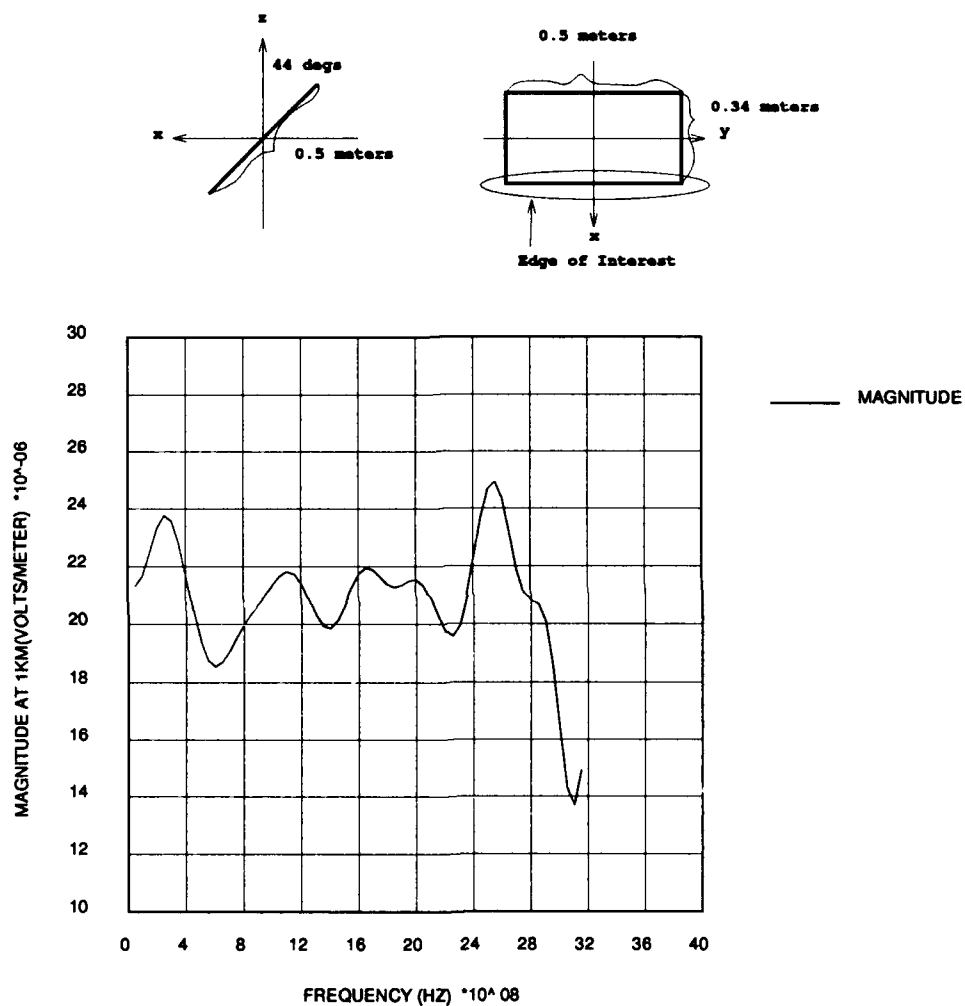
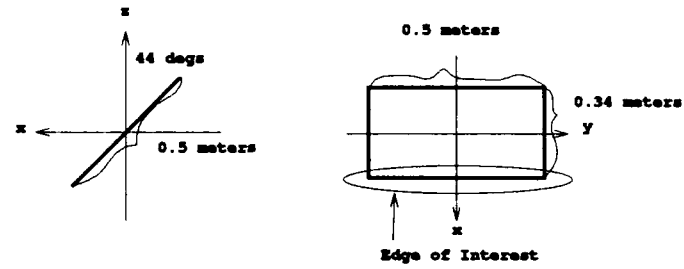


Figure 8: MM frequency domain data for the leading edge of the plate shown in Figure 7. The scattering angle is once again $\theta = 90^\circ$ and $\phi = 0^\circ$. The scattering center isolation technique described in the text was used to yield the above data.

the edge. The resolution problems associated with the MM solution are avoided by using the GTD. One of the useful features of the GTD and RCS-BSC 2.0 [49] is that the response for one corner of a plate can be found directly. The GTD determines the scattering from a structure by first calculating the scattering from each component, such as a corner or an edge, and then adds all of the components together to determine the overall scattering of the structure. Thus, the scattering from each component can be found directly, and the procedure of filtering to isolate scattering centers is not needed. This avoids the problems of Gibb's phenomena and the truncation of overlapping responses.

The GTD response for the edge of Figure 8 is shown in Figure 9. Figure 9 was generated using the computer code RCS-BSC 2.0. Note that the edge is basically a constant as a function of frequency for frequencies where the plate is over one wavelength in size, which is the region where the GTD results are accurate. Figure 10 is the frequency response of a corner as calculated by GTD. Figure 11 is the frequency response of the same corner found by using the MM, range gating and using the FFT as described earlier. From the GTD based corner scattering estimate, the frequency response of the corner is $\frac{1}{\omega}$, where ω is the radian frequency. The MM estimate follows this behavior for part of the bandwidth selected in Figure 11. Around the ends of the bandwidth for the MM estimate, the response does not follow the $\frac{1}{\omega}$ behavior. Gibb's phenomena may account for this due to the windowing required to isolate the corner in the range domain. Thus, the frequency behavior for the corner is estimated to be $\frac{1}{\omega}$ for all aspect angles and all polarizations. Thus, this frequency



— MAGNITUDE

GTD2,VV, 0.5M SQ. PLATE AT 1KM, PHI = 0.0 TH = 90.0

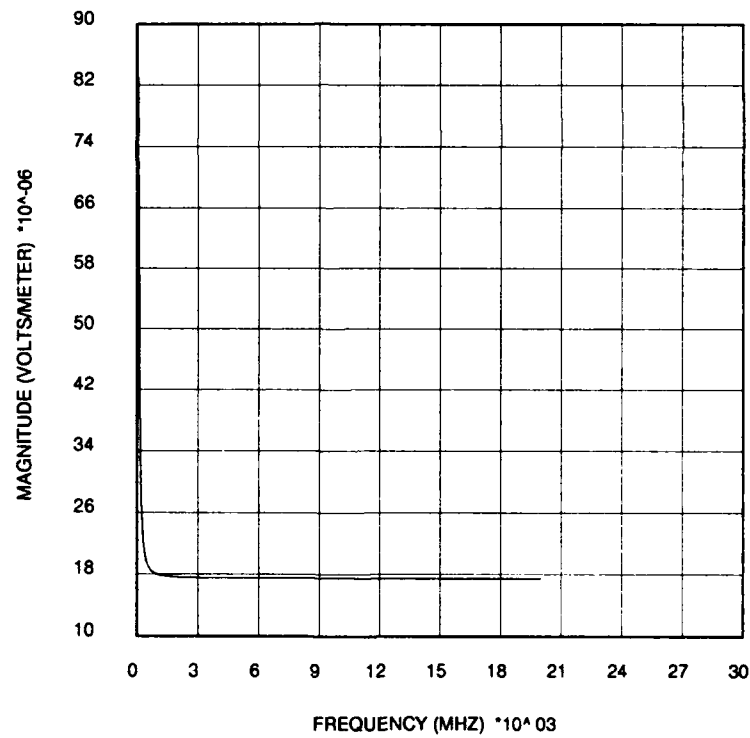


Figure 9: GTD impulse response estimation for the leading edge of the plate shown in Figure 7. Once again, the scattering angle is $\theta = 90^\circ$ and $\phi = 0^\circ$.

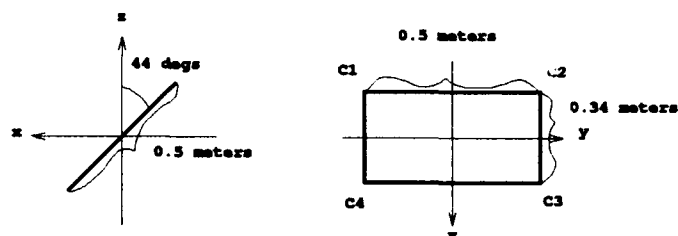
behavior is polarization independent. It is also true that the frequency behavior of an edge is also polarization independent.

Now that the frequency behavior of the edge and corner have been examined, their angular behavior will be examined. The corner and the edge exhibit highly variable angular behavior as shown in Figures 12, 13, and 14. Note that the scattering magnitudes in these plots are expressed in RCS, in units of dB relative to a square meter (DBSM). One noticeable characteristic is that there is a large jump in the scattered field when the radar approaches one of the edges that makes up the corner (that is $\phi = 0^\circ, 90^\circ, 180^\circ$, and 270°). The angles which are parallel with one of the edges that defines a corner will be called the 'grazing' angles. For the regions in-between these grazing angles, the angular response is almost constant.

For the edge, the scattering is relatively constant for angles of which are not perpendicular or parallel to the edge. For angles which are perpendicular or parallel to the edge, which are designated the grazing angles for the edge, the angular behavior is impulsive. Thus, the angular model for these scatterers will thus reflect two types of corners and edges, one with a constant angular behavior and one with an impulsive angular behavior.

3.2.4 Dihedral

A dihedral is sketched in Figure 15. The frequency response amplitude of a dihedral is proportional to frequency to the first power, or ω , for incident angles which look into the interior of the dihedral. This is illustrated in Figure 16 taken from [3] which used the GTD. The predominant scattering mechanism occurs at the apex of the



— MAGNITUDE

GTD2,VV, 0.5M SQ. PLATE AT 1KM, PHI = 45.0 TH = 90.0

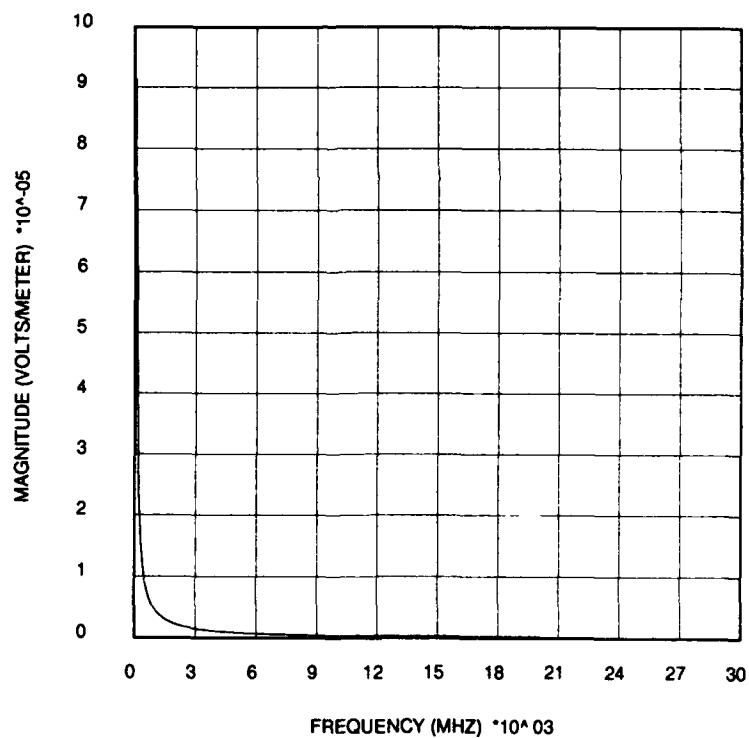


Figure 10: GTD frequency response estimation for the leading right corner (C3) of the plate shown in Figure 7. The scattering angle is fixed at $\theta = 90^\circ$ and $\phi = 45^\circ$. Frequency domain data extends from 50 MHz to 20 GHz in 50 MHz steps.

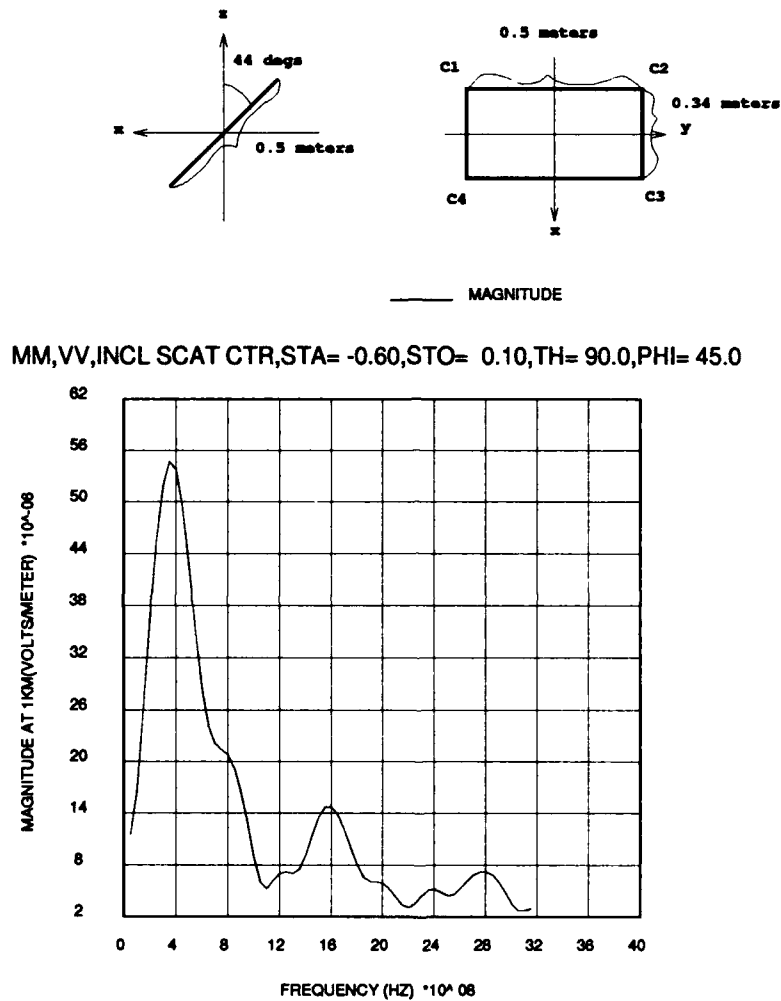


Figure 11: MM frequency response estimation for the leading right corner (C3) of the plate shown in Figure 7. Once again, the scattering angle is $\theta = 90^\circ$ and $\phi = 45^\circ$. The domain jumping techniques described in the text were used to yield the above frequency domain data.

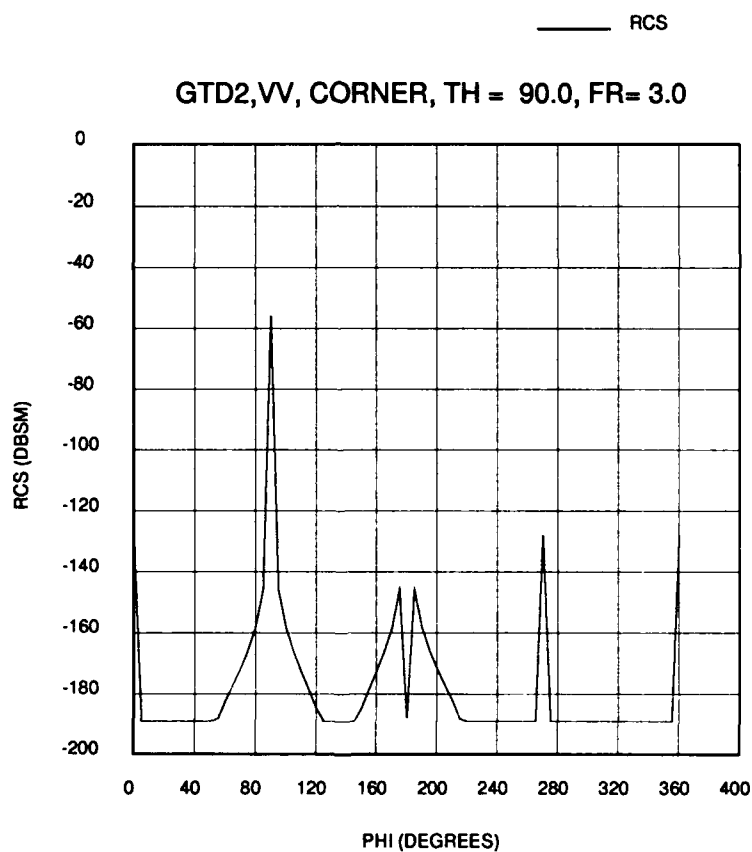
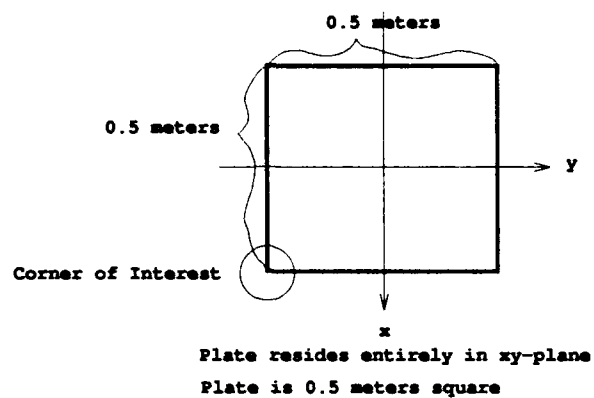


Figure 12: GTD azimuthal angular response estimation for the leading left corner of a 0.5m flat plate residing entirely in the xy -plane. The elevation angle, θ , is held constant at 90° while an azimuth scan is done in ϕ . The frequency is held constant at 3.0 GHz.

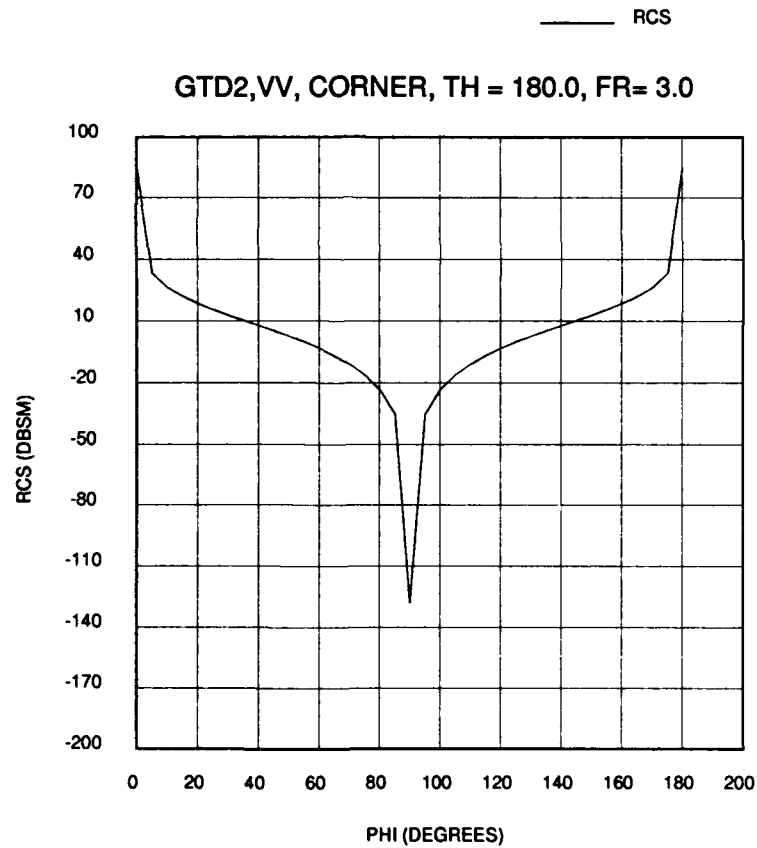
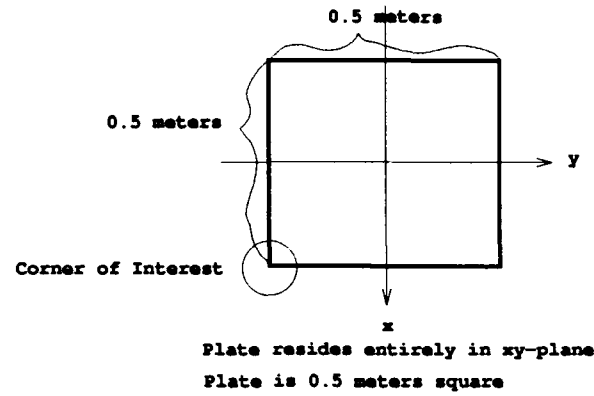


Figure 13: GTD elevation angular response estimation for the leading left corner of a 0.5m flat plate residing entirely in the xy -plane. The elevation angle, θ , is varied while the azimuth is fixed at $\phi = 0^\circ$. The frequency is held constant at 3.0 GHz.

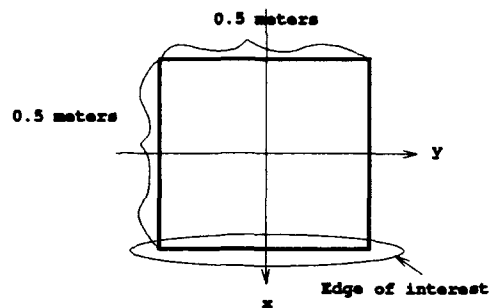


Plate resides entirely in xy -plane
 Plate is 0.5 meters square

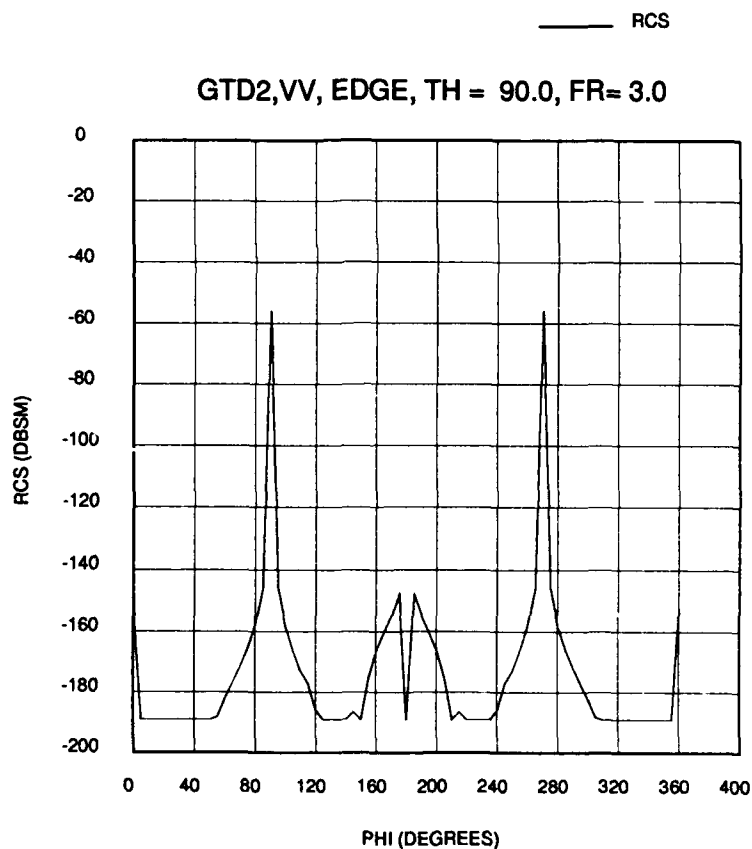


Figure 14: GTD azimuthal angular response estimation for the leading edge of a square 0.5m flat plate. The plate resides entirely in the xy -plane. Elevation is held constant at $\theta = 90^\circ$ while the azimuth is scanned in ϕ . The frequency is held constant at 3.0 GHz.

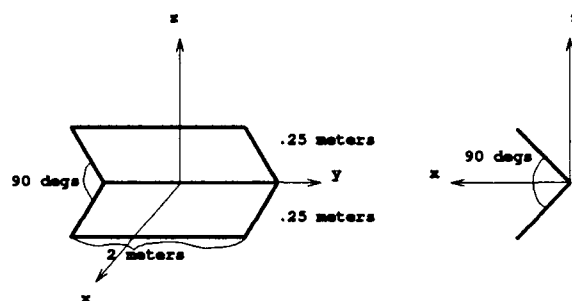


Figure 15: Sketch of a typical dihedral.

dihedral which can be seen by viewing the time domain waveform. The RCS-BSC 2.0 code does not have the capability to give as accurate estimates as those from [3]. The MM was run for the dihedral with the dimensions given in Figure 15. The time and frequency domain waveforms are given in Figures 17 and 18 respectively. These results confirm those in Figure 16, that the dihedral has a frequency dependence of ω .

Note that a dihedral only exhibits the ω frequency dependence when the angle of incidence is near $\phi = 0^\circ$ in azimuth and between $\theta = 45^\circ$ and $\theta = 135^\circ$ in elevation for the dihedral in Figure 15. If the dihedral is viewed from angles other than this, then the ω behavior is not valid and the dihedral response is more like that of corners and edges.

The angular behavior of the dihedral is shown in Figure 19. In this figure, the radar is looking into the opening of the dihedral, with $\theta = 90^\circ$ and fixed, and scanning in azimuth (ϕ). The angular behavior is basically constant except around two points. The largest return is at the specular point where there is an impulsive

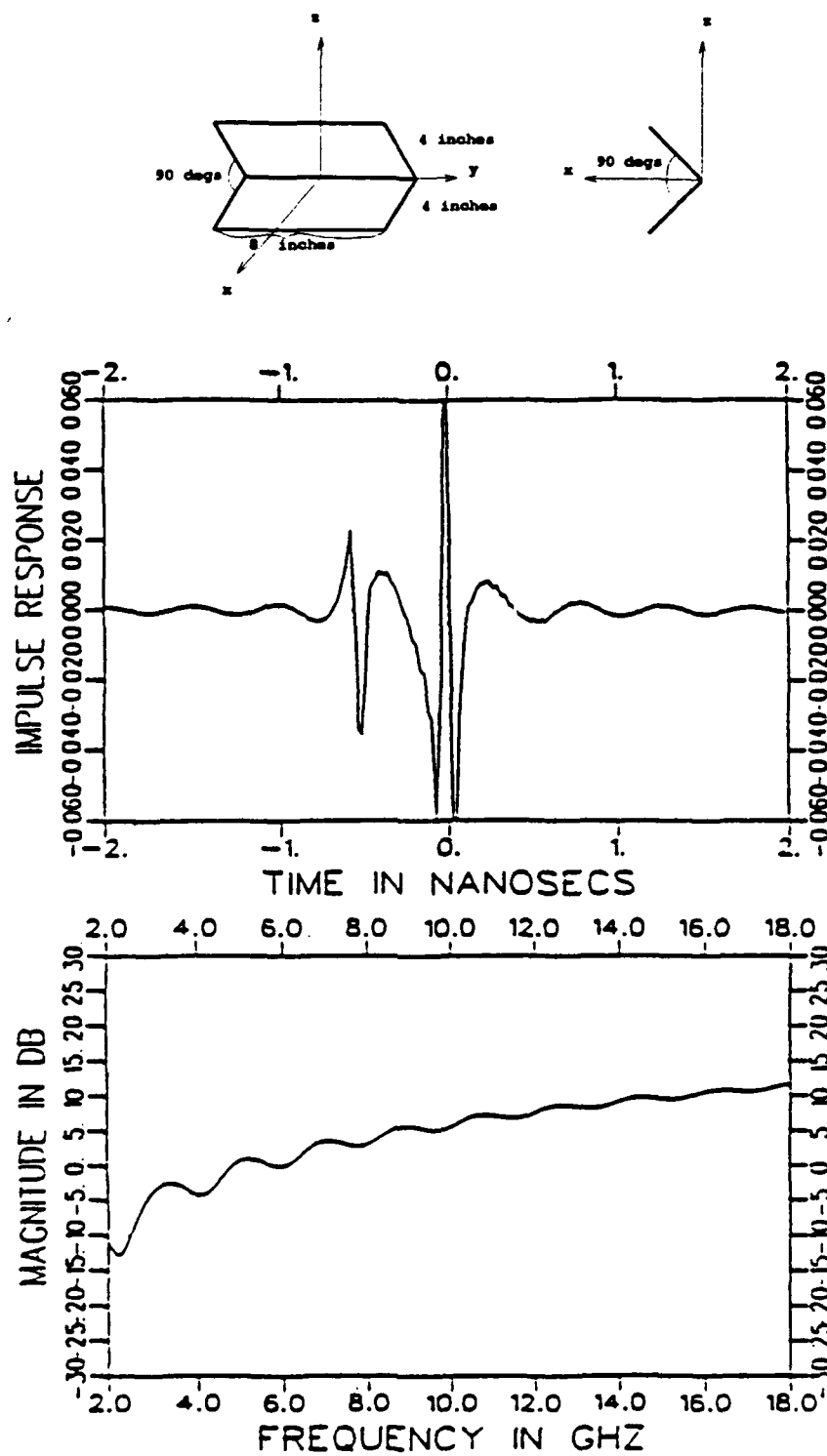


Figure 16: GTD frequency and time domain response estimates for the scattering from a rectangular dihedral, taken from [3]. The scattering angle is $\theta = 90^\circ$ and $\phi = 0^\circ$.

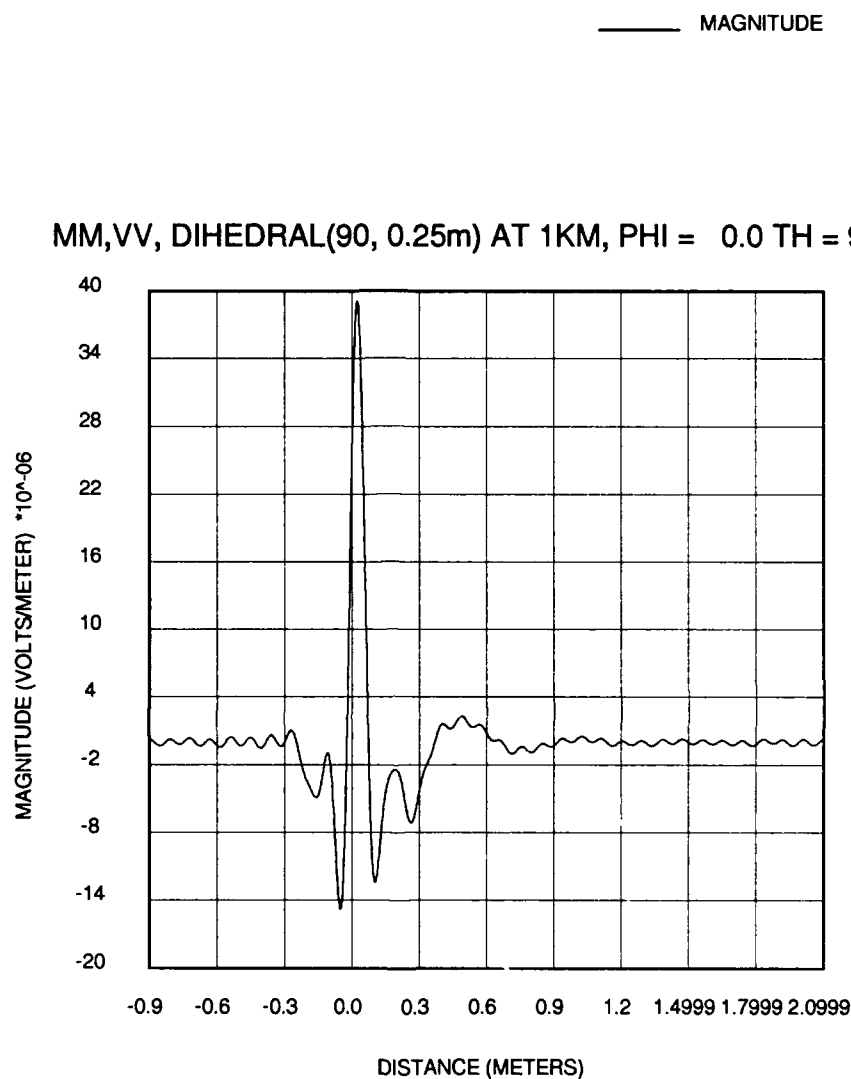


Figure 17: MM time domain response estimate for the scattering from the dihedral shown in Figure 15. The scattering angle is $\theta = 90^\circ$ and $\phi = 0^\circ$. The frequency domain data used to generate this time (or range) domain plot was from 50 MHz to 1.65 GHz in 50 MHz steps. The IFFT was used to yield the time domain data.

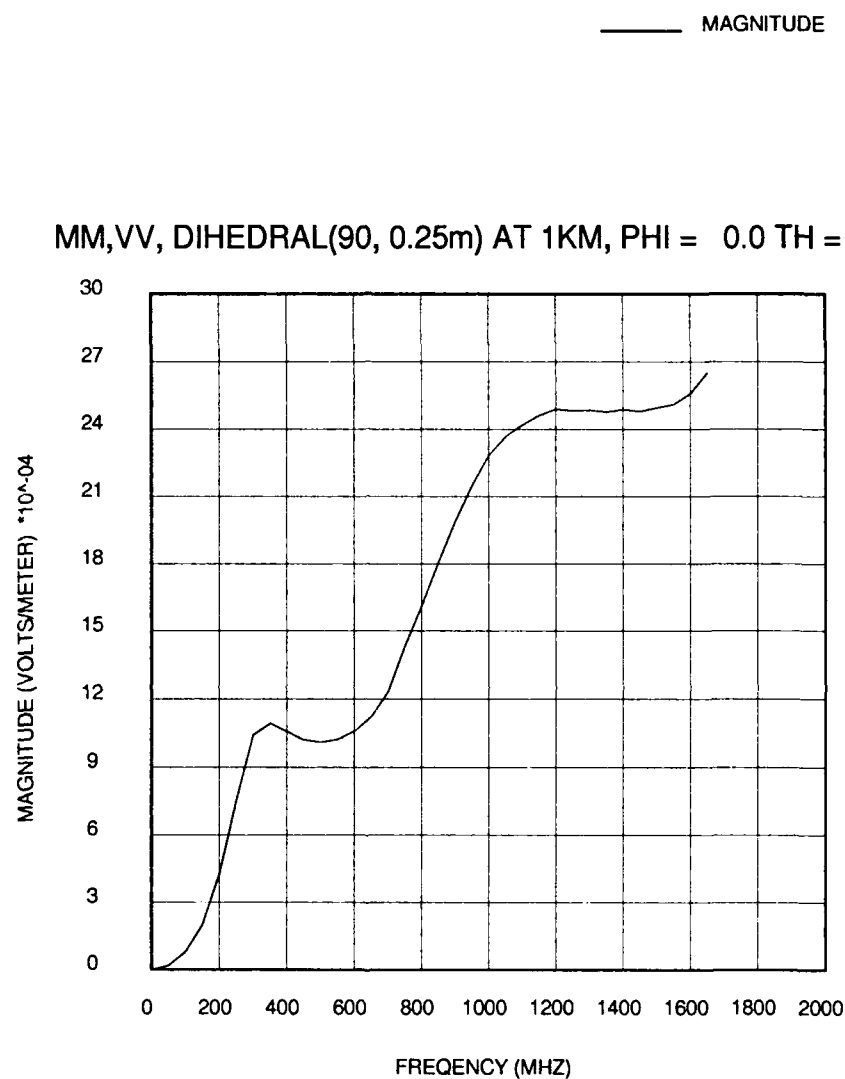


Figure 18: MM frequency response estimate for the scattering from the dihedral shown in Figure 15. The scattering angle is $\theta = 90^\circ$ and $\phi = 0^\circ$. The frequency domain data used to generate this time (or range) domain plot was from 50 MHz to 1.65 GHz in 50 MHz steps.

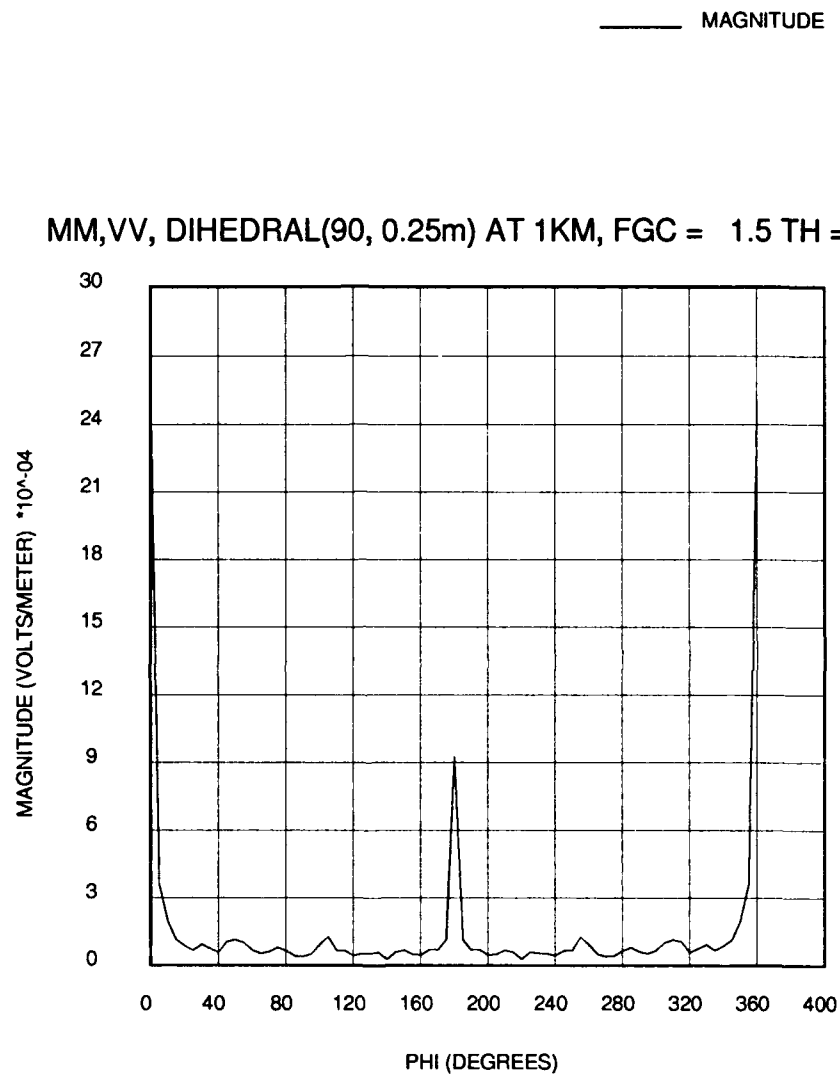


Figure 19: MM angular response estimate for the scattering from the dihedral shown in Figure 15. The scattering angle θ is held fixed at 90° while ϕ is scanned. The frequency is held constant at 1.5 GHz.

type behavior. The specular point corresponds to $\phi = 0^\circ$ and $\theta = 90^\circ$ in Figure 15. The other non-constant angular behavior occurs at $\phi = 180^\circ$ and $\theta = 90^\circ$. This corresponds to looking directly at the apex of the dihedral from behind.

An angular elevation scan of the dihedral (ϕ fixed at 0° and θ varied) is described in [3]. It consists of relatively constant behavior between the two faces of the dihedral (for θ between 45° and 135° for the dihedral in Figure 15) with a sharp drop off outside of these angles and back to a constant for $0^\circ < \theta < 45^\circ$ and $135^\circ < \theta < 180^\circ$. This is best modeled by a piecewise constant (step-like) function.

3.2.5 Trihedral

The trihedral is shown in Figure 20. No accurate GTD solutions for the trihedral exist. The MM was run for the trihedral and the frequency domain plot is shown in Figure 21. This figure shows that, in general, the scattering response is increasing in magnitude as frequency increases. The results shown in this figure do not support a simple frequency model for the trihedral. The validity of these MM results are suspect, since the basis functions chosen for the MM solution outlined in [47] may not represent the current distributions that exist on the trihedral. However, this MM solution is the best available scattering prediction technique for the trihedral. Thus, since a simple model is required, the most accurate simple model for the frequency domain response for the trihedral is that of ω , for incident angles which look into the interior of the trihedral. This is consistent with the model chosen for a dihedral when the incident angles for the dihedral are $\phi = 0^\circ$ and $45 < \theta < 135$. It is assumed that the same type of physical phenomena (that of specular return)

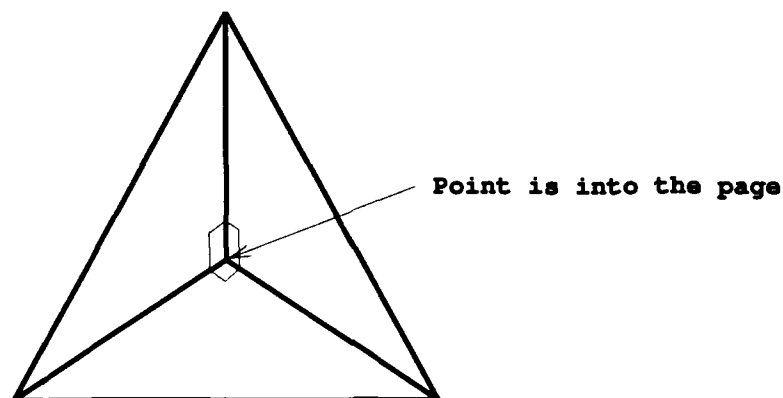


Figure 20: Definition of a trihedral.

occurs for the trihedral for viewing angles which are looking into the interior of the trihedral that occurs for the dihedral when the viewing angles of the dihedral are at $\phi = 0^\circ$ and $45 < \theta < 135$.

The angular behavior of the trihedral is shown in Figure 22. This behavior suggests that the scattering is much larger when the radar is looking into the concave (or interior) structure of the trihedral than it is when the radar is not. Over the viewing angles that look into the concave structure of the trihedral, the scattering behavior is nearly constant. The scattering behavior is also somewhat constant over the other regions (but much lower). This suggests the angular model of a piecewise constant (step-like) function.

3.2.6 Flat Plate

The flat plate can be described by the sum of the responses of the edges and corners which comprise the plate for almost all aspect angles. One physical phenomena

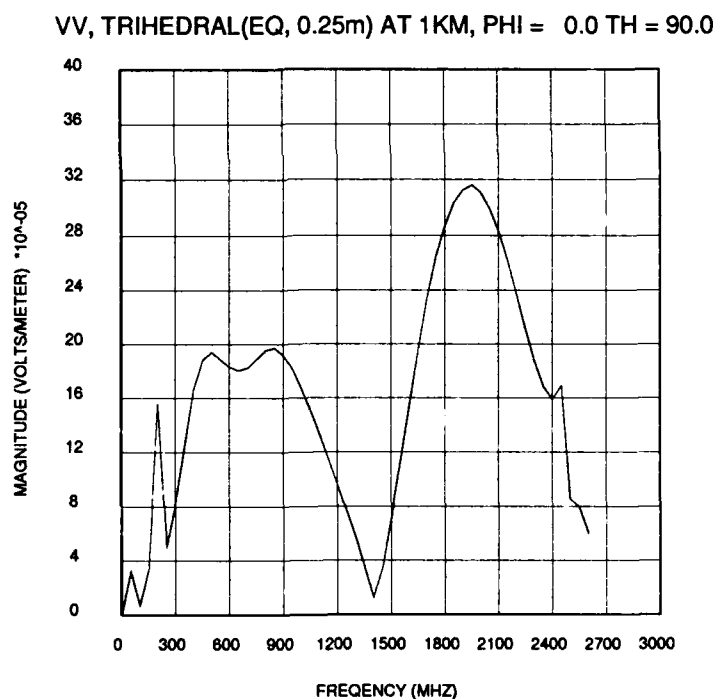
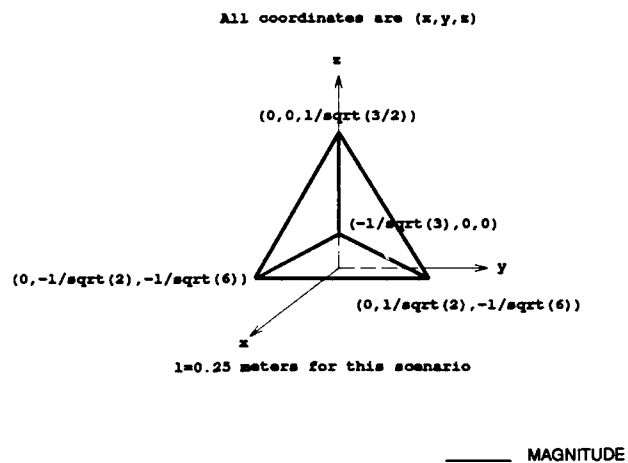
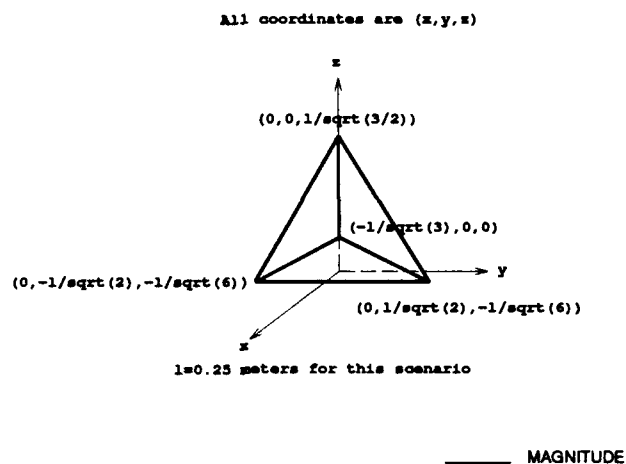


Figure 21: MM frequency domain response estimate for the scattering from the trihedral shown. The scattering angle is $\theta = 90^\circ$ and $\phi = 0^\circ$. The data is from 50 MHz to 2.65 GHz in 50 MHz steps.



MM,VV, TRIHEDRAL(90, 0.25m) AT 1KM, FGC = 2.5 TH = 90.0

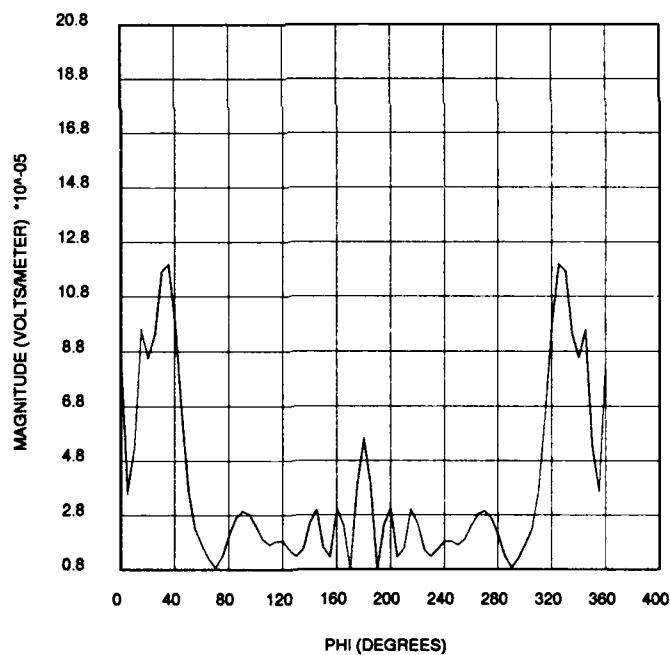


Figure 22: MM angular response estimate for the scattering from the trihedral shown. The frequency is held constant at 2.5 GHz. The elevation angle is fixed at $\theta = 90^\circ$ while the azimuth is scanned in ϕ .

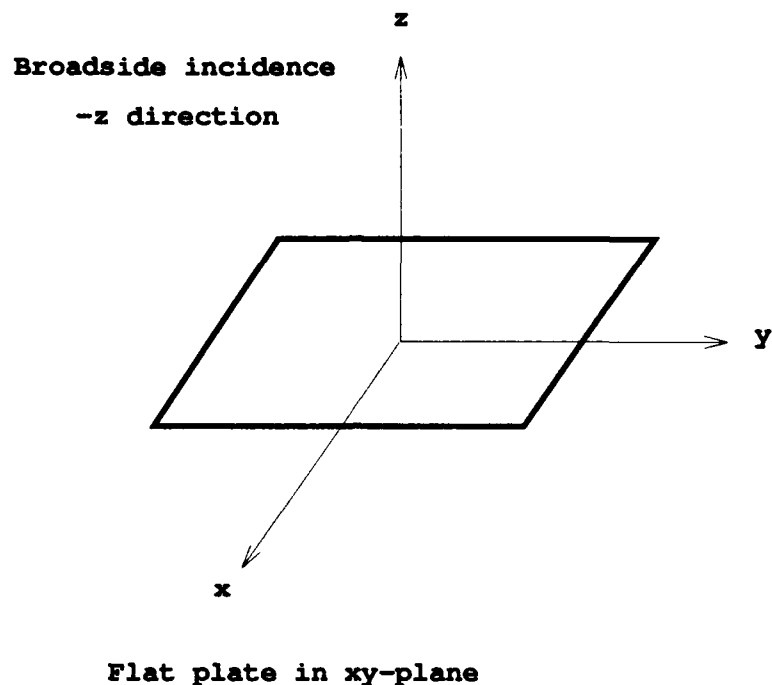


Figure 23: Broadside angle of incidence off of a flat plate.

associated with the flat plate is called the specular reflection. The specular reflection is negligible in magnitude, compared to the returns off the edges and corners of the plate, except around one angle of incidence. This angle of incidence is the one which is perpendicular to the flat face of the plate as shown in Figure 23. This angle will be called the broadside angle.

The GTD prediction of the scattering from a plate at broadside is shown in Figure 24. It is clear from this plot that the scattering from the flat plate at broadside is directly proportional to ω . The MM was used and confirmed this behavior. This behavior is only valid for a very small angular region around broadside. For angles off broadside, the energy associated with the specular phenomena is scattered in

directions other than the backscatter direction. Based on this information, the frequency model for the flat plate will be ω while the angular response will be $\delta(\theta)$.

3.2.7 Cylinder

The cylinder is the final canonical scattering center to be analyzed. A cylinder is sketched in Figure 25. An exact series solution for the scattering from an infinite circular cylinder [45] (infinite in the z -direction in Figure 25, finite in radius) exists for limited aspect angles. From [45], the frequency domain behavior for the cylinder is that of $\sqrt{\omega}$ for angles of incidence in the xy -plane in Figure 25. For angles of incidence between $\theta = 0^\circ$ and $\theta = 90^\circ$ in Figure 25, the behavior is that of $\frac{1}{\sqrt{\omega}}$ [51]. For $\theta = 0^\circ$, the cylinder is a flat circular plate which has a frequency response of ω . The angular characteristics of the cylinder are constant for scans in ϕ due to the physical symmetry of the problem. As for scans in θ , the cylinder will be modeled with a $\delta(\theta)$ function at $\theta = 0^\circ$ and $\theta = 90^\circ$ and a constant function between $\theta = 0^\circ +$ and $\theta = 90^\circ -$.

3.3 Summary of Scattering Characteristics for Canonical Scattering Centers

Table 1 is a summary of the frequency and angular models of the canonical scattering centers discussed in the previous section. The analyses presented in the previous section were used to determine the models in Table 1 based on two main criteria. The first is that the models are based upon electromagnetic theory. Second, the models must be simple enough to be used in inverse scattering algorithms. In Table 1, ω is

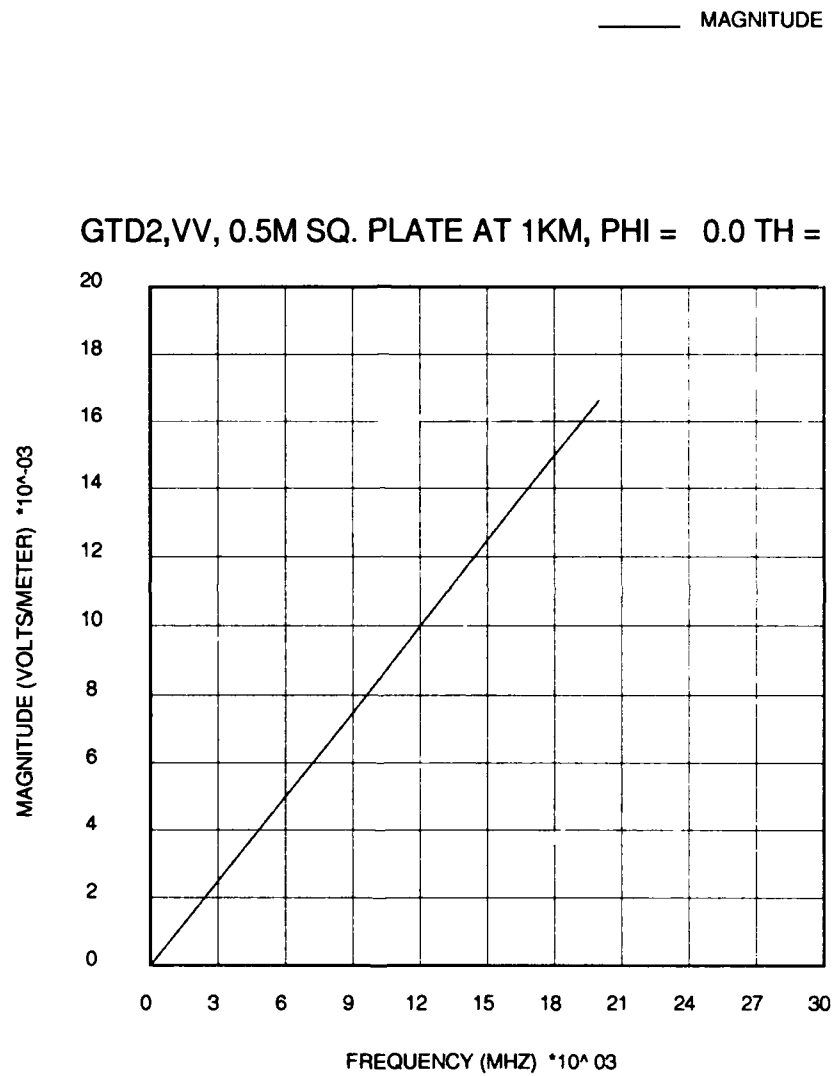


Figure 24: GTD frequency domain response estimate for the scattering from a 0.5m square flat plate. The scattering angle is $\theta = 0^\circ$. The data is from 50 MHz to 20 GHz in 50 MHz steps.

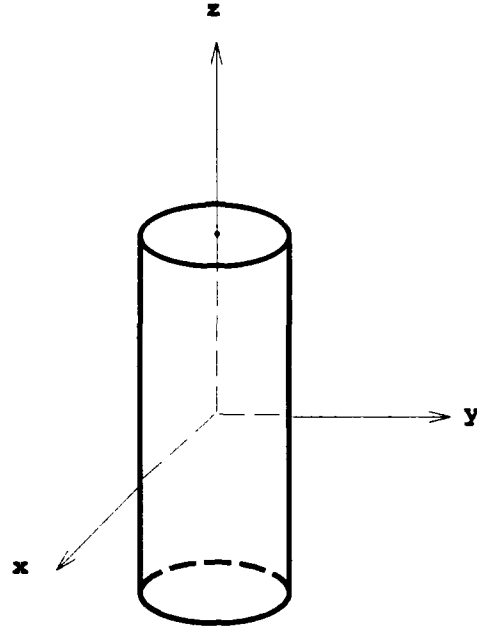


Figure 25: Sketch of a right circular cylinder.

the radian frequency and $\delta(\varphi)$ and $U(\varphi)$ are impulse and step functions of angle, respectively. $U(\varphi)$ is defined as

$$U(\varphi) = \begin{cases} 0, & \varphi < 0 \\ 1, & \varphi \geq 0 \end{cases} \quad (3.2)$$

and $\delta(\varphi)$ is the standard Dirac impulse function centered at $\varphi = 0$ as defined in [50]. Note that φ is an arbitrary angular coordinate which is needed to state the models. For example, from previous analysis, it is known that the dihedral in Figure 15 has its impulsive type behavior at $\phi = 0^\circ$ and $\theta = 90^\circ$. Thus in this case φ is the angular variable along any angular swath starting at this point, since $\delta(\varphi)$ has its impulsive behavior at $\varphi = 0^\circ$. For the canonical scattering centers with impulsive angular behavior, the angle at which the impulsive behavior occurs

Table 1: Approximate Frequency and Angle characteristics of canonical scattering centers.

Scatterer	Frequency Dependence	Angular Dependence
1. Point Scatterer, Sphere	constant	constant
2. Corner, no grazing	$\frac{1}{\omega}$	constant
3. Corner, grazing	$\frac{1}{\omega}$	$\delta(\varphi)$
4. Edge, no grazing nor \perp	constant	constant
5. Edge, grazing or \perp	constant	$\delta(\varphi)$
6. Dihedral, azimuth scan	ω	$\delta(\varphi)$
7. Dihedral, elevation scan	ω	$U(\varphi)$
8. Trihedral	ω	$U(\varphi)$
9. Cylinder, $\theta = 90^\circ$	$\sqrt{\omega}$	$\delta(\varphi)$
10. Cylinder, $0^\circ < \theta < 90^\circ$	$\frac{1}{\sqrt{\omega}}$	constant
11. Flat Plate (specular)	ω	$\delta(\varphi)$
12. Cylinder at $\theta = 90^\circ$	ω	$\delta(\varphi)$

corresponds to the $\varphi = 0^\circ$ angle. Also, for the canonical scattering centers with a step angular behavior, the angle at which the step behavior occurs corresponds to the $\varphi = 0^\circ$ angle. Of course, for the canonical scattering centers with a constant angular behavior, the origin of the φ coordinate is not fixed. Also note that θ in Table 1 is the θ in the standard spherical coordinate system (as in Figure 25).

As mentioned before, this list is not all inclusive for all of the types of canonical scattering centers which appear on all radar targets of interest. However, this list can be expanded to include other canonical scattering centers. Also, scattering behavior

such as multiple bounce mechanisms off of a plate and two scattering centers which are electrically very close can be modeled and added as new entries in the table.

3.4 Scattering Model for a Complicated Target

It is assumed that the scattering from an electrically large complicated target such as an aircraft or a tank can be accurately approximated by the sum of the scattering from a finite number of predominant scattering centers. The model in Equation 3.3 approximates the scattering from a complicated target in this way as

$$\begin{bmatrix} \mathbf{E}_h^s(\omega, \theta, \phi) \\ \mathbf{E}_v^s(\omega, \theta, \phi) \end{bmatrix} = \sum_{\gamma=1}^r \mathbf{S}_\gamma(\omega, \theta, \phi) \begin{bmatrix} \mathbf{E}_h^i(\omega, \theta, \phi) \\ \mathbf{E}_v^i(\omega, \theta, \phi) \end{bmatrix} \left(\frac{e^{-jk_o r}}{r} \right) \quad (3.3)$$

where

$$\mathbf{S}_\gamma(\omega, \theta, \phi) = \begin{bmatrix} s_{hh}^\gamma(\omega, \theta, \phi) & s_{hv}^\gamma(\omega, \theta, \phi) \\ s_{vh}^\gamma(\omega, \theta, \phi) & s_{vv}^\gamma(\omega, \theta, \phi) \end{bmatrix} \quad (3.4)$$

is the scattering matrix for the γ -th scattering center on the target. \mathbf{S}_γ can be further decomposed as

$$\mathbf{S}_\gamma(\omega, \theta, \phi) = \begin{bmatrix} \mathbf{P}_{hh}^\gamma(\theta, \phi) & \mathbf{P}_{hv}^\gamma(\theta, \phi) \\ \mathbf{P}_{vh}^\gamma(\theta, \phi) & \mathbf{P}_{vv}^\gamma(\theta, \phi) \end{bmatrix} F_\gamma(\omega) e^{-jk_o r_\gamma} \quad (3.5)$$

or

$$\mathbf{S}_\gamma(\omega, \theta, \phi) = \mathbf{P}_\gamma(\theta, \phi) F_\gamma(\omega) e^{-jk_o r_\gamma}. \quad (3.6)$$

\mathbf{P}_γ will be called the polarization matrix and is not a function of frequency. All of the terms in Equation 3.6, namely, \mathbf{S}_γ , \mathbf{P}_γ and F_γ , are, in general, complex. The distance between the phase center of the target and the arbitrarily designated phase center of the γ -th scattering center is given by r_γ . Note that r_γ is an implicit

function of θ and ϕ . It is assumed that there are Γ scattering centers on the target. It is also worth noting that this is a full-polarization scattering model.

As shown above, for the canonical scattering centers analyzed in this chapter, separating the frequency dependence from the remainder of the scattering matrix is reasonable. However, separating the angular dependence from the rest of the scattering matrix would be a poor assumption for canonical scattering centers such as the corner and the edge. Of course, for physically symmetric scattering centers such as a sphere, the angular dependence could be separated from the rest of the scattering matrix. Most radar targets of interest contain many corners and edges, and thus a model that separates the angular dependence from the rest of the scattering matrix would be inappropriate.

3.5 Damped Exponential Modeling of Scattering Behavior of Canonical Scattering Centers

The scattering behavior of the canonical scattering centers was outlined in Table 1. These characteristics were electromagnetically derived. Later, in Chapter V the scattering behavior of a complicated target, for a single transmit and receive polarization, in the frequency and angle domains, is modeled by

$$d(m, n) = \sum_{\gamma=1}^{\Gamma} \alpha_{\gamma} \rho_{x_{\gamma}}^m \rho_{y_{\gamma}}^n \quad (3.7)$$

where

$\rho_{x_{\gamma}}$ = γ th x -pole, x -component of 2-D exponential (complex number)

$\rho_{y_{\gamma}}$ = γ th y -pole, y -component of 2-D exponential (complex number)

α_γ = γ th amplitude coefficient (complex number)

Γ = number of scattering centers (integer)

and where $m = 0, 1, \dots, M - 1$ and $n = 0, 1, \dots, N - 1$. This is the 2-D extension of Prony's Model which is discussed in detail in Chapters V and VI. This model assumes the complicated target is comprised of Γ scattering centers. The γ -th scattering center's scattering behavior, for a single transmit and receive polarization, is modeled by the x -pole, y -pole and amplitude coefficient triple, $\{\rho_{x_\gamma}, \rho_{y_\gamma}, \alpha_\gamma\}$. The magnitude of the damped exponential, $|\rho_{x_\gamma}|$, determines the dispersion of the γ -th scattering center in the x -coordinate of the transform domain (time or range domain in this case) while the angle of the damped exponential, $\angle \rho_{x_\gamma}$, determines the location of the γ -th scattering center in the x -coordinate of the transform domain. Similarly, the magnitude of the damped exponential, $|\rho_{y_\gamma}|$, determines the dispersion of the γ -th scattering center in the y -coordinate of the transform domain while the angle of the damped exponential, $\angle \rho_{y_\gamma}$, determines the location of the γ -th scattering center in the y -coordinate of the transform domain.

From Equations 3.3 and 3.6, a single polarization version for the scattering from a complicated target is

$$\mathbf{E}_x^s(\omega, \theta, \phi) = \sum_{\gamma=1}^{\Gamma} \mathbf{p}_{xy}^\gamma(\theta, \phi) F_\gamma(\omega) \mathbf{E}_y^i(\omega, \theta, \phi) \left(\frac{e^{-jk_0 r}}{r} \right) \quad (3.8)$$

where $x \in \{h, v\}$, $y \in \{h, v\}$ and $xy \in \{hh, hv, vv\}$. Comparing Equations 3.7 and 3.8, the γ -th individual scattering center's frequency and angular dependencies are modeled by two damped exponentials, ρ_{x_γ} for the frequency dependence, and ρ_{y_γ} for the angular dependence. Note that there are two angular dependencies in

Table 2: Correspondence between terms in damped exponential scattering model and electromagnetically based scattering model. Note that $xy \in \{hh, hv, vv\}$ and $y \in \{h, v\}$.

Term	Electromagnetic Model	Damped Exp. Model
Frequency	$F_\gamma(\omega)$	ρ_{x_γ}
Angle	$\mathbf{p}_{xy}^\gamma(\theta, \phi)$	ρ_{y_γ}
Amplitude	$\frac{e^{-jk_0 r}}{r}$, $\mathbf{E}_y^i(\omega, \theta, \phi)$, and amp. diffs.	α_γ

Equation 3.8, θ and ϕ . When data is taken, it is taken over a specific angular swath, and this angular swath is a function of both θ and ϕ , but it can be parameterized by the singular angular variable ψ . Thus, there is really only one angular variable over which the data is taken. There is also an amplitude coefficient associated with the γ -th scattering center in Equation 3.7, α_γ , which accounts for the remaining terms in Equation 3.8 (namely, the incident field value, $\mathbf{E}_y^i(\omega, \theta, \phi)$, which is usually constant and equal to 1, the $\frac{e^{-jk_0 r}}{r}$ term, the amplitude differences between the angular variable $\mathbf{p}^\gamma(\theta, \phi)$ and ρ_{y_γ} , and the amplitude differences between the frequency variable $F(\omega)$ and ρ_{x_γ}). These relationships are summarized in Table 2. Recall that the terms $F_\gamma(\omega)$ and $\mathbf{p}_{xy}^\gamma(\theta, \phi)$ are, in general, complex.

The frequency dependencies of canonical scattering centers are well modeled using the damped exponentials. However, only one of the angular dependencies, that of constant, is well modeled. The other two, that of $U(\varphi)$ and $\delta(\varphi)$, are not well modeled by damped exponentials. This is demonstrated below.

First, the frequency dependencies are investigated. Consider a radar with center

frequency 10 GHz and a bandwidth of 2 GHz. Scattering data is generated in the 1-D frequency domain of the form

$$d_f(\eta) = \omega^t \quad \eta = 0, 1, \dots, 20 \quad (3.9)$$

where ω and η are related by

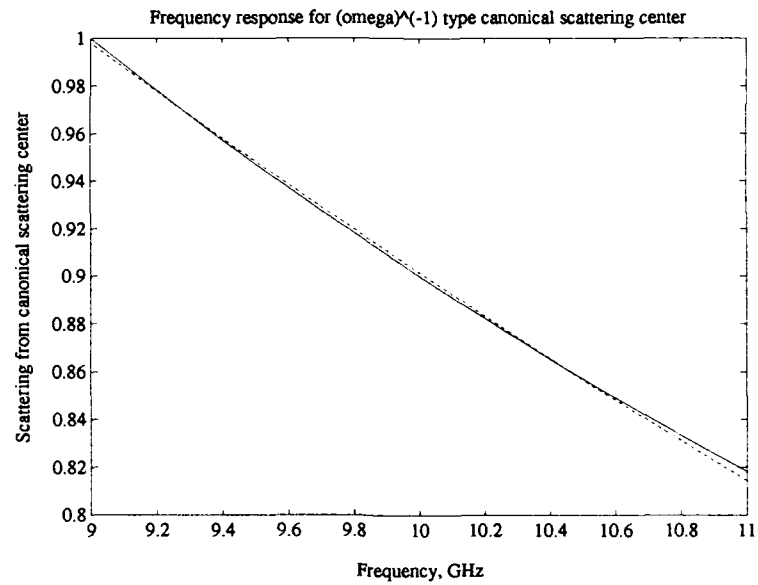
$$\omega = 2\pi\eta(50\text{MHz}) + 2\pi(9.0\text{GHz}), \quad (3.10)$$

and also where $t \in \{-1, -\frac{1}{2}, 0, \frac{1}{2}, 1\}$ (t is designated the “type” of the scattering center) and where $f = \frac{\omega}{2\pi}$ ranges from 9-11 GHz in 50 MHz steps, which yields 21 data points. This corresponds to a scattering center located at the origin of the transform domain (range or time domain) since the complex phase of the data is zero. Thus, ω^t represents all of the possible frequency dependencies from Table 1 that can appear in Equation 3.8. Next, consider the simple 1-D damped exponential model of a single canonical scattering center,

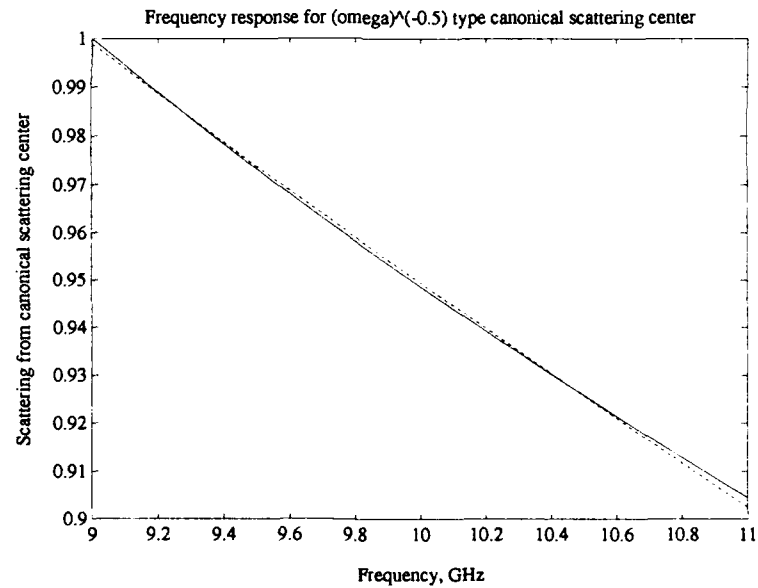
$$d(n) = \alpha\rho^n, \quad n = 0, 1, \dots, 20. \quad (3.11)$$

The 1-D TLS-Prony parameter estimation algorithm described in Chapter IV was used to estimate the parameters α and ρ from the data $d_f(\eta)$. Figures 26 through 28 show how well the damped exponential models all the frequency dependencies in Table 1 over this radar bandwidth. Table 3 gives the parameter estimates for ρ and α along with the relative error (RE) between the actual $F(\omega)$ and the damped exponential estimate for each of the $F(\omega)$'s. The RE is calculated by

$$\text{RE} = \frac{\| [d_f(0) \ d_f(1) \ \cdots \ d_f(20)] - [d(0) \ d(1) \ \cdots \ d(20)] \|}{\| [d_f(0) \ d_f(1) \ \cdots \ d_f(20)] \|} \quad (3.12)$$



(a)



(b)

Figure 26: Damped exponential modeling of frequency dependencies of canonical scattering centers with type (a) $t = -1$ and (b) $t = -0.5$. The actual frequency response is designated by the solid line while the damped exponential model is designated by the dashed line.

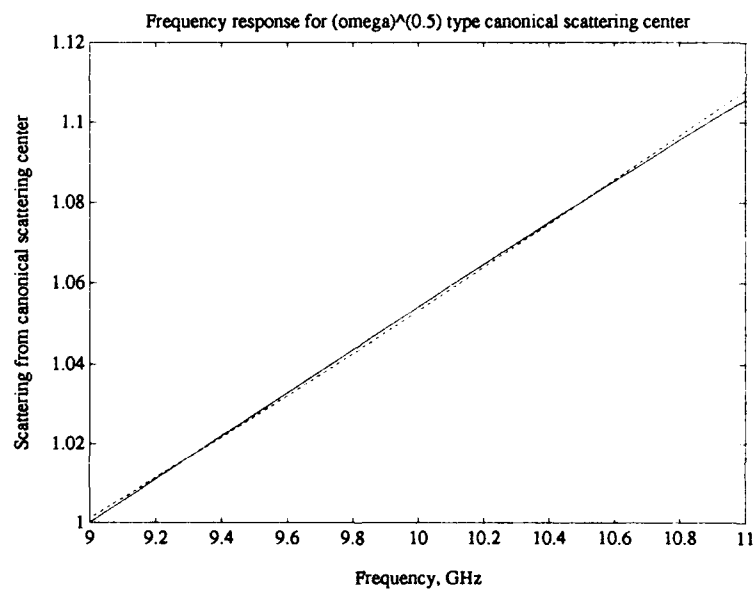
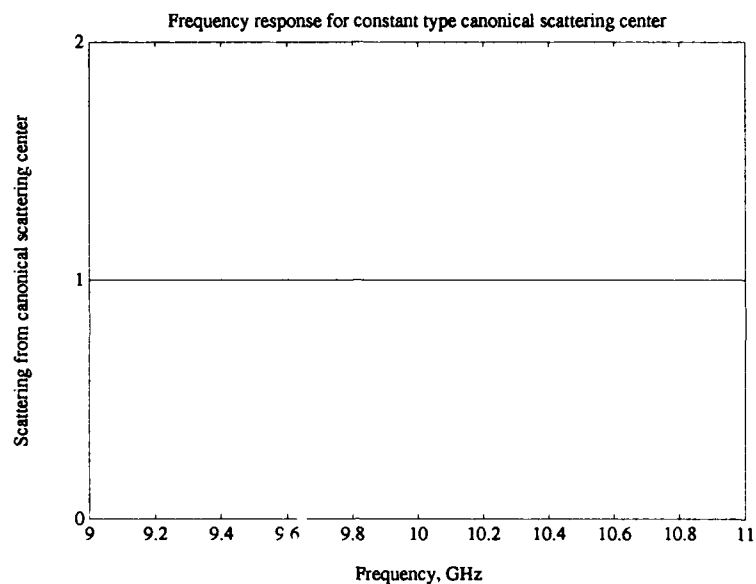


Figure 27: Damped exponential modeling of frequency dependencies of canonical scattering centers with type (a) $t = 0$ and (b) $t = 0.5$. The actual frequency response is designated by the solid line while the damped exponential model is designated by the dashed line.

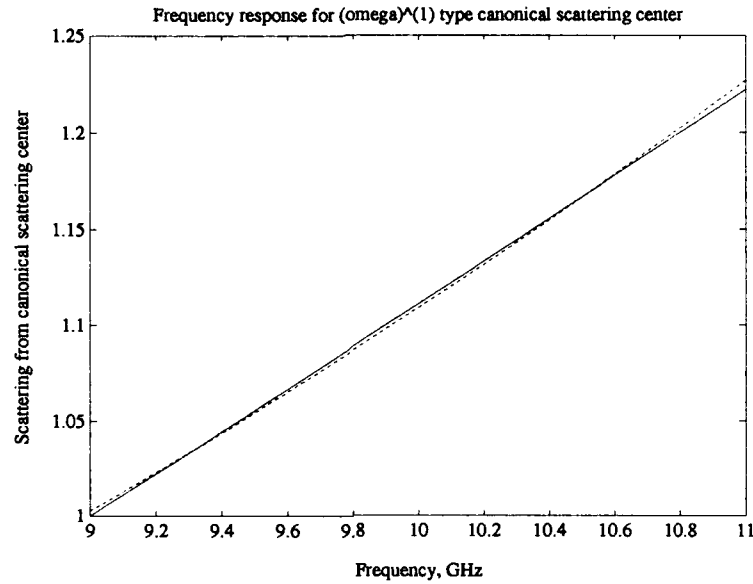


Figure 28: Damped exponential modeling of frequency dependence of canonical scattering center with type $t = 1$. The actual frequency response is designated by the solid line while the damped exponential model is designated by the dashed line.

where $\|\cdot\|$ denotes the 2-norm of the data (the square root of the sum of the squares of the elements of the vector). Note that all of the estimates for α and ρ were real. The estimates of ρ are expected to be real since the scattering center is located at the origin of the range domain, and thus $\angle \rho = 0$ is the correct estimate. Note that the REs in Table 3 are small, which confirms that damped exponentials are able to closely model the frequency dependencies of the canonical scattering centers.

Next, the angular dependencies are investigated. Two of the three angular dependencies in Table 1 are not modeled well using damped exponentials. The other, that of constant, is modeled well. The exponential model for the angular dependence of the scattering centers is identical to the model for the frequency dependence,

Table 3: Summary of amplitude coefficients and poles for 1-D frequency domain scattering from canonical scattering centers.

$F(\omega)$	type, t	α	ρ	RE
$\frac{1}{\omega}$	-1	0.9979	0.9949	0.00171
$\frac{1}{\sqrt{\omega}}$	-0.5	0.9989	0.9975	0.00085
constant	0	1.0000	1.0000	0
$\sqrt{\omega}$	0.5	1.0012	1.0025	0.00085
ω	1	1.0026	1.0051	0.00171

which is given in Equation 3.11. Consider data corresponding to the three angular dependencies, gathered over a 10 degree azimuth swath, in 0.5 degree steps, given by

$$d'_U(n) = \begin{cases} 0, & n = 0, 1, \dots, 9 \\ 1, & n = 10, 12, \dots, 20 \end{cases}, \quad (3.13)$$

$$d'_\delta(n) = \begin{cases} 0, & n = 0, 1, \dots, 10 \\ 1, & n = 11 \\ 0, & n = 12, 13, \dots, 20 \end{cases}, \quad (3.14)$$

$$d'_c(n) = 1, \quad n = 0, 1, \dots, 20, \quad (3.15)$$

where d'_U corresponds to the step-function angular dependence, d'_δ corresponds to the impulse-function angular dependence and d'_c corresponds to the constant angular dependence. The angle, designated by ψ , is assumed to vary from -5° to 5° over the data length. This data corresponds to a scattering center located at the origin of the transform domain (range or time domain) since the angle of the data is zero. As with the frequency dependencies, the above data was modeled using the 1-D damped exponential model and the results are shown in Figures 29 and 30 and summarized

Table 4: Summary of amplitude coefficients and poles for 1-D angular domain scattering from canonical scattering centers.

angular dependence	α	ρ	RE
constant	1.0000	1.0000	0
$U(\psi)$	0.1051	1.1569	0.5214
$\delta(\psi)$	0.0476	1.0000	0.9759

in Table 4. Table 4 gives the parameter estimates for ρ and α along with the RE between the actual angular dependencies and the damped exponential estimates for each of the angular responses. Note that all of the estimates for α and ρ were real, as before.

From the above analysis, it can be concluded that the damped exponential model does not model the step or impulsive angular nature of the scattering centers well from a RE standpoint. This high modeling error is also observed in Chapter VI for scenarios when the data demonstrates this angular behavior. However, this does not preclude the damped exponential model from being a useful model for the scattering from radar targets. Even though the RE is high for scattering centers whose angular behavior is that of a step or impulse function, the locations of the scattering centers are well estimated, as demonstrated above and also in Chapter VI.

Even though the damped exponential does not model all of the scattering centers well, it is still an improvement in the modeling of radar scattering. Much of the previous work in RTI assumed a point scatterer model for the scattering from all

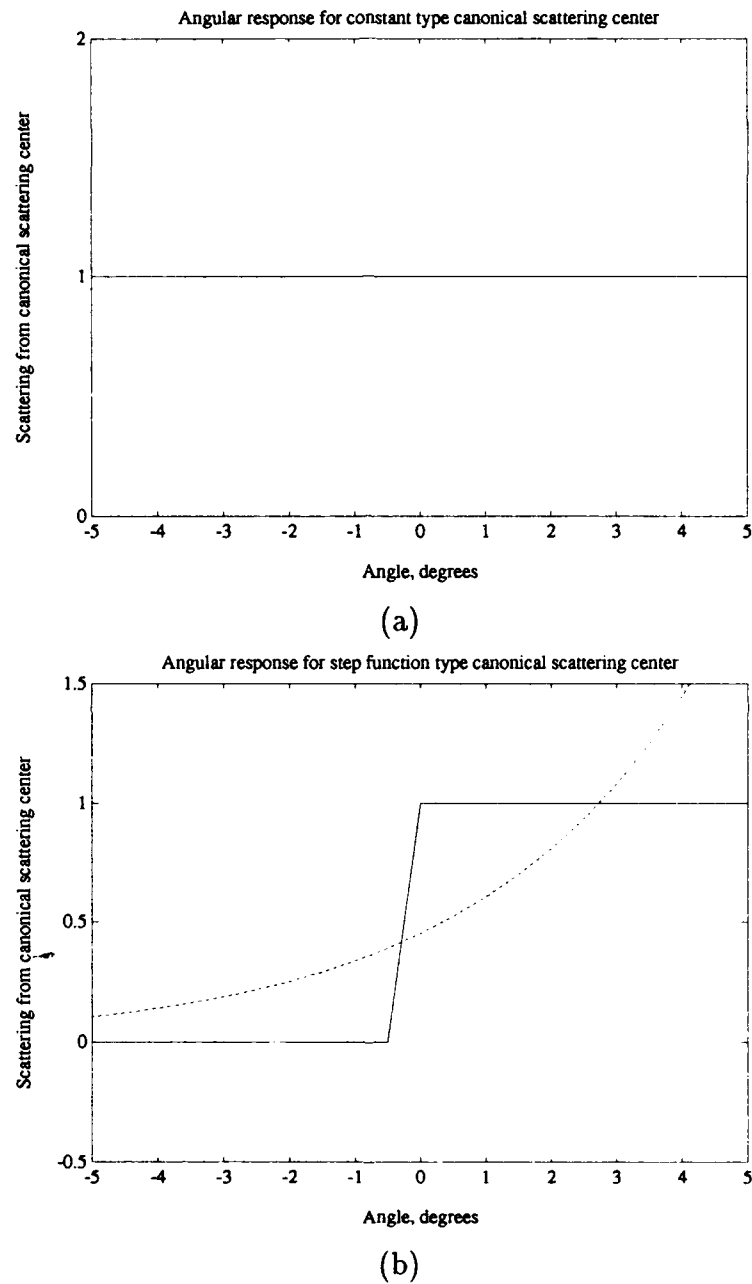


Figure 29: Damped exponential modeling for scattering center angular dependencies of (a) constant and (b) $U(\psi)$. The actual angular response is designated by the solid line while the damped exponential model is designated by the dashed line.

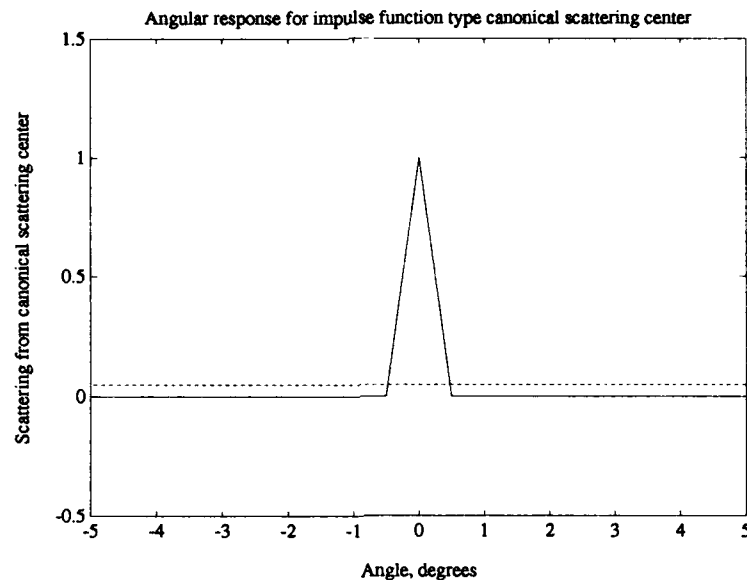


Figure 30: Damped exponential modeling for scattering center angular dependence of $\delta(\psi)$. The actual angular response is designated by the solid line while the damped exponential model is designated by the dashed line.

types of canonical scattering centers [34], [35], [39]. The extension to a 2-D damped exponential model is an improvement over the point scatterer model.

3.6 Summary

In this chapter the scattering characteristics of several canonical scattering centers were examined. Techniques such as The Method of Moments (MM) and The Geometrical Theory of Diffraction (GTD) along with others were used to determine the scattering characteristics of structures such as the edge, corner, dihedral, trihedral and cylinder. The scattering characteristics of each canonical shape were estimated as a function of frequency, radar-target orientation and polarization. The

high-frequency scattering model for a complicated radar target was defined, which is the sum of the scattering responses from a finite number of canonical scattering centers. The ability of a damped exponential model to accurately model the scattering characteristics of the canonical scattering centers was discussed in detail. The use of a damped exponential is an improvement over the use of a point scatterer model for the scattering from canonical scattering centers, as was done in much of the previous work in RTI. It was concluded that the damped exponential models the frequency responses of the canonical scattering centers well, but does not model all of angular responses well. Scattering centers exhibiting impulsive or step angular behavior are not well modeled utilizing a damped exponential. However, scattering centers exhibiting constant angular behavior are well modeled utilizing a damped exponential. This does not preclude the use of the 2-D damped exponential to model the scattering from radar targets.

CHAPTER IV

Signal Processing Fundamentals

4.1 Background and Introduction

This research involves the analysis of multiple angle and multiple frequency radar data. The analysis of 1-D multiple frequency radar data has been investigated for many years [6]–[9]. One method of obtaining a down-range profile of the target is to perform a simple Inverse Fast Fourier Transform (IFFT) on the frequency domain data. Issues such as bandwidth, resolution and unambiguous range must be considered using this approach. High resolution parametric techniques such as ARMA modeling and Prony modeling can also be applied to the data. These models are appropriate for data that contains localized peaks in the transform domain, as is the case for most multiple frequency radar data.

The analysis of 2-D multiple frequency and multiple angle radar data has mainly utilized the 2-D Fourier Transform [13]. These techniques are also applied in tomography and have applications in electron microscopy, x-rays, radio astronomy, geology and medical imaging. The same issues involving bandwidth, sampling and unambiguous range which exist in 1-D also exist in 2-D. High resolution parametric techniques exist in 2-D [10], [52] and are appropriate for radar targets which have

range-domain profiles which contain localized scattering centers. Many radar targets do not have range domain profiles which fit this description, but parametric techniques still may be appropriate in some of these cases.

First, 1-D techniques are described and some simple examples are shown. Then, 2-D techniques are introduced and several examples are shown.

4.2 One-Dimensional Techniques

It is assumed that we are given complex noisy 1-D data which has the form

$$d'(n) = d(n) + w(n), \quad (4.1)$$

where $n = 0, 1, \dots, N-1$, $w(n)$ is the noise sequence and $d(n)$ are the noiseless data. Usually this data consists of the scattering coefficients as a function of frequency which are also the scattered field values as a function of frequency at the radar (with the $\frac{e^{-jk_0 r}}{r}$ term removed) for a unity incident field ($E_h^i(f) = 1$). All of the data samples are taken with the radar-target orientation fixed. The frequency spacing between samples is δ_f and thus the total bandwidth of the data is $(N-1)\delta_f$. This type of radar data is usually called stepped CW data (where the CW stands for continuous wave). This refers to a radar measurement taken at a specific frequency for CW illumination. The frequency of the radar is stepped to the next value and another measurement is taken; this process is continued until all of the data is collected. Radar data which is collected over a non-zero bandwidth, such as with an FM ramp, can be used to approximate the stepped CW type of data.

The unambiguous range, R_u , is the total size (in the range domain) that the

target must fit in to avoid aliasing. This is different than a more classical definition for unambiguous range which involves the Pulse Repetition Frequency of a pulsed radar. Thus, for this research the unambiguous range is related to δ_f by

$$R_u = \frac{c}{2\delta_f}. \quad (4.2)$$

The 2 in the denominator accounts for the two-way travel of the electromagnetic wave. The Fourier resolution limit in the range domain is related to the bandwidth $(N - 1)\delta_f$ by

$$F_{res} = \frac{c}{2(N - 1)\delta_f}. \quad (4.3)$$

The first method of obtaining a time-domain or down-range profile of the target is to simply take the IFFT of the data. Recall that the IFFT is given by

$$D'(l) = \sum_{n=0}^{N-1} d'(n) e^{j\frac{2\pi nl}{N}} \quad l = 0, 1, \dots, N - 1 \quad (4.4)$$

where $\{D'(l)\}_{l=0}^{N-1}$ are the time domain data. By properly scaling the time axis to the range domain (as in Equation 3.1), the range domain profile can be obtained from the data $\{D'(l)\}_{l=0}^{N-1}$. Typically, the range profile plots in this dissertation are plots of the magnitude of $D'(l)$ versus range. Examples of these types of plots were shown throughout Chapter III.

Examples using actual radar data are shown here in Figures 31 and 32. These figures show the range domain profiles generated from data obtained at the compact range at The ElectroScience Laboratory (ESL) at The Ohio State University. The scattering object is an inclined flat plate which is sketched in Figure 31. Frequency domain data was obtained from 2000 MHz to 17980 MHz in 20 MHz steps for hh

polarization. The 1-D FFT was used to transform the frequency domain data to the range domain. Figure 31 shows the entire unambiguous range while Figure 32 shows only the section of the unambiguous range which contains the scattering from the plate.

Bandwidth is an important factor in the processing of radar data. Obtaining data over a large bandwidth is difficult as most radars operate over a relatively small bandwidth (relative to the radar's center frequency). This is why parametric techniques such as ARMA and Prony's Method are useful. These techniques can achieve greater resolution than Fourier methods for the same bandwidth. Because of this, if a resolution criterion is set, then parametric techniques require data over a smaller bandwidth than that required by Fourier techniques.

Prony's Model is given by [29]

$$d(n) = \sum_{k=1}^K a_k p_k^n, \quad n = 0, 1, \dots, N-1, \quad (4.5)$$

where

p_k = k th pole

a_k = k th amplitude coefficient

K = number of modes (or number of down-range scattering centers).

Prony's Model models the frequency domain data. Parameter estimation is required to estimate the poles and amplitude coefficients from the given data. A backward linear prediction approach which utilizes a Singular Value Decomposition (SVD) based noise cleaning (which is described in [29] and in Chapter V) technique is used

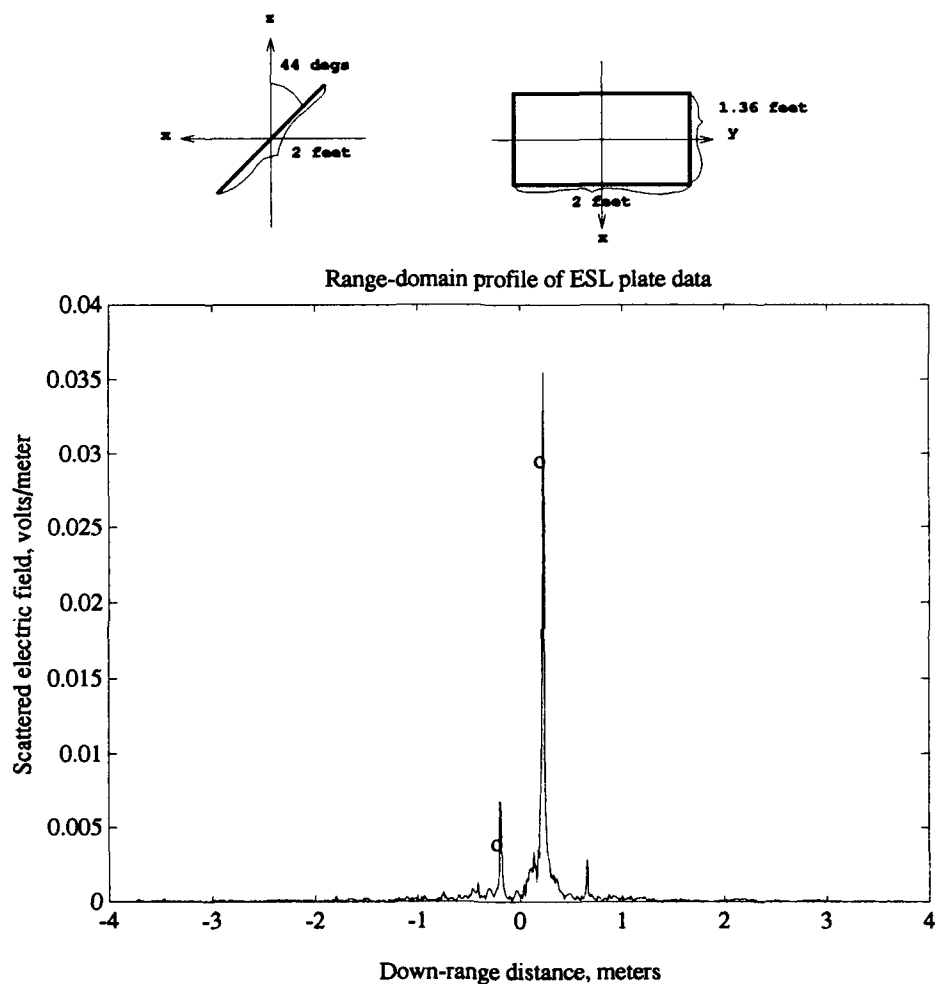


Figure 31: Impulse response estimation for an inclined flat plate from ESL data. The scattering angle is $\theta = 90^\circ$ and $\phi = 0^\circ$. Frequency domain data is from 2000 MHz to 17980 MHz in 20 MHz steps. The polarization is hh . The 1-D FFT was used to transform the frequency domain data to the range domain. The circles on the plot indicate the down-range locations of the leading and trailing edges of the plate.

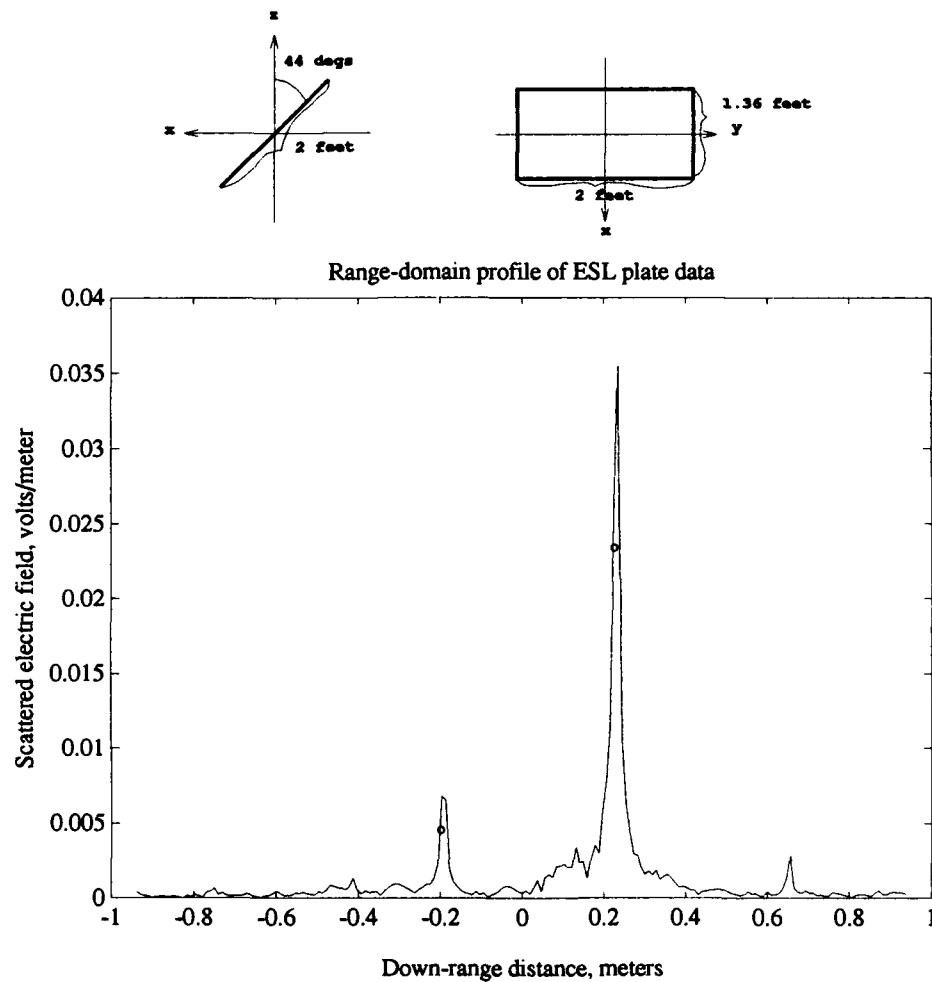


Figure 32: Impulse response estimation for an inclined flat plate from ESL data. The scattering angle is $\theta = 90^\circ$ and $\phi = 0^\circ$. Frequency domain data is from 2000 MHz to 17980 MHz in 20 MHz steps. The polarization is hh . Only the part of the impulse response which contains the plate data is shown. The 1-D FFT was used to transform the frequency domain data to the range domain. The circles on the plot indicate the down-range locations of the leading and trailing edges of the plate.

to determine the pole estimates. The backward linear prediction equations are

$$\begin{bmatrix} d'(0) & d'(1) & d'(2) & \cdots & d'(Q) \\ d'(1) & d'(2) & d'(3) & \cdots & d'(Q+1) \\ \vdots & \vdots & \vdots & & \vdots \\ d'(N-Q-1) & d'(N-Q) & d'(N-Q+1) & \cdots & d'(N-1) \end{bmatrix} \begin{bmatrix} 1 \\ b_1 \\ b_2 \\ \vdots \\ b_Q \end{bmatrix} \approx 0. \quad (4.6)$$

or

$$S \begin{bmatrix} 1 \\ b \end{bmatrix} \approx 0 \quad (4.7)$$

where Q is the order of prediction, and b is the coefficient vector of the polynomial $B(z)$ given by

$$B(z) = 1 + b_1 z^{-1} + b_2 z^{-2} + \cdots + b_Q z^{-Q}. \quad (4.8)$$

Ideally, Q can be any integer greater than or equal to the model order K ; in practice, choosing $Q > K$ results in more accurate parameter estimates [53]–[55].

Equation 4.6 is now solved for b by performing an SVD of the matrix S and truncating all but the first K singular values to arrive at a noise cleaned estimate \hat{S} [29]. Next, \hat{S} can be written as $[\hat{s}_1 \ \hat{S}_1]$, where \hat{s}_1 is a column vector consisting of the first column of \hat{S} and where \hat{S}_1 is a matrix consisting of the remaining columns of \hat{S} . Next, the estimate of b , \hat{b} , is found using a least squares solution, which can be written as

$$\hat{b} = -(\hat{S}_1^H \hat{S}_1)^{-1} \hat{S}_1^H \hat{s}_1, \quad (4.9)$$

although numerically more robust solutions (using, *e.g.*, the QR decomposition [56]) are preferred to direct computation of Equation 4.9.

Finally, the estimated poles are found by

$$\hat{p}_q = \frac{1}{\text{zerof}(\hat{B}(z))}, \quad q = 1, 2, \dots, Q. \quad (4.10)$$

Because only K singular values of \hat{S} are nonzero, there are at most K pole estimates which can correspond to true modes. Therefore, only the K poles which have the largest energy will be retained. To determine the energy, the amplitude coefficients must first be estimated. Consider Equation 4.5 in matrix form,

$$\begin{bmatrix} 1 & 1 & \cdots & 1 \\ p_1 & p_2 & \cdots & p_Q \\ p_1^2 & p_2^2 & \cdots & p_Q^2 \\ \vdots & \vdots & & \vdots \\ p_1^{N-1} & p_2^{N-1} & \cdots & p_Q^{N-1} \end{bmatrix} \begin{bmatrix} a_1 \\ a_2 \\ \vdots \\ a_Q \end{bmatrix} = \begin{bmatrix} d'(0) \\ d'(1) \\ \vdots \\ d'(N-1) \end{bmatrix}, \quad (4.11)$$

or

$$PA = \mathcal{D}'. \quad (4.12)$$

The amplitude coefficients are found from a least squares solution to equation 4.12 using the pole estimates; this can be written

$$\hat{A} = (\hat{P}^H \hat{P})^{-1} \hat{P}^H \mathcal{D}' \quad (4.13)$$

although numerically more robust solutions (using, *e.g.*, the QR decomposition [56]) are preferred to direct computation of Equation 4.13.

Next, the Q mode energies are calculated using

$$E_q = |\hat{a}_q|^2 \sum_{n=0}^{N-1} |\hat{p}_q|^{2n} \quad q = 1, 2, \dots, Q. \quad (4.14)$$

The K poles whose corresponding energies are highest are retained. The final set of K amplitude coefficients are re-estimated in a manner analogous to that outlined in Equations 4.11 to 4.13. The only differences are that now there are only K pole estimates to be utilized and only K amplitude coefficients to be estimated.

Prony's model is now applied to the radar data of a flat plate obtained at the ElectroScience Laboratory. In order to make this example more realistic in terms of radar data, only a limited bandwidth of the data will be used. Frequencies from 8-9 GHz are used, with a frequency step of 20 MHz between samples. The FFT of this limited bandwidth data is shown in Figure 33. The 'o's in the plot denote the locations of the leading and trailing edges of the flat plate. From this figure we see that the edges and multiple bounce phenomena associated with the plate are unresolvable using the IFFT. Using the SVD-Prony method described above, with model orders $Q, K = 18, 4$, the impulse response shown in Figure 34 was found from the original 51 data points.

Figure 34 shows how the SVD-Prony method easily resolved the leading and trailing edges of the plate along with the multiple bounce phenomena. This example demonstrates the utility of parametric techniques such as Prony's model to superresolve scattering centers on a target.

4.3 Two-Dimensional Techniques

As in 1-D, methods of obtaining range-domain profiles of the target have centered around the 2-D Fourier Transform. First, the relationship between the frequency domain and the time domain will be established. The 2-D image of a radar target is sometimes called "the reflectivity density function" [57] and is denoted $h(x, y)$.

The radar-target geometry for 2-D imaging purposes is shown in Figure 35. The uv -coordinates are fixed to the radar while the xy -coordinates are fixed to the target. The range between the maximum extent of the target and the radar is assumed to

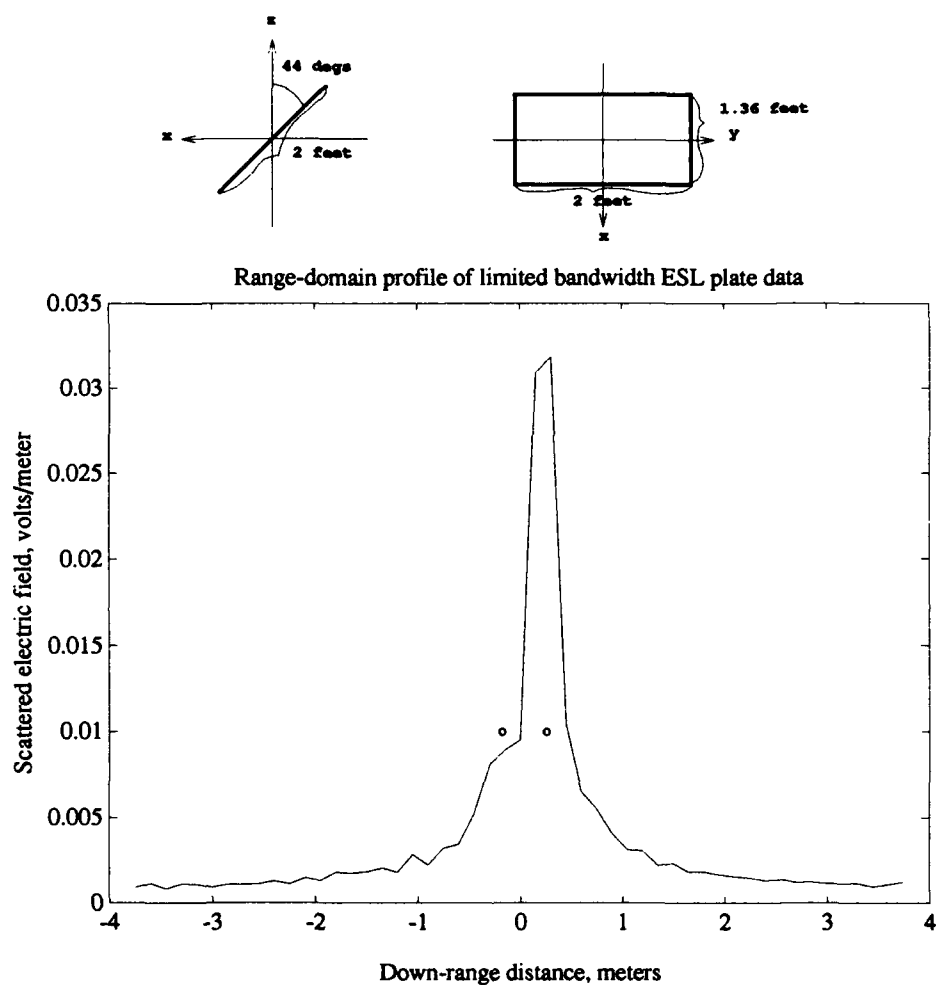


Figure 33: Impulse response estimation for an inclined flat plate from ESL data for limited bandwidth. The scattering angle is $\theta = 90^\circ$ and $\phi = 0^\circ$. Frequency domain data is from 9 GHz to 10 GHz in 20 MHz steps. The IFFT was used to generate the range-domain data. The circles on the plot indicate the down-range locations of the leading and trailing edges of the plate.

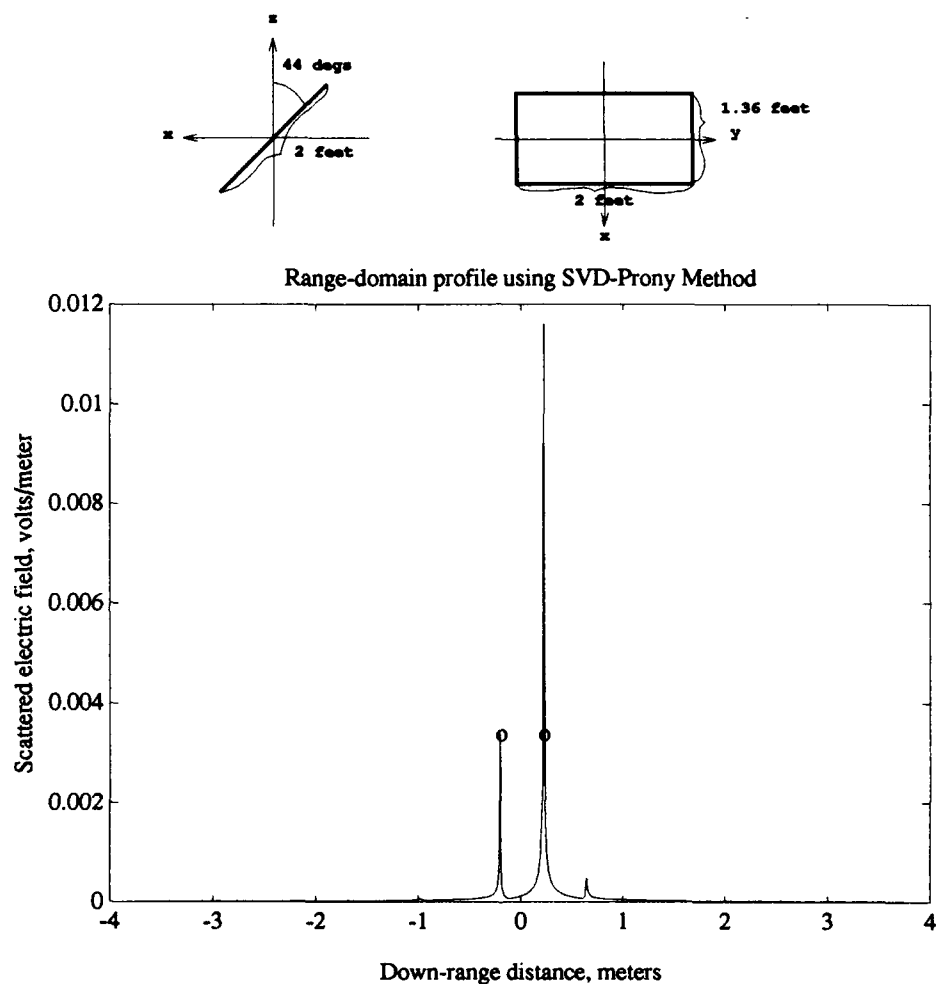


Figure 34: Impulse response estimation for an inclined flat plate from ESL data for limited bandwidth using SVD-Prony method. The scattering angle is $\theta = 90^\circ$ and $\phi = 0^\circ$. Frequency domain data is from 9 GHz to 10 GHz in 20 MHz steps. The circles on the plot indicate the down-range locations of the leading and trailing edges of the plate. The model orders chosen were $Q, K = 18, 4$.

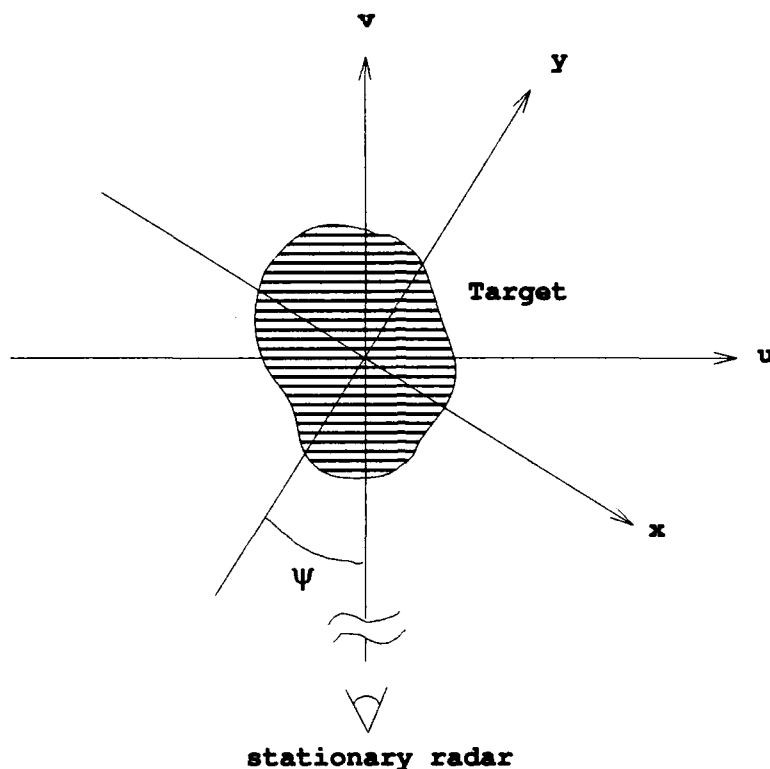


Figure 35: Radar-target geometry for 2-D imaging.

be much greater than the maximum extent of the target. Also, the target is assumed to be in the far field of the radar. When measurements are taken by the radar, it is assumed that there is no relative velocity between the radar and the target. As a start, it is assumed that the radar is radiating a single frequency, f . For a fixed ψ and a particular range v , the signal received by the radar is

$$p(v, \psi) \propto \int_{-\infty}^{\infty} h_{\psi}(u, v) du \quad (4.15)$$

where

$$h_{\psi}(u, v) = h(x, y) \quad (4.16)$$

and

$$x = u \cos(\psi) - v \sin(\psi)$$

$$y = u \sin(\psi) + v \cos(\psi).$$

The total signal received at a given ψ , $H(\psi)$, is an integral of all signals along the projection of $h(x, y)$ onto the v -axis modified by a phase factor which accounts for the round-trip phase delay along the v -axis. Thus,

$$H(\psi) = \int_{-\infty}^{\infty} p(v, \psi) e^{\frac{-j4\pi v}{\lambda}} dv \quad (4.17)$$

Utilizing Equation 4.15, Equation 4.17 becomes

$$H(\psi) = \int_{-\infty}^{\infty} \int_{-\infty}^{\infty} h_{\psi}(u, v) e^{\frac{-j4\pi v}{\lambda}} du dv. \quad (4.18)$$

Realizing $v = y \cos(\psi) - x \sin(\psi)$, using Equation 4.16 and defining

$$f_x = \frac{2 \sin(\psi)}{\lambda} \quad (4.19)$$

$$f_y = \frac{-2 \cos(\psi)}{\lambda}, \quad (4.20)$$

the received signal at the radar becomes

$$H(f_x, f_y) = \int_{-\infty}^{\infty} \int_{-\infty}^{\infty} h(x, y) e^{-j2\pi(f_x x + f_y y)} dx dy. \quad (4.21)$$

This is the standard 2-D Fourier Transform. All of the useful properties which exist for the Fourier Transform exist for the 2-D Fourier Transform pair

$$h(x, y) \Leftrightarrow H(f_x, f_y). \quad (4.22)$$

From Fourier Theory [50],

$$h(x, y) = \int_{-\infty}^{\infty} \int_{-\infty}^{\infty} H(f_x, f_y) e^{j2\pi(f_x x + f_y y)} df_x df_y. \quad (4.23)$$

This relationship can be written in polar form by defining $f = \sqrt{f_x^2 + f_y^2}$. Thus

$$h(x, y) = \int_0^{\infty} \int_0^{2\pi} H(f, \psi) e^{-j2\pi f(x \sin(\psi) - y \cos(\psi))} d\psi df \quad (4.24)$$

relates the reflectivity density function to the frequency domain data. Equations 4.15 through 4.24 form the Projection-Slice Theorem [13].

In practice, we will have samples of $H(f, \psi)$, as in Figure 37, and wish to approximate $h(x, y)$ from these samples. The samples of $H(f, \psi)$ are usually the scattering matrix coefficients of the target as a function of frequency and angle. Usually one of the two spherical angles is fixed and the other is varied to yield a 2-D “slice” of the target. However, any angular slice of the target can be used to generate an image.

There are several methods which are used to approximate $h(x, y)$ from the samples of $H(f, \psi)$. If the samples of $H(f, \psi)$ are on a polar grid, as in Figure 37, one method is to interpolate the data to a rectangular grid and apply the 2-D IFFT. The quality of this method depends on the interpolation method used. Another method is to numerically approximate the double integral in Equation 4.24. Yet another option is to use the convolution-backprojection method [13]. One type of data set in the frequency domain is shown in Figure 36, which corresponds to full angular coverage. Figure 37 shows the case of the data available for limited angular coverage.

In practice, data is usually only available over a limited angular extent (usually the maximum angular extent is between 3° and 20° for spotlight mode SAR [57]).

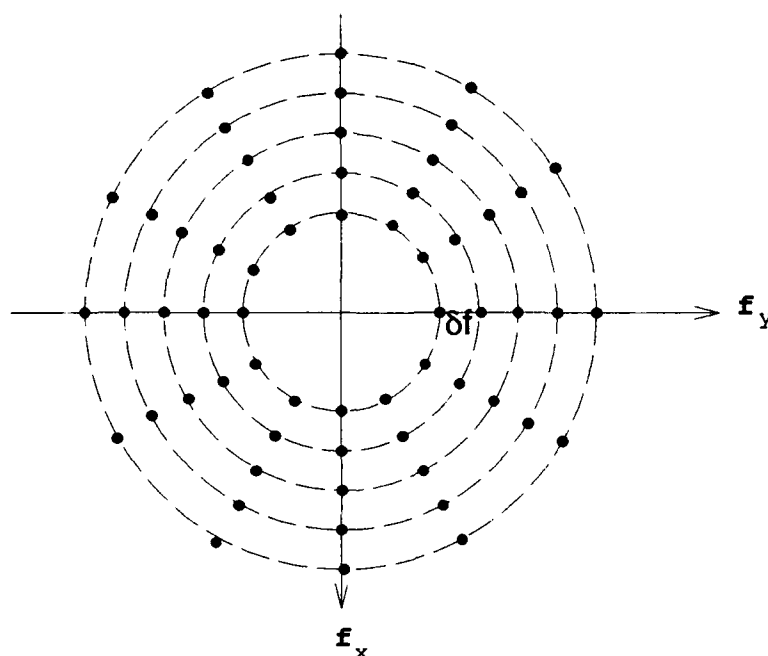


Figure 36: 2-D frequency domain data set for full angular coverage.

However, since there is full angular coverage data available, both types of data sets are examined.

To illustrate the application of the various types of imaging methods, images of a flat plate are generated using two methods. The first two data sets correspond to full-angular coverage data for the scattering from a thin, perfectly conducting flat plate. These data sets were generated using the MM. First, a direct numerical integration of Equation 4.24 is utilized to obtain two images. Then the polar data is interpolated onto a square grid and the 2-D IFFT is used to generate the image. Also, two limited angular data sets exist for the same structure generated using the GTD. Images are formed from these limited angular data sets by using the polar

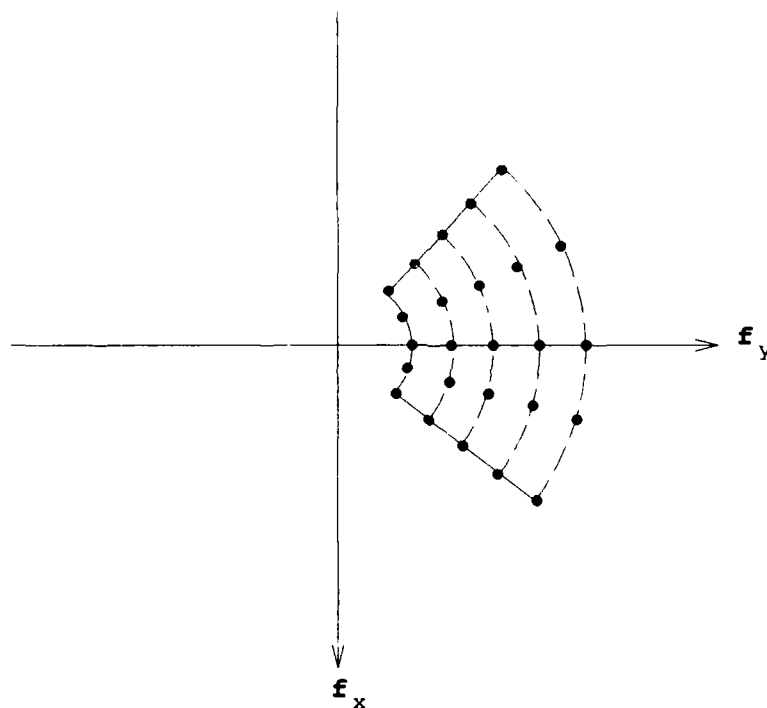


Figure 37: 2-D frequency domain data set for limited angular coverage.

data directly in the 2-D IFFT (without interpolating the data onto a rectangular grid).

The two sets of full-angular coverage images correspond to images of the same structure, but over different angular swaths. The angular swaths in each case are over the same spherical coordinates, but the plate is oriented differently in the spherical coordinate system for each image. The first plate orientation, which is called the flat plate orientation, is sketched at the top of Figure 38. In this orientation, the plate resides entirely in the xy -plane. The second plate orientation, which is called the inclined plate orientation, is sketched at the top of Figure 41. The two sets of images are shown to demonstrate the dependence of the image on the angular swath

of the scattering data.

Figure 38 shows the image generated from MM data of the flat plate sketched in the figure (flat plate orientation). This image was calculated by directly integrating Equation 4.24. The data samples were 5° apart in angle and the frequency extent was from 50 MHz to 3150 MHz in 50 MHz steps. The angular sweep was done entirely in the xy -plane ($\theta = 90^\circ$). The unambiguous range in each direction is three meters, but not all of this range is shown in the image. The data samples were the complex-valued scattering matrix coefficients $s_{hh}(f, \phi)$.

Figure 39 shows the image generated from MM data of the inclined flat plate sketched in the figure (inclined plate orientation). As with the previous image, this image was calculated by directly integrating Equation 4.24. The data samples were 5° apart in angle and 50 MHz apart in frequency. The frequency extent was from 50 MHz to 3100 MHz. The unambiguous range in each direction is once again three meters, but not all of this range is shown in the image. The angular sweep was also done entirely in the xy -plane. Note that the image of the plate for the inclined plate orientation is narrower in one direction while the image of the plate for the flat plate orientation is square. This is as expected since the inclined plate does not reside entirely in the xy -plane. The expected image for the inclined plate is the projection of the plate onto the xy -plane. From Figure 38, since the flat plate resides entirely in the xy -plane, its image is expected to be square (since its projection onto the xy -plane is square). Figures 38 and 39 demonstrate that the image is dependent upon the angular swath over which the scattering data is taken. These two figures

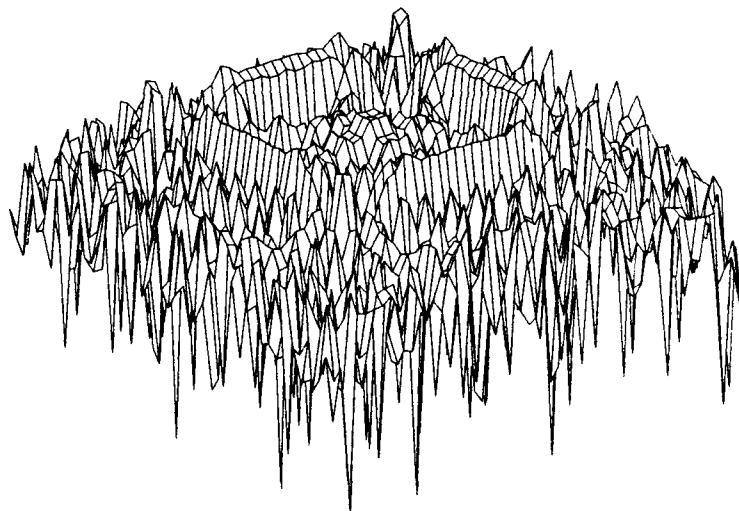
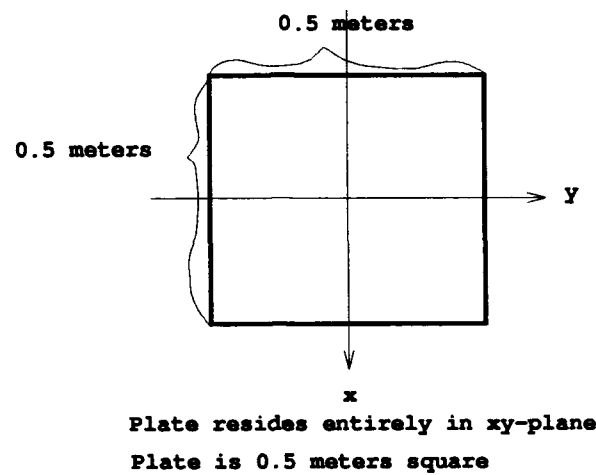


Figure 38: Image of a plate, in the flat plate orientation, generated by direct numerical integration of Equation 4.24 for full angular coverage data (hh -polarization).

also demonstrate that the scattering from the plates occurs from the corners and edges of the plates.

Another method of generating an image from full-angular coverage polar data is to interpolate the data onto a rectangular grid in the 2-D frequency domain and then use a 2-D IFFT. Usually, it is desired to form a square grid in the 2-D frequency plane so that the image will not be distorted in one of the cardinal directions, but the 2-D IFFT can accept data for the more general case of the rectangular grid. The image corresponding to data on a rectangular (and not square) grid will be distorted in one of the cardinal directions. Two interpolation methods are examined. Consider the desired point on the rectangular grid, as shown in Figure 40. The first method (called INT1) calculates the data value at the desired point on the rectangular grid as

$$d(f_x, f_y) = \frac{d(f_{x1}, f_{y1})(l_t - l_1)}{l_t} + \frac{d(f_{x2}, f_{y2})(l_t - l_2)}{l_t} + \frac{d(f_{x3}, f_{y3})(l_t - l_3)}{l_t} + \frac{d(f_{x4}, f_{y4})(l_t - l_4)}{l_t} \quad (4.25)$$

where

$$l_t = l_1 + l_2 + l_3 + l_4. \quad (4.26)$$

The second method (called INT2) calculates the data value as

$$d(f_x, f_y) = \frac{d(f_{x1}, f_{y1})}{l_t l_1} + \frac{d(f_{x2}, f_{y2})}{l_t l_2} + \frac{d(f_{x3}, f_{y3})}{l_t l_3} + \frac{d(f_{x4}, f_{y4})}{l_t l_4}. \quad (4.27)$$

These two methods were applied to the plate for both the flat and inclined plate orientation data and the difference between the two images for both interpolation methods was insignificant. Figure 41 shows the image generated from the flat plate

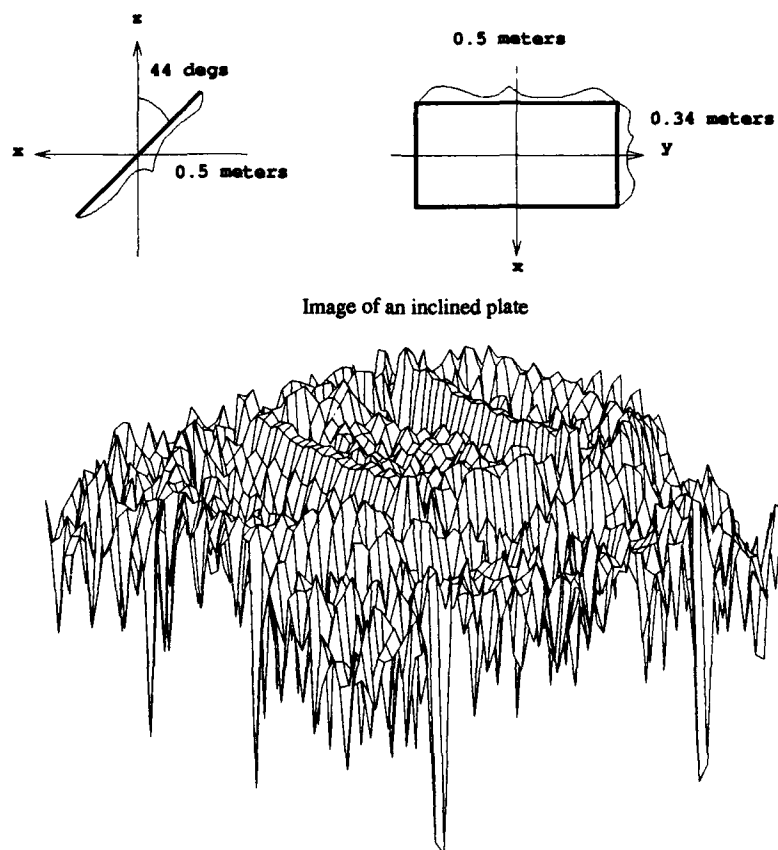


Figure 39: Image of a plate (inclined plate orientation) generated by direct numerical integration of Equation 4.24 for full angular coverage data (*hh*-polarization).

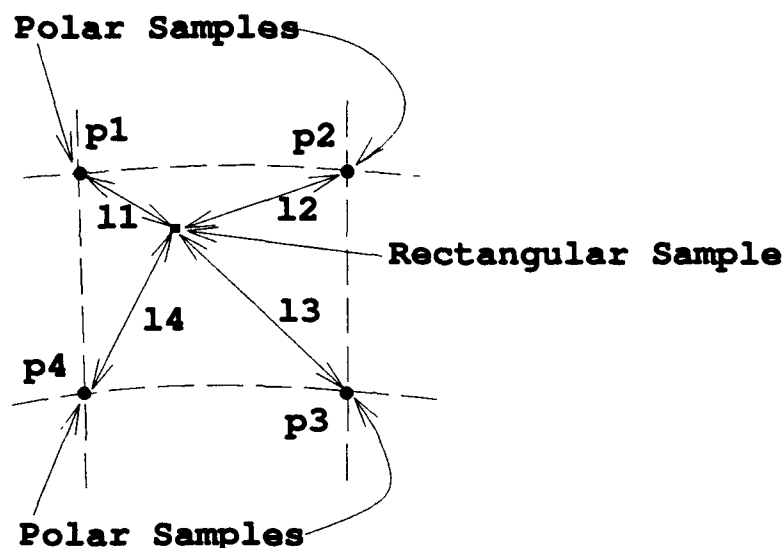


Figure 40: Desired point on rectangular grid between data points on polar grid.

orientation data while Figure 42 shows the image generated from the inclined plate orientation data. The INT2 method of Equation 4.27 was used to generate these two images. Once again, these two figures demonstrate the fact that the image is dependent upon the angular swath over which the scattering data is taken. The images in Figures 41 and 42 are images of the same plate but taken over different angular swaths.

By comparing Figures 38 and 41, and also comparing Figures 39 and 42, it is apparent that the two imaging methods described here, that of numerical integration and interpolation coupled with the 2-D IFFT, yield somewhat different images. Notice how the corners of the plate are much more pronounced in Figures 41 and 42, which were generated using interpolation along with the 2-D IFFT, than they are in Figures 38 and 39 which were generated utilizing numerical integration.

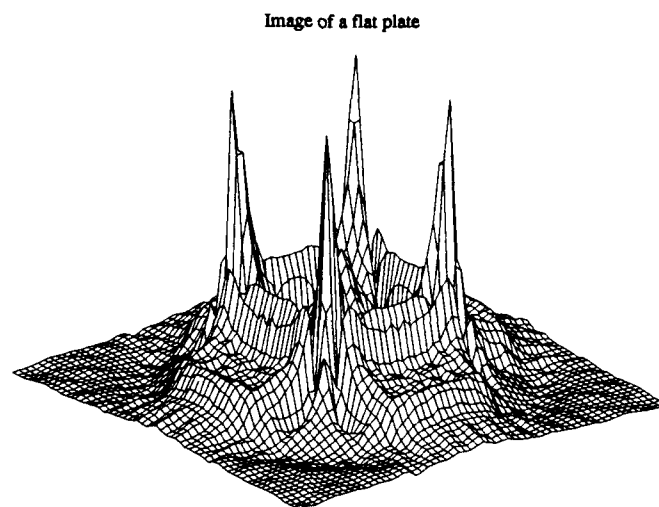


Figure 41: Image of a flat plate generated by interpolation to a square grid followed by the 2-D IFFT for full angular coverage data (*hh*-polarization).

A more practically realistic case is that of limited angular extent data. An airborne SAR illuminating either a stationary or a moving target usually will not be able to gather full angular coverage data. One way to treat the limited angular extent data shown in Figure 37 is to treat the polar grid data as if it actually lies on a rectangular grid. This is a good approximation if the center frequency to bandwidth ratio is large and the total angular swath is small. Another way to treat this data is to interpolate the polar data to a rectangular grid just as with the full angular coverage data. In either case, the 2-D IFFT is used to generate the image.

To show an example of a limited angular extent image, Figure 43 shows the image of the plate for the inclined plate orientation generated from limited angular data. The 2-D frequency domain data, generated by the GTD, was taken from

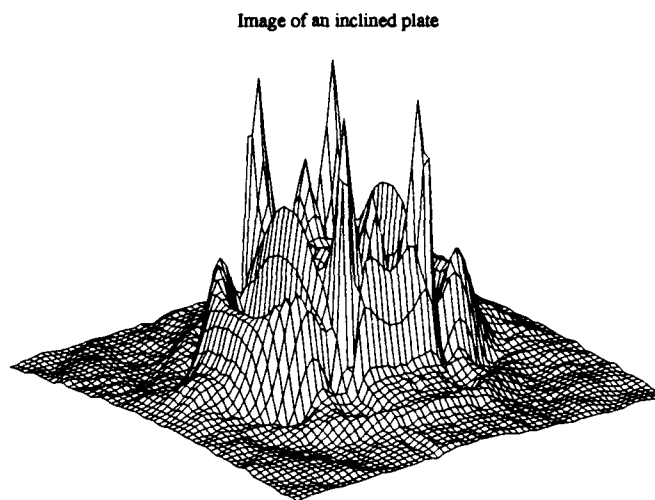


Figure 42: Image of an inclined plate generated by interpolation to a square grid followed by the 2-D IFFT for full angular coverage data (*hh*-polarization).

$\phi = 37.5^\circ$ to $\phi = 52.5^\circ$ in 0.5° steps with θ fixed at 90° and f ranging from 9 to 11.55 GHz in 0.085 GHz steps. Thus, the data set is 31×31 data points. The polar data was directly utilized by the 2-D IFFT. It is assumed that the polar grid in the 2-D frequency plane is a good approximation to a square grid. The image shows that the scattering off of the inclined plate occurs at the corners of the plate. The edges of the plate are not visible in the image since the scattering response from an edge is comparable in magnitude to the return off of a corner only when the edge is illuminated broadside (if the illumination angle was at $\phi = 0^\circ$). The image can be thought of as the view one would get of the plate if one were viewing the plate from $\phi \approx 45^\circ$ and $\theta = 90^\circ$.

Figure 44 shows the image of the same inclined plate but the limited angular

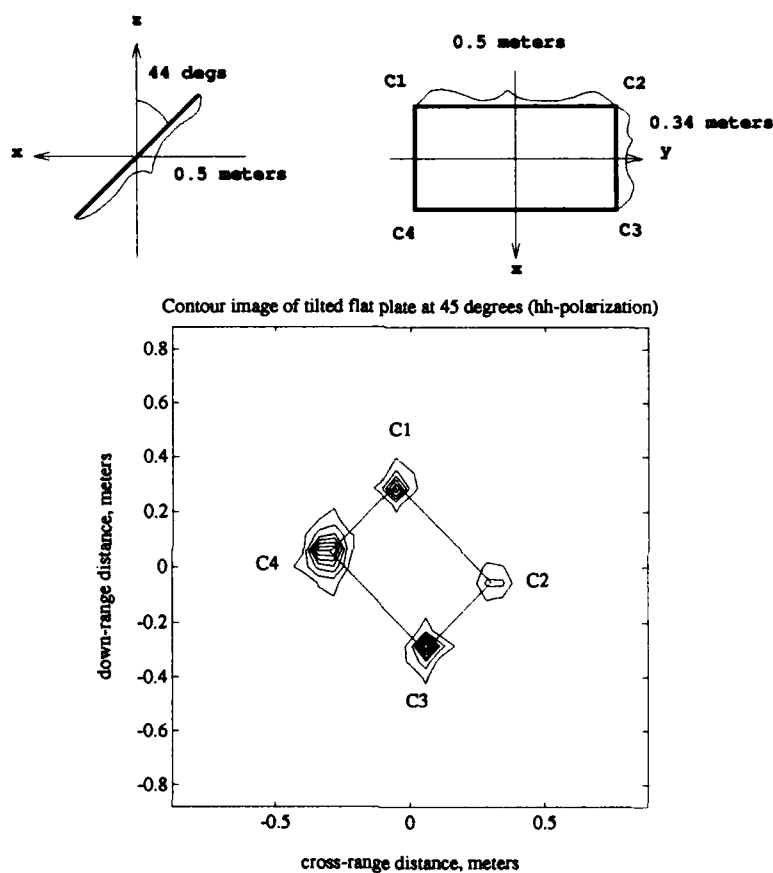


Figure 43: Image of an inclined plate generated for limited angular coverage data (*hh*-polarization). Frequency domain data was taken from $\phi = 37.5^\circ$ to $\phi = 52.5^\circ$ in 0.5° steps with θ fixed at 90° and f ranging from 9 to 11.55 GHz in 0.085 GHz steps. The GTD was used to generate the data. The plate is drawn in at the middle of the rotation, at $\phi = 45^\circ$.

data is taken over a different angular sector. The frequency domain data was taken from $\phi = -7.5^\circ$ to $\phi = 7.5^\circ$ in 0.5° steps with θ fixed at 90° and f ranging from 9 to 11.55 GHz in 0.085 GHz steps. Again, the GTD was used to generate the data and the data set consists of 31×31 data points. The polar data was directly input into the 2-D IFFT. This image shows how the edges of the plate appear in images when the viewing angles include those broadside to the edge ($\phi = 0^\circ$ in this case). For this plate, the hh -polarization response from the front edge is much larger than the response from the rear edge (the front edge is the one at $x = 0.173$ meters).

In the above examples the angular and frequency spacing was chosen so that the data points in the 2-D frequency plane were roughly evenly spaced. Also, the GTD was used for the limited angular extent examples so that the data would be at frequencies around 10 GHz, which allows the spacing at the lowest frequency to be no less than 0.78 times the spacing at the highest frequency. The MM could not produce data at frequencies this high due to CPU/memory constraints.

4.4 Summary

This chapter was a background signal processing chapter which was needed to introduce 1-D and 2-D signal processing techniques. Non-parametric techniques such as the 1-D and 2-D IFFTs were introduced and examples were shown on how these techniques produce a down-range profile and an image of a target, respectively. The 1-D TLS-Prony Technique was described, which is a 1-D parametric signal processing technique. Prony's model (in 1-D) was introduced, which is the 1-D damped exponential model utilized by the 1-D TLS-Prony Technique. The estimation algorithm

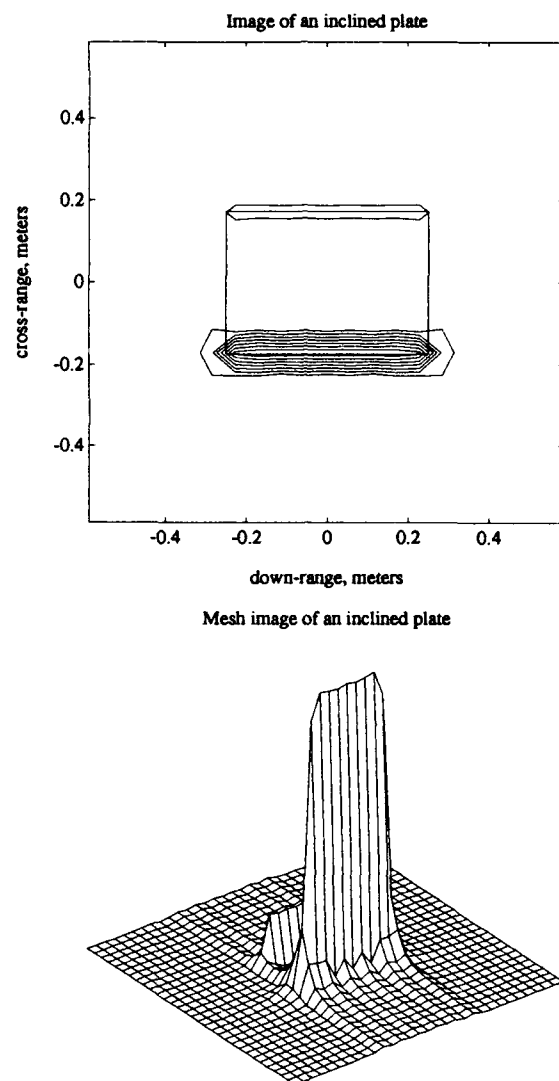


Figure 44: Image of an inclined plate generated for limited angular coverage data (hh -polarization). Frequency domain data was taken from $\phi = -7.5^\circ$ to $\phi = 7.5^\circ$ in 0.5° steps with θ fixed at 90° and f ranging from 9 to 11.55 GHz in 0.085 GHz steps. The GTD was used to generate the data. The plate is drawn in at the middle of the rotation for the contour plot. The mesh plot is shown to demonstrate the magnitude differences between the responses from the front and rear edges.

utilized by this technique was described, and examples were shown on its abilities. Several 2-D IFFT based image generation techniques were described such as numerical integration, interpolation to a rectangular grid and convolution-backprojection. Images generated by the various techniques were shown and issues such as angular swath orientation and 2-D frequency and angular bandwidths were discussed.

CHAPTER V

The Two-Dimensional TLS-Prony Technique

5.1 Introduction

This chapter presents a new technique to estimate two-dimensional (2-D) exponentials and their associated amplitude coefficients from a 2-D data set. It is called the 2-D TLS-Prony Technique. First, the model and estimation algorithm are developed for a basic 2-D data set. This data set could correspond, for example, to the data set collected by a SAR for a single transmit and receive polarization. The algorithm is then extended to utilize multiple data sets which can correspond to multiple transmit and receive polarization data. This is designated the full-polarization case.

5.2 Basic Technique Description

5.2.1 Background and Introduction

The 2-D TLS-Prony Technique is a parametric technique for the estimation of 2-D exponentials and their associated amplitude coefficients. The model used for the data is a 2-D extension of the 1-D Prony Model in Equation 4.5. Prony's method coupled with a total least squares (TLS) technique in 1-D has been successfully used to estimate frequencies in the presence of noise [29] as shown in Chapter IV. With the 2-D TLS-Prony Technique, 2-D exponentials and amplitude coefficients

are estimated by a two-step method using a 1-D TLS-based Prony model and estimation technique in each step. This technique is capable of estimating 2-D damped exponentials.

A related method, developed by Hua [28], estimates 2-D frequencies. In Hua's method, two estimation steps are performed to separately estimate the x -components and y -components of the 2-D frequencies. Then, a matching step is performed to find the correct x -component and y -component frequency pairings. The 2-D TLS-Prony Technique is similar to Hua's in some respects, but different in others. With the 2-D TLS-Prony Technique, the x -components of the exponentials are estimated first. Then amplitude coefficients corresponding to each x -component exponential are estimated and these estimates are used to estimate a set of y -component exponentials. In this way the requirement of a matching step is avoided. This algorithm is computationally less expensive than Hua's method, and more amenable to parallel implementation. A second algorithm is also presented in which the first algorithm is used twice, first to estimate x then y -component exponentials and then y then x -component exponentials. The second algorithm does require matching, but the computational load is still smaller than the one in [28]. This second algorithm gives more accurate parameter estimates than the first algorithm.

5.2.2 Data Model

The given noisy 2-D data is assumed to have the form

$$d'(m, n) = d(m, n) + w(m, n), \quad (5.1)$$

where $m = 0, 1, \dots, M-1$ and $n = 0, 1, \dots, N-1$ and $w(m, n)$ is 2-D noise sequence. The first index of $d(m, n)$ is referred to as the x -component, and the second index as the y -component. The x -component is analogous to the frequency component and the y -component is analogous to the angular component in the 2-D frequency plane. However, the data which is used in this algorithm is assumed to lie on a rectangular grid on the 2-D frequency plane, not a polar grid as is associated with data on the 2-D frequency plane which is collected by SARs. Thus, if the initial data lies on a polar grid, it should be interpolated onto a rectangular grid before it is used by the 2-D TLS-Prony Technique. This issue is investigated in Chapter VI.

The noiseless data is assumed to fit the 2-D damped exponential model

$$d(m, n) = \sum_{k=1}^K \sum_{l=1}^{L_k} a_{k,l} p_{x_k}^m p_{y_{k,l}}^n, \quad (5.2)$$

where

p_{x_k} = k th x -pole, x -component of 2-D exponential

$p_{y_{k,l}}$ = k, l th y -pole, y -component of 2-D exponential

$a_{k,l}$ = k, l th amplitude coefficient

K = number of x -poles

L_k = number of y -poles corresponding to the k th x -pole.

The 2-D Z -transform is defined for the model in equation 5.2 as

$$D_z(u, v) = \sum_{k=1}^K \sum_{l=1}^{L_k} \frac{a_{k,l}}{(1 - p_{x_k} z_u^{-1})(1 - p_{y_{k,l}} z_v^{-1})} \quad (5.3)$$

where $z_u = e^{ju}$ and $z_v = e^{jv}$ [58]. Thus, each 2-D frequency is determined by the intersection of its x and y -pole locations.

Given noisy data $d'(m, n)$, $m = 0, 1, \dots, M - 1$ and $n = 0, 1, \dots, N - 1$, the parameters in the model 5.2 must be estimated. Below two TLS-Prony based algorithms for estimating these parameters are presented, called Algorithm One and Algorithm Two.

5.2.3 Estimation Algorithms

Algorithm One

Algorithm One consists of four steps. The x -poles, $\{p_{x_k}\}_{k=1}^K$, are first estimated using a TLS-Prony algorithm. Second, a set of amplitude coefficients corresponding to these x -pole estimates are computed. The amplitude coefficients are themselves used in a set of second TLS-Prony estimates to obtain the y -pole estimates, $\{p_{y_{k,l}}\}_{k,l=1}^{K,L_k}$, which is the third step. Finally, a least squares technique is used to estimate the amplitude coefficients $\{a_{k,l}\}_{k,l=1}^{K,L_k}$. These steps are detailed below and summarized in Table 5.

Step 1: Estimation of the x -poles. The first step in the parameter estimation problem is to estimate the x -poles, $\{p_{x_k}\}_{k=1}^K$. A matrix composed of the noisy data, $\{d'(m, n)\}_{m,n=0}^{M-1,N-1}$, is defined as

$$D' = \begin{bmatrix} d'(0, 0) & d'(1, 0) & \cdots & d'(M-1, 0) \\ d'(0, 1) & d'(1, 1) & \cdots & d'(M-1, 1) \\ \vdots & \vdots & & \vdots \\ d'(0, N-1) & d'(1, N-1) & \cdots & d'(M-1, N-1) \end{bmatrix}. \quad (5.4)$$

Moving across a row in D' is considered moving in the x -direction (frequency, or down-range) while moving down a column is considered moving in the y -direction

(angle, or cross-range) in the 2-D frequency plane. Each row of D' can be used to provide an estimate of the x -poles. However, in order to use 1-D Prony estimation procedures, all of the rows of D' will be used simultaneously in the estimation of the x -poles. A total least squares (TLS) backward linear prediction approach similar to [29] is used. The backward linear prediction equations are

$$\begin{bmatrix} d'(0,0) & d'(1,0) & d'(2,0) & \cdots & d'(Q,0) \\ d'(1,0) & d'(2,0) & d'(3,0) & \cdots & d'(Q+1,0) \\ \vdots & \vdots & \vdots & \ddots & \vdots \\ d'(M-Q-1,0) & d'(M-Q,0) & d'(M-Q+1,0) & \cdots & d'(M-1,0) \\ \hline d'(0,1) & d'(1,1) & d'(2,1) & \cdots & d'(Q,1) \\ d'(1,1) & d'(2,1) & d'(3,1) & \cdots & d'(Q+1,1) \\ \vdots & \vdots & \vdots & \ddots & \vdots \\ d'(M-Q-1,1) & d'(M-Q,1) & d'(M-Q+1,1) & \cdots & d'(M-1,1) \\ \hline \vdots & \vdots & \vdots & \ddots & \vdots \\ d'(0,N-1) & d'(1,N-1) & d'(2,N-1) & \cdots & d'(Q,N-1) \\ d'(1,N-1) & d'(2,N-1) & d'(3,N-1) & \cdots & d'(Q+1,N-1) \\ \vdots & \vdots & \vdots & \ddots & \vdots \\ d'(M-Q-1,N-1) & d'(M-Q,N-1) & d'(M-Q+1,N-1) & \cdots & d'(M-1,N-1) \end{bmatrix} \begin{bmatrix} 1 \\ b_1 \\ b_2 \\ \vdots \\ b_Q \end{bmatrix} \approx 0. \quad (5.5)$$

or

$$S \begin{bmatrix} 1 \\ b \end{bmatrix} \approx 0 \quad (5.6)$$

where Q is the order of prediction, and b is the coefficient vector of the polynomial $B(z)$ given by

$$B(z) = 1 + b_1 z^{-1} + b_2 z^{-2} + \cdots + b_Q z^{-Q}. \quad (5.7)$$

Ideally, Q can be any integer greater than or equal to the model order K ; in practice, choosing $Q > K$ results in more accurate parameter estimates [53]–[55]. Note that all of the rows of D' are used simultaneously to estimate a single set of prediction coefficients (and therefore, a single set of x -poles).

Equation 5.6 is used to solve for the estimate of b , \hat{b} , in a total least squares sense to arrive at a minimum norm (TLS) estimate, where the $Q + 1 - K$ smallest singular values of S are truncated to arrive at a noise cleaned estimate \hat{S} . This is outlined in [29] in detail, but a summary is given here. Consider the singular value decomposition (SVD) of S ,

$$S = U\Sigma V^H \quad (5.8)$$

where

$$\Sigma = \begin{bmatrix} \sigma_1 & & & \circ \\ & \sigma_2 & & \\ & & \ddots & \\ & & & \sigma_{Q+1} \\ & \circ & & \end{bmatrix} \quad (5.9)$$

and $\{\sigma_1, \sigma_2, \dots, \sigma_{Q+1}\}$ are the singular values of S , which are ordered from largest to smallest (*i.e.* $\sigma_1 > \sigma_2 > \dots > \sigma_{Q+1}$). Note that Σ is a $(M - Q)N \times (Q + 1)$ matrix. The form in which Σ is written assumes that $(M - Q)N > (Q + 1)$, and if this is not true, then Σ should be written with more columns than rows. The noise cleaned estimate of S , \hat{S} , is formed by truncating the smallest $Q + 1 - K$ singular values in Σ and replacing them with zero. Thus, \hat{S} is formed by

$$\hat{S} = U\hat{\Sigma}V^H \quad (5.10)$$

where

$$\hat{\Sigma} = \begin{bmatrix} \sigma_1 & & & & & \\ & \sigma_2 & & & & \\ & & \ddots & & & \\ & & & \sigma_K & & \\ & & & & 0 & \\ & & & & & \ddots \\ & & & & & & 0 \\ & & \circ & & & & & \end{bmatrix}. \quad (5.11)$$

Note that $\hat{\Sigma}$ is a $(M-Q)N \times (Q+1)$ matrix, just as Σ is. Next, \hat{S} can be written as $[\hat{s}_1 \ \hat{S}_1]$, where \hat{s}_1 is a column vector consisting of the first column of \hat{S} and where \hat{S}_1 is a matrix consisting of the remaining columns of \hat{S} . Next, the estimate of b , \hat{b} , is found using a least squares solution, which can be written as

$$\hat{b} = -(\hat{S}_1^H \hat{S}_1)^{-1} \hat{S}_1^H \hat{s}_1, \quad (5.12)$$

although numerically more robust solutions (using, *e.g.*, the QR decomposition [56]) are preferred to direct computation of Equation 5.12. The estimated x -poles are found by

$$\hat{p}_{x_q} = \frac{1}{\text{zero}_q(\hat{B}(z))}, \quad q = 1, 2, \dots, Q. \quad (5.13)$$

Because only K singular values of \hat{S} are nonzero, there are at most K x -pole estimates which can correspond to data modes. Therefore, only the K x -poles which have the largest energy will be retained (as discussed in Step 2 below).

As stated before, this method of noise cleaning S by truncating all but the K largest singular values of S is described in detail in [29]. This is considered a total least squares (TLS) solution since the entire S matrix is noise cleaned in the SVD

step. There is another method of noise cleaning which was investigated in this work. That is, that the SVD of the S_1 matrix, which is a matrix composed of all but the first column of S , is taken and the same noise cleaning techniques which were applied to S are applied to S_1 . This is considered a solution in the least squares (LS) sense since the data vector (s_1 which is the first column of S) is not perturbed in the solution. This LS method of noise cleaning was found to yield larger variances in the x -poles estimates than the TLS method presented above. This is expected since the TLS method noise cleans both the S_1 and the s_1 matrices simultaneously, while the LS method only noise cleans the S_1 matrix.

Step 2: Estimation of the x -amplitude Coefficients. Before the y -poles are estimated, x -amplitude coefficients must first be estimated. They are defined as

$$c_{q,n} = \sum_{l=1}^{L_k} a_{q,l} p_{y_{q,l}}^n, \quad q = 1, 2, \dots, Q. \quad (5.14)$$

With this definition, the model associated with equation 5.2, using the estimated x -poles, is written as

$$d(m, n) = \sum_{q=1}^Q c_{q,n} p_{x_q}^m \quad (5.15)$$

where $c_{q,n}$ is the q th x -amplitude coefficient associated with the n th row of D' .

Note that the equations in 5.15 are uncoupled for different values of n . Thus, each row of D' will give an x -amplitude coefficient estimate for each x -pole. The x -amplitude coefficients are an intermediate step in the estimation procedure and are completely defined in Equation 5.14. Also note that the y -pole model orders, $\{L_k\}_{k=1}^K$, may be different for each of the K x -poles. Equation 5.15 is used to solve

for the $c_{q,n}$ s as follows

$$\begin{bmatrix} 1 & 1 & \cdots & 1 \\ p_{x_1} & p_{x_2} & \cdots & p_{x_Q} \\ p_{x_1}^2 & p_{x_2}^2 & \cdots & p_{x_Q}^2 \\ \vdots & \vdots & & \vdots \\ p_{x_1}^{M-1} & p_{x_2}^{M-1} & \cdots & p_{x_Q}^{M-1} \end{bmatrix} \begin{bmatrix} c_{1,0} & c_{1,1} & \cdots & c_{1,N-1} \\ c_{2,0} & c_{2,1} & \cdots & c_{2,N-1} \\ \vdots & \vdots & & \vdots \\ c_{Q,0} & c_{Q,1} & \cdots & c_{Q,N-1} \end{bmatrix} = D'^T, \quad (5.16)$$

or

$$P_x C = D'^T. \quad (5.17)$$

The initial set of x -amplitude coefficients are found from a least squares solution to Equation 5.17 using the x -pole estimates; this can be written as

$$\hat{C} = (\hat{P}_x^H \hat{P}_x)^{-1} \hat{P}_x^H D'^T, \quad (5.18)$$

although numerically more robust solutions (using, *e.g.*, the QR decomposition [56]) are preferred to direct computation of Equation 5.18.

As previously stated, because only K singular values of \hat{S} are nonzero, there are at most K x -pole estimates which can correspond to data modes. Therefore, only the K x -poles which have the largest energy are retained. This is done by computing the Q x -mode energies as

$$E_q = \sum_{n=0}^{N-1} |\hat{c}_{q,n}|^2 \sum_{m=0}^{M-1} |\hat{p}_{x_q}|^{2m} \quad q = 1, 2, \dots, Q \quad (5.19)$$

and retaining those K x -poles whose corresponding energies are highest.

The final set of K x -amplitude coefficients, the $c_{k,n}$ s, are estimated using a procedure identical to the one used above to estimate the initial set of x -amplitude coefficients. This method is outlined here. A shortened version of Equation 5.15 is

used, given by

$$d(m, n) = \sum_{k=1}^K c_{k,n} p_{x_k}^m \quad (5.20)$$

where $c_{k,n}$ is the k th x -amplitude coefficient associated with the n th row of D' .

Thus, Equation 5.20 is used to solve for the $c_{k,n}$ s as follows

$$\begin{bmatrix} 1 & 1 & \cdots & 1 \\ p_{x_1} & p_{x_2} & \cdots & p_{x_K} \\ p_{x_1}^2 & p_{x_2}^2 & \cdots & p_{x_K}^2 \\ \vdots & \vdots & & \vdots \\ p_{x_1}^{M-1} & p_{x_2}^{M-1} & \cdots & p_{x_K}^{M-1} \end{bmatrix} \begin{bmatrix} c_{1,0} & c_{1,1} & \cdots & c_{1,N-1} \\ c_{2,0} & c_{2,1} & \cdots & c_{2,N-1} \\ \vdots & \vdots & & \vdots \\ c_{K,0} & c_{K,1} & \cdots & c_{K,N-1} \end{bmatrix} = D'^T, \quad (5.21)$$

or

$$P_x^K C = D'^T. \quad (5.22)$$

As with the initial set of x -amplitude coefficients, the final set of x -amplitude coefficients are found from a least squares solution to Equation 5.22 using the x -pole estimates; this can be written as

$$\hat{C} = \left(\widehat{P}_x^K^H \widehat{P}_x^K \right)^{-1} \widehat{P}_x^K^H D'^T, \quad (5.23)$$

although numerically more robust solutions (using, *e.g.*, the QR decomposition [56]) are preferred to direct computation of Equation 5.23.

Note that the final set of x -amplitude coefficients are estimated from the K true x -pole estimates, as opposed to simply taking the initial set of x -amplitude coefficients which correspond to the K highest energy modes. This re-estimation of x -amplitude coefficients should allow the parameter estimates (when used in the model in Equation 5.2) to better model the original data.

The x -amplitude coefficients serve as the input data to the second Prony model which determines the y -pole locations and ultimately the amplitude coefficients. For

each x -pole, there are N x -amplitude coefficients, each corresponding to a different y -direction data set (a different column of D'). The x -amplitude coefficients hold the information which yields the y -pole's locations in the transform domain.

Step 3: Estimation of the y -poles. The x -amplitude coefficients are now used to solve for the y -poles. For each of the K high energy x -poles, the backward linear prediction equations for the model given by Equation 5.14 become

$$\begin{bmatrix} c_{k,0} & c_{k,1} & \cdots & c_{k,R_k} \\ c_{k,1} & c_{k,2} & \cdots & c_{k,R_k+1} \\ \vdots & \vdots & & \vdots \\ c_{k,N-R_k-1} & c_{k,N-R_k} & \cdots & c_{k,N-1} \end{bmatrix} \begin{bmatrix} 1 \\ b_1^k \\ b_2^k \\ \vdots \\ b_{R_k}^k \end{bmatrix} \approx 0 \quad k = 1, 2, \dots, K \quad (5.24)$$

or

$$F^k \begin{bmatrix} 1 \\ b^k \end{bmatrix} \approx 0 \quad (5.25)$$

where R_k is the order of prediction for the y -poles, and b^k is the coefficient vector of the polynomial $B^k(z)$ given by

$$B^k(z) = 1 + b_1^k z^{-1} + b_2^k z^{-2} + \cdots + b_{R_k}^k z^{-R_k}. \quad (5.26)$$

Again, R_k can be any integer greater than or equal to L_k , while in practice choosing $R_k > L_k$ results in more accurate parameter estimates [53]–[55].

Equation 5.25 is used to solve for the estimate of b^k , \hat{b}^k , in a total least squares sense, analogous to the manner described in Step 1, to arrive at a minimum norm (TLS) estimate, where the $R_k + 1 - L_k$ singular values of F^k are truncated to arrive at a noise cleaned estimate \hat{F}^k (see [29] or Step 1 for details).

The y -pole estimates are thus given by

$$\hat{p}_{y_k, r_k} = \frac{1}{\text{zero}_{r_k}(\hat{B}^k(z))}, \quad r_k = 1, 2, \dots, R_k. \quad (5.27)$$

The procedure from Equation 5.24 to Equation 5.27 is carried out K times to estimate the y -poles corresponding to each of the K x -poles. Because only L_k singular values of \hat{F}^k are nonzero, there are at most L_k y -pole estimates which can correspond to data modes. Therefore, only the L_k y -poles which have the largest energy are retained (as discussed in Step 4 below).

Step 4: Estimation of the Amplitude Coefficients. Now that all of the required y -poles have been estimated, the amplitude coefficients will be estimated next. Using Equation 5.14,

$$\begin{bmatrix} 1 & 1 & \dots & 1 \\ p_{y_k,1} & p_{y_k,2} & \dots & p_{y_k,R_k} \\ p_{y_k,1}^2 & p_{y_k,2}^2 & \dots & p_{y_k,R_k}^2 \\ \vdots & \vdots & \ddots & \vdots \\ p_{y_k,1}^{N-1} & p_{y_k,2}^{N-1} & \dots & p_{y_k,R_k}^{N-1} \end{bmatrix} \begin{bmatrix} a_{k,1} \\ a_{k,2} \\ \vdots \\ a_{k,R_k} \end{bmatrix} = \begin{bmatrix} c_{k,0} \\ c_{k,1} \\ c_{k,2} \\ \vdots \\ c_{k,N-1} \end{bmatrix} \quad (5.28)$$

or

$$P_y^k A^k = c^k. \quad (5.29)$$

The initial set of amplitude coefficients are found from a least squares solution to Equation 5.29 using the y -pole estimates along the x -amplitude coefficients; this can be written as

$$\hat{A}^k = \left(\hat{P}_y^k H \hat{P}_y^k \right)^{-1} \hat{P}_y^k H \hat{c}^k, \quad (5.30)$$

although numerically more robust solutions (using, *e.g.*, the QR decomposition [56]) are preferred to direct computation of Equation 5.30. The procedure from Equa-

Table 5: Summary of steps performed in Algorithm One.

Step	Estimated Parameters	Method of Solution
1	$\{p_{x_k}\}_{k=1}^K$ (x -poles)	TLS of Eq. 5.6 w/ SVD truncation
2	$\{c_{q,n}\}_{q,n=1,0}^{Q,N-1}$ (x -amp coefs)	LS of Eq. 5.16 via QR decomposition
3	$\{p_{y_k,l}\}_{k,l=1,1}^{K,L_k}$ (y -poles)	TLS of Eq. 5.24 w/ SVD truncation
4	$\{a_{k,l}\}_{k,l=1,1}^{K,L_k}$ (amp coefs)	LS of Eq. 5.28 via QR decomposition

tion 5.28 to Equation 5.30 is carried out K times to determine the entire initial set of amplitude coefficients (there are $\sum_{k=1}^K R_k$ amplitude coefficients in the initial set).

As stated before, because only L_k singular values of \hat{F}^k are nonzero, there are at most L_k y -pole estimates which can correspond to data modes. Therefore, only the L_k y -poles which have the largest energy are retained. This is done by computing the R_k y -mode energies for each of the k th x -poles as

$$E_{r_k} = |\hat{a}_{k,r_k}|^2 \sum_{n=0}^{N-1} |\hat{p}_{y_k,r_k}|^{2n} \quad r_k = 1, 2, \dots, R_k \quad (5.31)$$

and retaining those L_k poles whose corresponding energies are highest.

The final set of amplitude coefficients (the final set consists of $\sum_{k=1}^K L_k$ amplitude coefficients) are then estimated utilizing a procedure identical to the one used to estimate the initial set of amplitude coefficients outlined above. The only difference is that there are only L_k y -poles which are used in Equation 5.28. Also, there are only L_k amplitude coefficients to be estimated for each of the K x -poles.

Algorithm Two

Algorithm Two uses the first three steps of Algorithm One twice, and then requires a matching step and a final amplitude coefficient calculation step. The steps involved in Algorithm Two are summarized in Table 6. The first three steps of Algorithm One are carried out using the data $d'(m, n)$ yielding x and y -pole estimates, $\{p_{x_k}\}_{k=1}^K$ and $\{p_{y_{k,l}}\}_{l=1}^{L_k}$. Next, the data is transposed (*i.e.* $d''(n, m) = d'(m, n)$), and Algorithm One is applied to $d''(n, m)$ to arrive at a second set of poles, $\{p_{x_{k^t}}^t\}_{k^t=1}^{K^t}$ and $\{p_{y_{k^t,l^t}}^t\}_{l^t=1}^{L_{k^t}^t}$. Note that the model orders K and L_k are related to K^t and $L_{k^t}^t$, depending on the structure of a particular model, and are in general different. Also note that included with steps 3 and 6 (which involve the estimation of the y and y^t -poles) of Algorithm Two is an amplitude coefficient estimation procedure in order to determine the highest energy modes. This is required to insure that only the correct number of true modes are retained in each step.

The two sets of estimates are combined, and the more accurate part of the estimates from each set is retained. The more accurate part of each estimate is the set of poles which were estimated first, (*i.e.* the x -poles from each set). The y -poles are less accurate than the x -poles because they are estimates based on the x -pole estimates. A matching algorithm is used to combine both sets of pole estimates yielding a single set of pole estimates.

The matching is performed using the following metric

$$\Delta \left((p_{x_k}, p_{y_{k,l}}), (p_{x_{k^t}}^t, p_{y_{k^t,l^t}}^t) \right) = \sqrt{|p_{x_k} - p_{y_{k^t,l^t}}^t|^2 + |p_{y_{k,l}} - p_{x_{k^t}}^t|^2} \quad (5.32)$$

for the distance between 2-D exponential modes $(p_{x_k}, p_{y_{k,l}})$ and $(p_{x_{k^t}}^t, p_{y_{k^t,l^t}}^t)$, esti-

mated in the first six steps of Algorithm Two. These distances are calculated for all of the possible pairs. Then the closest match is made and the respective pole pairs and distances are eliminated from consideration. The next-to-closest match is then made in the same fashion and so on, until there are no modes remaining from one of the two sets of pole pairs parts (any leftover pole pairs are discarded). Note that the x -poles, p_{x_k} and $p_{x_{k^t}}^t$, from each of the two estimations are retained and the y -poles are discarded as discussed above. Thus, the y -poles are only necessary for the pairing performed in the matching step. Note that $p_{x_{k^t}}^t$ takes on the role of y -pole in the original model. The final set of matched pole pairs for Algorithm Two are thus designated $\{\rho_{x_\gamma}, \rho_{y_\gamma}\}_{\gamma=1}^\Gamma$, where the ρ 's are given by the paired p_x 's and p_x^t 's and $\Gamma = \min \left\{ \sum_{k=1}^K L_k, \sum_{k^t=1}^{K^t} L_{k^t}^t \right\}$.

Using this definition, the model in Equation 5.2 can be expressed as

$$d(m, n) = \sum_{\gamma=1}^{\Gamma} \alpha_{\gamma} \rho_{x_{\gamma}}^m \rho_{y_{\gamma}}^n. \quad (5.33)$$

Equation 5.33 now is used to solve for amplitude coefficients, $\{\alpha_{\gamma}\}_{\gamma=1}^{\Gamma}$, as follows

$$\begin{bmatrix} P(0) \\ P(1) \\ \vdots \\ P(M-1) \end{bmatrix} \begin{bmatrix} \alpha_1 \\ \alpha_2 \\ \vdots \\ \alpha_{\Gamma} \end{bmatrix} = \begin{bmatrix} d'(0) \\ d'(1) \\ \vdots \\ d'(M-1) \end{bmatrix}, \quad (5.34)$$

where each $P(m)$ and $d'(m)$ are given by

$$P(m) = \begin{bmatrix} \rho_{x_1}^m & \rho_{x_2}^m & \cdots & \rho_{x_{\Gamma}}^m \\ \rho_{x_1}^m \rho_{y_1} & \rho_{x_2}^m \rho_{y_2} & \cdots & \rho_{x_{\Gamma}}^m \rho_{y_{\Gamma}} \\ \vdots & \vdots & & \vdots \\ \rho_{x_1}^m \rho_{y_1}^{N-1} & \rho_{x_2}^m \rho_{y_2}^{N-1} & \cdots & \rho_{x_{\Gamma}}^m \rho_{y_{\Gamma}}^{N-1} \end{bmatrix} \quad (5.35)$$

and

$$d'(m) = \begin{bmatrix} d'(m, 0) & d'(m, 1) & \cdots & d'(m, N-1) \end{bmatrix}^T. \quad (5.36)$$

Table 6: Summary of steps performed in Algorithm Two.

Step	Estimated Parameters	Method of Solution
1	$\{p_{x_k}\}_{k=1}^K$ (x -poles)	TLS of Eq. 5.6 w/ SVD truncation
2	$\{c_{q,n}\}_{q,n=1,0}^{Q,N-1}$ (x -amp coefs)	LS of Eq. 5.16 via QR decomposition
3	$\{p_{y_{k,l}}\}_{k,l=1,1}^{K,L_k}$ (y -poles)	TLS of Eq. 5.24 w/ SVD truncation
4	$\{p_{x_{k^t}}^t\}_{k^t=1}^{K^t}$ (x^t -poles)	TLS similar to Step 1
5	$\{c_{q^t,m}^t\}_{q^t,m=1,0}^{Q^t,M-1}$ (x^t -amp coefs)	LS similar to Step 2
6	$\{p_{y_{k^t,l^t}}^t\}_{k^t,l^t=1,1}^{K^t,L_{k^t}^t}$ (y^t -poles)	TLS similar to Step 3
7	$\{\rho_{x_\gamma}, \rho_{y_\gamma}\}_{\gamma=1}^\Gamma$ (x and y -poles)	Matching using Eq. 5.32
8	$\{\alpha_\gamma\}_{\gamma=1}^\Gamma$ (amp coefs)	LS of Eq. 5.34 via QR decomposition

Equation 5.34 can be expressed as

$$\mathcal{P}\mathcal{A} = \mathcal{D}'. \quad (5.37)$$

The amplitude coefficients are found using the pole estimates from a least squares solution to Equation 5.34 which can be written as

$$\hat{\mathcal{A}} = (\hat{\mathcal{P}}^H \hat{\mathcal{P}})^{-1} \hat{\mathcal{P}}^H \mathcal{D}', \quad (5.38)$$

although numerically more robust solutions (using, *e.g.*, the QR decomposition [56]) are preferred to direct computation of Equation 5.38.

Implementation Issues

In this section operation counts for the four steps of Algorithm One and for the eight steps of Algorithm Two are presented. These operation counts are given for the case when the data is real. For complex data considered in the examples which follow the counts were observed to be about a factor of 2 to 3 larger for the SVDs and about 4 times larger for the QR decompositions. An alternative to the larger SVD steps is presented which provides a reduction in computation.

Operation Count for Algorithm One. To obtain the operation counts for the four steps of Algorithm One, the counts for the SVD computations and the computation of the QR decompositions used for the least squares solutions are needed.

The approximate floating point operation (flop) count, fc_{SVD} , associated with the computation of the singular values and left singular vectors of a real $r \times c$ matrix is given by $fc_{SVD} \approx 4rc^2 + 8c^3$ [56]. Thus the flop count for the SVD of Step 1, fc_{One}^1 , is given by

$$fc_{One}^1 \approx 4N(M - Q)(Q + 1)^2 + 8(Q + 1)^3. \quad (5.39)$$

The approximate flop count, fc_{QR} , associated with the QR decomposition of a real $r \times c$ matrix is given by $fc_{QR} \approx 2rc^2 - \frac{2}{3}c^3$ [56]. Thus, the flop count for the QR decomposition required for the LS solution of Step 2 is given by

$$fc_{One}^2 \approx 2MQ^2 - \frac{2}{3}Q^3. \quad (5.40)$$

For the K SVDs in Step 3 the approximate flop count is given by

$$\text{fc}_{\text{One}}^3 \approx \sum_{k=1}^K \left(4(N - R_k)(R_k + 1)^2 + 8(R_k + 1)^3 \right). \quad (5.41)$$

For the K QR decompositions in Step 4 the approximate flop count is given by

$$\text{fc}_{\text{One}}^4 \approx \sum_{k=1}^K \left(2NR_k^2 - \frac{2}{3}R_k^3 \right). \quad (5.42)$$

The flop count for the SVDs and QR decompositions of Algorithm One is given by the sum of the individual flop counts above.

To achieve near optimal performance (with respect to the Cramér-Rao Bound (CRB)), the model order used for Steps 1 and 3 of Algorithm One should be integers near $Q = \frac{M}{3}$ and $R_k = \frac{N}{3}$ [59]. Using these substitutions and further approximations the estimate for the total flop count is

$$\text{fc}_{\text{One}} \approx \frac{1}{3}M^3N + \frac{1}{2}KN^3. \quad (5.43)$$

Note that the K estimations of Steps 3 and 4 are independent of each other and can thus be done in parallel.

Operation Count for Algorithm Two. Since Algorithm Two first uses the first three steps Algorithm One $\text{fc}_{\text{TWO}}^1 = \text{fc}_{\text{One}}^1$, $\text{fc}_{\text{TWO}}^2 = \text{fc}_{\text{One}}^2$, and $\text{fc}_{\text{TWO}}^3 = \text{fc}_{\text{One}}^3$ for the flop counts of those steps. For Steps 4–6, the roles of M and N are reversed, and Q^t and $R_{k^t}^t$ are used instead of Q and R_k . Their flop counts are thus

$$\begin{aligned} \text{fc}_{\text{TWO}}^4 &\approx 4M(N - Q^t)(Q^t + 1)^2 + 8(Q^t + 1)^3 \\ \text{fc}_{\text{TWO}}^5 &\approx 2NQ^{t2} - \frac{2}{3}Q^{t3} \\ \text{fc}_{\text{TWO}}^6 &\approx \sum_{k^t=1}^{K^t} \left(4(M - R_{k^t}^t)(R_{k^t}^t + 1)^2 + 8(R_{k^t}^t + 1)^3 \right). \end{aligned} \quad (5.44)$$

Each distance ($\Delta(\cdot, \cdot)$) calculation requires 16 flops. Thus, the flop count for Step 7 is given by

$$fc_{\text{Two}}^7 = 16 \sum_{k=1}^K L_k \sum_{k^t=1}^{K^t} L_{k^t}^k \quad (5.45)$$

For the QR decomposition in Step 8 the approximate flop count is given by

$$fc_{\text{Two}}^8 \approx 2MN\Gamma^2 - \frac{2}{3}\Gamma^3. \quad (5.46)$$

The flop count for the SVDs, QR decompositions, and matching of Algorithm Two is given by the sum of the individual flop counts above.

Again, to achieve near optimal performance (with respect to the CRB), the model order used for Steps 1, 3, 4, and 6 of Algorithm Two should be integers near $Q = R_{k^t}^t = \frac{M}{3}$, $R_k = Q^t = \frac{N}{3}$ [59]. Using these substitutions and further approximations the total flop count is estimated as

$$fc_{\text{Two}} \approx \frac{1}{3}M^3N + \frac{1}{2}KN^3 + \frac{1}{3}N^3M + \frac{1}{2}K^tM^3 + 2MN\Gamma^2 - \frac{2}{3}\Gamma^3. \quad (5.47)$$

Note that the number of flops required for Step 7 is negligible when compared to the other steps. Also note that the K estimations of Step 3 are independent and the K^t estimations of Step 6 are independent and can thus be done in parallel.

Alternative Method for x -pole Estimation. The solution for \hat{b} using Equation 5.5 can become computationally intensive for large data sets. For example, if $M = N = 64$ and $Q = 20$, then S is of dimension (2816×21) . Since only the right singular vectors and the singular values are needed, one can instead obtain \hat{b} from

a related eigen-decomposition problem. Consider $S^H S$,

$$S^H S = \begin{bmatrix} s_1^H s_1 & s_1^H S_2 \\ S_2^H s_1 & S_2^H S_2 \end{bmatrix}, \quad (5.48)$$

where s_1 is the first column of S and S_2 are the remaining Q columns (i.e. $S = \begin{bmatrix} s_1 & S_2 \end{bmatrix}$). Note that for typical problems S contains many more rows than columns, so $S^H S$ is smaller than S . An eigen-decomposition of $S^H S$ is performed, and all but the K largest eigenvalues are truncated to give $\widehat{S^H S}$. Finally the minimum norm estimate of \hat{b} is given by,

$$\hat{b} = - \left(\widehat{S_2^H S_2} \right)^+ \widehat{S_2^H s_1} \quad (5.49)$$

where $\widehat{S_2^H S_2}$ and $\widehat{S_2^H s_1}$ are the lower right and lower left submatrices of $\widehat{S^H S}$, respectively (*cf.* see Equation 5.48).

Note that this procedure is less numerically accurate than the previous procedure because of the squaring of the data (which occurs in $S^H S$), so extended precision should be used in the computations.

5.2.4 Examples

Below numerical examples are presented to assess model validity and noise effects. Two examples are presented. The first example considers the estimation of three 2-D undamped exponentials; this example was also considered in [28]. The second example considers the estimation of three 2-D damped exponentials.

Example 1

In this example the variances of frequency and magnitude estimates are compared to their Cramér-Rao Bounds (CRBs) at various signal to noise ratios (SNRs) for the three 2-D frequency scenario presented in [28] using Algorithm One and Algorithm Two. Data was generated using the model in Equation 5.2 for $M = N = 20$ and

$$\begin{aligned} \begin{bmatrix} p_{x_1} & p_{y_{1,1}} & a_{1,1} \end{bmatrix} &= \begin{bmatrix} e^{j2\pi 0.24} & e^{j2\pi 0.24} & 1 \end{bmatrix} \\ \begin{bmatrix} p_{x_1} & p_{y_{1,2}} & a_{1,2} \end{bmatrix} &= \begin{bmatrix} e^{j2\pi 0.24} & e^{j2\pi 0.26} & 1 \end{bmatrix} \\ \begin{bmatrix} p_{x_2} & p_{y_{2,1}} & a_{2,1} \end{bmatrix} &= \begin{bmatrix} e^{j2\pi 0.26} & e^{j2\pi 0.24} & 1 \end{bmatrix}. \end{aligned} \quad (5.50)$$

It can be seen that from the angles of the above poles the corresponding frequencies are 0.24 and 0.26. For the purposes of identification the $(x\text{-pole}, y\text{-pole})$ pairs above are labeled with frequencies $(0.24, 0.24)$, $(0.24, 0.26)$, and $(0.26, 0.24)$ as 2-D frequencies f_1 , f_2 , and f_3 , respectively. Note that these frequencies are spaced at four-tenths of a Fourier bin in both directions ($1 \text{ Fourier bin} = \frac{1}{20} = 0.05$). Also note that this data consists of undamped exponentials. These 2-D frequencies are shown on the 2-D frequency plane in Figure 45.

Figures 46(a) and 46(b) show the simulation results for the x -pole frequencies and y -pole frequencies, respectively where Algorithm One was used. One hundred different noise realizations were run for each integer SNR between 0 and 50dB. The SNR is defined as the total signal power divided by the total noise power. Specifically these figures show the estimated frequency variances for the various SNRs (they are

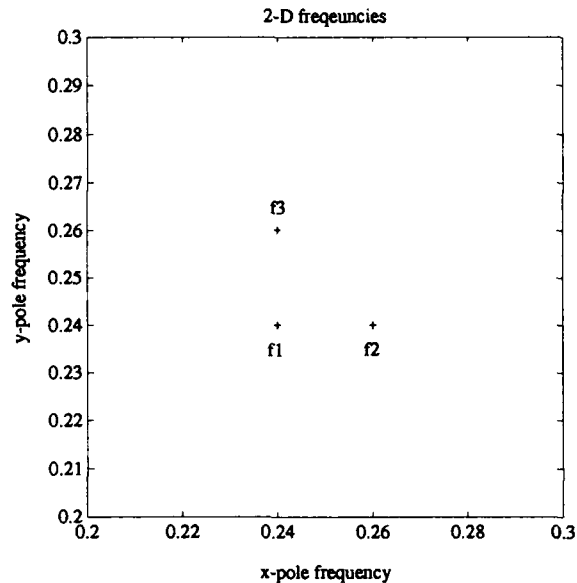
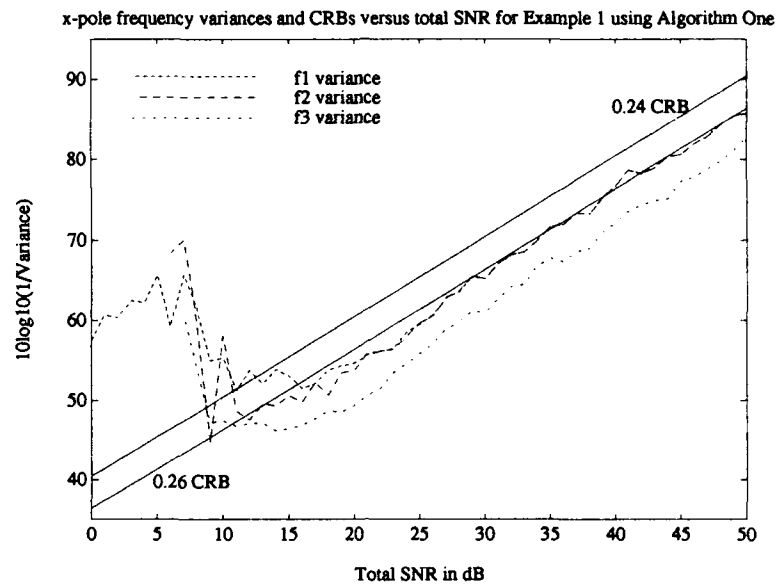


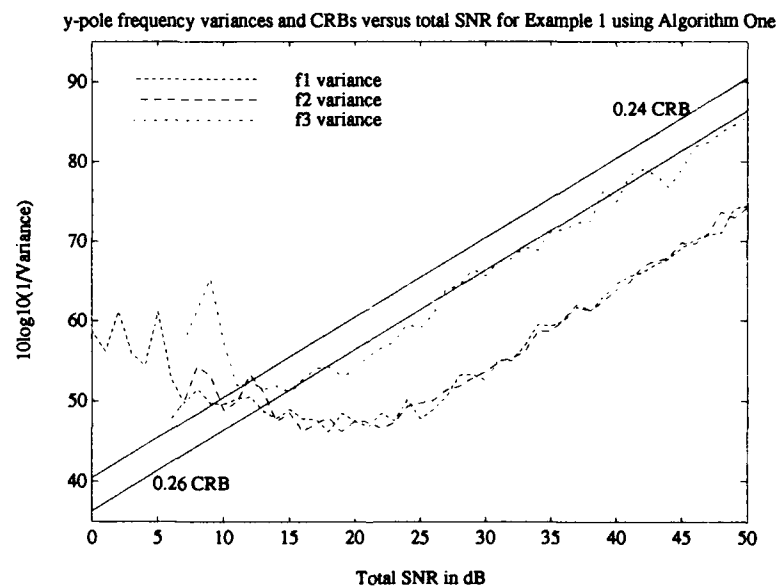
Figure 45: 2-D frequency locations for Example 1.

given by the dashed lines as indicated). The corresponding CRBs are given by the solid lines; the CRBs of the model were found using the expressions in [37]. The algorithm parameters were set at $Q = 8, K = 2, R_1 = R_2 = 8, L_1 = L_2 = 2$ for this example. Note that $Q \approx \frac{M}{3}$ and $R_k \approx \frac{N}{3}$ are used because these values give maximum parameter accuracy in the SVD estimation step [59].

From Figure 46(a) it can be seen that the threshold SNR is 15dB in this case. For SNRs above 15dB, the variances are within about 4dB of the CRB; below 15dB the algorithm fails to reliably resolve the frequencies. The simulation variance lines even cross the CRB due to the fact that the pole estimates become so erratic and most cannot be used in the variance calculations. Theoretically, the variance curves for f1 and f2 are identical, however the variance curves from the Monte-Carlo simulations



(a)



(b)

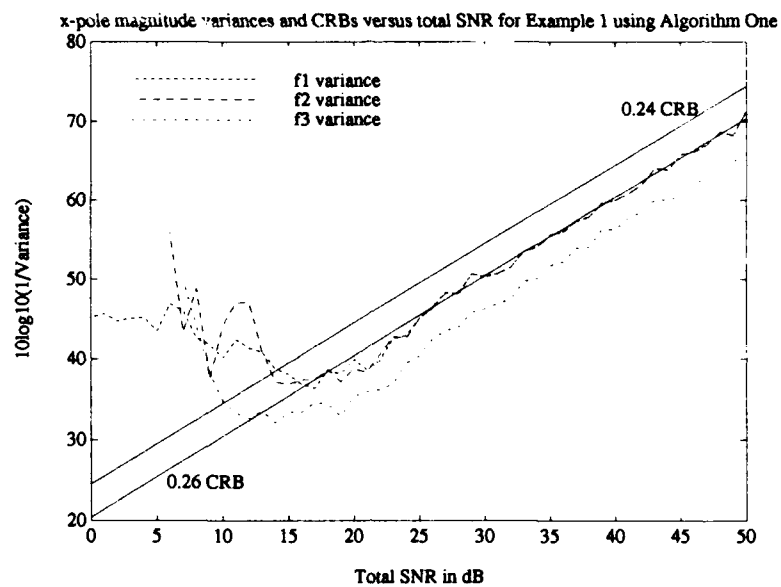
Figure 46: Example 1. $10\log_{10}(1/\text{Variance})$ versus total SNR in dB for (a) x -pole and (b) y -pole frequencies using Algorithm One.

separate at the lower SNRs due to differences in the y -pole estimates which cause some outliers to not be included in the variance calculations. The results in [28] are for an SNR per pole of 10dB, which corresponds to a total SNR of 17.7dB used here. In comparison, the estimation scheme in [28] gives x -pole frequency variances which are about 3 or 4dB better for f_1 and f_3 and about 8dB better for f_2 .

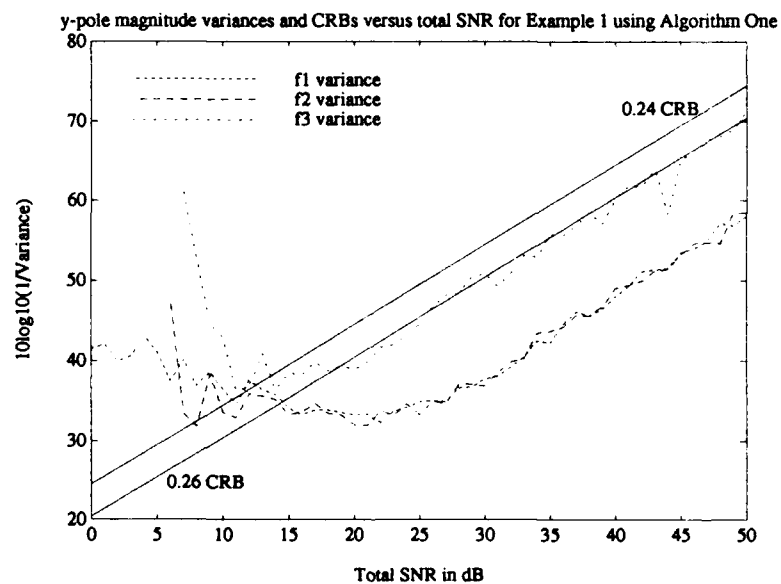
Figure 46(b) is a plot of the inverses of the y -pole frequency variances for the various SNRs along with the corresponding CRBs as before. From this figure it can be seen that the curve for the y -pole variance for f_3 exhibits the same properties as those discussed for the x -pole frequency variances above. The y -pole frequency variances for f_1 and f_2 are about 13 and 10 dB away from their respective CRB lines, respectively. Also, the y -pole estimation for f_1 and f_2 breaks down at SNRs below 25dB. The fact that these variances are farther away from their CRBs and that the resolution threshold is higher is expected because of the accumulation of error which occurs in the y -pole estimates in Algorithm One. This accumulation of error does not occur in Algorithm Two, as shown below.

Figure 47 shows the estimated x -pole and y -pole magnitude variances for this example when Algorithm One is used. The characteristics are the same as those for the frequency variances, with respect to the CRBs.

Figure 48 shows the estimated x -pole and y -pole frequency variances for this example when Algorithm Two is used. As expected, the x -pole frequency variances are much the same as those for Figure 46(a), but the y -pole frequency variances have been improved to match the x -pole frequency variance performance. The esti-



(a)



(b)

Figure 47: Example 1. $10\log_{10}(1/\text{Variance})$ versus total SNR in dB for (a) x -pole and (b) y -pole magnitudes using Algorithm One.

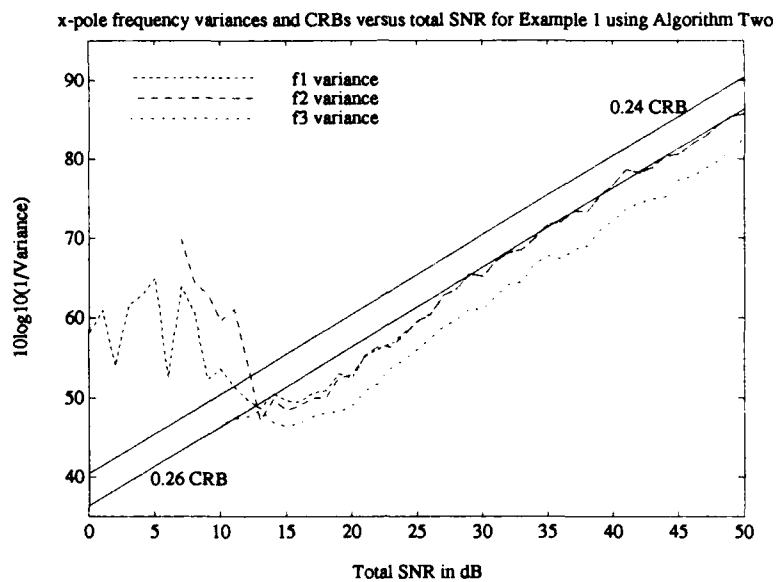
mation scheme in [28] gives variances which are about 3 or 4dB better for the y -pole frequencies of f_1 and f_2 and variances which are about 8dB better for the y -pole frequency of f_3 .

Figure 49 shows the estimated x -pole and y -pole magnitude variances for this example when Algorithm Two is used. The improvements in the magnitude estimates are comparable to the improvements in the frequency estimates.

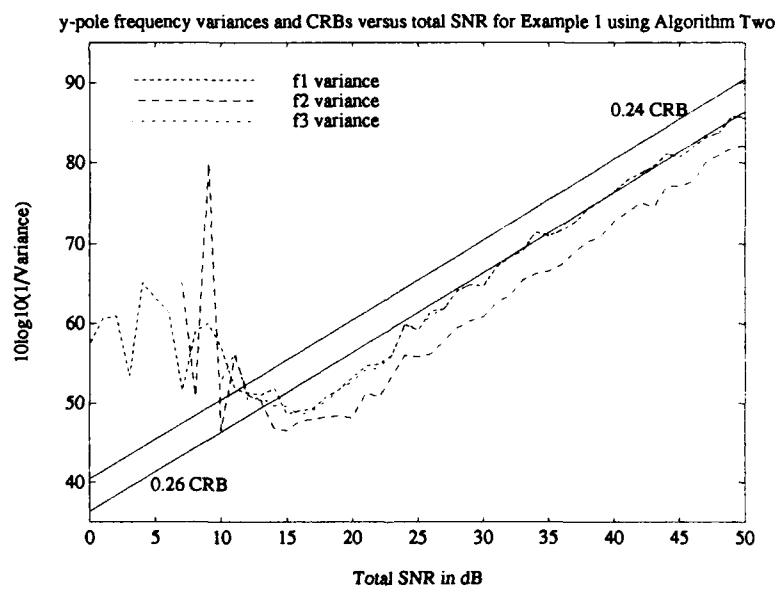
Next consider the SVD operation counts for this example for Algorithm Two. The SVD steps are major computational parts. Each noise realization required SVDs of two 240×9 matrices and four 9×11 matrices where only the singular values and right singular vectors were computed. For the same example, the algorithm in [28] required SVDs of two 49×169 matrices for each noise realization where the singular values and left singular vectors are computed. Looking at expressions in [56] for SVD computations, Algorithm Two requires fewer flops than the algorithm in [28] for the SVDs. Note that the SVDs for both algorithms can be performed with fewer computations by computing the eigen-decomposition of smaller square matrices as discussed in Section 5.2.3. Using this idea the total number of computations are reduced for both methods, however there is still savings with Algorithm Two over the algorithm in [28].

Example 2

In this example the estimation of damped exponentials in noise is examined using Algorithm Two. Data was generated using the model in Equation 5.2 for

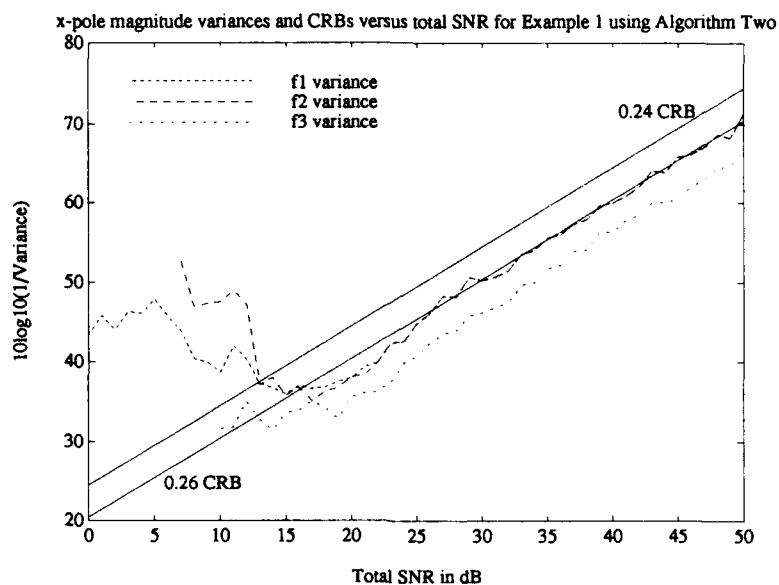


(a)

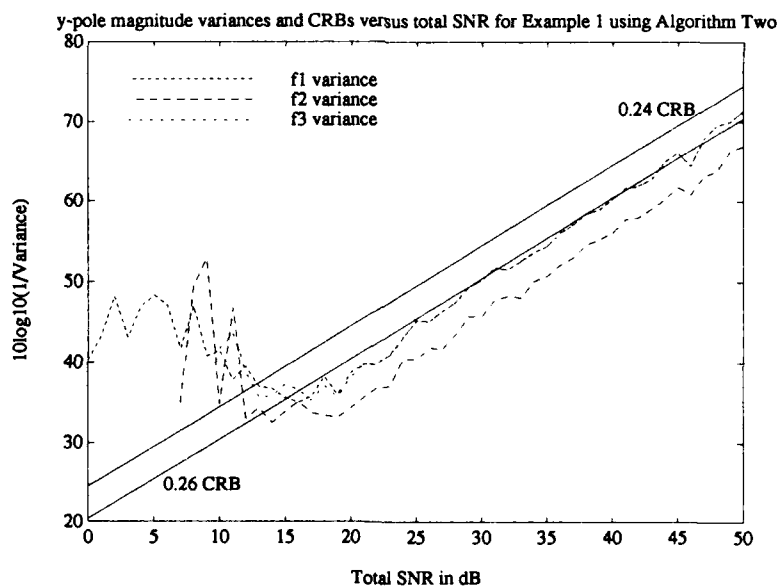


(b)

Figure 48: Example 1. $10\log_{10}(1/\text{Variance})$ versus total SNR in dB for (a) x -pole and (b) y -pole frequencies using Algorithm Two.



(a)



(b)

Figure 49: Example 1. $10\log_{10}(1/\text{Variance})$ versus total SNR in dB for (a) x -pole and (b) y -pole magnitudes using Algorithm Two.

$M = N = 20$ and

$$\begin{aligned} \begin{bmatrix} p_{x_1} & p_{y_{1,1}} & a_{1,1} \end{bmatrix} &= \begin{bmatrix} 0.92e^{j2\pi 0.24} & 0.92e^{j2\pi 0.24} & 3.185 \end{bmatrix} \\ \begin{bmatrix} p_{x_1} & p_{y_{1,2}} & a_{1,2} \end{bmatrix} &= \begin{bmatrix} 0.92e^{j2\pi 0.24} & 0.94e^{j2\pi 0.26} & 2.846 \end{bmatrix} \\ \begin{bmatrix} p_{x_2} & p_{y_{2,1}} & a_{2,1} \end{bmatrix} &= \begin{bmatrix} 0.94e^{j2\pi 0.26} & 0.92e^{j2\pi 0.24} & 2.846 \end{bmatrix}. \end{aligned} \quad (5.51)$$

For the purposes of identification the (x -pole, y -pole) pairs above with frequencies (0.24,0.24), (0.24,0.26), and (0.26,0.24) are labeled as 2-D poles p_1 , p_2 , and p_3 , respectively. The amplitude coefficients are chosen so that the energy of each mode is identical to the corresponding mode's energy in Example 1.

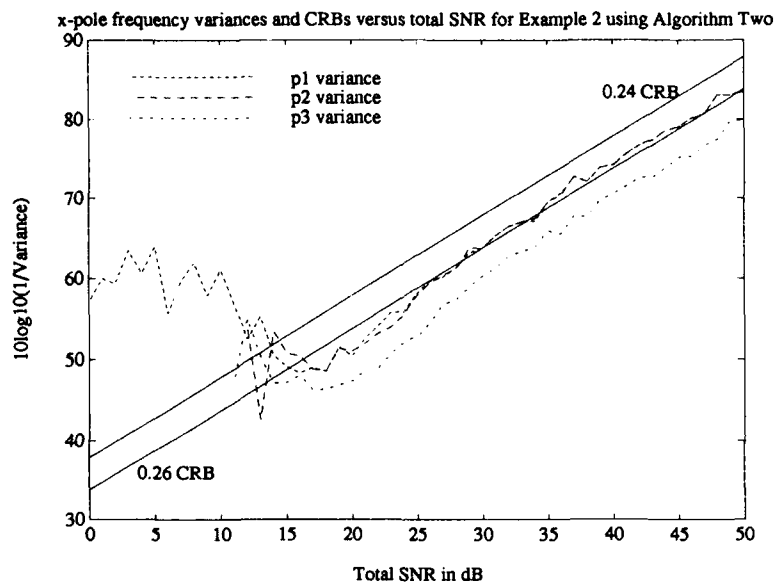
Figures 50 and 51 show the simulation results for the x -pole and y -pole frequency and magnitude variances, respectively. The results are similar to the undamped results in Example 1 using Algorithm Two. The variances track the CRBs as before, with the exception being that the resolution threshold is at an SNR of about 20dB rather than 15dB.

These results show that the algorithm is capable of estimating damped as well as undamped exponentials in noise. The modeling of many canonical shapes requires damped exponential models.

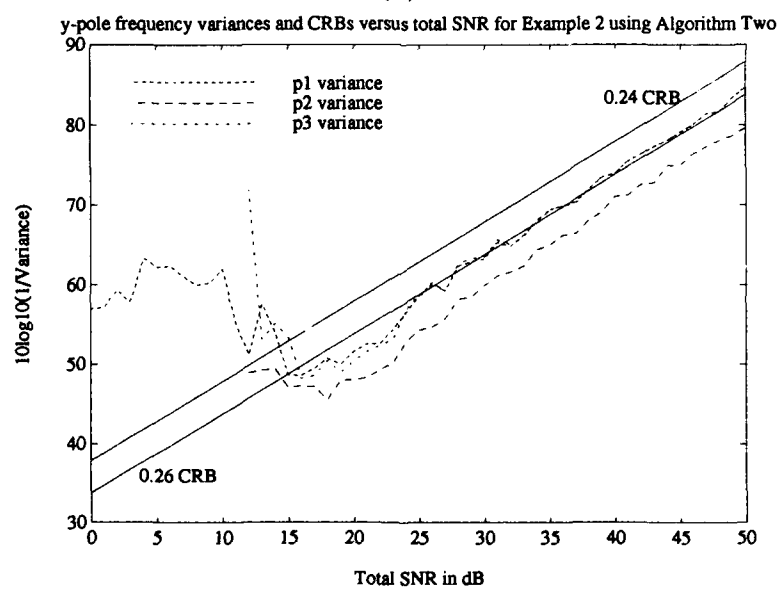
5.3 Full-Polarization Extension of TLS-Prony Technique

5.3.1 Background and Introduction

The preceding algorithms determined the scattering center locations based upon a single polarization 2-D data set. These algorithms can easily be extended to the full-polarization case to examine the polarimetric properties of scattering centers



(a)



(b)

Figure 50: Example 2. $10\log_{10}(1/\text{Variance})$ versus total SNR in dB for (a) x -pole and (b) y -pole frequencies using Algorithm Two.

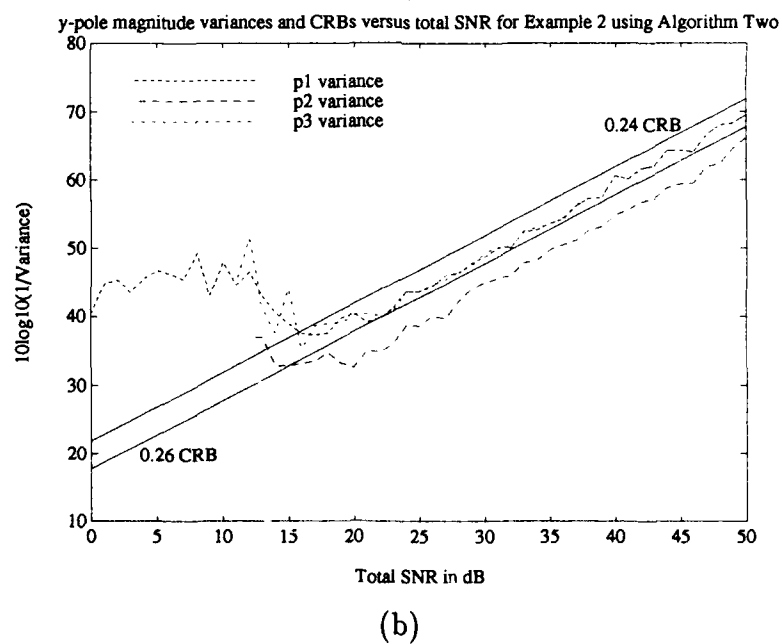
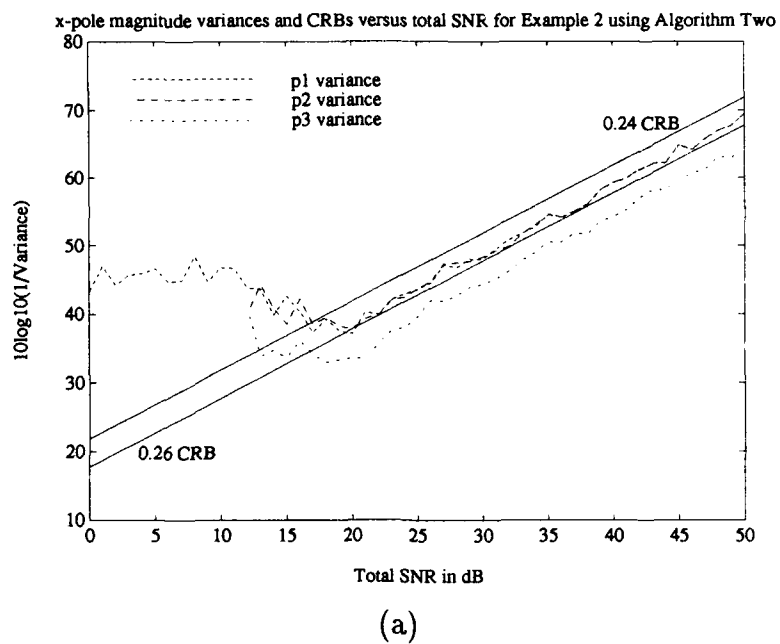


Figure 51: Example 2. $10\log_{10}(1/\text{Variance})$ versus total SNR in dB for (a) x -pole and (b) y -pole magnitudes using Algorithm Two.

on a 2-D image. A method to examine full-polarization data is presented which is based on the concept of a transient polarization response (TPR) [4, 35, 36]. According to the TPR concept, the target is illuminated with an impulsive circularly polarized electromagnetic wave, and as the wave interacts with each scattering center on the target, each scattering center will reflect back a wave with a polarization which is determined by the polarimetric characteristics of that scattering center. This concept has been investigated in 1-D for both nonparametric [4, 35, 36] and parametric [37, 38] techniques. The nonparametric techniques use the IFFT of the full-polarization stepped frequency data to form the TPR of a target. The peaks in the TPR profile give the scattering center locations. Polarization ellipses are then given by the polarization properties of the TPR at the scattering center locations. Thus, the amplitude and orientation of each ellipse characterize the polarimetric properties of each scattering center. Parametric techniques employing the 1-D TLS-Prony technique described in Chapter IV have been developed for the TPR [37, 38]. This technique has the advantage of higher resolution than the IFFT method and of direct estimation of the scattering center locations.

The technique presented here is a 2-D extension of the 1-D TLS-Prony based parametric TPR technique developed in [37, 38]. The 2-D TLS-Prony Technique algorithms previously presented, with slight modifications, are used to determine the scattering center locations and amplitude coefficients. The ellipse parameters are then calculated from the amplitude coefficients.

5.3.2 Data Model

Assume that we are given full-polarization, 2-D scattering coefficient data. These coefficients are denoted $s_{hh}(f, \psi)$, $s_{hv}(f, \psi) = s_{vh}(f, \psi)$ and $s_{vv}(f, \psi)$, where ψ is the angular variable along the angular path on which the data was taken. Depending upon the locations of the samples in the 2-D frequency plane, the scattering coefficients can serve as the input data to the 2-D TLS-Prony algorithm. However, it may be desirable to interpolate the data onto a rectangular or square grid in the 2-D frequency plane. These issues were discussed in Chapter IV. Thus the data which is input to this algorithm is denoted as $d'_{hh}(m, n)$, $d'_{hv}(m, n) = d'_{vh}(m, n)$ and $d'_{vv}(m, n)$ where $m = 0, 1, \dots, M-1$ and $n = 0, 1, \dots, N-1$ and the ' denotes that the data has been noise corrupted.

The 2-D TPR can be modeled in the 2-D frequency domain as

$$\begin{bmatrix} d_{hh}(m, n) & d_{hv}(m, n) \\ d_{vh}(m, n) & d_{vv}(m, n) \end{bmatrix} = \sum_{k=1}^K \sum_{l=1}^{L_k} \begin{bmatrix} a_{hh_{k,l}} & a_{hv_{k,l}} \\ a_{vh_{k,l}} & a_{vv_{k,l}} \end{bmatrix} p_{x_k}^m p_{y_{k,l}}^n \quad (5.52)$$

where

p_{x_k} = k th x -pole, x -component of the 2-D exponential

$p_{y_{k,l}}$ = k, l th y -pole, y -component of the 2-D exponential

$a_{hh_{k,l}}$ = k, l th linear basis amplitude coefficient for hh -polarization

$a_{vh_{k,l}}$ = k, l th linear basis amplitude coefficient for vh -polarization

$a_{hv_{k,l}}$ = k, l th linear basis amplitude coefficient for hv -polarization

$a_{vv_{k,l}}$ = k, l th linear basis amplitude coefficient for vv -polarization.

This is designated the linear-basis model. Note that due to reciprocity, $a_{hv_{k,l}} = a_{vh_{k,l}}$.

The polarization properties of each scattering center are more clearly seen by considering the horizontal and vertical responses to a circularly polarized incident wave. Left circular is arbitrarily chosen. It is assumed that there are no scattering centers on the target which will exhibit large scattering behavior to left circular transmit and no scattering behavior to right circular transmit, and vice versa. Thus, the data is reduced from four sets to two by the transformation [4]

$$\begin{bmatrix} d_{hl}(m, n) \\ d_{vl}(m, n) \end{bmatrix} = \begin{bmatrix} d_{hh}(m, n) & d_{hv}(m, n) \\ d_{vh}(m, n) & d_{vv}(m, n) \end{bmatrix} \begin{bmatrix} 1 \\ j \end{bmatrix} \frac{1}{\sqrt{2}}. \quad (5.53)$$

The 2-D full-polarization model can also be written in terms of the hl and vl -polarization based data as

$$\begin{bmatrix} d_{hl}(m, n) \\ d_{vl}(m, n) \end{bmatrix} = \sum_{k=1}^K \sum_{l=1}^{L_k} \begin{bmatrix} a_{hk,l} \\ a_{vk,l} \end{bmatrix} p_{x_k}^m p_{y_{k,l}}^n \quad (5.54)$$

where

$a_{hk,l}$ = k, l th horizontal amplitude coefficient for hl -polarization

$a_{vk,l}$ = k, l th vertical amplitude coefficient for vl -polarization.

This is designated the linear-circular basis model. Note that p_{x_k} and $p_{y_{k,l}}$ are identical to the poles for the linear-basis model. The conversion between the linear-basis amplitude coefficients and the linear-circular basis amplitude coefficients is given by

$$\begin{bmatrix} a_{hk,l} \\ a_{vk,l} \end{bmatrix} = \begin{bmatrix} a_{hh_{k,l}} & a_{hv_{k,l}} \\ a_{vh_{k,l}} & a_{vv_{k,l}} \end{bmatrix} \begin{bmatrix} 1 \\ j \end{bmatrix} \frac{1}{\sqrt{2}} \quad (5.55)$$

where the linear-circular basis amplitude coefficients are $a_{hk,l}$ and $a_{vk,l}$.

The problem now becomes one of parameter estimation, where the parameters in Equation 5.2, namely p_{x_k} , $p_{y_{k,l}}$, $a_{hk,l}$ and $a_{vk,l}$ for $k = 1, 2, \dots, K$ and $l = 1, 2, \dots, L_k$

must be estimated from the data. The model orders, K and L_k also need to be chosen.

The horizontal and vertical amplitude coefficients associated with each pole contain the information which yields the polarimetric characteristics of each scattering center. These polarimetric characteristics are in the form of an ellipse. This ellipse, corresponding to a given scattering center, is characteristic of the polarization of the electric field scattered from that scattering center. For each scattering center, the tilt $\tau_{k,l}$ and ellipticity $\epsilon_{k,l}$ of this ellipse can be found, using the amplitude coefficients, from the following equations [43, 60]:

$$\tau_{k,l} = \frac{1}{2} \tan^{-1} [\tan(2\gamma_{k,l}) \cos(\delta_{k,l})] \quad (5.56)$$

$$\epsilon_{k,l} = \frac{1}{2} \sin^{-1} (\sin(2\gamma_{k,l}) \sin(\delta_{k,l})) \quad (5.57)$$

$$\gamma_{k,l} = \tan^{-1} \left(\frac{|a_{v_{k,l}}|}{|a_{h_{k,l}}|} \right) \quad (5.58)$$

$$\delta_{k,l} = \angle a_{v_{k,l}} - \angle a_{h_{k,l}}. \quad (5.59)$$

The above calculations lead to use of only one quarter of the Poincaré polarization sphere. To avoid this ambiguity, the following alterations to the tilt need to be made [43]:

$$\tau_{k,l} = \begin{cases} \tau_{k,l} + \frac{\pi}{2} & \text{if } \gamma_{k,l} > \frac{\pi}{4} \\ \tau_{k,l} + \pi & \text{if } \gamma_{k,l} \leq \frac{\pi}{4} \text{ and } \tau_{k,l} < 0 \end{cases} \quad (5.60)$$

The major axis $A_{k,l}$ of each ellipse can be determined as [43, 60]

$$A_{k,l} = \left| |a_{h_{k,l}}| \cos(\tau_k) + |a_{v_{k,l}}| e^{j\delta_{k,l}} \sin(\tau_{k,l}) \right|. \quad (5.61)$$

This set of parameters $\{A_{k,l}, \epsilon_{k,l}, \tau_{k,l}\}$ along with the locations of the scattering

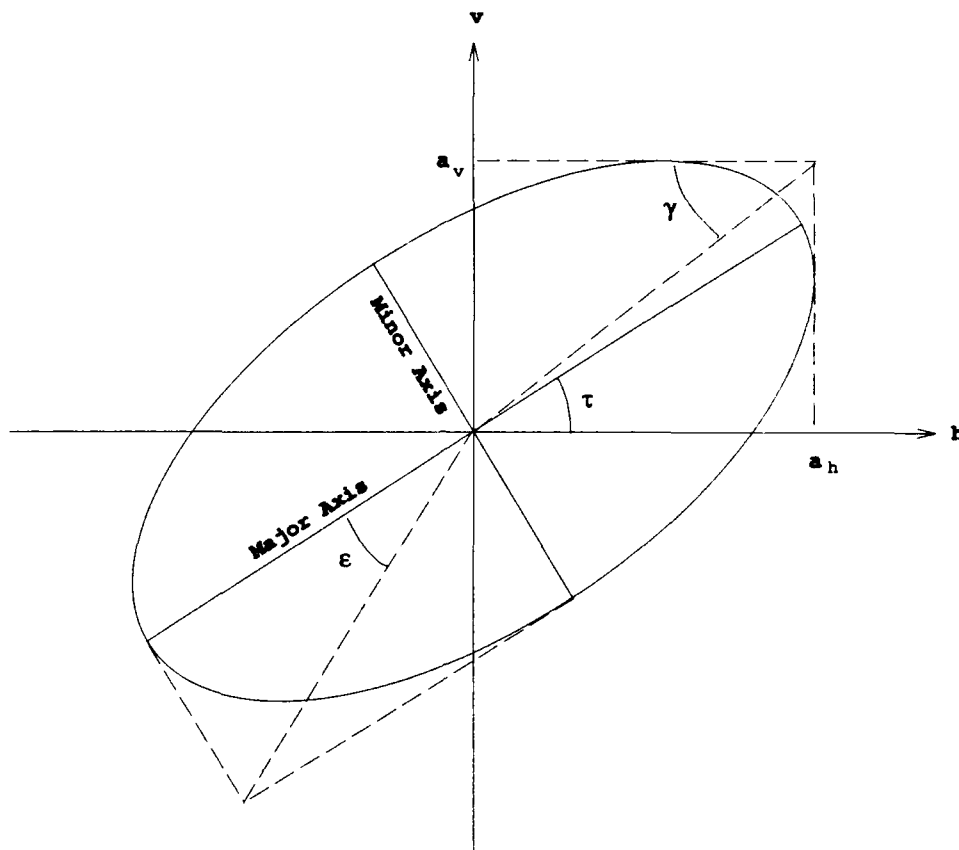


Figure 52: Polarization ellipse of scattering center consistent with IEEE standard.

centers provides a concise description of a target. This parameter set characterizes a target as a set of Γ scattering centers, each described by location, amplitude, ellipticity and tilt of a scattering polarization ellipse. These parameters are demonstrated on the ellipse sketched in Figure 52. The location of the scattering center determines where on the image the ellipse is placed. The origin in Figure 52 is considered the location of the scattering center.

The definitions of the ellipse parameters given above are consistent with the

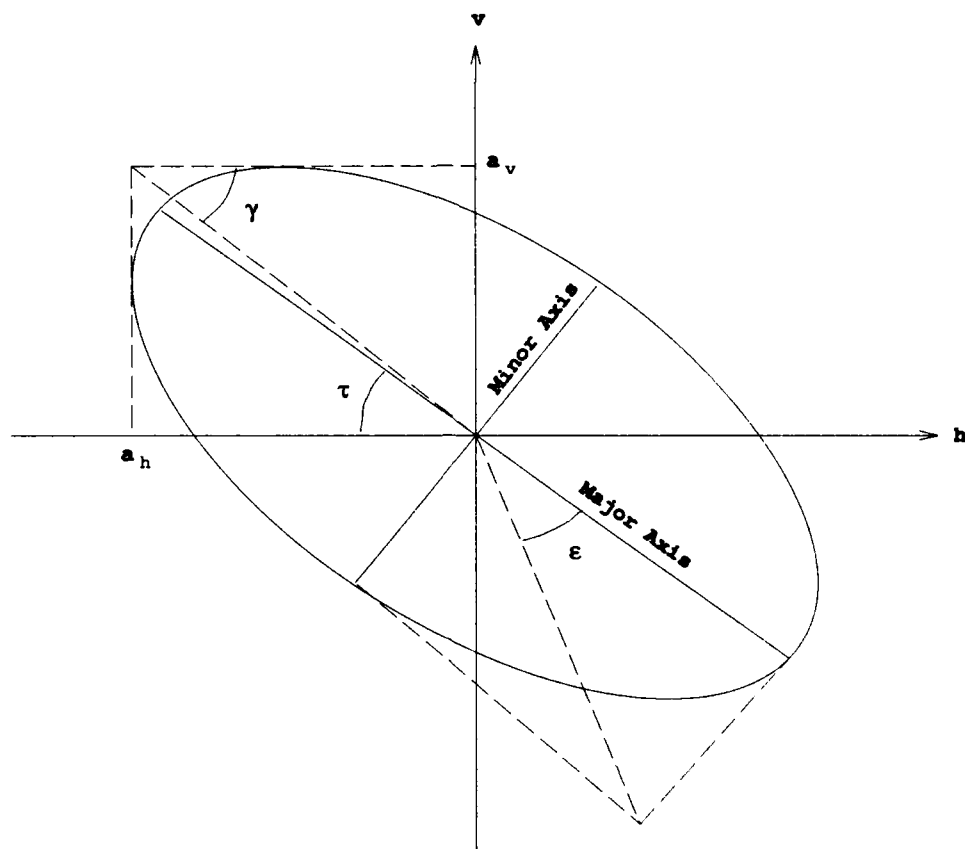


Figure 53: Polarization ellipse of scattering center as viewed traveling toward the radar (observer). All of the ellipses plotted in this dissertation follow this convention.

IEEE standard for the polarization of an electromagnetic wave which is viewing the tip of the electric field vector as the electric field propagates away from the viewer. However, in the simulations which are shown in Chapter VI, it is desired to view the scattered field as it propagates toward the viewer, which corresponds to how the radar would view the scattered field. Thus, the ellipse must be rotated 180° around the v -axis in Figure 52 to achieve this situation. The ellipse in Figure 52 would now be viewed as shown in Figure 53. All of the ellipses plotted in this dissertation

follow the convention of Figure 53, assuming that the viewer is at the radar and the scattered field is propagating toward the radar.

5.3.3 Estimation Algorithms

This section describes two algorithms for estimation of the x and y -poles along with both sets of amplitude coefficients. The two full-polarization algorithms are called Full-Polarization Algorithm One (FPA1) and Full-Polarization Algorithm Two (FPA2). These algorithms are very similar to the single-polarization versions, Algorithm One and Algorithm Two, which were presented earlier in this chapter. The main differences are that there are two input data sets and that there are two sets of amplitude coefficients to estimate in the full-polarization case. Also, an additional step unique to the full-polarization case is the calculation of the ellipse parameters from the parameter estimates. The two input data matrices are defined as follows

$$D'_h = \begin{bmatrix} d'_{hl}(0,0) & d'_{hl}(1,0) & \cdots & d'_{hl}(M-1,0) \\ d'_{hl}(0,1) & d'_{hl}(1,1) & \cdots & d'_{hl}(M-1,1) \\ \vdots & \vdots & & \vdots \\ d'_{hl}(0,N-1) & d'_{hl}(1,N-1) & \cdots & d'_{hl}(M-1,N-1) \end{bmatrix} \quad (5.62)$$

and

$$D'_v = \begin{bmatrix} d'_{vl}(0,0) & d'_{vl}(1,0) & \cdots & d'_{vl}(M-1,0) \\ d'_{vl}(0,1) & d'_{vl}(1,1) & \cdots & d'_{vl}(M-1,1) \\ \vdots & \vdots & & \vdots \\ d'_{vl}(0,N-1) & d'_{vl}(1,N-1) & \cdots & d'_{vl}(M-1,N-1) \end{bmatrix}. \quad (5.63)$$

Moving across a row in D'_h or D'_v is considered moving in frequency while moving down a column of either matrix is considered moving in angle in the 2-D frequency plane.

Full-Polarization Algorithm One (FPA1)

The five steps of FPA1 are described below and summarized in Table 7. The first four steps of FPA1 are nearly identical to the four steps of Algorithm One in the single-polarization case. The fifth step of FPA1 involves the calculation of the ellipse parameters.

FPA1 Step 1 : x -pole estimation. Step 1 is once again to estimate the x -poles, p_{x_k} . All of the rows of D'_h and D'_v are used simultaneously in the estimation of the x -poles. The backward linear prediction equations are

$$\begin{bmatrix}
 d'_{hl}(0,0) & d'_{hl}(1,0) & d'_{hl}(2,0) & \cdots & d'_{hl}(Q,0) \\
 d'_{hl}(1,0) & d'_{hl}(2,0) & d'_{hl}(3,0) & \cdots & d'_{hl}(Q+1,0) \\
 \vdots & \vdots & \vdots & \vdots & \vdots \\
 d'_{hl}(M-Q-1,0) & d'_{hl}(M-Q,0) & d'_{hl}(M-Q+1,0) & \cdots & d'_{hl}(M-1,0) \\
 d'_{hl}(0,1) & d'_{hl}(1,1) & d'_{hl}(2,1) & \cdots & d'_{hl}(Q,1) \\
 d'_{hl}(1,1) & d'_{hl}(2,1) & d'_{hl}(3,1) & \cdots & d'_{hl}(Q+1,1) \\
 \vdots & \vdots & \vdots & \vdots & \vdots \\
 d'_{hl}(M-Q-1,1) & d'_{hl}(M-Q,1) & d'_{hl}(M-Q+1,1) & \cdots & d'_{hl}(M-1,1) \\
 \vdots & \vdots & \vdots & \vdots & \vdots \\
 d'_{hl}(0,N-1) & d'_{hl}(1,N-1) & d'_{hl}(2,N-1) & \cdots & d'_{hl}(Q,N-1) \\
 d'_{hl}(1,N-1) & d'_{hl}(2,N-1) & d'_{hl}(3,N-1) & \cdots & d'_{hl}(Q+1,N-1) \\
 \vdots & \vdots & \vdots & \vdots & \vdots \\
 d'_{hl}(M-Q-1,N-1) & d'_{hl}(M-Q,N-1) & d'_{hl}(M-Q+1,N-1) & \cdots & d'_{hl}(M-1,N-1) \\
 \hline
 d'_{vl}(0,0) & d'_{vl}(1,0) & d'_{vl}(2,0) & \cdots & d'_{vl}(Q,0) \\
 d'_{vl}(1,0) & d'_{vl}(2,0) & d'_{vl}(3,0) & \cdots & d'_{vl}(Q+1,0) \\
 \vdots & \vdots & \vdots & \vdots & \vdots \\
 d'_{vl}(M-Q-1,0) & d'_{vl}(M-Q,0) & d'_{vl}(M-Q+1,0) & \cdots & d'_{vl}(M-1,0) \\
 d'_{vl}(0,1) & d'_{vl}(1,1) & d'_{vl}(2,1) & \cdots & d'_{vl}(Q,1) \\
 d'_{vl}(1,1) & d'_{vl}(2,1) & d'_{vl}(3,1) & \cdots & d'_{vl}(Q+1,1) \\
 \vdots & \vdots & \vdots & \vdots & \vdots \\
 d'_{vl}(M-Q-1,1) & d'_{vl}(M-Q,1) & d'_{vl}(M-Q+1,1) & \cdots & d'_{vl}(M-1,1) \\
 \vdots & \vdots & \vdots & \vdots & \vdots \\
 d'_{vl}(0,N-1) & d'_{vl}(1,N-1) & d'_{vl}(2,N-1) & \cdots & d'_{vl}(Q,N-1) \\
 d'_{vl}(1,N-1) & d'_{vl}(2,N-1) & d'_{vl}(3,N-1) & \cdots & d'_{vl}(Q+1,N-1) \\
 \vdots & \vdots & \vdots & \vdots & \vdots \\
 d'_{vl}(M-Q-1,N-1) & d'_{vl}(M-Q,N-1) & d'_{vl}(M-Q+1,N-1) & \cdots & d'_{vl}(M-1,N-1)
 \end{bmatrix}
 \begin{bmatrix}
 1 \\
 b_1 \\
 b_2 \\
 \vdots \\
 b_Q
 \end{bmatrix}
 \approx 0.$$

(5.64)

or

$$\begin{bmatrix} S_h \\ S_v \end{bmatrix} \begin{bmatrix} 1 \\ b \end{bmatrix} \approx 0 \quad (5.65)$$

or

$$S \begin{bmatrix} 1 \\ b \end{bmatrix} \approx 0. \quad (5.66)$$

The solution of the backward linear prediction equations and the x -pole estimates are determined in a manner analogous to the manner outlined in Algorithm One, Step 1 in Equations 5.6 to 5.13. The result is Q x -poles estimates.

As in Algorithm One, because only K singular values of \hat{S} (the SVD truncated version of S) are nonzero, there are at most K x -pole estimates which can correspond to data modes. Therefore, only the K x -poles which have the largest energy will be retained (as discussed in Step 2 below).

FPA1 Step 2 : x -amplitude estimation. The x -amplitude coefficients for the full-polarization case are defined as

$$\begin{bmatrix} c_{h_{q,n}} \\ c_{v_{q,n}} \end{bmatrix} = \sum_{l=1}^{L_k} \begin{bmatrix} a_{h_{k,l}}(m, n) \\ a_{v_{k,l}}(m, n) \end{bmatrix} p_{y_{q,l}}^n, \quad q = 1, 2, \dots, Q. \quad (5.67)$$

With this definition, the model associated with Equation 5.54 using the estimated x -poles is written as

$$\begin{bmatrix} d'_{hl}(m, n) \\ d'_{vl}(m, n) \end{bmatrix} = \sum_{q=1}^Q \begin{bmatrix} c_{h_{q,n}} \\ c_{v_{q,n}} \end{bmatrix} p_{x_q}^m \quad (5.68)$$

where $c_{h_{q,n}}$ is the q th x -amplitude coefficient associated with the n th row of D_h and where $c_{v_{q,n}}$ is the q th x -amplitude coefficient associated with the n th row of D_v . Equation 5.68 is used to solve for the $c_{h_{q,n}}$ s and $c_{v_{q,n}}$ s using

$$\begin{bmatrix} 1 & 1 & \cdots & 1 \\ p_{x_1} & p_{x_2} & \cdots & p_{x_Q} \\ p_{x_1}^2 & p_{x_2}^2 & \cdots & p_{x_Q}^2 \\ \vdots & \vdots & & \vdots \\ p_{x_1}^{M-1} & p_{x_2}^{M-1} & \cdots & p_{x_Q}^{M-1} \end{bmatrix} \begin{bmatrix} c_{\eta_1,0} & c_{\eta_1,1} & \cdots & c_{\eta_1,N-1} \\ c_{\eta_2,0} & c_{\eta_2,1} & \cdots & c_{\eta_2,N-1} \\ \vdots & \vdots & & \vdots \\ c_{\eta_Q,0} & c_{\eta_Q,1} & \cdots & c_{\eta_Q,N-1} \end{bmatrix} = D'_\eta{}^T, \quad (5.69)$$

or

$$P_x C_\eta = D'_\eta{}^T. \quad (5.70)$$

where

$$\eta \in \{h, v\}. \quad (5.71)$$

Both sets of x -amplitude coefficients are found from least squares solutions to Equation 5.70 using the x -pole estimates.

As before, we retain only the K x -pole estimates with the highest energy, where now the energy is defined as

$$E_q = \sum_{n=0}^{N-1} |\hat{c}_{h_q,n} \hat{c}_{v_q,n}|^2 \sum_{m=0}^{M-1} |\hat{p}_{x_q}|^{2m} \quad q = 1, 2, \dots, Q. \quad (5.72)$$

The final x -amplitude coefficient estimates are found using a procedure identical to the one used to determine the initial of x -amplitude coefficient estimates outlined above. The only difference is that there are only K x -poles which are used in Equation 5.69. Also, there are only L_k x -amplitude coefficients (per polarization) to be estimated for each of the K x -poles.

FPA1 Step 3: Estimation of the y -poles. As in Algorithm One, the x -amplitude coefficient estimates are now used to solve for the y -pole estimates. For

each of the K high energy x -poles, the backward linear prediction equations for the model given by Equation 5.67 become

$$\begin{bmatrix} c_{h_k,0} & c_{h_k,1} & \cdots & c_{h_k,R_k} \\ c_{h_k,1} & c_{h_k,2} & \cdots & c_{h_k,R_k+1} \\ \vdots & \vdots & & \vdots \\ c_{h_k,N-R_k-1} & c_{h_k,N-R_k} & \cdots & c_{h_k,N-1} \\ \hline c_{v_k,0} & c_{v_k,1} & \cdots & c_{v_k,R_k} \\ c_{v_k,1} & c_{v_k,2} & \cdots & c_{v_k,R_k+1} \\ \vdots & \vdots & & \vdots \\ c_{v_k,N-R_k-1} & c_{v_k,N-R_k} & \cdots & c_{v_k,N-1} \end{bmatrix} \begin{bmatrix} 1 \\ b_1^k \\ b_2^k \\ \vdots \\ b_{R_k}^k \end{bmatrix} \approx 0 \quad k = 1, 2, \dots, K \quad (5.73)$$

or

$$F^{R_k} \begin{bmatrix} 1 \\ b^k \end{bmatrix} \approx 0. \quad (5.74)$$

The solution of the backward linear prediction equations and the y -pole estimates are determined in a manner analogous to the manner outlined in Algorithm One, Step 3 in Equations 5.25 to 5.27. The result is R_k y -poles estimates for each of the K x -pole estimates.

As in the basic algorithm, because only L_k singular values of \hat{F}^{R_k} (the SVD truncated version of F^{R_k}) are nonzero, there are at most L_k y -pole estimates which can correspond to data modes. Therefore, only the L_k y -poles which have the largest energy are retained (as discussed in Step 4 below).

FPA1 Step 4: Estimation of the Amplitude Coefficients. Now that all of the required y -poles have been estimated, both sets of amplitude coefficients are estimated next. Using Equation 5.67,

$$\begin{bmatrix} 1 & 1 & \cdots & 1 \\ p_{y_k,1} & p_{y_k,2} & \cdots & p_{y_k,R_k} \\ p_{y_k,1}^2 & p_{y_k,2}^2 & \cdots & p_{y_k,R_k}^2 \\ \vdots & \vdots & \ddots & \vdots \\ p_{y_k,1}^{N-1} & p_{y_k,2}^{N-1} & \cdots & p_{y_k,R_k}^{N-1} \end{bmatrix} \begin{bmatrix} a_{\eta_k,1} \\ a_{\eta_k,2} \\ \vdots \\ a_{\eta_k,R_k} \end{bmatrix} = \begin{bmatrix} c_{\eta_k,0} \\ c_{\eta_k,1} \\ c_{\eta_k,2} \\ \vdots \\ c_{\eta_k,N-1} \end{bmatrix} \quad (5.75)$$

or

$$P_y^k A_\eta^k = c_\eta^k, \quad (5.76)$$

where

$$\eta \in \{h, v\}. \quad (5.77)$$

Both sets of amplitude coefficients are found from least squares solutions to Equation 5.76 using the y -pole estimates along with the x -amplitude coefficient estimates.

As before, we retain only the L_k y -pole estimates with the highest energy for each of the K x -poles, where now the energy is defined as

$$E_{r_k} = |\hat{a}_{h_k, r_k} \hat{a}_{v_k, r_k}|^2 \sum_{n=0}^{N-1} |\hat{p}_{y_k, r_k}|^{2n} \quad r_k = 1, 2, \dots, R_k. \quad (5.78)$$

The final amplitude coefficient estimates are found utilizing a procedure identical to the one used to determine the initial of amplitude coefficient estimates outlined above. The only difference is that there are only L_k y -poles which are used in Equation 5.75. Also, there are only L_k amplitude coefficients (per polarization) to be estimated for each of the K x -poles.

FPA1 Step 5: Calculation of the Ellipse Parameters. Now that all of the poles and amplitude coefficients have been estimated, the ellipse parameters can be determined from these estimates using Equations 5.56 to 5.61.

Table 7: Summary of steps performed in FPA1.

Step	Estimated Parameters	Method of Solution
1	$\{p_{x_k}\}_{k=1}^K$ (x -poles)	TLS of Eq. 5.66 w/ SVD trunc.
2	$\{c_{h_{q,n}}, c_{v_{q,n}}\}_{q,n=1,0}^{Q,N-1}$ (x -amp coefs)	LS of Eqs. 5.69 via QR decomp.
3	$\{p_{y_{k,l}}\}_{k,l=1,1}^{K,L_k}$ (y -poles)	TLS of Eq. 5.73 w/ SVD trunc.
4	$\{a_{h_{k,l}}, a_{v_{k,l}}\}_{k,l=1,1}^{K,L_k}$ (amp coefs)	LS of Eqs. 5.75 via QR decomp.
5	$\{\tau_{k,l}, \epsilon_{k,l}, A_{k,l}\}_{k,l=1,1}^{K,L_k}$ (ellipse params)	Eqs. 5.56 to 5.61

Full Polarization Algorithm Two (FPA2)

FPA2 extends FPA1 just as Algorithm Two extends Algorithm One in the single-polarization case. FPA2 uses the first three steps of FPA1 twice, and then requires a matching step and a final amplitude coefficient calculation step followed by the ellipse parameter calculation step. The steps involved in FPA2 are summarized in Table 8. The first three steps of FPA1 are carried out using the data $d'_{hl}(m, n)$ and $d'_{vl}(m, n)$ yielding x and y -pole estimates, $\{p_{x_k}\}_{k=1}^K$ and $\{p_{y_{k,l}}\}_{l=1}^{L_k}$. Next, the data is transposed (*i.e.* $d'_{hl}{}^t(n, m) = d'_{hl}(m, n)$ and $d'_{vl}{}^t(n, m) = d'_{vl}(m, n)$), and FPA1 is applied to $d'_{hl}{}^t(n, m)$ and $d'_{vl}{}^t(m, n)$ to arrive at a second set of poles, $\{p_{x_{k^t}}^t\}_{k^t=1}^{K^t}$ and $\{p_{y_{k^t,l^t}}^t\}_{l^t=1}^{L_{k^t}^t}$. Note that the model orders K and L_k are related to K^t and $L_{k^t}^t$, depending on the structure of a particular model, and are in general different.

Just as in the single-polarization case, the two sets of estimates are combined, and the more accurate part of the estimates from each set is retained. The match-

ing is performed in an identical manner to the single-polarization case using the metric in Equation 5.32. The final set of matched pole pairs for FPA2 are thus designated $\{\rho_{x_\gamma}, \rho_{y_\gamma}\}_{\gamma=1}^\Gamma$, where the ρ 's are given by the paired p_x 's and p_x^t 's and $\Gamma = \min \left\{ \sum_{k=1}^K L_k, \sum_{k^t=1}^{K^t} L_{k^t}^t \right\}$.

Using this definition, the model in Equation 5.54 can be expressed as

$$\begin{bmatrix} d_{hl}(m, n) \\ d_{vl}(m, n) \end{bmatrix} = \sum_{\gamma=1}^\Gamma \begin{bmatrix} \alpha_{h_\gamma} \\ \alpha_{v_\gamma} \end{bmatrix} \rho_{x_\gamma}^m \rho_{y_\gamma}^n \quad (5.79)$$

Equation 5.79 now is used to solve for amplitude coefficients, $\{\alpha_{h_\gamma}, \alpha_{v_\gamma}\}_{\gamma=1}^\Gamma$, as follows

$$\begin{bmatrix} P(0) \\ P(1) \\ \vdots \\ P(M-1) \end{bmatrix} \begin{bmatrix} \alpha_{\eta_1} \\ \alpha_{\eta_2} \\ \vdots \\ \alpha_{\eta_\Gamma} \end{bmatrix} = \begin{bmatrix} d'_\eta(0) \\ d'_\eta(1) \\ \vdots \\ d'_\eta(M-1) \end{bmatrix}, \quad (5.80)$$

where each $P(m)$ and $d'_\eta(m)$ are given by

$$P(m) = \begin{bmatrix} \rho_{x_1}^m & \rho_{x_2}^m & \cdots & \rho_{x_\Gamma}^m \\ \rho_{x_1}^m \rho_{y_1} & \rho_{x_2}^m \rho_{y_2} & \cdots & \rho_{x_\Gamma}^m \rho_{y_\Gamma} \\ \vdots & \vdots & & \vdots \\ \rho_{x_1}^m \rho_{y_1}^{N-1} & \rho_{x_2}^m \rho_{y_2}^{N-1} & \cdots & \rho_{x_\Gamma}^m \rho_{y_\Gamma}^{N-1} \end{bmatrix} \quad (5.81)$$

and

$$d'_\eta(m) = \begin{bmatrix} d'_\eta(m, 0) & d'_\eta(m, 1) & \cdots & d'_\eta(m, N-1) \end{bmatrix}^T \quad (5.82)$$

Equation 5.80 can be expressed as

$$\mathcal{P}\mathcal{A}_\eta = \mathcal{D}_\eta'. \quad (5.83)$$

where

$$\eta \in \{hl, vl\}. \quad (5.84)$$

Table 8: Summary of steps performed in FPA2.

Step	Estimated Parameters	Method of Solution
1	$\{p_{x_k}\}_{k=1}^K$ (x -poles)	TLS of Eq. 5.66 w/ SVD trunc.
2	$\{c_{h_{q,n}}, c_{v_{q,n}}\}_{q,n=1,0}^{Q,N-1}$ (x -amp coefs)	LS of Eq. 5.69 via QR decomp.
3	$\{p_{y_{k,l}}\}_{k,l=1,1}^{K,L_k}$ (y -poles)	TLS of Eq. 5.73 w/ SVD trunc.
4	$\{p_{x_{k^t}}^t\}_{k^t=1}^{K^t}$ (x^t -poles)	TLS similar to Step 1
5	$\{c_{h_{q^t,m}}^t, c_{v_{q^t,m}}^t\}_{q^t,m=1,0}^{Q,M-1}$ (x^t -amp coefs)	LS similar to Step 2
6	$\{p_{y_{k^t,l^t}}^t\}_{k^t,l^t=1,1}^{K^t,L_{k^t}^t}$ (y^t -poles)	TLS similar to Step 3
7	$\{\rho_{x_\gamma}, \rho_{y_\gamma}\}_{\gamma=1}^\Gamma$ (x and y -poles)	Matching using Eq. 5.32
8	$\{\alpha_{h_\gamma}, \alpha_{v_\gamma}\}_{\gamma=1}^\Gamma$ (amp coefs)	LS of Eq. 5.83 via QR decomp.
9	$\{\tau_{k,l}, \epsilon_{k,l}, A_{k,l}\}_{k,l=1,1}^{K,L_k}$ (ellipse params)	Eqs. 5.56 to 5.61

The two sets of amplitude coefficients are found using the pole estimates from a least squares solution to Equation 5.83. Finally, the ellipse parameters are calculated from the pole and amplitude coefficient estimates using Equations 5.56 to 5.61.

5.3.4 Examples

Examples are presented to assess model validity and noise effects. As in the single polarization case, two examples are presented. The first example, called Example FP1, considers the estimation of three 2-D undamped exponentials. The second example, called Example FP2, considers the estimation of three 2-D damped exponentials. These examples are very similar to Examples 1 and 2 presented for the

single polarization case.

Example FP1

In this example the variances of frequency and magnitude estimates are compared to their CRBs at various signal to noise ratios (SNRs) for a three 2-D frequency scenario (similar to the one presented in Example 1 earlier in this chapter) utilizing FPA2. Data was generated using the model in Equation 5.54 for $M = N = 20$ and

$$\begin{aligned} \begin{bmatrix} p_{x_1} & p_{y_{1,1}} & a_{h_{1,1}} & a_{v_{1,1}} \end{bmatrix} &= \begin{bmatrix} e^{j2\pi 0.24} & e^{j2\pi 0.24} & \frac{1}{\sqrt{2}} & j\frac{1}{\sqrt{2}} \end{bmatrix} \\ \begin{bmatrix} p_{x_1} & p_{y_{1,2}} & a_{h_{1,2}} & a_{v_{1,2}} \end{bmatrix} &= \begin{bmatrix} e^{j2\pi 0.24} & e^{j2\pi 0.26} & \frac{1}{\sqrt{2}} & j\frac{1}{\sqrt{2}} \end{bmatrix} \\ \begin{bmatrix} p_{x_2} & p_{y_{2,1}} & a_{h_{2,1}} & a_{v_{2,1}} \end{bmatrix} &= \begin{bmatrix} e^{j2\pi 0.26} & e^{j2\pi 0.24} & \frac{1}{\sqrt{2}} & j\frac{1}{\sqrt{2}} \end{bmatrix}. \end{aligned} \quad (5.85)$$

The linear basis amplitude coefficients corresponding to the linear-circular basis amplitude coefficients above are

$$\begin{aligned} \begin{bmatrix} a_{hh_{1,1}} & a_{hv_{1,1}} & a_{vv_{1,1}} \end{bmatrix} &= \begin{bmatrix} 1 & 0 & 1 \end{bmatrix} \\ \begin{bmatrix} a_{hh_{1,2}} & a_{hv_{1,2}} & a_{vv_{1,2}} \end{bmatrix} &= \begin{bmatrix} 1 & 0 & 1 \end{bmatrix} \\ \begin{bmatrix} a_{hh_{2,1}} & a_{hv_{2,1}} & a_{vv_{2,1}} \end{bmatrix} &= \begin{bmatrix} 1 & 0 & 1 \end{bmatrix}. \end{aligned} \quad (5.86)$$

Recall that $a_{hv_{k,l}} = a_{vh_{k,l}}$.

It can be seen that from the angles of the above poles the corresponding frequencies are 0.24 and 0.26, just as in Example 1. Also, the amplitude coefficients are chosen so that the total energy for all polarizations is equal to the total energy of the data in the single polarization Example 1. For the purposes of identification the (x -pole, y -pole) pairs above with frequencies (0.24, 0.24), (0.24, 0.26), and (0.26, 0.24)

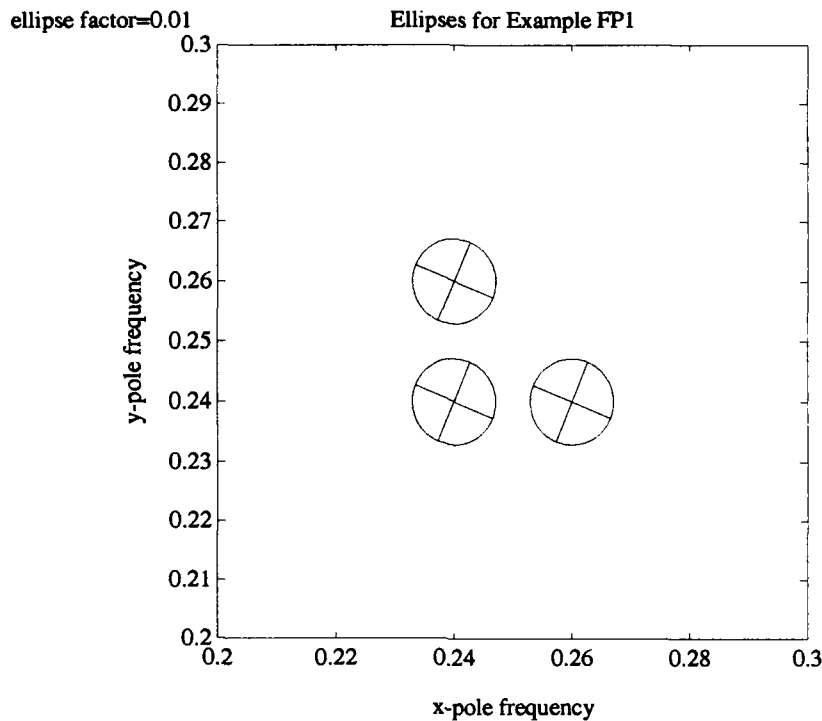
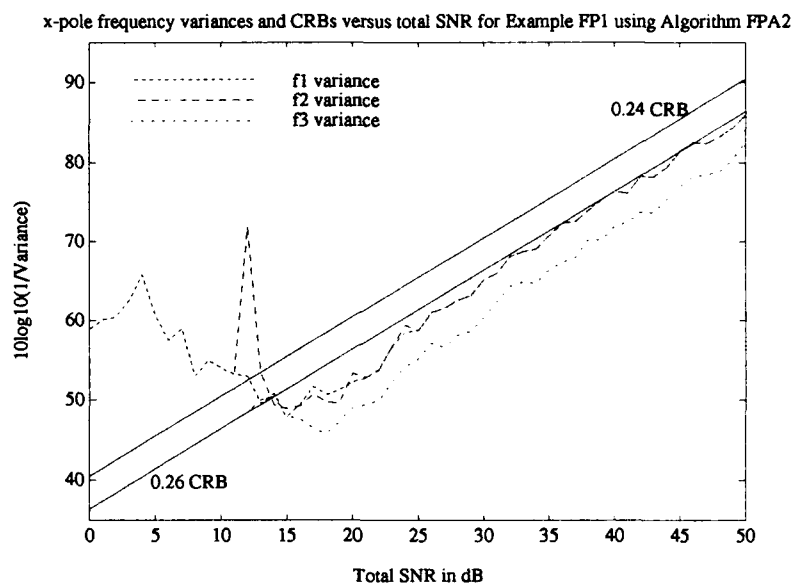


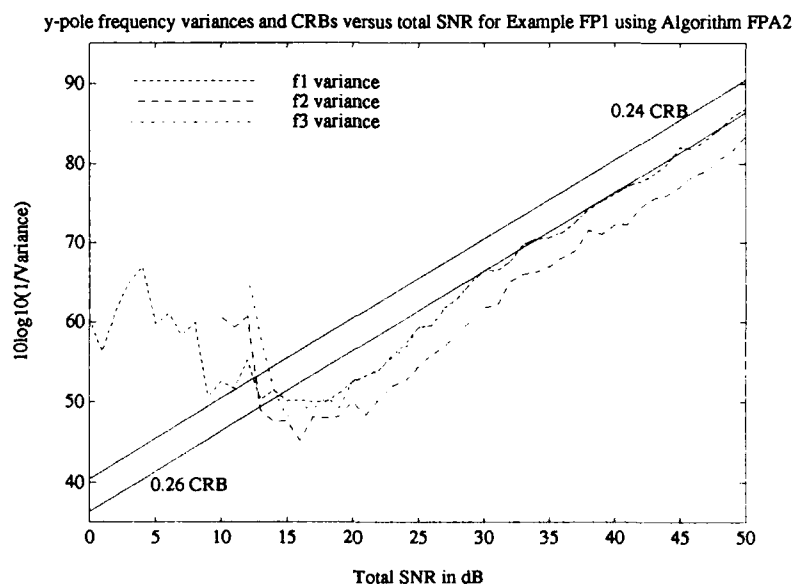
Figure 54: Polarization ellipses for Example FP1.

are again labeled as 2-D frequencies f_1 , f_2 , and f_3 , respectively. The polarization ellipses corresponding to the above data are shown in Figure 54. The ellipse factor in this figure is defined as the ratio between the size of the ellipses as viewed in the figure and the actual size of the ellipses.

Figures 55 and 56 show the simulation results for the x and y -pole frequencies and magnitudes. One hundred different noise realizations were run for each integer total SNR between 0 and 50dB. The algorithm parameters were set at $Q = 8, K = 2, R_1 = R_2 = 8, L_1 = L_2 = 2$ for this example. The characteristics of these curves are very similar to the characteristics of the corresponding curves in Example 1.

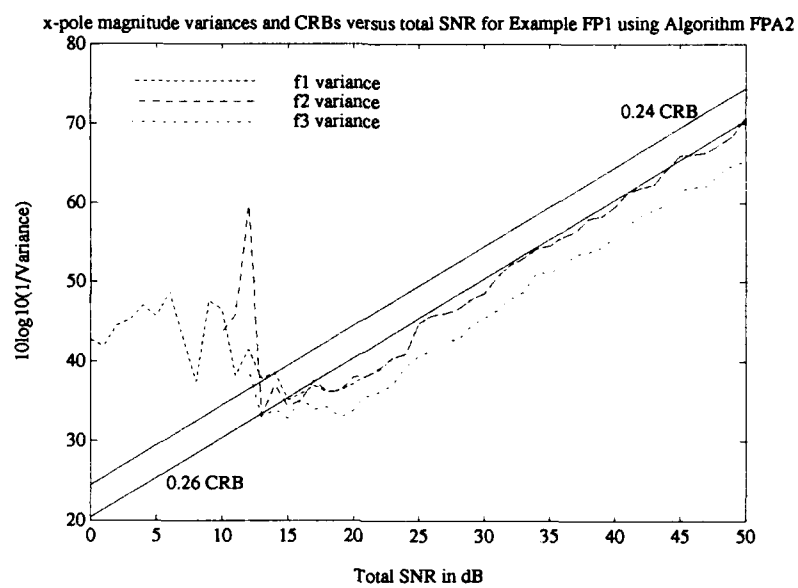


(a)

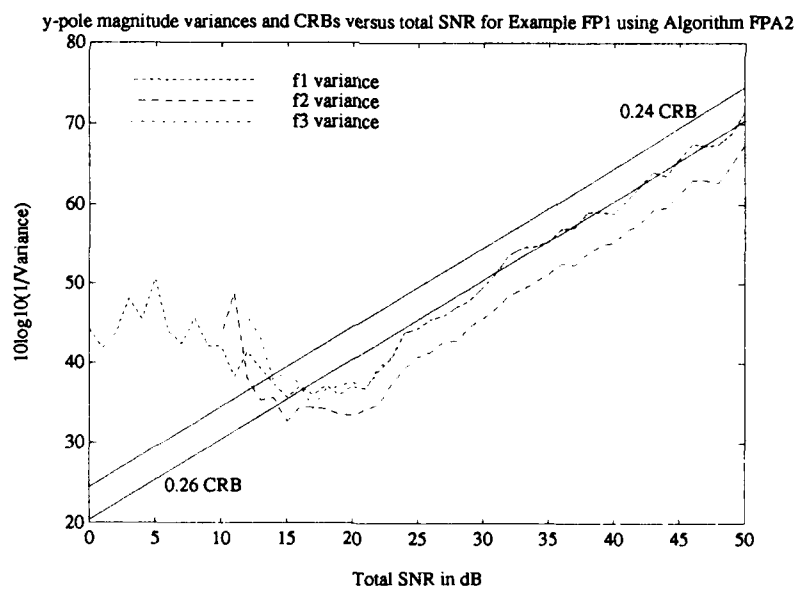


(b)

Figure 55: Example FP1. $10\log_{10}(1/\text{Variance})$ versus total SNR in dB for (a) x -pole and (b) y -pole frequencies using FPA2.



(a)



(b)

Figure 56: Example FP1. $10\log_{10}(1/\text{Variance})$ versus total SNR in dB for (a) x -pole and (b) y -pole magnitudes using FPA2.

Example FP2

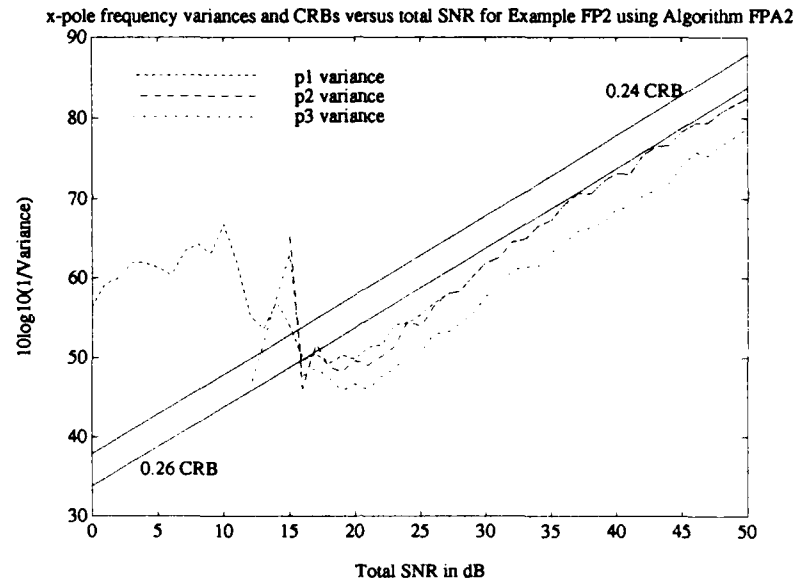
In this example the variances of frequency and magnitude estimates are compared to their CRBs at various signal to noise ratios (SNRs) for a three 2-D damped exponential scenario (similar to the one presented in Example 2 earlier in this chapter) utilizing FPA2. Data was generated using the model in Equation 5.54 for $M = N = 20$ and

$$\begin{aligned} \begin{bmatrix} p_{x1} & p_{y1,1} & a_{h1,1} & a_{v1,1} \end{bmatrix} &= \begin{bmatrix} 0.92e^{j2\pi 0.24} & 0.92e^{j2\pi 0.24} & \frac{1}{\sqrt{2}} & j\frac{1}{\sqrt{2}} \end{bmatrix} \\ \begin{bmatrix} p_{x1} & p_{y1,2} & a_{h1,2} & a_{v1,2} \end{bmatrix} &= \begin{bmatrix} 0.92e^{j2\pi 0.24} & 0.94e^{j2\pi 0.26} & \frac{1}{\sqrt{2}} & j\frac{1}{\sqrt{2}} \end{bmatrix} \\ \begin{bmatrix} p_{x2} & p_{y2,1} & a_{h2,1} & a_{v2,1} \end{bmatrix} &= \begin{bmatrix} 0.94e^{j2\pi 0.26} & 0.92e^{j2\pi 0.24} & \frac{1}{\sqrt{2}} & j\frac{1}{\sqrt{2}} \end{bmatrix}. \end{aligned} \quad (5.87)$$

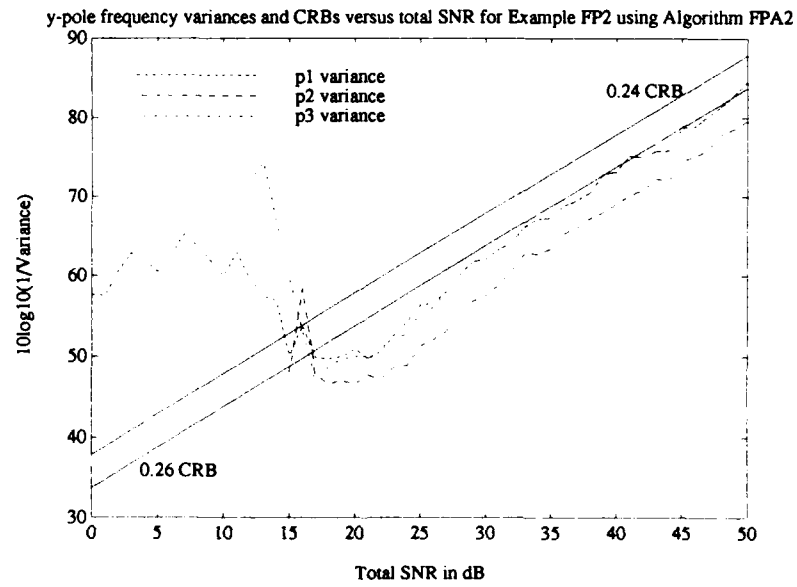
The linear basis amplitude coefficients corresponding to the above linear-circular basis coefficients are given by Equation 5.86. The ellipses corresponding to the above data are identical to the ellipses for Example FP1, and are shown in Figure 54.

For the purposes of identification the (x -pole, y -pole) pairs above with frequencies (0.24,0.24), (0.24,0.26), and (0.26,0.24) are labeled as 2-D poles p1, p2, and p3, respectively, as in Example 2. The amplitude coefficients are chosen so that the total energy of this data set is equal to the total energy of the data set in Example 2 (and Example 1 and Example FP1).

Figures 57 and 58 show the simulation results for the x -pole and y -pole frequency and magnitude variances. The results are very similar to the results in Example 2 using Algorithm Two.

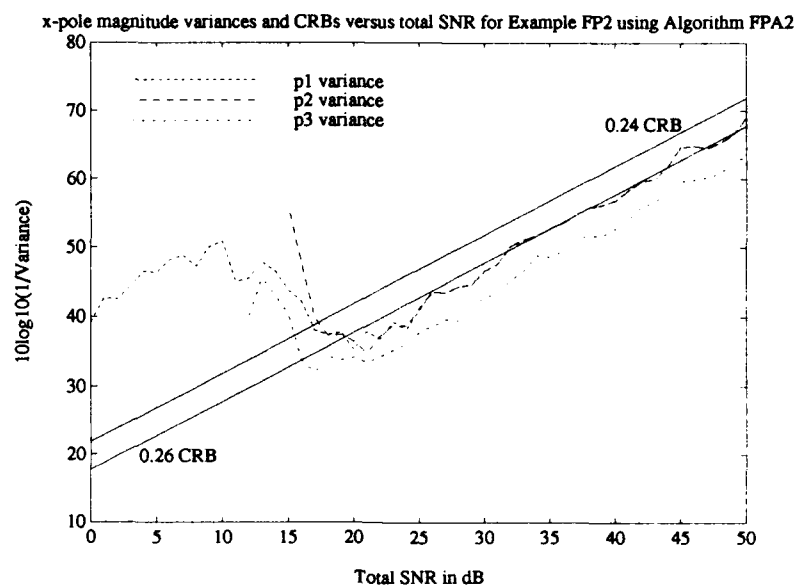


(a)

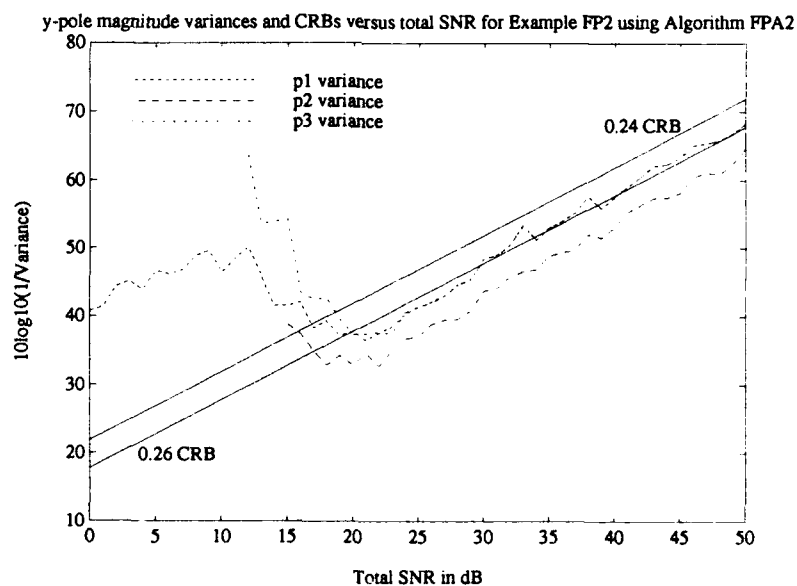


(b)

Figure 57: Example FP2. $10\log_{10}(1/\text{Variance})$ versus total SNR in dB for (a) x -pole and (b) y -pole frequencies using Algorithm FPA2.



(a)



(b)

Figure 58: Example FP2. $10\log_{10}(1/\text{Variance})$ versus total SNR in dB for (a) x -pole and (b) y -pole magnitudes using Algorithm Two.

5.4 Summary

In this chapter the 2-D TLS-Prony Technique was developed. This is a new technique for estimating two-dimensional (2-D) poles and amplitude coefficients in a 2-D Prony-based model. The fundamental estimation algorithm (Algorithm One) involves two parts, each utilizing a 1-D singular value decomposition-based technique, and is capable of locating frequencies anywhere in the 2-D frequency plane. The basic algorithm was first developed for a single 2-D data set, such as a set of radar measurements with a single transmit and receive polarization. Simulations were shown which demonstrate the performance of the algorithm for various noise levels. Then, the algorithm was extended to the full-polarization case which requires full-polarization 2-D measurements of a target. Simulations were shown which demonstrate the performance of this algorithm for various noise levels. The performance characteristics for both the single-polarization and full-polarization algorithms are shown to be nearly identical.

CHAPTER VI

Simulations Utilizing GTD Flat Plate Data

6.1 Introduction

In order to demonstrate the utility and the limitations of the 2-D TLS-Prony Technique described in the previous chapter, radar scattering data (both single polarization and full-polarization) are analyzed using this technique. The structure analyzed is a thin metal perfectly conducting square plate 0.5 meters long on a side. This plate is oriented in the spherical coordinate system as shown in Figure 59.

The scattering data was simulated using the GTD-based code described in [49]. All of the scattering mechanisms which are modeled by the GTD code were used to generate the data. For example, the corner scattering coefficients, the edge scattering

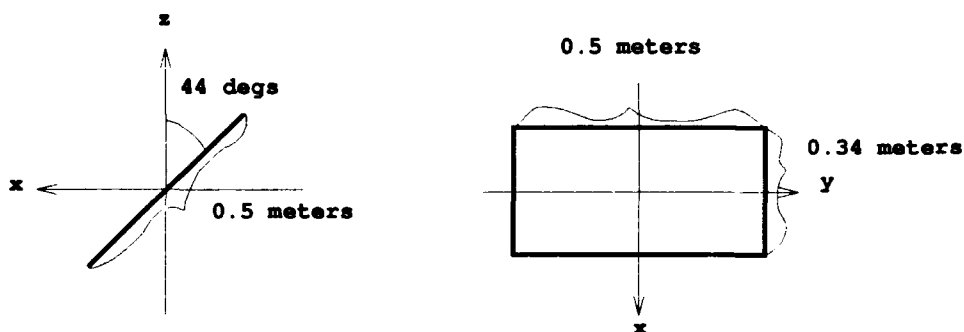


Figure 59: Thin metal perfectly conducting square plate analyzed.

coefficients and the double-bounce coefficients are included in the data set. However, the corner scattering coefficients are the dominant terms in the data.

The locations, damping factors and polarimetric properties of the scattering centers which exist on the plate are estimated using both the single-polarization TLS-Prony Technique and the full-polarization TLS-Prony Technique. This structure contains corners and edges at both grazing and non-grazing angles. Thus, the abilities of the 2-D TLS-Prony Technique to estimate non-point scatterer type scattering centers is demonstrated.

The examples that are shown in this chapter are intended to investigate several issues. First, the quality of the parameter estimates as a function of 2-D angular and frequency bandwidth is demonstrated. Limited angular data sets over several 2-D angular and frequency bandwidths are analyzed in this chapter. Second, the ability of the estimation algorithms to use data directly in polar form, rather than interpolating the data onto a rectangular data grid in the 2-D frequency plane, is investigated. Third, the effects of noise on the parameter estimates for the various data sets is examined. Also, the effects (on the parameter estimates) of choosing model orders which are equal to and greater than the expected number of scattering centers are examined.

Recall that the 2-D TLS-Prony Technique requires data on a rectangular grid in the 2-D frequency plane. However, if the data (gathered by a radar) lies on a polar grid, it is possible to treat this data as if it lies on a rectangular grid if the polar grid is over a relatively small angular bandwidth (usually under 15°) and the

center frequency is larger than several times the frequency bandwidth of the data. Thus, the polar data is assumed to lie directly on a rectangular (or square) grid. A polar data set over a 15° angular swath with a center frequency to bandwidth ratio of 4.029 is utilized directly as the data in the 2-D TLS-Prony Technique. Then this data set is interpolated onto a square data grid and the results of the two sets of simulations are compared. Another polar data set over a 3° angular swath is also analyzed. The polar data over this angular swath is also directly utilized by the 2-D TLS-Prony Technique, but in this case the center frequency to bandwidth ratio is 19.250. The interpolation of this 3° onto a square grid is not examined in detail since the polar grid closely resembles the square grid for such a small 2-D angular and frequency bandwidth.

Most of the examples shown involve scenarios where no noise is added to the scattering data. The effects of noise on the parameter estimates are demonstrated by considering the relative error (RE) versus total SNR for the various data sets. It is shown that for two of the three data sets examined, the RE and thus the parameter estimates are not effected by noise for total SNRs over 15 dB. The single data set which yields parameter estimates which are effected by noise for SNRs up to and over 50 dB is the polar data set over a 3° angular swath. This data set is more sensitive to noise since the resolution (in the 2-D range domain) is the smallest of all of the data sets (due to the fact that the 2-D angular and frequency bandwidths are the smallest for this data set). The 2-D TLS-Prony Technique is superresolving the scattering centers, and the parameter estimates are more sensitive to noise. It is demonstrated

in [10] that the parameter estimates associated with various parametric techniques, such as Prony's Method, are sensitive to noise when the parametric techniques are superresolving modes. The effects of noise for the 3° polar swath data are shown in the form of scatter plots for scattering center locations for various total SNRs.

6.2 Description of Data

The first data set analyzed consists of the monostatic scattering matrix from the plate for incidence angles of $-7.5^\circ < \phi < 97.5^\circ$ with θ fixed at 90° . The frequency range is from 9 GHz to 11.55 GHz in 0.085 GHz steps. The angular step size is 0.5° . Thus, the data set is 31×211 (number of frequencies \times number of angles). Data segments of size 31×31 are analyzed using Algorithm Two and FPA2. This corresponds to a 15° polar swath of data. The unambiguous range for this data set is 1.7637 meters in each direction. Note that this data, which lies on the polar grid, is used directly by the 2-D TLS-Prony Technique, without being interpolated onto a square grid. Recall that the 2-D TLS-Prony Technique requires data which lies on a rectangular grid in the 2-D frequency plane. Thus, it is assumed that since these polar data sets are over a relatively small angular swath (15°) and the center frequency is 4.029 times the bandwidth, it is a reasonable approximation to assume that the polar grid is close enough to a square grid to treat the data as if it lies on a square grid. The frequency and angular step sizes of 0.085 GHz and 0.5° were chosen to make the spacing in the frequency direction very close to the spacing between data samples in the angular direction on the 2-D frequency plane. This validity of this assumption is investigated in the examples which utilize this data set, which is

designated the 15° polar swath of data.

The second data set analyzed consists of several 29×29 data segments which lie on a square grid in the 2-D frequency plane. These data sets were interpolated from the 15° polar swaths of data segments. Twenty-seven different square grid data sets are interpolated from the 15° polar swaths of data. There are nine different center angles for the square grid data sets, and three polarizations per center angle. The interpolation method in Equation 4.27 was used to interpolate the 31×31 15° polar swath data sets to the 29×29 square grid data sets. The spacing between the square grid data points is 0.085 GHz in each direction on the 2-D frequency plane. The reason that the square grid is only 29×29 while the polar grid is 31×31 is that by making the square grid fit entirely within the polar grid, the need to extrapolate to square grid data points which lie outside of the original polar grid is avoided.

The third data set analyzed consists of several 3° polar swaths of data. The frequency range is from 9 GHz to 9.48 GHz in 0.016 GHz steps. The angular range is $\pm 1.5^\circ$ around the center angle in 0.1° steps. Thus, these data sets are also of size 31×31 points. The unambiguous range for these data sets is 9.3684 meters in each direction. These 3° polar data sets are utilized directly by the 2-D TLS-Prony Technique in polar form. Since this data set is over a very small angular swath (3°) and the center frequency is 19.250 times the bandwidth, it is a good approximation to assume that the polar grid is close enough to a square grid to treat the data as if it lies on a square grid. This is a much safer assumption than that made for the 15° polar swath of data. Results for scenarios where this 3° data is interpolated

onto a square grid as the 15° data are not shown since the polar grid is such a close approximation to the square grid. Several sets of this 3° polar data were interpolated onto a square grid and the results obtained (which are not shown) were, in general, worse in a relative error sense to the results obtained using the polar data directly. This is most probably due to the interpolation error which was introduced in the interpolation step. The interpolation method is a linear function, and this is not an accurate model for this data. The development of a more appropriate interpolation technique is an area for future research.

The measurement geometry is shown in Figure 60. The four corners of the plate are labeled C1, C2, C3, C4 in this figure. The projection of the plate onto the xy -plane is the expected form of the image for all of the data sets since the slice of data obtained is always limited to $\theta = 90^\circ$ (or the xy -plane). The angle ϕ in this figure is designated the center angle of rotation of the data. The data collected in the 2-D frequency plane is depicted in Figure 61. First, a single-polarization TLS-Prony algorithm (Algorithm Two) is applied to the data. Then, a full-polarization TLS-Prony algorithm (FPA2) is applied to the data.

6.3 Single-Polarization Analysis of Plate

Figure 62 shows a contour image of the plate obtained by directly taking a 2-D IFFT of the hh -polarization 15° polar swath of data and then re-scaling the axes. The 15° sector of data used was for azimuth angles of $37.5^\circ \leq \phi \leq 52.5^\circ$. The outline of the plate corresponds to a plate at the center of this azimuth sweep, $\phi = 45^\circ$. The corners of the plate, labeled C1, C2, C3, C4 in this figure correspond to the

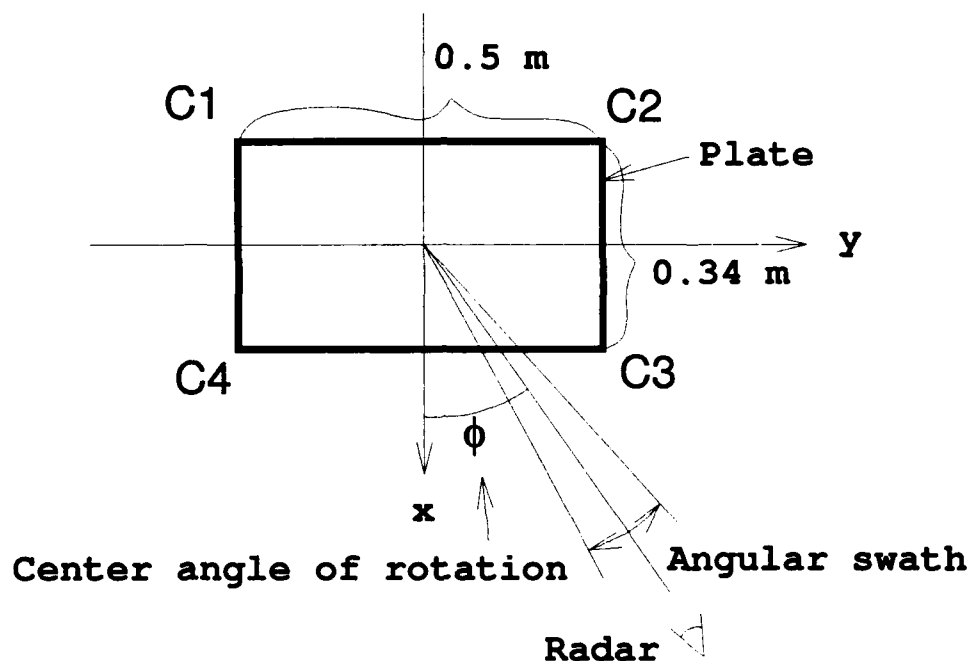


Figure 60: Geometry for scattering measurements from plate.

corners shown in Figure 60. These corner definitions remain unchanged throughout this chapter. Comparing Figures 60 and 62, the meanings of down-range distance and cross-range distance become apparent. For $\phi = 0^\circ$, the down-range scale is the negative x -axis and the cross-range scale is the positive y -axis in Figure 60.

For the initial analysis of the data, the model orders chosen will reflect the expected number of scattering centers. For example, for a center angle of $\phi = 45^\circ$, model orders of $Q, K, R, L = 10, 4, 10, 1$ are reasonable since there are four corners, each at different down-range and cross-range distances. For center angles of $15^\circ \leq \phi \leq 75^\circ$ the expected number of scattering centers is four (the four corners of the plate). Each of the corners of the plate are at a different down-range distance,

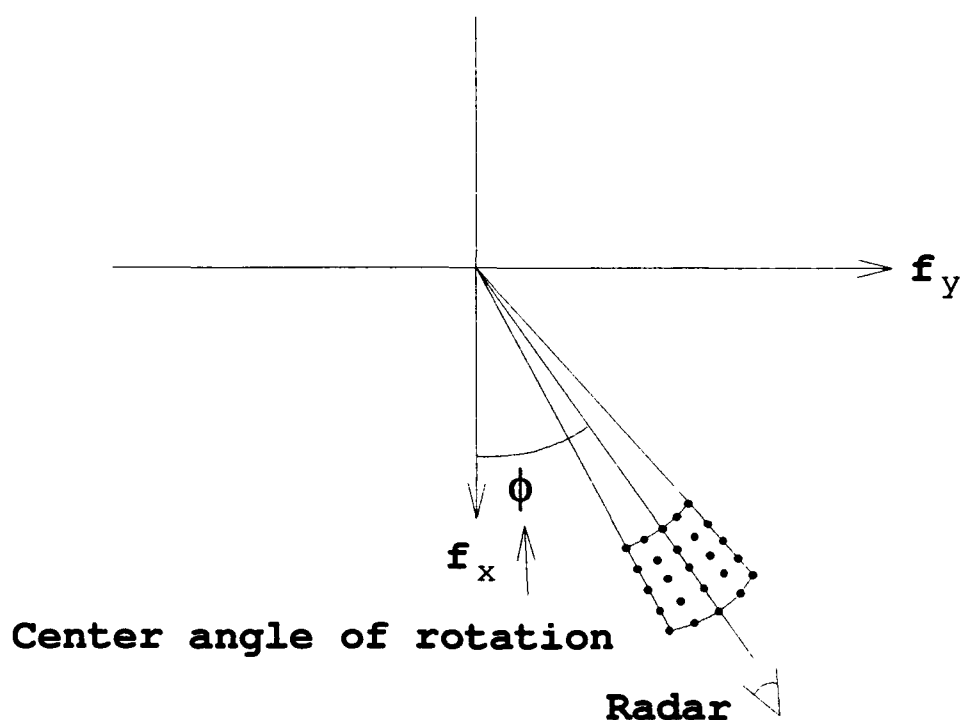


Figure 61: 2-D frequency plane plot of scattering data collected by radar.

and thus the appropriate model orders for these center angles are $Q, K, R, L = 10, 4, 10, 1$. Recall that the choice of Q and R depends upon the data length ($Q = 10 \approx \frac{31}{3}$ and $R = 10 \approx \frac{31}{3}$ [59]) while the choice of K and L depend upon the expected number of scattering centers. For center angles of $0^\circ \leq \phi < 15^\circ$ and $75^\circ < \phi \leq 90^\circ$, the scattering response of the plate is edge dominated, and the model orders are chosen to reflect this. Since the damped exponential is not a good model for the scattering from an edge for these grazing angles, the model orders are chosen slightly larger than the expected number of scattering centers in an attempt to more completely model the data.

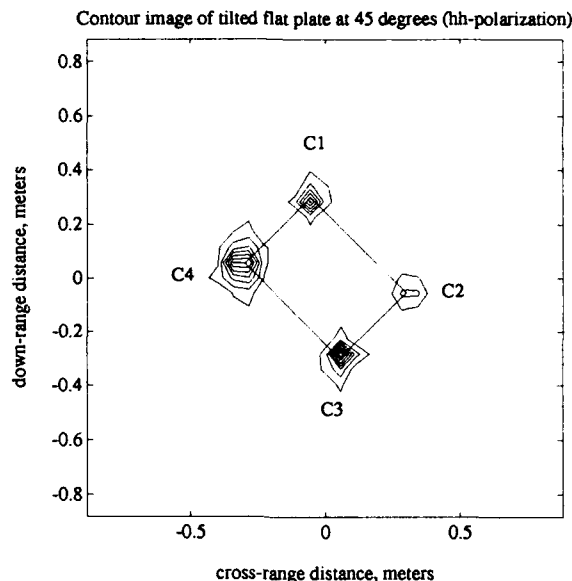


Figure 62: Contour image of plate for $\phi = 45^\circ$ generated from a 15° polar swath of hh -polarization data.

6.3.1 Single Polarization Analysis of Fifteen Degree Polar Swaths of Data

The first set of simulations use the 15° polar swaths of data. The polar data is directly used by Algorithm Two (the polar data is not interpolated onto a square grid). Nine 15° sections of the hh , hv and vv -polarization data are analyzed using Algorithm Two. The results are shown in Figures 63 through 76. Shown for each angle are three contour images of the plate, each image corresponding to one of the three polarizations, found by directly using the polar data in the 2-D IFFT. Since the polar data is directly used by the 2-D TLS-Prony Technique, it is reasonable to use the polar data directly to form the images of the plate. Also shown are three sets of pole locations, each set corresponding to one of the three polarizations,

estimated by Algorithm Two with no noise added to the original data. In the cases where there are more than four poles, only the four highest energy poles are shown in these plots.

Along with these plots are shown contour images which were generated from the estimated parameters. The parameters estimated by Algorithm Two are used in the 2-D model in Equation 5.2 to generate data in the 2-D frequency domain. Note that all of the parameters estimated by Algorithm Two are used to generate this data (not just the four highest energy poles). This data is then transformed into the image domain and the results are shown in the figures. Outlines of the plate are shown for the center of the azimuth sweep. The data used to generate each contour image is a 31×31 data set, where the angular data was taken at $\pm 7.5^\circ$ around the angle indicated, which is the center of the rotation. For each plot, the entire unambiguous range is shown which is 1.7637 meters in each direction.

It must be pointed out that all of the contour images shown in this chapter, in general, are on different magnitude scales. That is, the value of a given contour line for one contour plot is not necessarily the same value on another contour plot. Thus, the contour plots are shown to demonstrate the form of each individual image, and relative magnitude comparisons between images can not be made. The differences between an original data generated contour image and its corresponding model generated contour image are reflected in the relative error (RE) between the two images, which is defined in Equation 6.1. It also must be emphasized that an outline of the plate (projected onto the xy -plane) is sketched in most plots shown in

Table 9: Model orders and relative errors for single polarization results for the scattering from an inclined plate. The data is a 15° polar swath.

Angle	Model Order; Q, K, R, L	RE (hh)	RE (hv)	RE (vv)
0	10,2,10,2	0.9818	0.5896	0.9817
7.5	10,4,10,2	0.7035	0.7054	0.6902
15	10,4,10,1	0.6777	0.7311	0.6343
30	10,4,10,1	0.6518	0.5989	0.5883
45	10,4,10,1	0.5644	0.6448	0.6191
60	10,4,10,1	0.6993	0.6390	0.5855
75	10,4,10,1	0.4608	0.4490	0.4919
82.5	10,4,10,2	0.6520	0.6577	0.5639
90	10,2,10,2	0.9230	0.9210	0.9256

this chapter, and this plate outline is not part of the contour image or the estimated pole locations. This outline is sketched to show the relationship between the images or estimated pole locations and the structure of the plate.

The model orders used and the relative error (RE) for the Algorithm Two generated estimates are given in Table 9. The RE is defined as

$$\text{RE} = \frac{\|D' - D\|}{\|D\|} \quad (6.1)$$

where D' is the data matrix generated by the parameter estimates and D is the actual data matrix. The $\|\cdot\|$ denotes the Frobenius-norm, which is calculated for a matrix B as the square root of the sum of the squares of all of the elements in B .

Figures 64 and 65 show results for $\phi = 7.5^\circ$. From the contour images in this figure it can be seen that the front edge (the edge at $x=0.173$ meters, between C3 and C4, in Figure 59) is dominant in the hh -polarization response while the rear edge

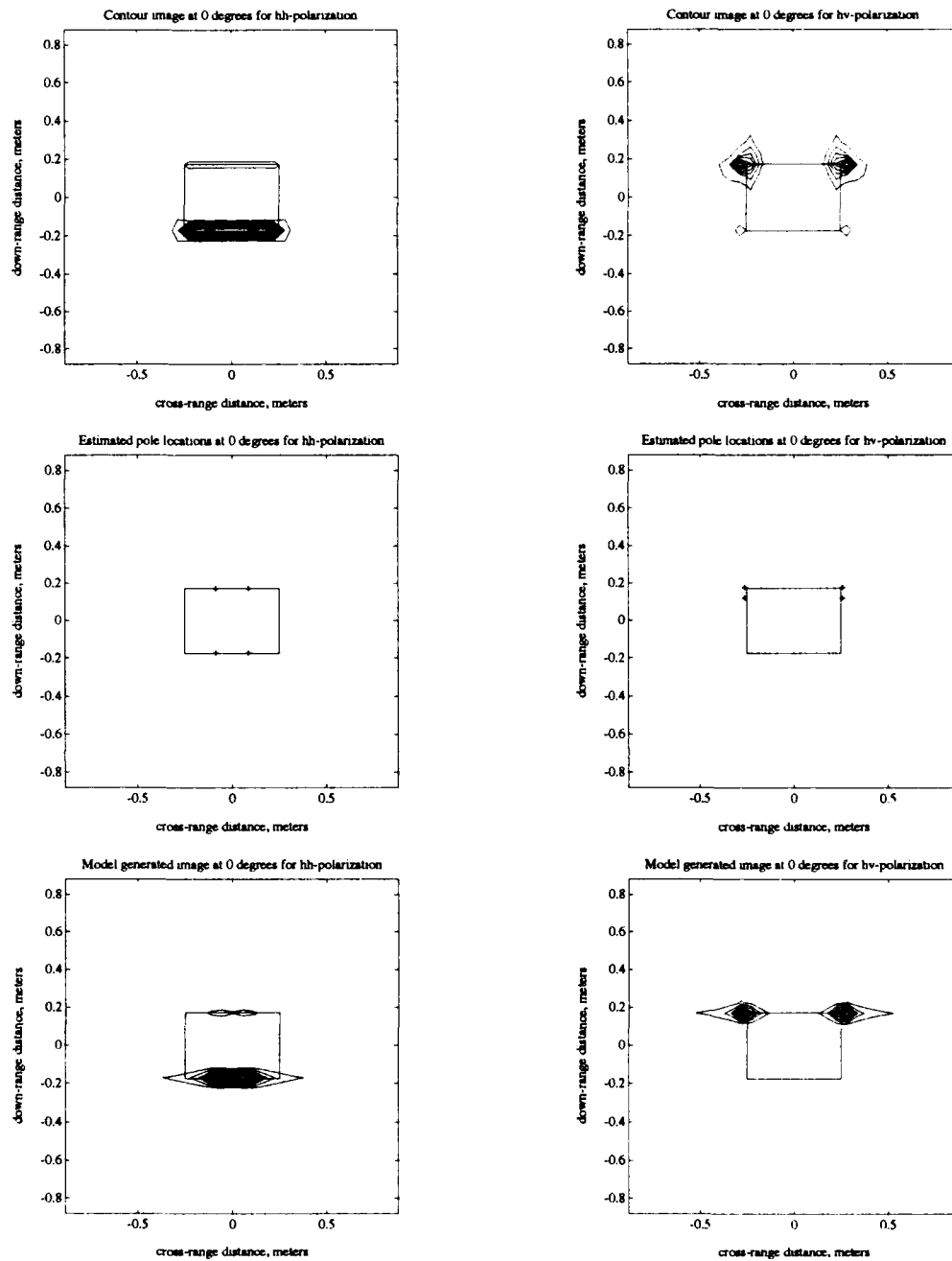


Figure 63: Single polarization inclined plate example for a 15° swath of polar data centered around 0° . Contour images, estimated pole locations and model generated images are shown for hh and hv -polarizations. Pole locations were estimated by Algorithm Two. Model orders were $Q, K, R, L = 10, 2, 10, 2$.

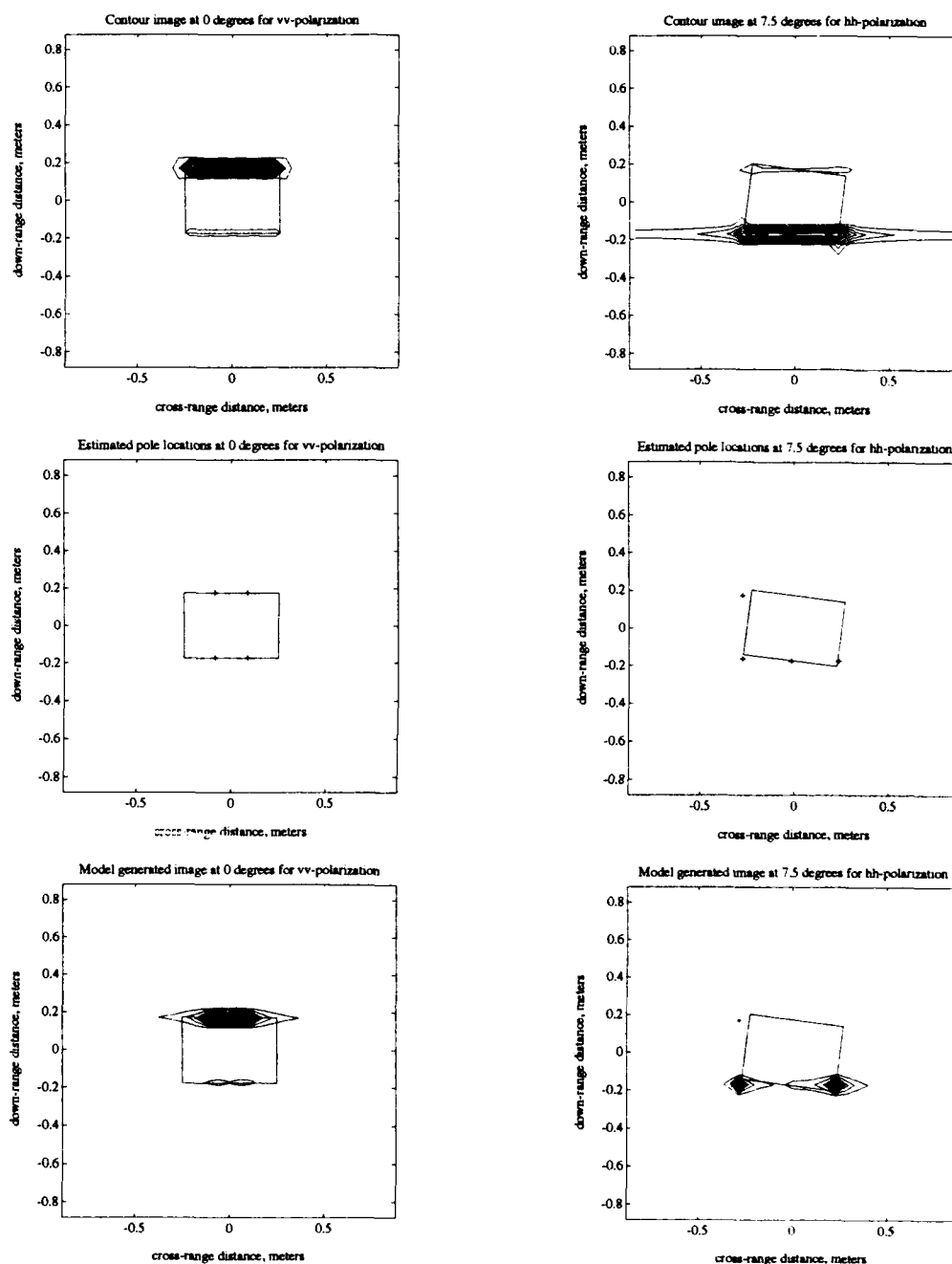


Figure 64: Single polarization inclined plate example for a 15° swath of polar data centered around 0° and 7.5°. Contour images, estimated pole locations and model generated contour images of the plate are shown for vv polarization at 0° and hh -polarization at 7.5°. Pole locations were estimated by Algorithm Two. Model orders were $Q, K, R, L = 10, 2, 10, 2$ for 0° and $Q, K, R, L = 10, 4, 10, 2$ for 7.5°.

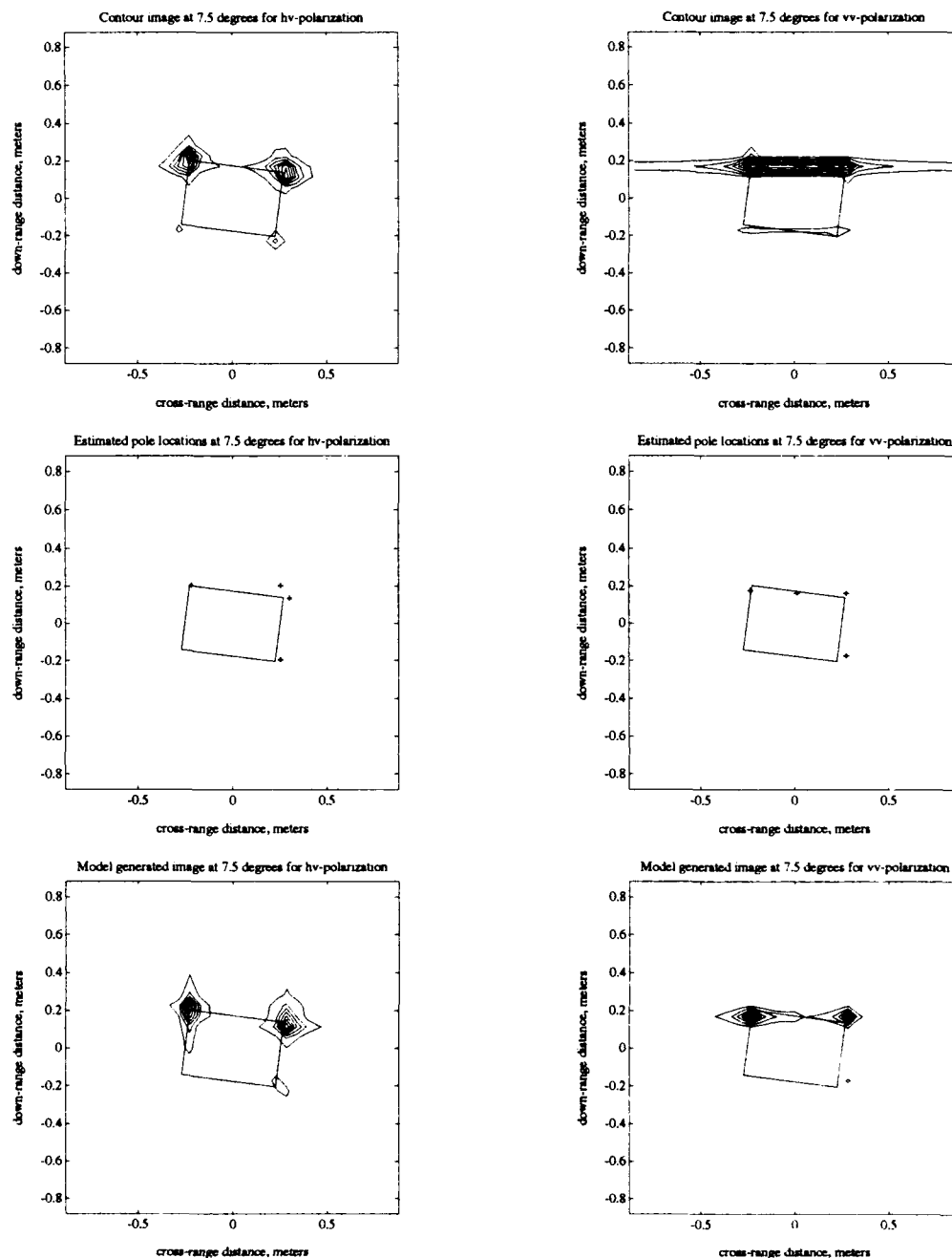


Figure 65: Single polarization inclined plate example for a 15° swath of polar data centered around 7.5° . Contour images, estimated pole locations and model generated images are shown for hh and vv -polarizations. Pole locations were estimated by Algorithm Two. Model orders were $Q, K, R, L = 10, 4, 10, 2$.

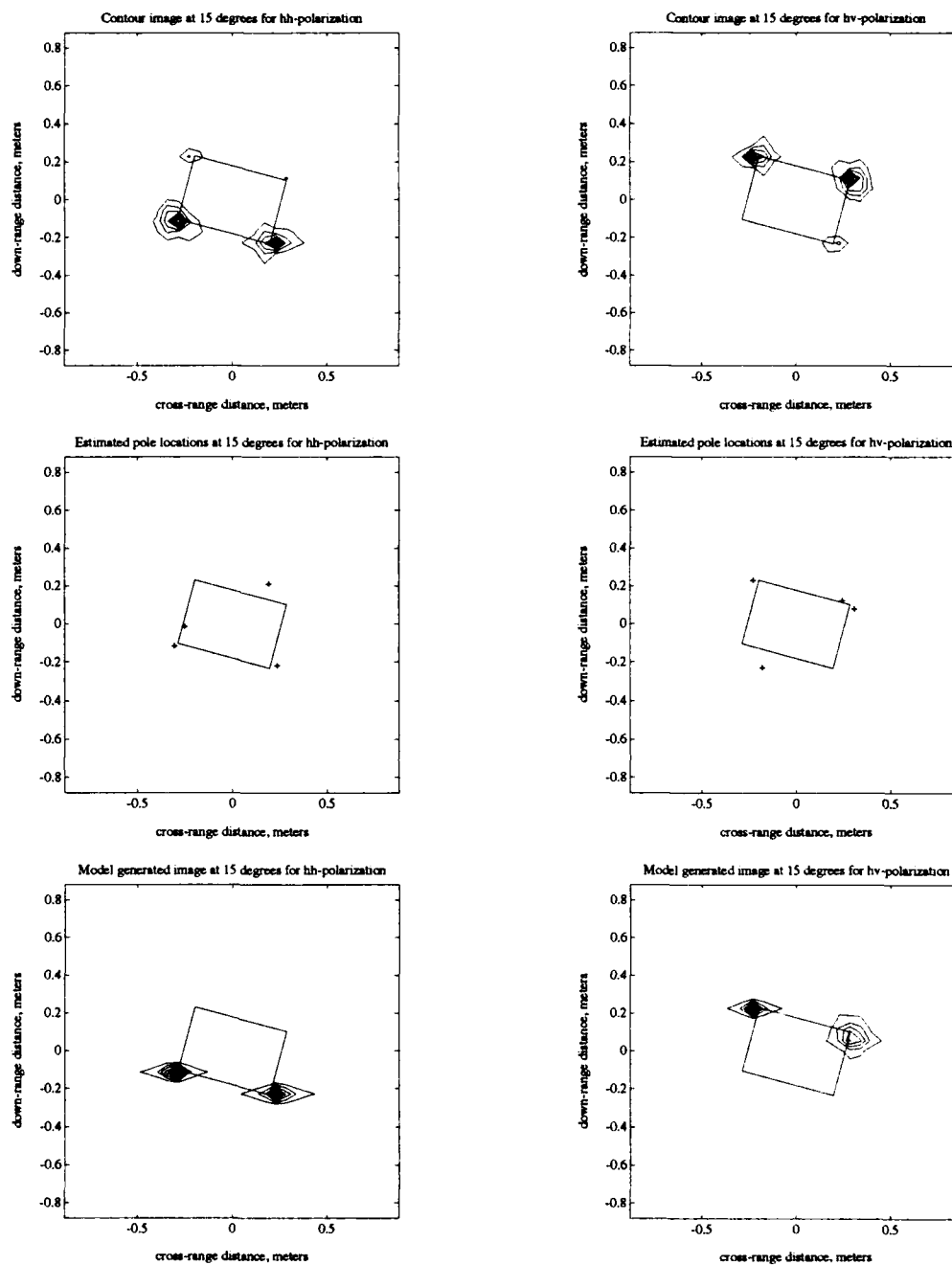


Figure 66: Single polarization inclined plate example for a 15° swath of polar data centered around 15°. Contour images, estimated pole locations and model generated images are shown for *hh* and *hv*-polarizations. Pole locations were estimated by Algorithm Two. Model orders were $Q, K, R, L = 10, 4, 10, 1$.

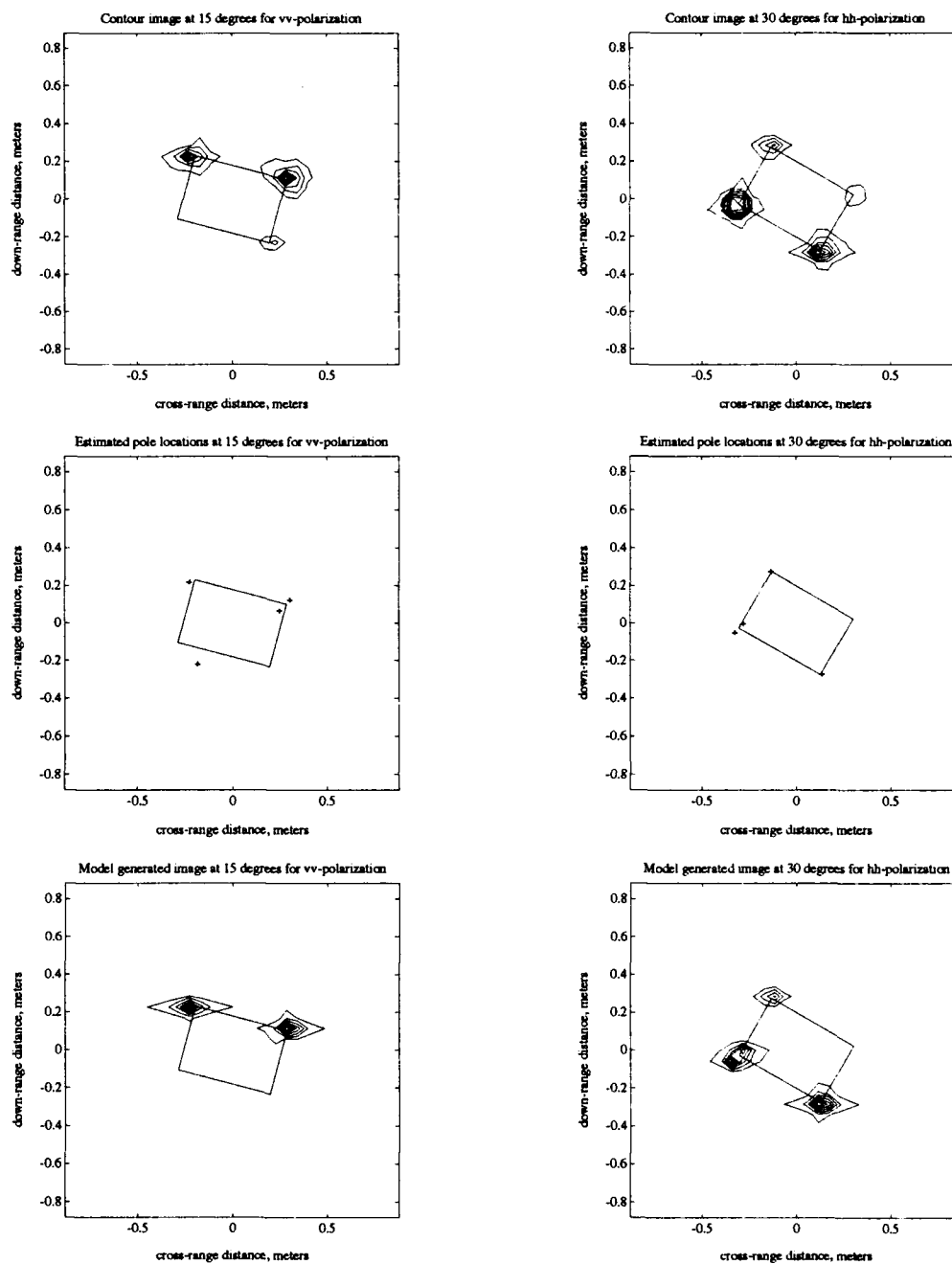


Figure 67: Single polarization inclined plate example for a 15° swath of polar data centered around 15° and 30° . Contour images, estimated pole locations and model generated contour images of the plate are shown for vv polarization at 15° and hh -polarization at 30° . Pole locations were estimated by Algorithm Two. Model orders were $Q, K, R, L = 10, 4, 10, 1$ for 15° and 30° .

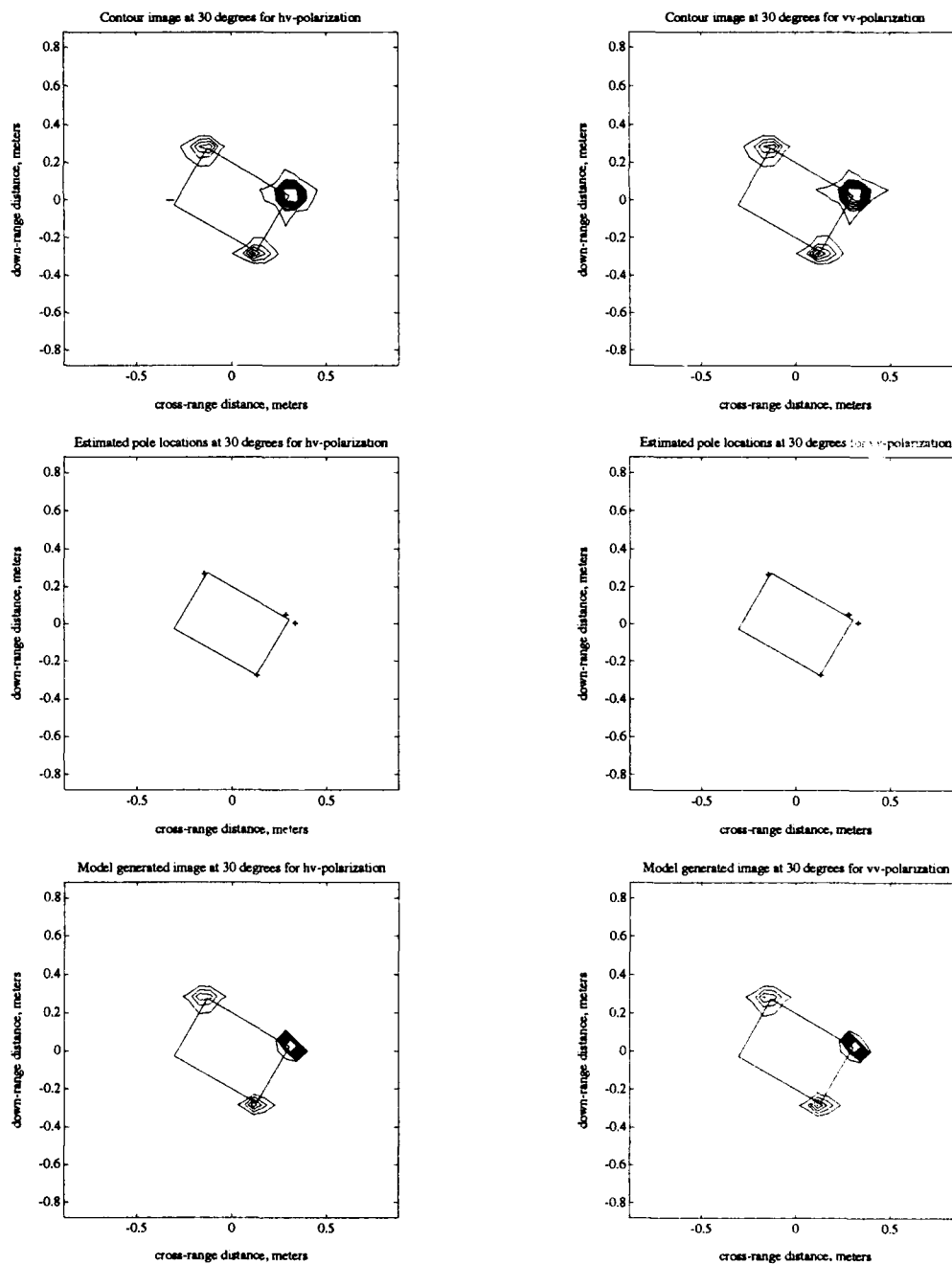


Figure 68: Single polarization inclined plate example for a 15° swath of polar data centered around 30°. Contour images, estimated pole locations and model generated images are shown for hh and hv -polarizations. Pole locations were estimated by Algorithm Two. Model orders were $Q, K, R, L = 10, 4, 10, 1$.

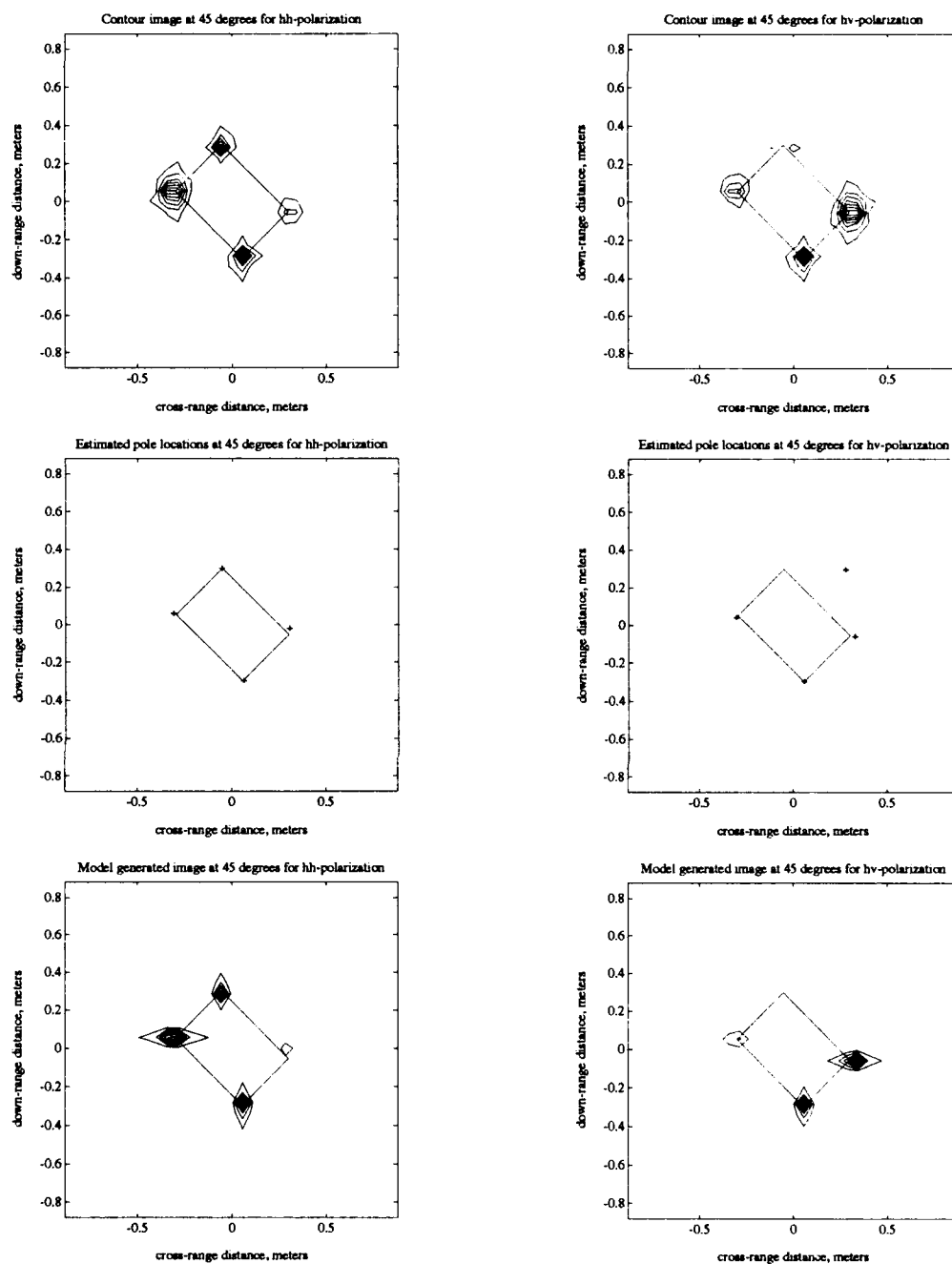


Figure 69: Single polarization inclined plate example for a 15° swath of polar data centered around 45° . Contour images, estimated pole locations and model generated images are shown for hh and vv -polarizations. Pole locations were estimated by Algorithm Two. Model orders were $Q, K, R, L = 10, 4, 10, 1$.

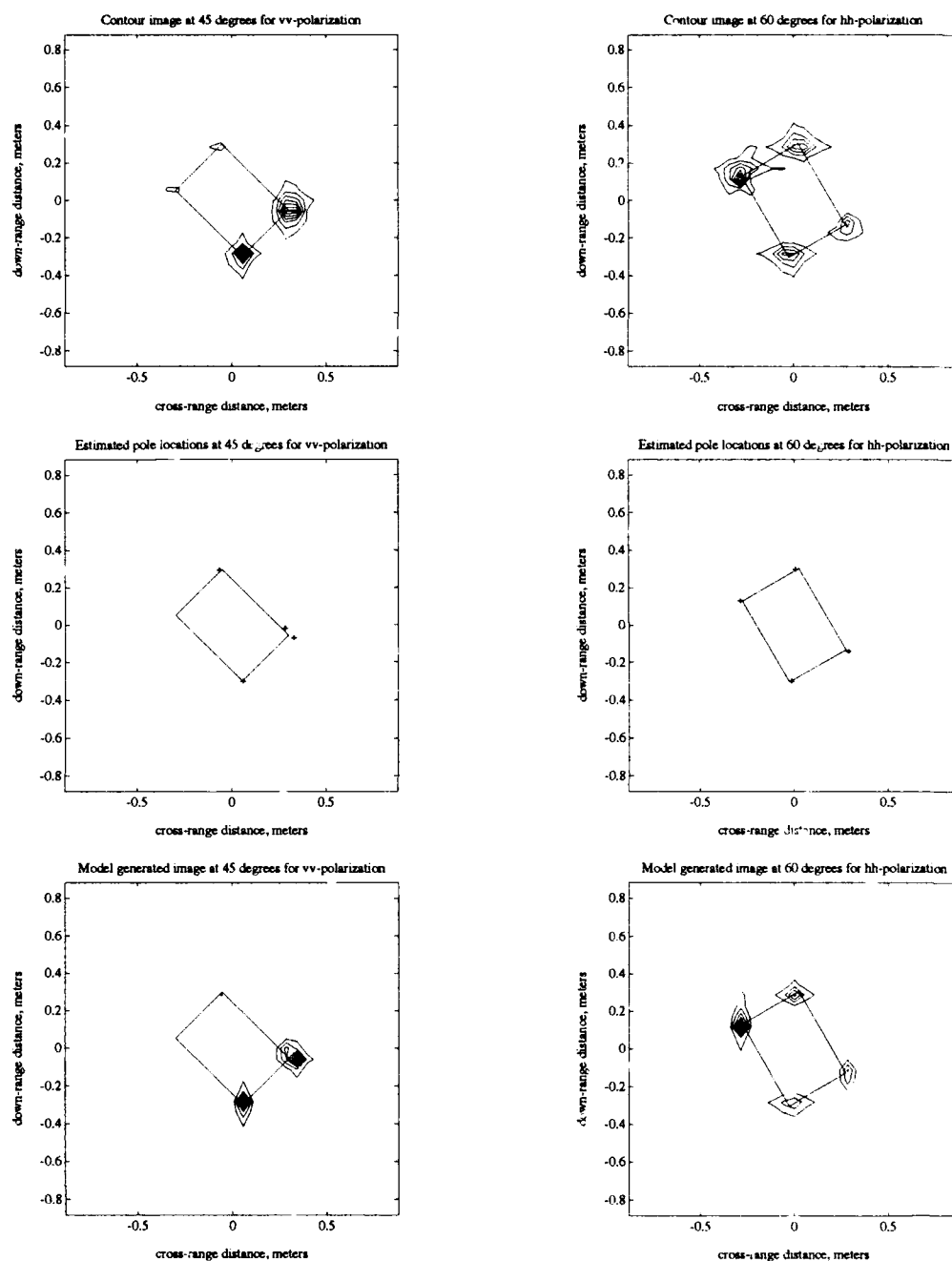


Figure 70: Single polarization inclined plate example for a 15° swath of polar data centered around 45° and 60° . Contour images, estimated pole locations and model generated contour images of the plate are shown for vv polarization at 45° and hh -polarization at 60° . Pole locations were estimated by Algorithm Two. Model orders were $Q, K, R, L = 10, 4, 10, 1$ for 45° and 60° .

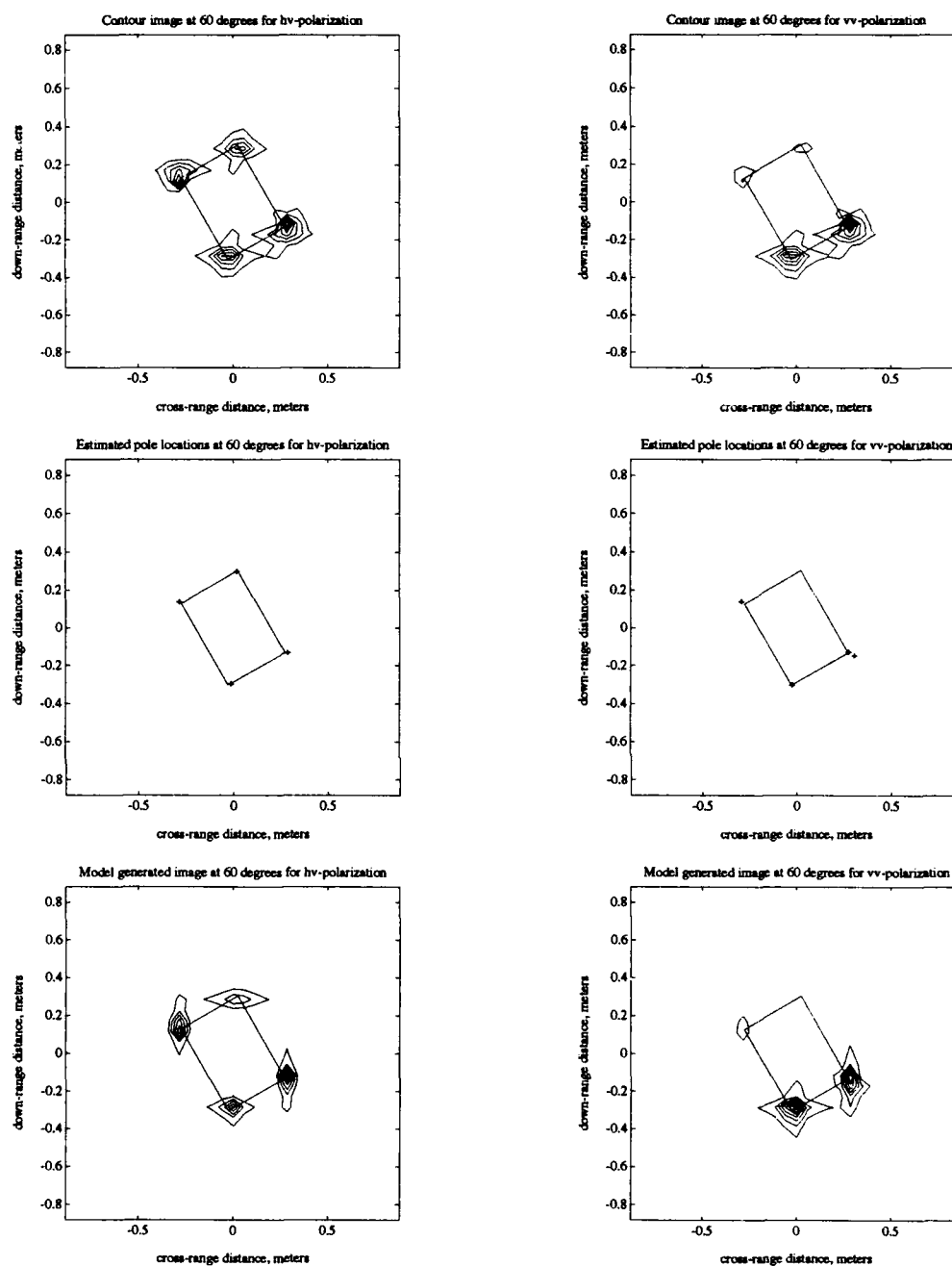


Figure 71: Single polarization inclined plate example for a 15° swath of polar data centered around 60° . Contour images, estimated pole locations and model generated images are shown for hh and vv -polarizations. Pole locations were estimated by Algorithm Two. Model orders were $Q, K, R, L = 10, 4, 10, 1$.

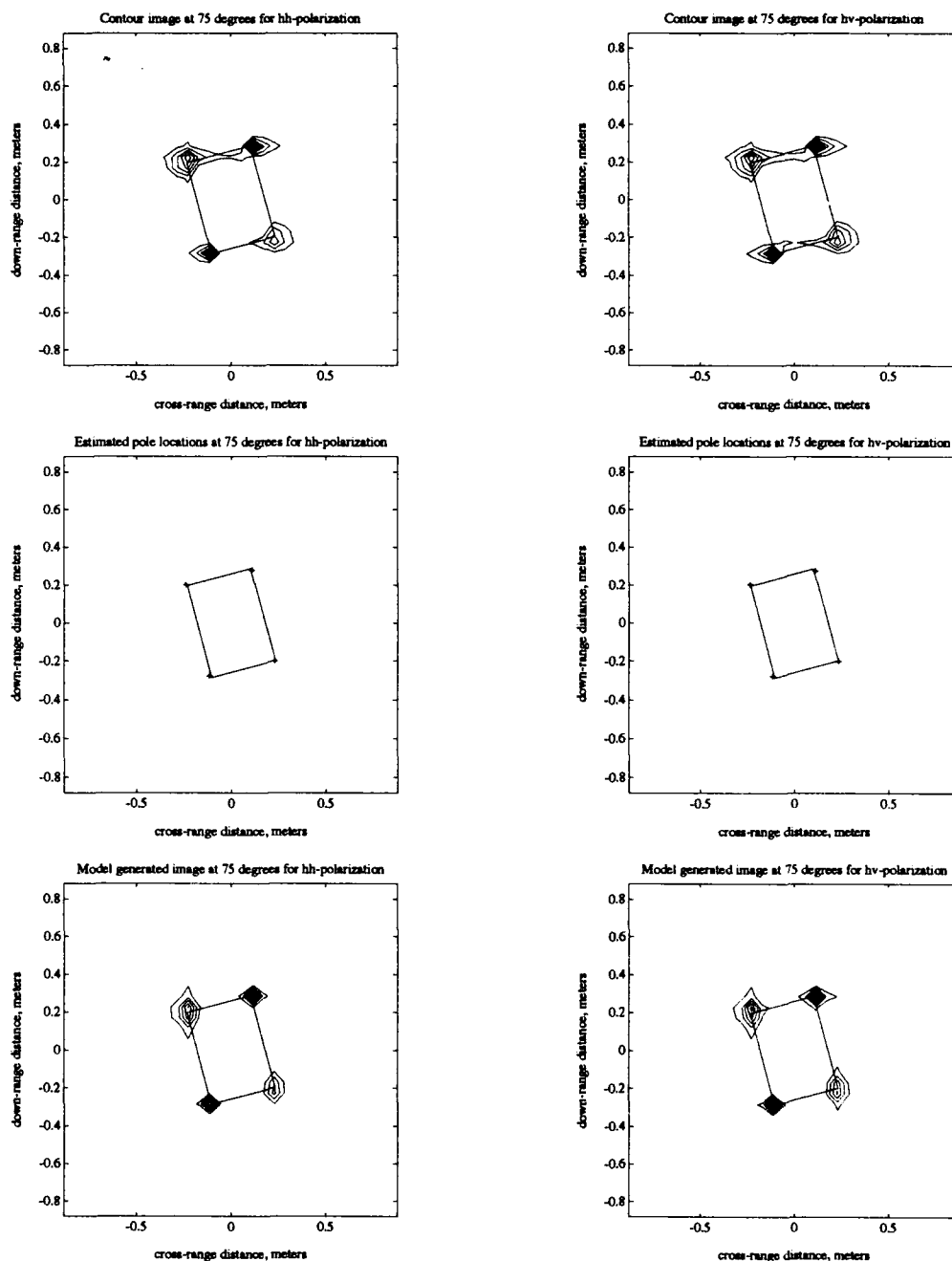


Figure 72: Single polarization inclined plate example for a 15° swath of polar data centered around 75° . Contour images, estimated pole locations and model generated images are shown for hh and hv -polarizations. Pole locations were estimated by Algorithm Two. Model orders were $Q, K, R, L = 10, 4, 10, 1$.

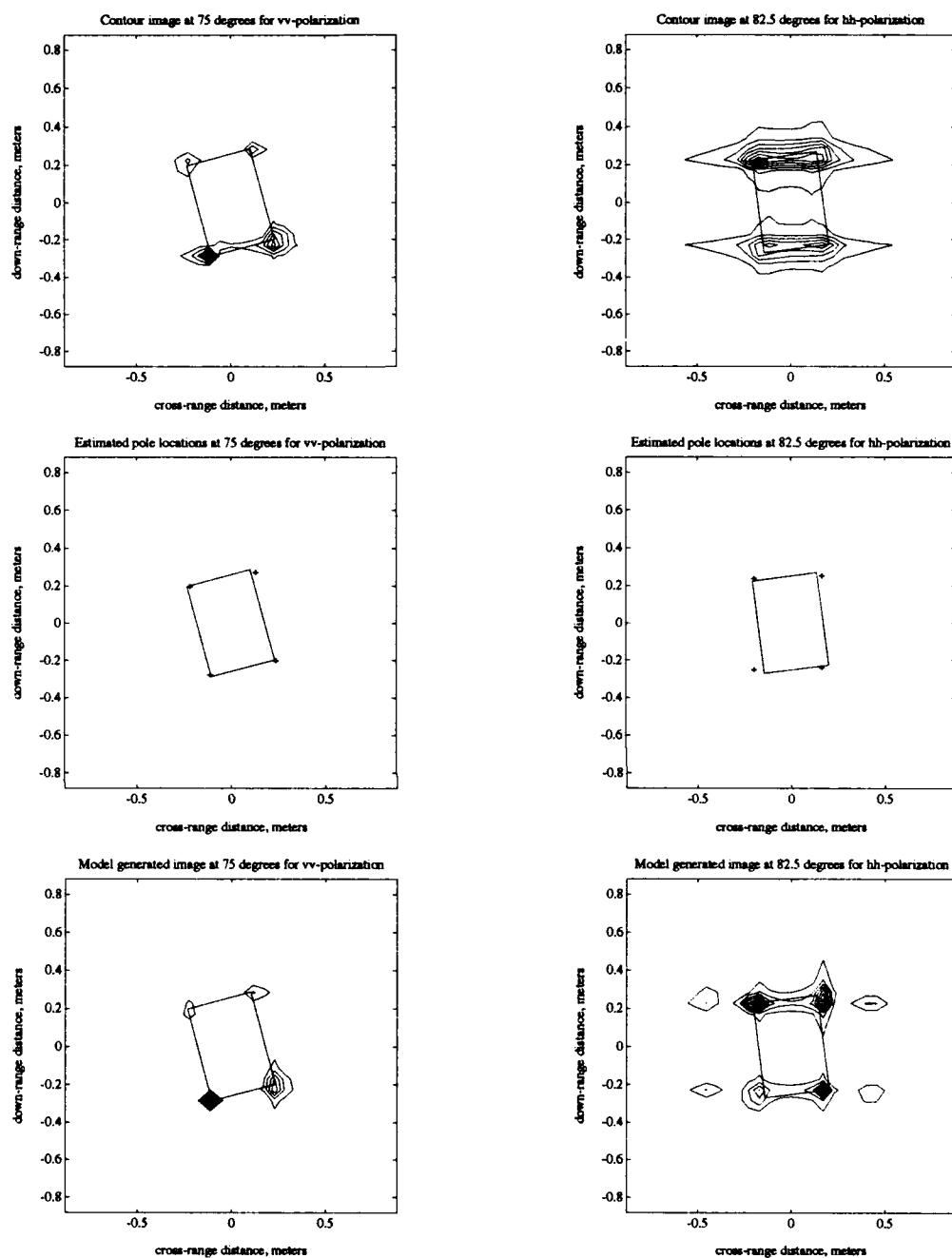


Figure 73: Single polarization inclined plate example for a 15° swath of polar data centered around 75° and 82.5°. Contour images, estimated pole locations and model generated contour images of the plate are shown for vv -polarization at 75° and hh -polarization at 82.5°. Pole locations were estimated by Algorithm Two. Model orders were $Q, K, R, L = 10, 4, 10, 1$ for 75° and $Q, K, R, L = 10, 4, 10, 2$ for 82.5°.

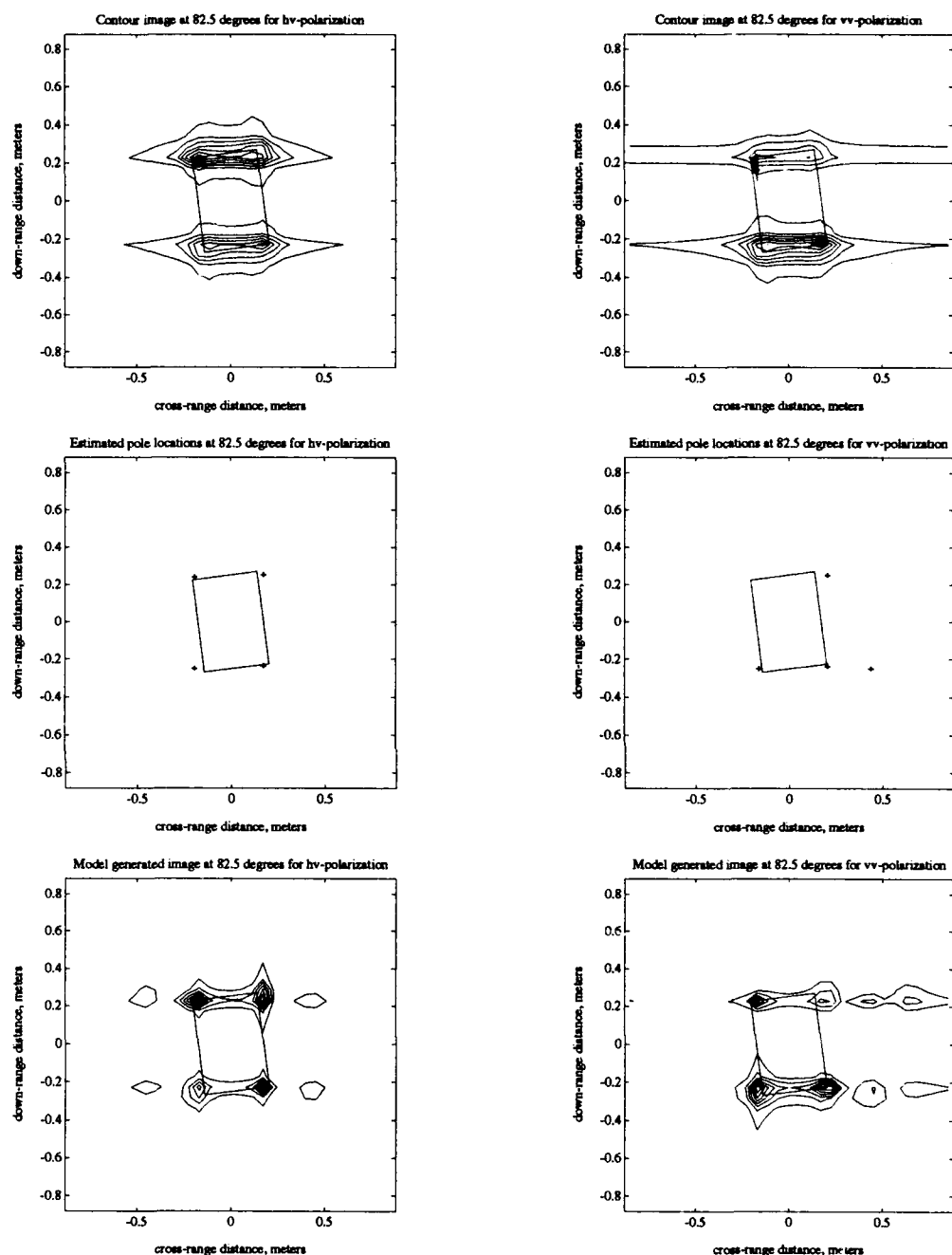


Figure 74: Single polarization inclined plate example for a 15° swath of polar data centered around 82.5° . Contour images, estimated pole locations and model generated images are shown for hh and hv -polarizations. Pole locations were estimated by Algorithm Two. Model orders were $Q, K, R, L = 10, 4, 10, 2$.

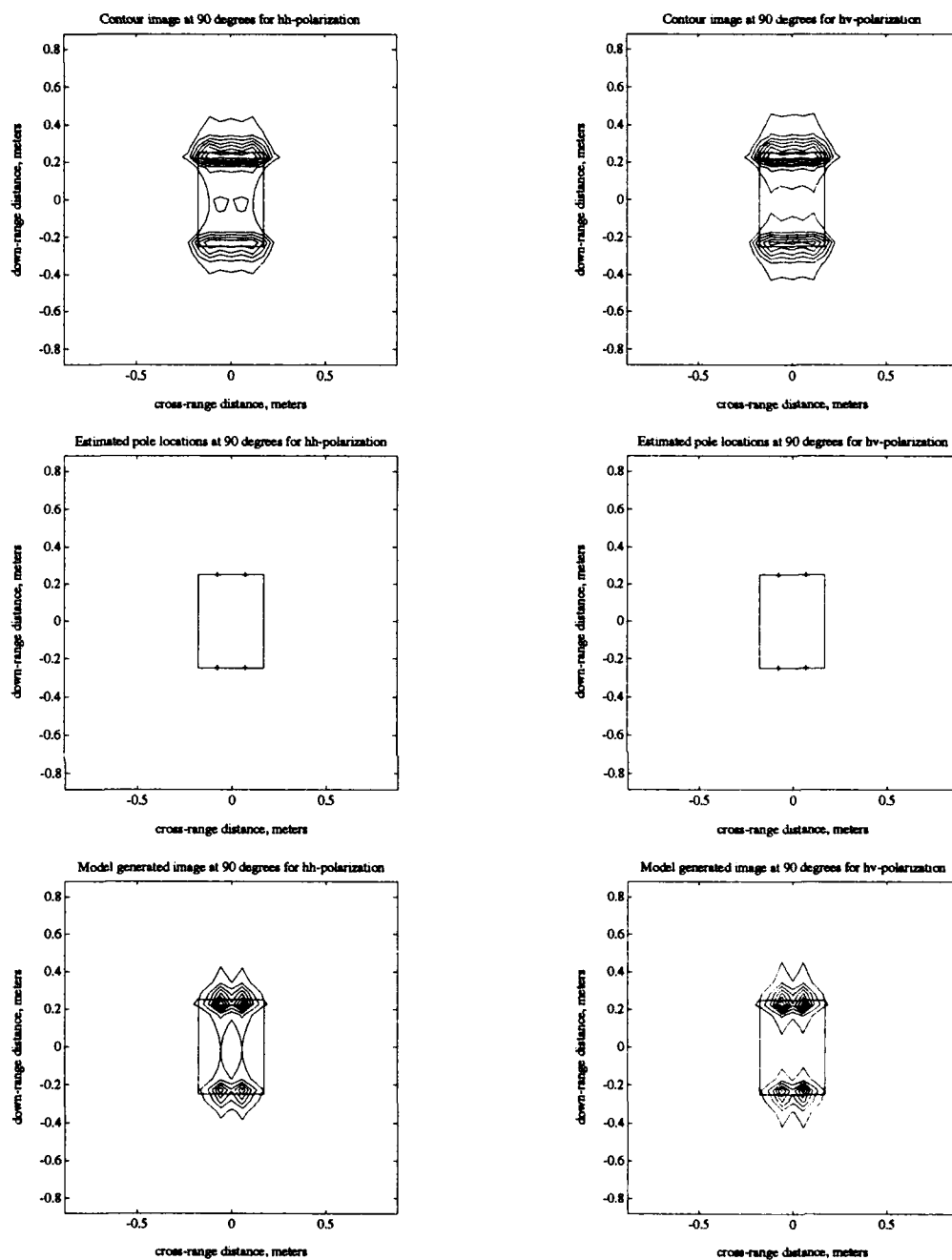


Figure 75: Single polarization inclined plate example for a 15° swath of polar data centered around 90° . Contour images, estimated pole locations and model generated images are shown for hh and hv -polarizations. Pole locations were estimated by Algorithm Two. Model orders were $Q, K, R, L = 10, 2, 10, 2$.

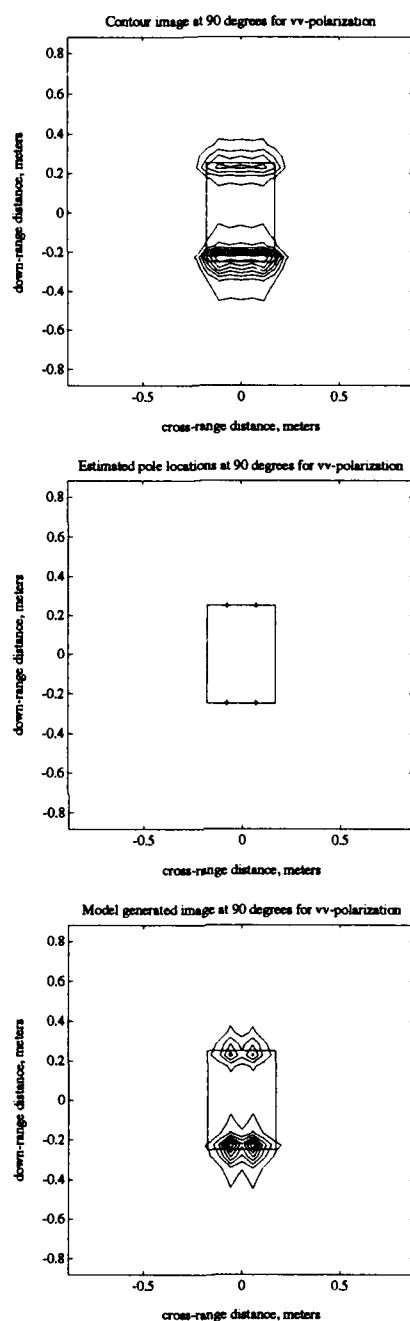


Figure 76: Single polarization inclined plate example for a 15° swath of polar data centered around 90° . Contour images, estimated pole locations and model generated images are shown for vv -polarization. Pole locations were estimated by Algorithm Two. Model orders were $Q, K, R, L = 10, 2, 10, 2$.

(the edge at $x=-0.173$ meters, between C1 and C2, in Figure 59) is dominant in the vv -polarization response. The estimated pole locations confirm this as they cluster on the dominant edge in the hh and vv -polarization cases. For the hv -polarization response, the corners C1 and C2 are dominant.

Figures 66 and 67 show results for $\phi = 15^\circ$. From the contour images it can be seen that this response is corner dominated. This can also be seen in the estimated pole plots. The same conclusions can be made for the scenarios analyzed in Figures 68 through 73. Figures 73 and 74 show the results for $\phi = 82.5^\circ$. This is an edge dominated scenario similar to the $\phi = 7.5^\circ$ scenario. For many of the scenarios, some corners or edges are dominant for one polarization while the other edges or corners are dominant for another polarization. This can be taken advantage of by estimating the pole locations using the full-polarization data, and this is done in the next section.

The estimated pole locations in Figures 63 through 76, in general, lie on the corners of the plate. For many of the plots, one corner of the plate has several poles clustering on it and other corner(s) of the plate have no poles associated with them. In these cases, the corner with more than one associated pole is usually the largest energy corner on the plate, which can be seen by looking at the image of the plate. Also, the corner(s) with no associated poles is usually the lowest energy corner(s). The model generated contour images should, ideally, be identical to the original data plate images. However, there are differences between the two sets of images. These differences demonstrate that the 2-D Prony Model has difficulty in modeling

this data set.

The REs in Table 9 are relatively high to consider the 2-D Prony Model “good” at modeling the plate scattering centers. The larger REs for center angles of $15^\circ \leq \phi \leq 75^\circ$ are an indication that the original assumption that the polar grid is close enough to a square grid in the 2-D frequency plane as if to be treated as on a square grid was not as reasonable as first thought. This issue is investigated in Section 6.3.3 when this polar data is interpolated onto a true square grid and the same examples are shown. For center angles near $\phi = 0^\circ$ or $\phi = 90^\circ$, the large REs can also be attributed to the inability of the damped exponential to model the scattering response (in angle) of an edge near grazing angles.

In order to see if the high RE is dominated by modeling error, noise is added to the data and the RE evaluated for various total SNRs. Figure 77 shows the RE of the data versus the total SNR for total SNRs between -20 and 50 dB, for all three polarizations for $\phi = 0^\circ$ and $\phi = 45^\circ$. Fifty simulations were run every 5 dB and the RE for each SNR is the average RE over all of the simulations run at that SNR. The ‘o’ in the plot at 50 dB is the value of the RE with no noise added to the GTD data (this is the value in Table 9).

From the plots in Figure 77 it can be seen that the REs are near their infinite SNR values around an SNR of 10 dB. From these plots, it can be concluded that the REs are dominated by modeling error for the 15° polar swaths of data. Thus, since the REs are relatively constant for total SNRs over 10 dB, it can be assumed that the parameter estimates are not effected much by noise for total SNRs over 10 dB.

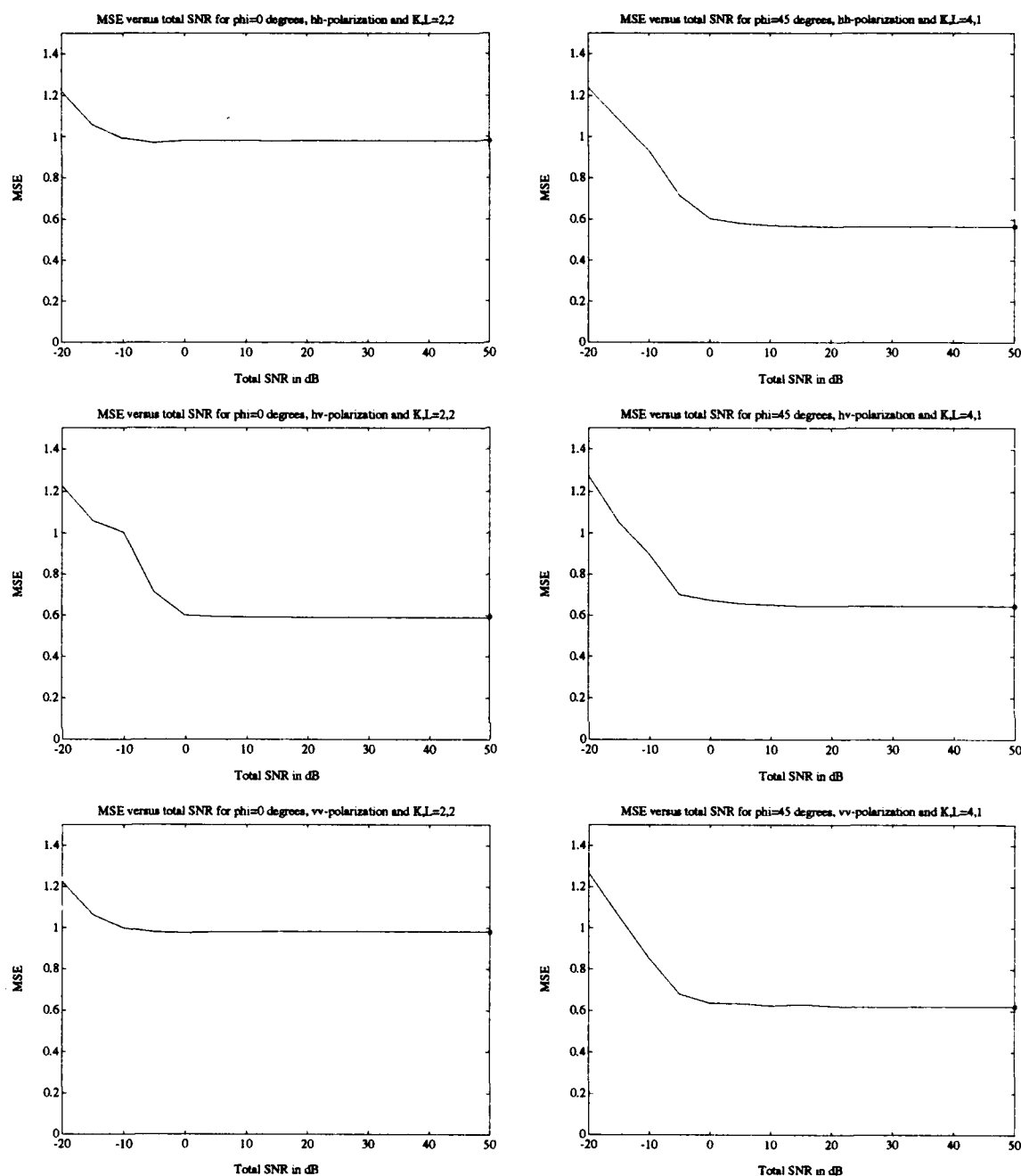


Figure 77: RE versus SNR for noise added to the GTD data of the plate. All three polarizations are shown for $\phi = 0^\circ$ and $\phi = 45^\circ$. The model orders were $Q, K, R, L = 10, 2, 10, 2$ for the $\phi = 0^\circ$ plots and $Q, K, R, L = 10, 4, 10, 1$ for the $\phi = 45^\circ$ plots. The 'o' at 50 dB in each plot is the RE for no noise added to the data for that scenario. The data is a 15° swath of polar data.

This was confirmed by comparing parameter estimates at several total SNRs over 10 dB for multiple noise realizations. These results are not shown here.

6.3.2 Single Polarization Analysis of Fifteen Degree Polar Swaths of Data with Larger Model Orders Chosen

Next the 15° polar swaths of data are again analyzed, with the model orders being chosen larger than in the previous section. This analysis is performed for two reasons. First, the effect of larger model orders on the REs is examined. Second, how larger model orders effect the parameter estimates (specifically, the pole locations) is investigated.

Figures 78 through 86 show the estimated pole locations and model generated contour images for model orders which are larger than the model orders chosen in Figures 63 through 76. Only the six highest energy poles are shown on the estimated poles plots. The contour images are generated by taking the 2-D IFFT of the data generated by the model in Equation 5.2 using all of the parameters estimated by Algorithm Two (not just the six highest energy poles). Table 10 summarizes the model orders chosen and shows the REs with no noise added to the GTD data. The criteria for choosing the model orders was to increase them until the point where there was no significant reduction in RE. Thus, raising the model orders above the values in Table 10 will not significantly reduce the RE.

Examining Figures 78 through 86, and comparing with the corresponding figures in Section 6.3.1, it can be seen that choosing larger model orders allows the model generated images, in general, to appear closer to the original data images. This

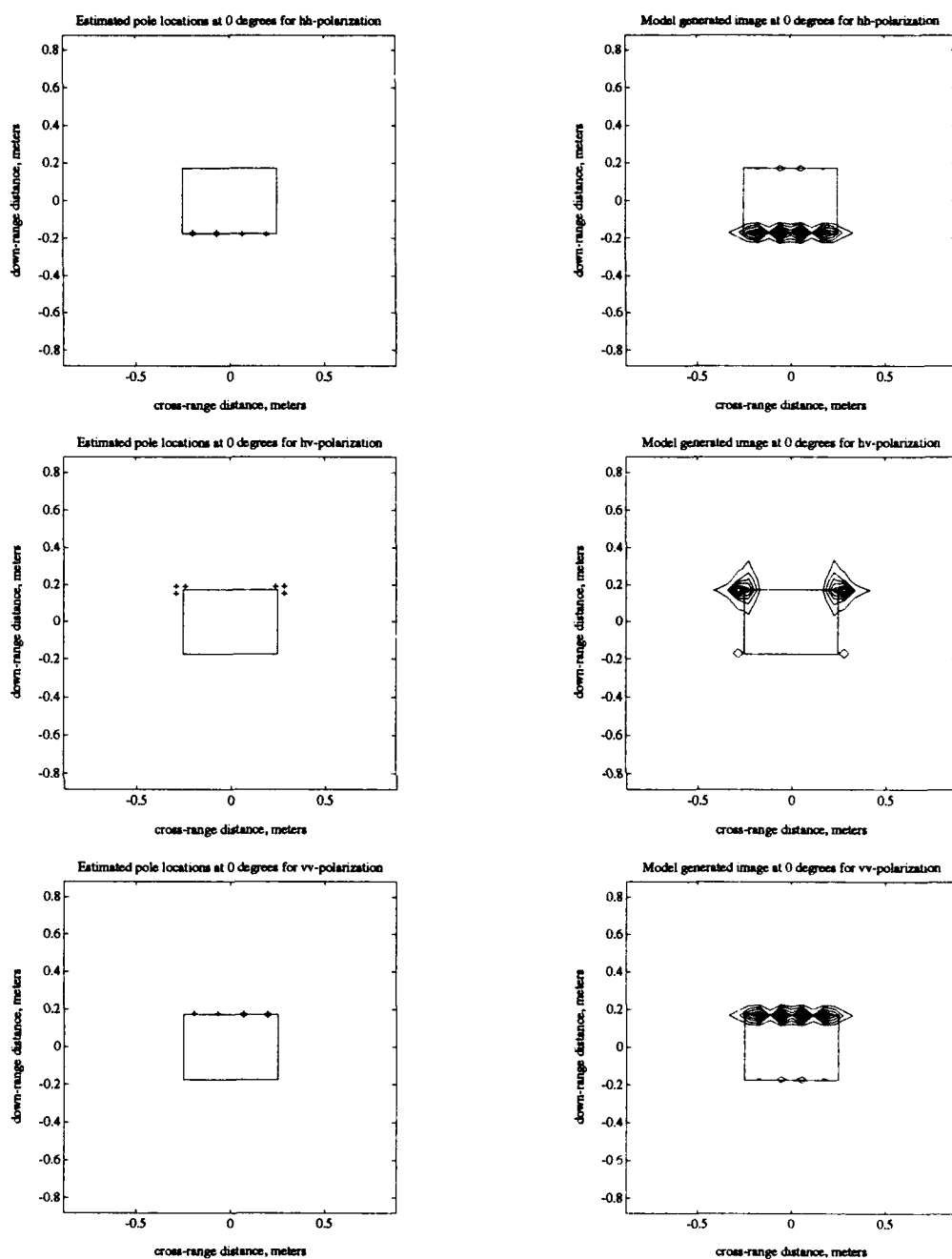


Figure 78: Single polarization inclined plate example for a 15° swath of polar data centered around 0° . Pole locations were estimated by Algorithm Two for hh , hv and vv polarizations. Estimated pole locations are designated by '+'s, where only the six highest energy poles are shown. Contour images of the plate are shown for hh , hv and vv -polarizations. Model orders were $Q, K, R, L = 10, 4, 10, 4$.

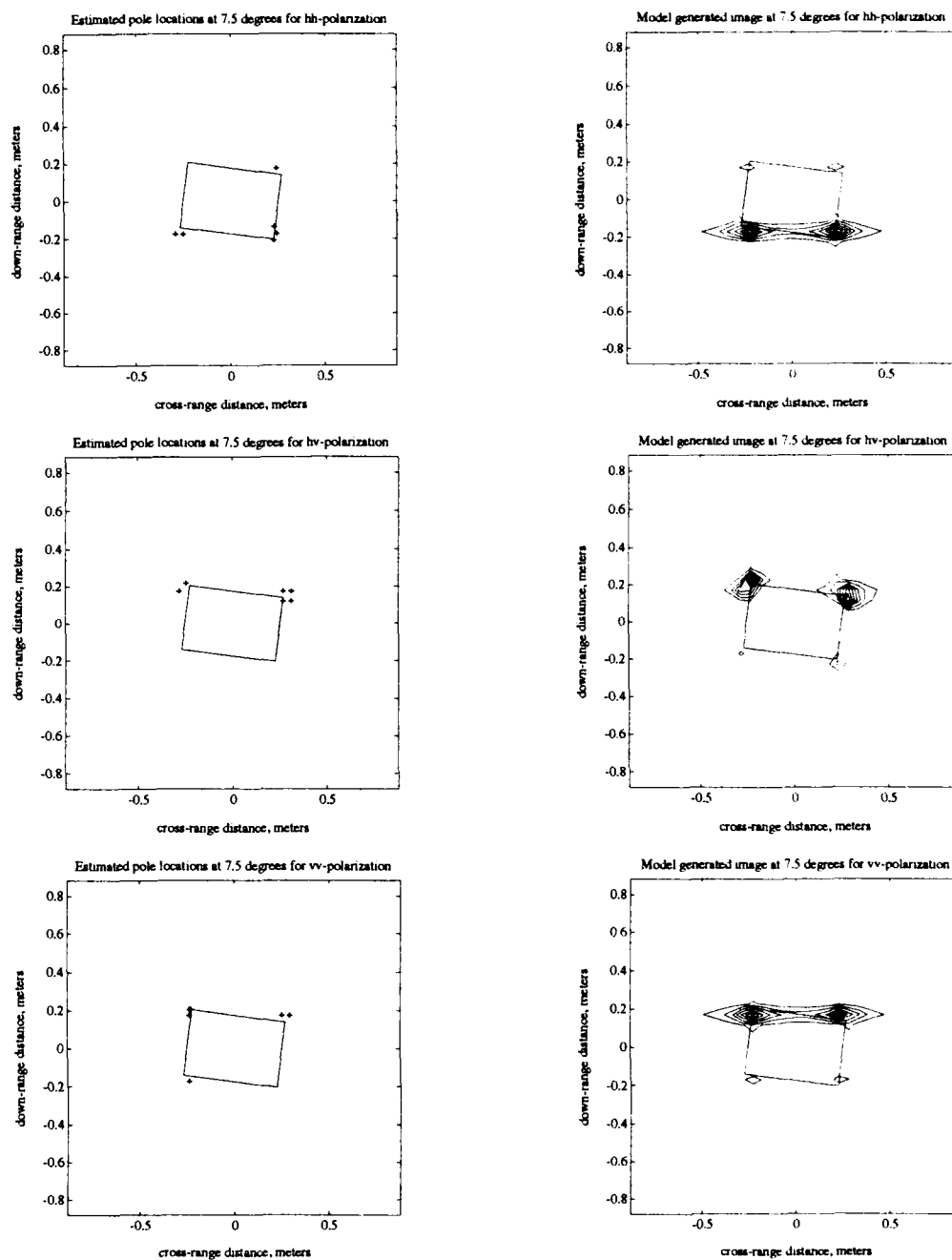


Figure 79: Single polarization inclined plate example for a 15° swath of polar data centered around 7.5° . Pole locations were estimated by Algorithm Two for hh , hv and vv polarizations. Estimated pole locations by are designated by '+'s, where only the six highest energy poles are shown. Contour images of the plate are shown for hh , hv and vv -polarizations. Model orders were $Q, K, R, L = 10, 6, 10, 4$.

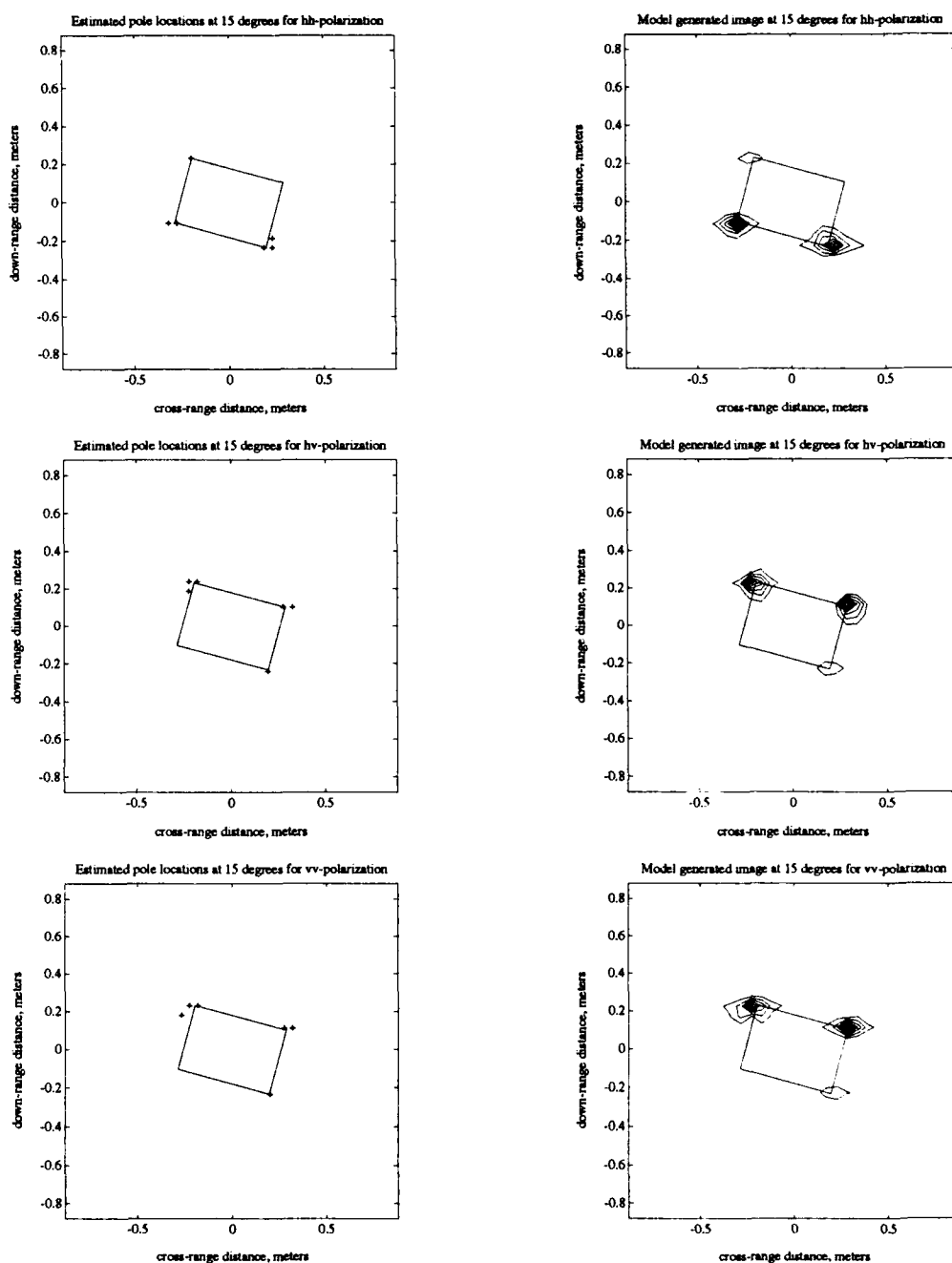


Figure 80: Single polarization inclined plate example for a 15° swath of polar data centered around 15° . Pole locations were estimated by Algorithm Two for hh , hv and vv polarizations. Estimated pole locations by are designated by '+'s, where only the six highest energy poles are shown. Contour images of the plate are shown for hh , hv and vv -polarizations. Model orders were $Q, K, R, L = 10, 6, 10, 4$.

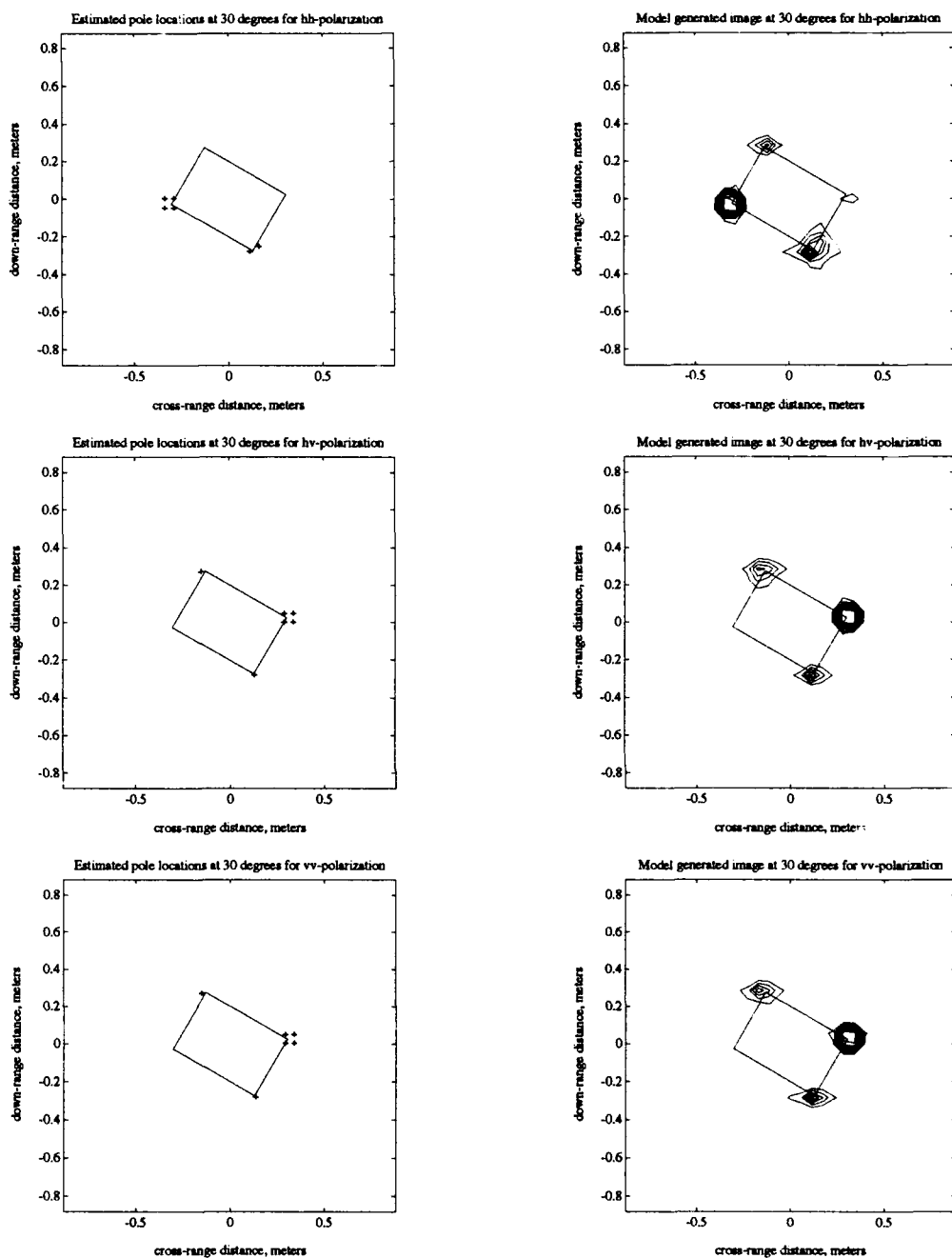


Figure 81: Single polarization inclined plate example for a 15° swath of polar data centered around 30° . Pole locations were estimated by Algorithm Two for hh , hv and vv polarizations. Estimated pole locations by are designated by '+'s, where only the six highest energy poles are shown. Contour images of the plate are shown for hh , hv and vv -polarizations. Model orders were $Q, K, R, L = 10, 6, 10, 4$.

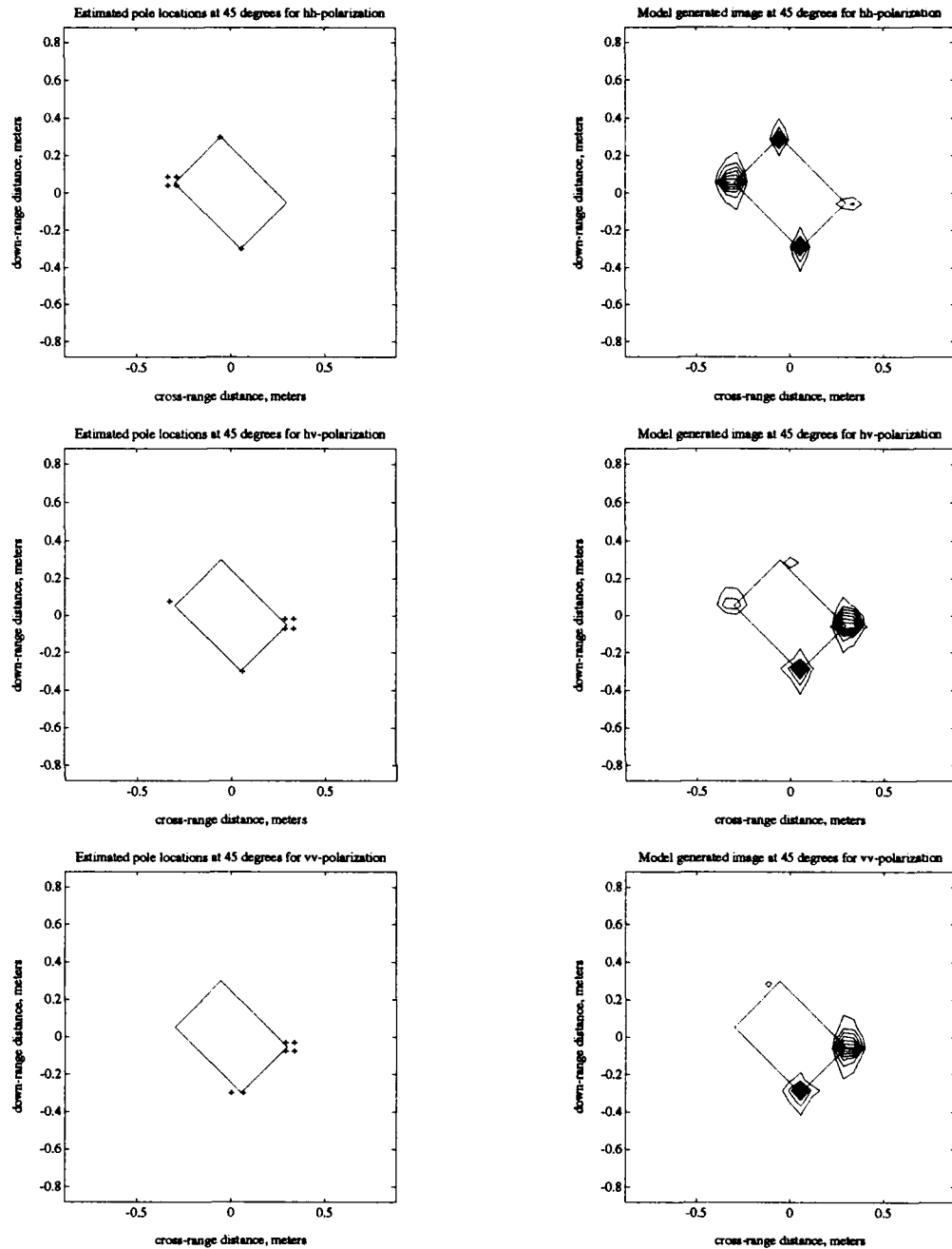


Figure 82: Single polarization inclined plate example for a 15° swath of polar data centered around 45° . Pole locations were estimated by Algorithm Two for hh , hv and vv polarizations. Estimated pole locations by are designated by '+'s, where only the six highest energy poles are shown. Contour images of the plate are shown for hh , hv and vv -polarizations. Model orders were $Q, K, R, L = 10, 6, 10, 4$.

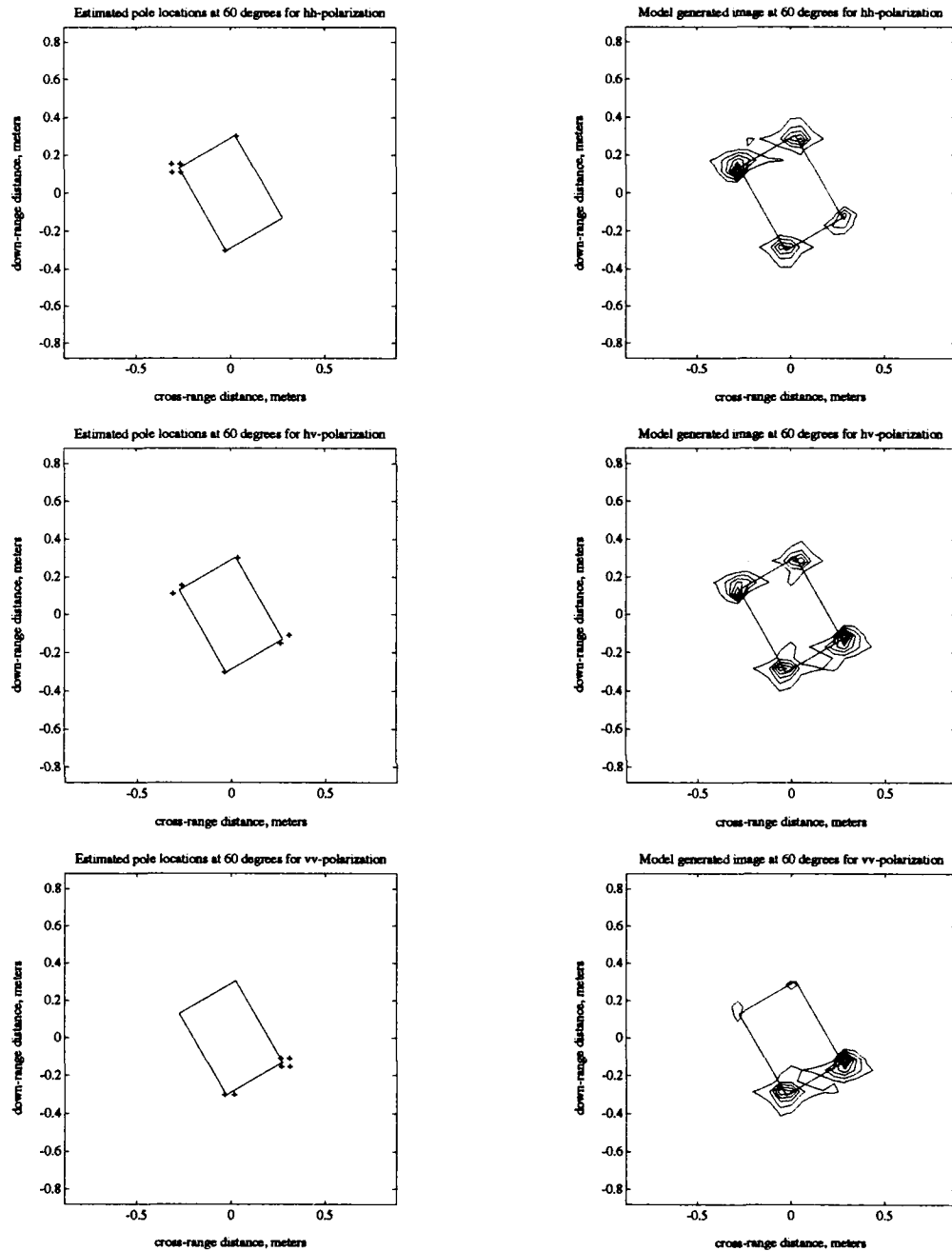


Figure 83: Single polarization inclined plate example for a 15° swath of polar data centered around 60° . Pole locations were estimated by Algorithm Two for hh , hv and vv polarizations. Estimated pole locations by are designated by '+'s, where only the six highest energy poles are shown. Contour images of the plate are shown for hh , hv and vv -polarizations. Model orders were $Q, K, R, L = 10, 6, 10, 4$.

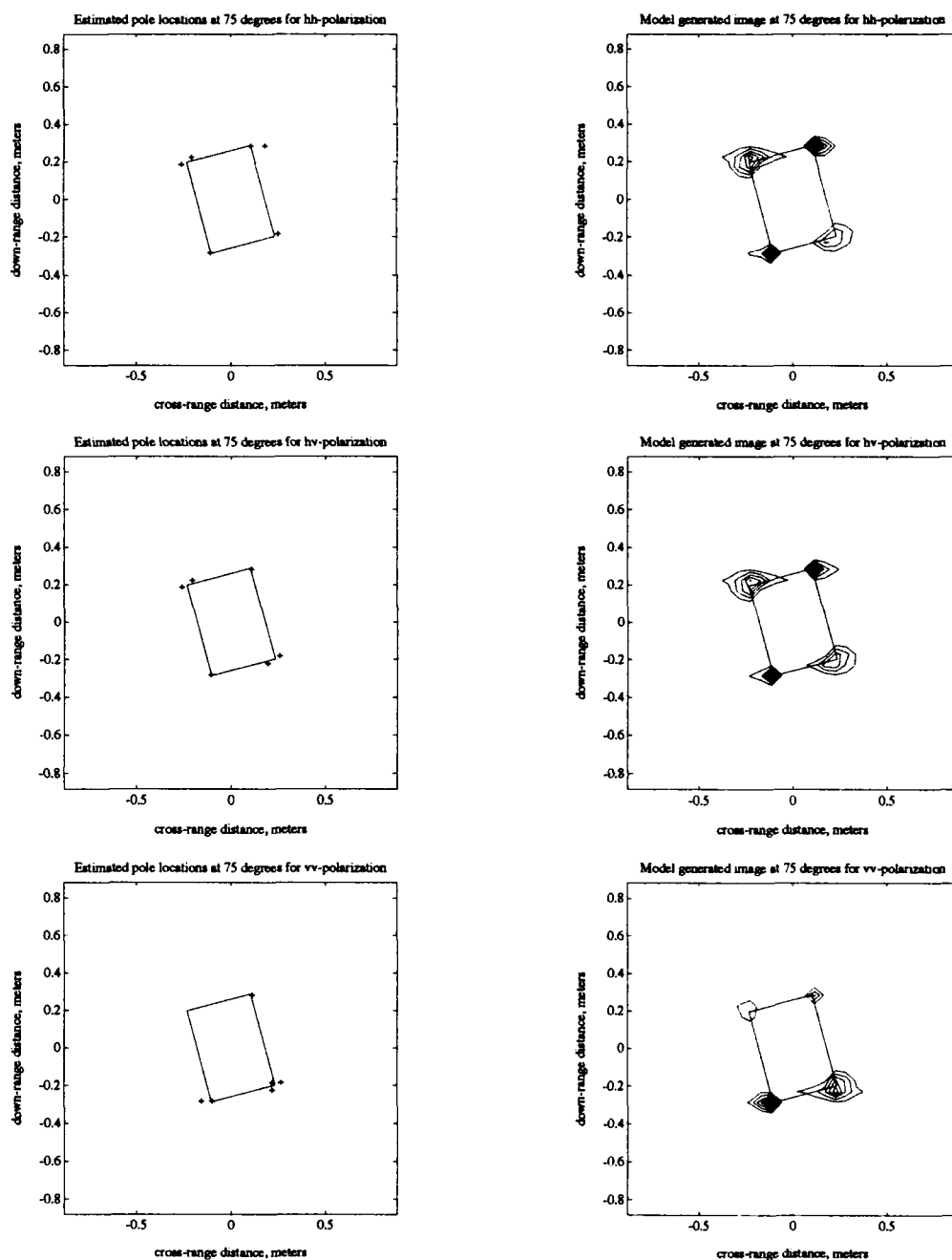


Figure 84: Single polarization inclined plate example for a 15° swath of polar data centered around 75° . Pole locations were estimated by Algorithm Two for hh , hv and vv polarizations. Estimated pole locations by are designated by '+'s, where only the six highest energy poles are shown. Contour images of the plate are shown for hh , hv and vv -polarizations. Model orders were $Q, K, R, L = 10, 6, 10, 4$.

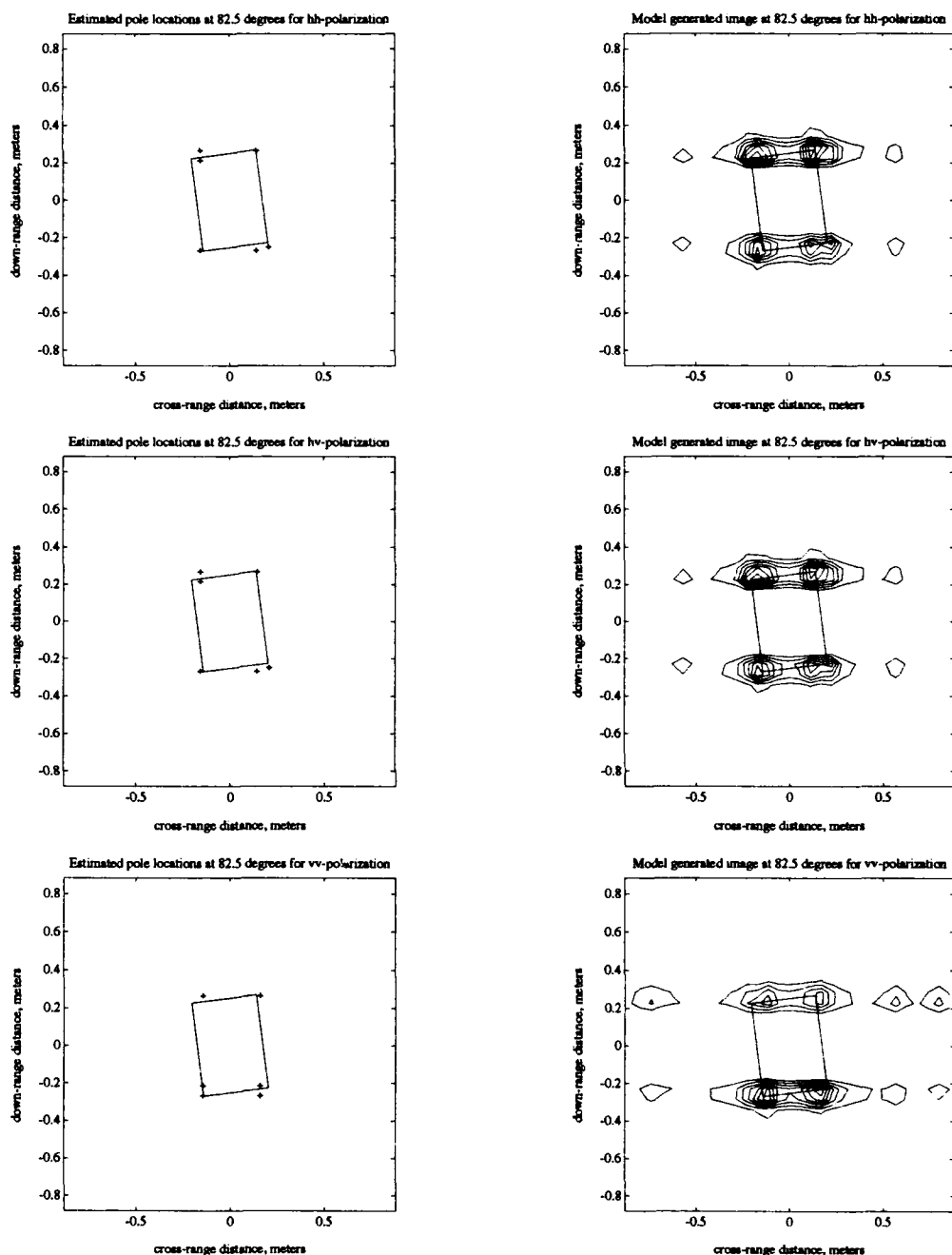


Figure 85: Single polarization inclined plate example for a 15° swath of polar data centered around 82.5° . Pole locations were estimated by Algorithm Two for hh , hv and vv polarizations. Estimated pole locations are designated by '+'s, where only the six highest energy poles are shown. Contour images of the plate are shown for hh , hv and vv -polarizations. Model orders were $Q, K, R, L = 10, 6, 10, 4$.

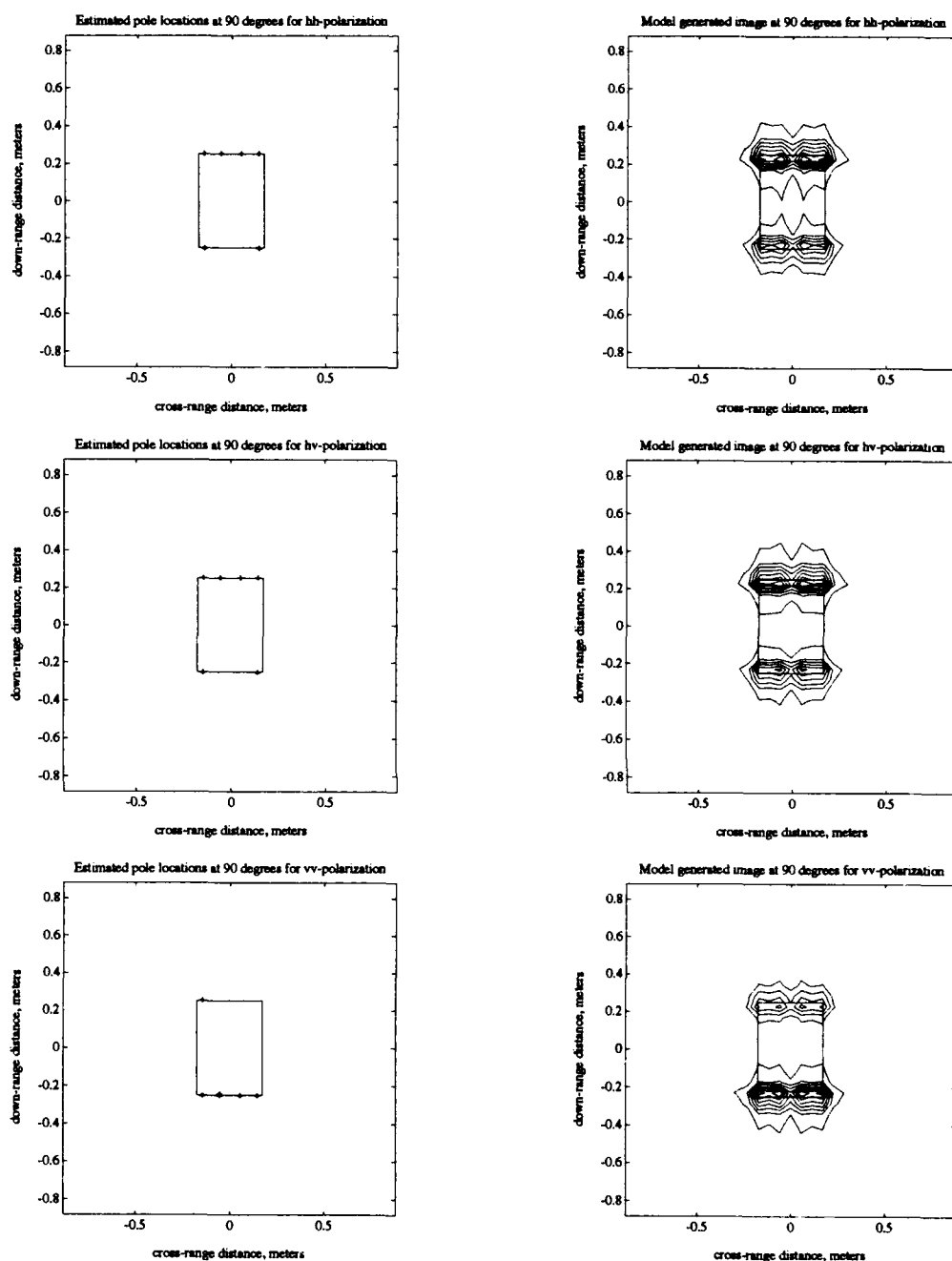


Figure 86: Single polarization inclined plate example for a 15° swath of polar data centered around 90° . Pole locations were estimated by Algorithm Two for hh , hv and vv polarizations. Estimated pole locations by are designated by '+'s, where only the six highest energy poles are shown. Contour images of the plate are shown for hh , hv and vv -polarizations. Model orders were $Q, K, R, L = 10, 4, 10, 4$.

is reflected by the REs in Table 10 which are lower than their respective REs in Table 9. The pole locations in Figures 78 through 86 tend to cluster multiple poles on the largest energy corners or edges. Thus, the larger energy scattering centers on the plate are modeled by several poles, and this reduces the REs.

The use of model orders which are larger than the expected number of scattering centers is deviating from the intent of the 2-D TLS-Prony Technique to model one scattering center by one 2-D mode. Ideally, the choice of model orders should reflect the expected number of scattering centers. However, in cases where the damped exponential does not model the scattering behavior of the scattering centers present in the data, raising the model order will enable the 2-D damped exponential to better model the data.

For this data set (the 15° polar swath of data) there are two reasons why the 2-D damped exponential model does not model the data well. First, for angles near $\phi = 0^\circ$ and $\phi = 90^\circ$, the response is edge dominated and the angular response for these angles is impulsive which is not well modeled by a damped exponential. Second, the initial assumption that the polar data can be used directly by the 2-D TLS-Prony Technique was not as good as first assumed. This is demonstrated in the next section (Section 6.3.3) when this polar data set is interpolated onto a square grid.

Figure 87 shows the RE of the data versus the total SNR for total SNRs between -20 and 50 dB, for all three polarizations for $\phi = 0^\circ$ and $\phi = 45^\circ$. As before, fifty simulations were run every 5 dB and the RE for each SNR is the average RE over all

Table 10: Model orders and relative errors for single polarization results for the scattering from an inclined plate with model orders larger than the model orders in Table 9. The data is a 15° polar swath.

Angle	Model Order; Q, K, R, L	RE (hh)	RE (hv)	RE (vv)
0	10,4,10,4	0.8240	0.1908	0.8249
7.5	10,6,10,4	0.5082	0.3289	0.4934
15	10,6,10,4	0.4679	0.4922	0.4851
30	10,6,10,4	0.3193	0.2869	0.3140
45	10,6,10,4	0.3585	0.3392	0.2501
60	10,6,10,4	0.2313	0.2225	0.2483
75	10,6,10,4	0.3138	0.3214	0.2845
82.5	10,6,10,4	0.4797	0.4526	0.4155
90	10,4,10,4	0.3712	0.3565	0.4147

of the simulations run at that SNR. The 'o' in the plot at 50 dB is the value of the RE with no noise added to the GTD data (this is the value in Table 10). From these RE plots, as was the case for the lower model orders, the REs (and the parameter estimates) are not dependent upon SNR for SNRs over 15 dB. Thus, the REs are dependent upon modeling error for these examples.

6.3.3 Single Polarization Analysis of Square Grids of Data Interpolated from Fifteen Degree Polar Swaths of Data

Next, the 15° sections of data are interpolated from the polar grid to a square grid using the method of Equation 4.27. The square grid data set is 29×29 and is centered around the midpoint of the polar grid, namely, $f_x = \cos(\phi)(10.275\text{GHz})$ and $f_y = \sin(\phi)(10.275\text{GHz})$ where ϕ is the center angle of rotation of the polar

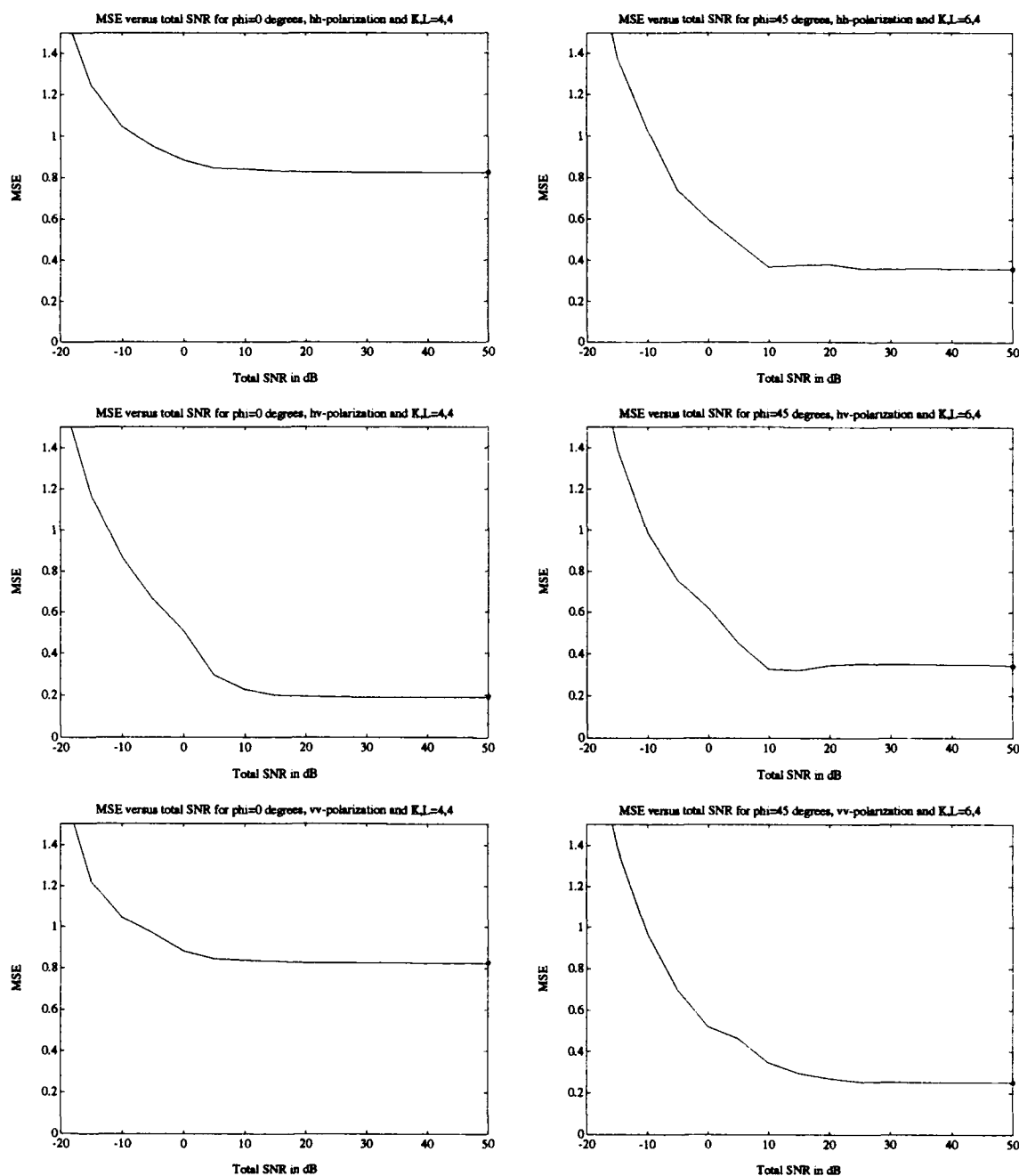


Figure 87: RE versus SNR for noise added to the GTD data of the plate. All three polarizations are shown for $\phi = 0^\circ$ and $\phi = 45^\circ$. The model orders were $Q, K, R, L = 10, 4, 10, 4$ for the $\phi = 0^\circ$ plots and $Q, K, R, L = 10, 6, 10, 4$ for the $\phi = 45^\circ$ plots. The 'o' at 50 dB in each plot is the RE for no noise added to the data for that scenario. The data is a 15° swath of polar data.

data. The steps in the square grid, in each direction, are 0.085 GHz. The square grid is tilted on the 2-D frequency plane, by ϕ , to account for the center angle of rotation (ϕ) of the data set. The local 2-D coordinate system for the square grid data set is designated by rectilinear coordinates (f_x^l, f_y^l) and these are related to the absolute coordinates of the 2-D frequency plane, (f_x, f_y) , which are shown in Figure 61, by

$$f_x^l = f_x \cos \phi - f_y \sin \phi + f_{\text{mid}} \cos \phi \quad (6.2)$$

$$f_y^l = f_x \sin \phi + f_y \cos \phi + f_{\text{mid}} \sin \phi$$

where f_{mid} is the center frequency of the data set, which is 10.275 GHz for this data set and ϕ is the center angle rotation of the polar (and square) grid data sets. Thus the square grid data set lies centered on this local coordinate system which is translated and rotated from the absolute coordinates of the 2-D frequency plane.

The square grid was chosen to be slightly smaller than the polar grid from which it was interpolated so that all of the data points on the square grid lie within the boundaries of the original polar grid. This avoids the requirement to extrapolate for data points on the square grid that would lie outside of the original polar grid. The slightly reduced size of the square grid should have little effects on the resolution capabilities of the 2-D TLS-Prony Technique. As before, the unambiguous range for this scenario is 1.7637 meters in each direction, and this entire range is shown in the figures which follow.

Figures 88 through 101 show the results for the square grid data. As for the polar data based plots, shown for each center angle are three contour images of the

plate, each image corresponding to one of the three polarizations, found by directly using the square grid data in the 2-D IFFT. Also shown are three sets of estimated pole locations, each set corresponding to one of the three polarizations, estimated by Algorithm Two with no noise added to the original data. In the cases where there are more than four estimated poles, only the four highest energy poles are shown in these plots. Along with these plots contour images are shown which were generated from all of the estimated parameters (not just the four highest energy poles). For each plot, the entire unambiguous range is shown. As stated before, all of the contour images shown, in general, are on different magnitude scales. The REs for the square grid examples are given in Table 11.

Since the square grid data is in the form required by the 2-D TLS-Prony Technique, the model orders are chosen to reflect the expected number of scattering centers for the corner dominated scenarios, and slightly larger model orders are used for edge dominated scenarios. Thus, for the corner dominated scenarios, model orders of $Q, K, R, L = 10, 4, 10, 1$ are used; and for edge dominated scenarios, $Q, K, R, L = 10, 4, 10, 2$ and $Q, K, R, L = 10, 2, 10, 2$ are used.

Figures 88 through 101 show the results for the square grid data. Comparing these results with the results for the 15° polar grid data, the original data images for the square grid data are of slightly different form than the corresponding images for the 15° polar grid data. The images for the square grid data are considered more representative since the 2-D IFFT requires data on a square grid, not a polar grid. Also, the estimated pole locations are, in general, closer to the corners of the plate

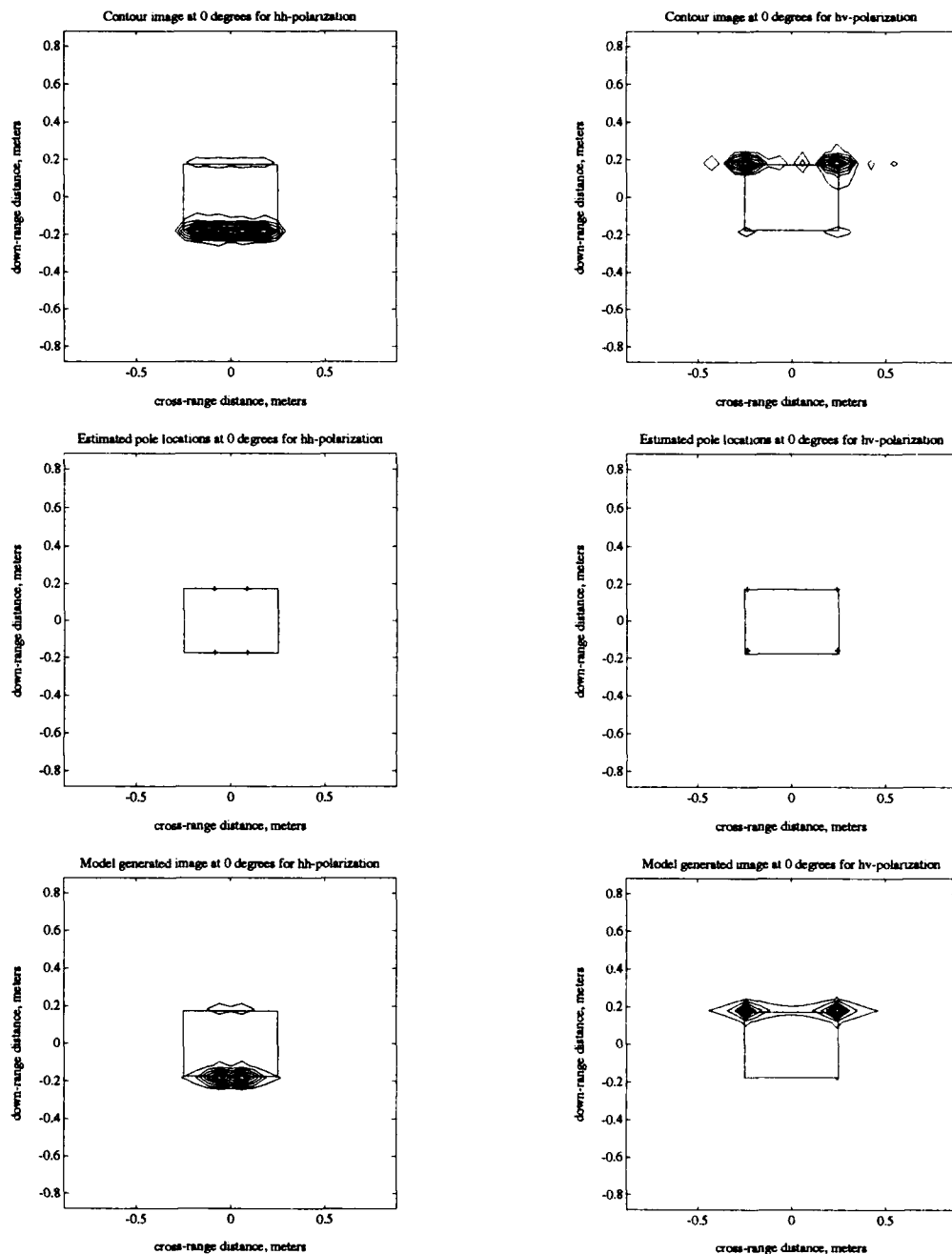


Figure 88: Single polarization inclined plate example for a square grid (from 15° polar) of data centered around 0° . Contour images, estimated pole locations and model generated images are shown for hh and hv -polarizations. Pole locations were estimated by Algorithm Two. Model orders were $Q, K, R, L = 10, 2, 10, 2$.

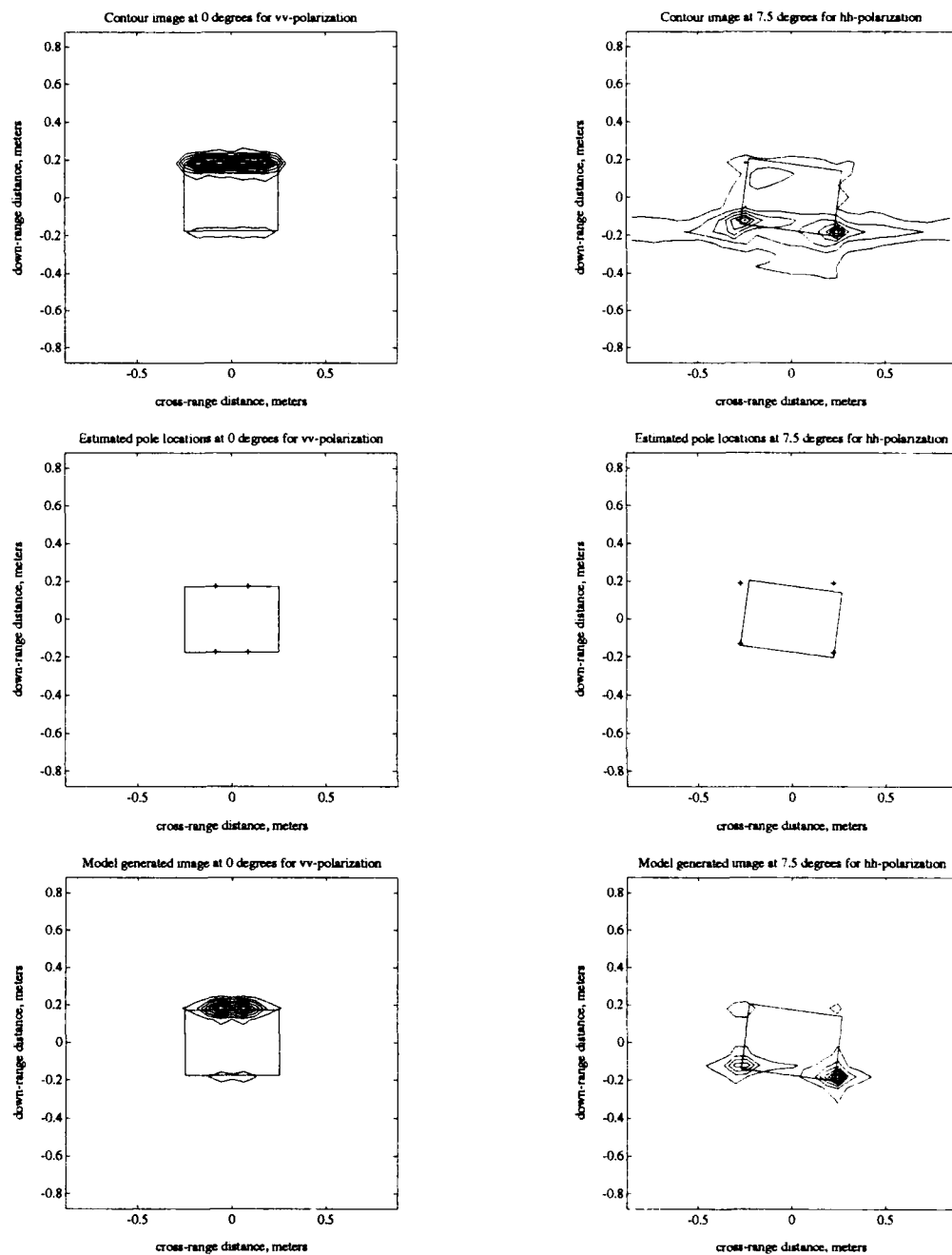


Figure 89: Single polarization inclined plate example for a square grid (from 15° polar) of data centered around 0° and 7.5° . Contour images, estimated pole locations and model generated contour images of the plate are shown for vv -polarization at 0° and hh polarization at 7.5° . Pole locations were estimated by Algorithm Two. Model orders were $Q, K, R, L = 10, 2, 10, 2$ for 0° and $Q, K, R, L = 10, 4, 10, 2$ for 7.5° .

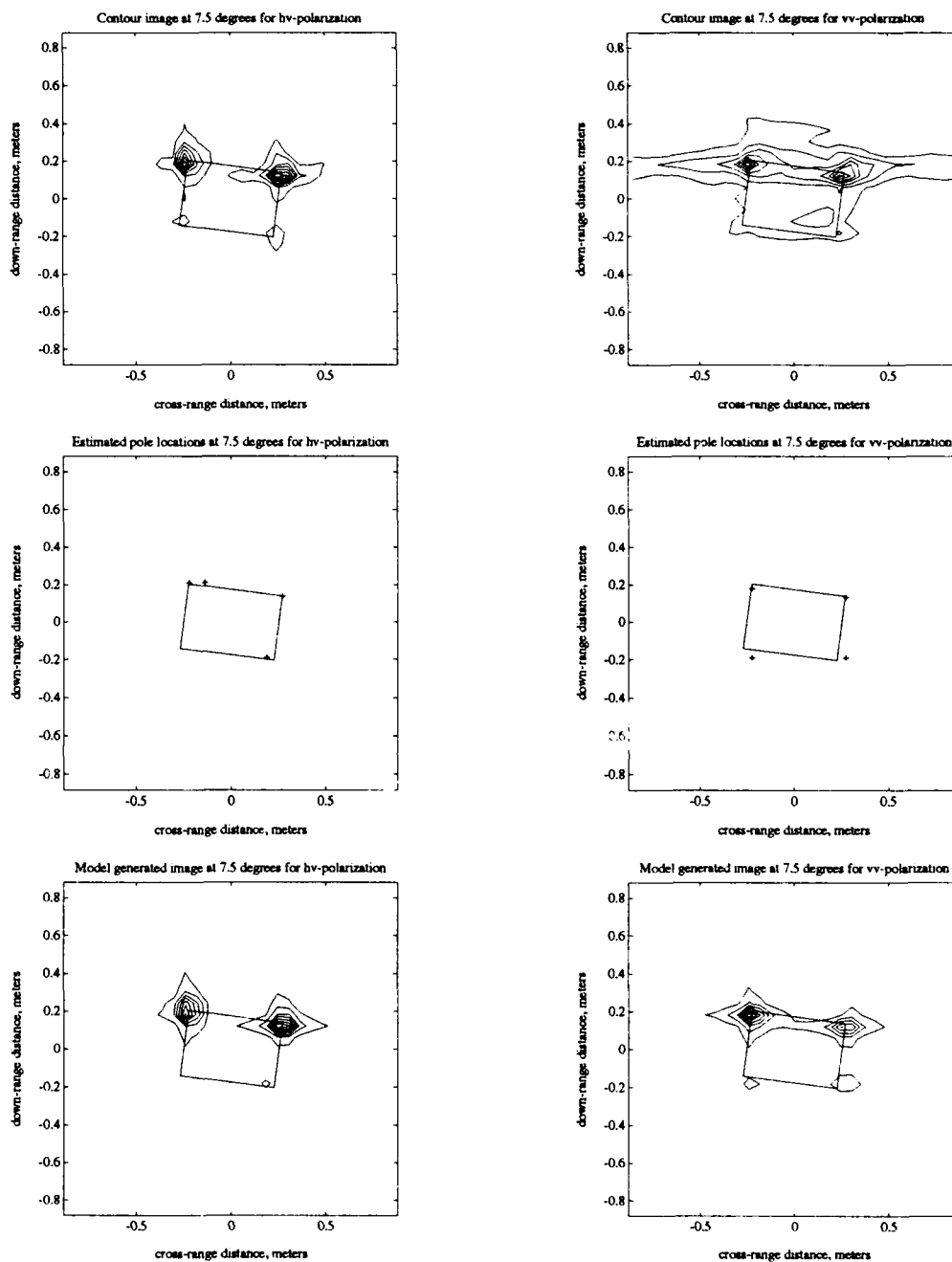


Figure 90: Single polarization inclined plate example for a square grid (from 15° polar) of data centered around 7.5° . Contour images, estimated pole locations and model generated images are shown for hh and vv -polarizations. Pole locations were estimated by Algorithm Two. Model orders were $Q, K, R, L = 10, 4, 10, 2$.

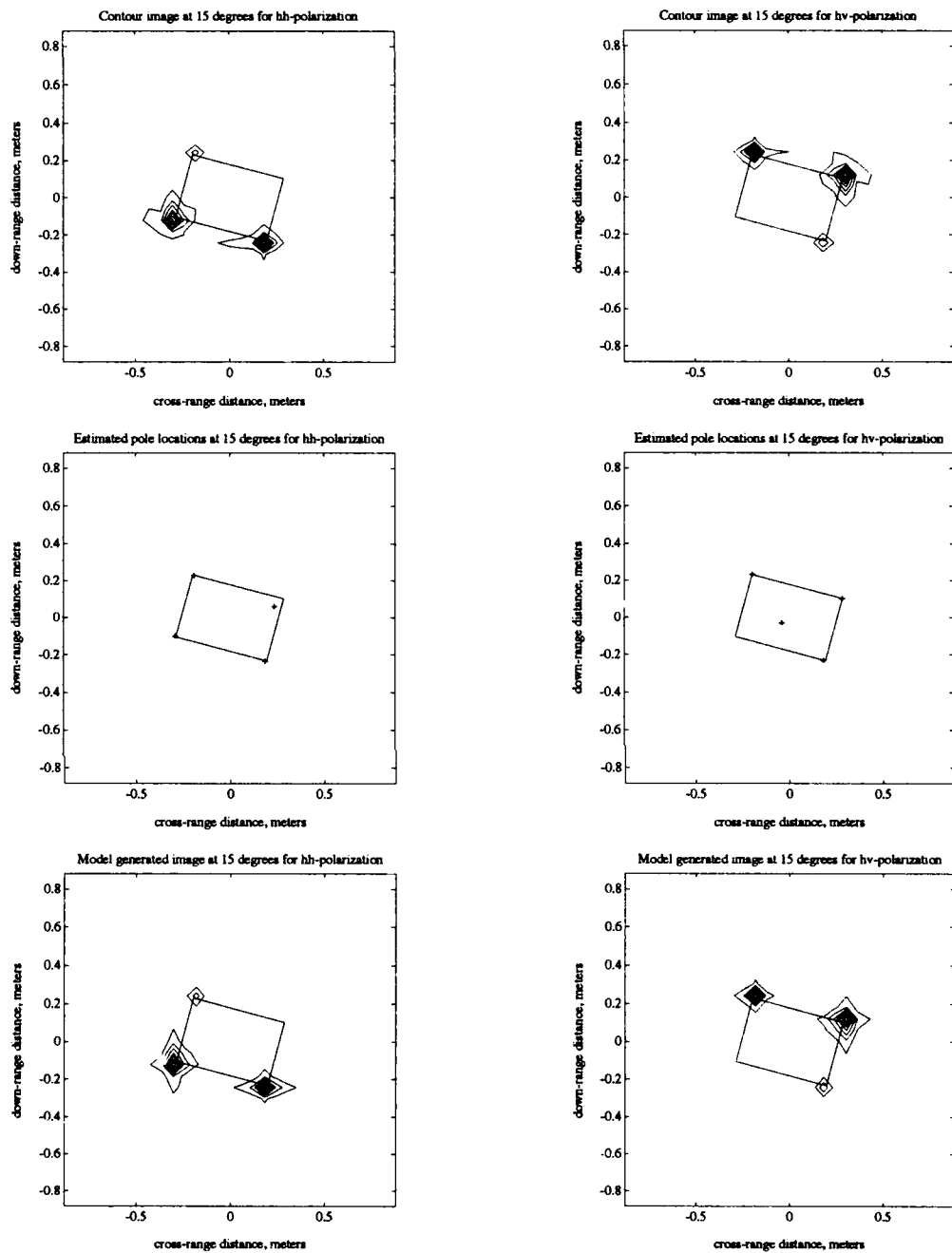


Figure 91: Single polarization inclined plate example for a square grid (from 15° polar) of data centered around 15°. Contour images, estimated pole locations and model generated images are shown for hh and hv -polarizations. Pole locations were estimated by Algorithm Two. Model orders were $Q, K, R, L = 10, 4, 10, 1$.

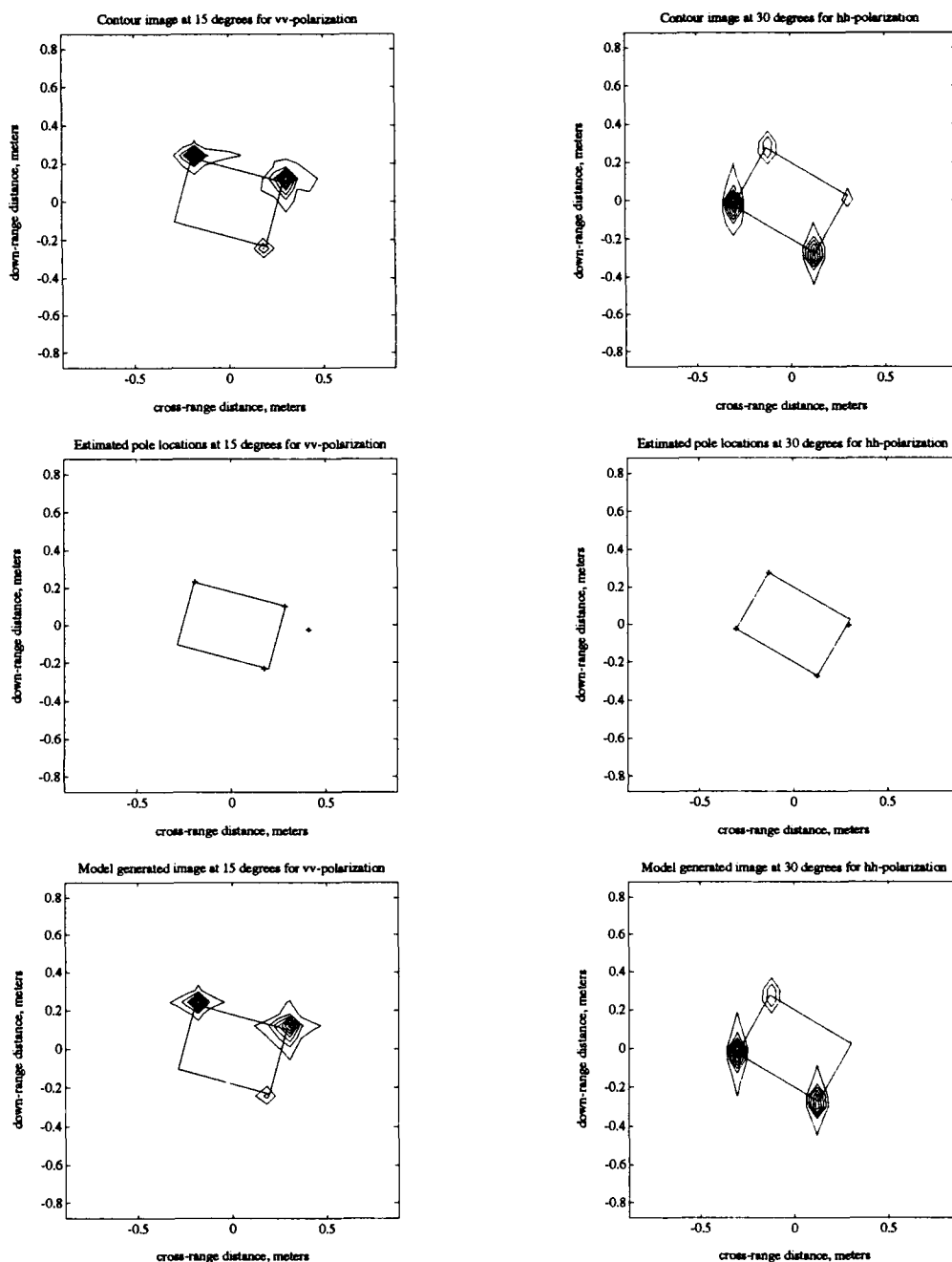


Figure 92: Single polarization inclined plate example for a square grid (from 15° polar) of data centered around 15° and 30°. Contour images, estimated pole locations and model generated contour images of the plate are shown for *vv*-polarization at 15° and *hh* polarization at 30°. Pole locations were estimated by Algorithm Two. Model orders were $Q, K, R, L = 10, 4, 10, 1$ for 15° and 30°.

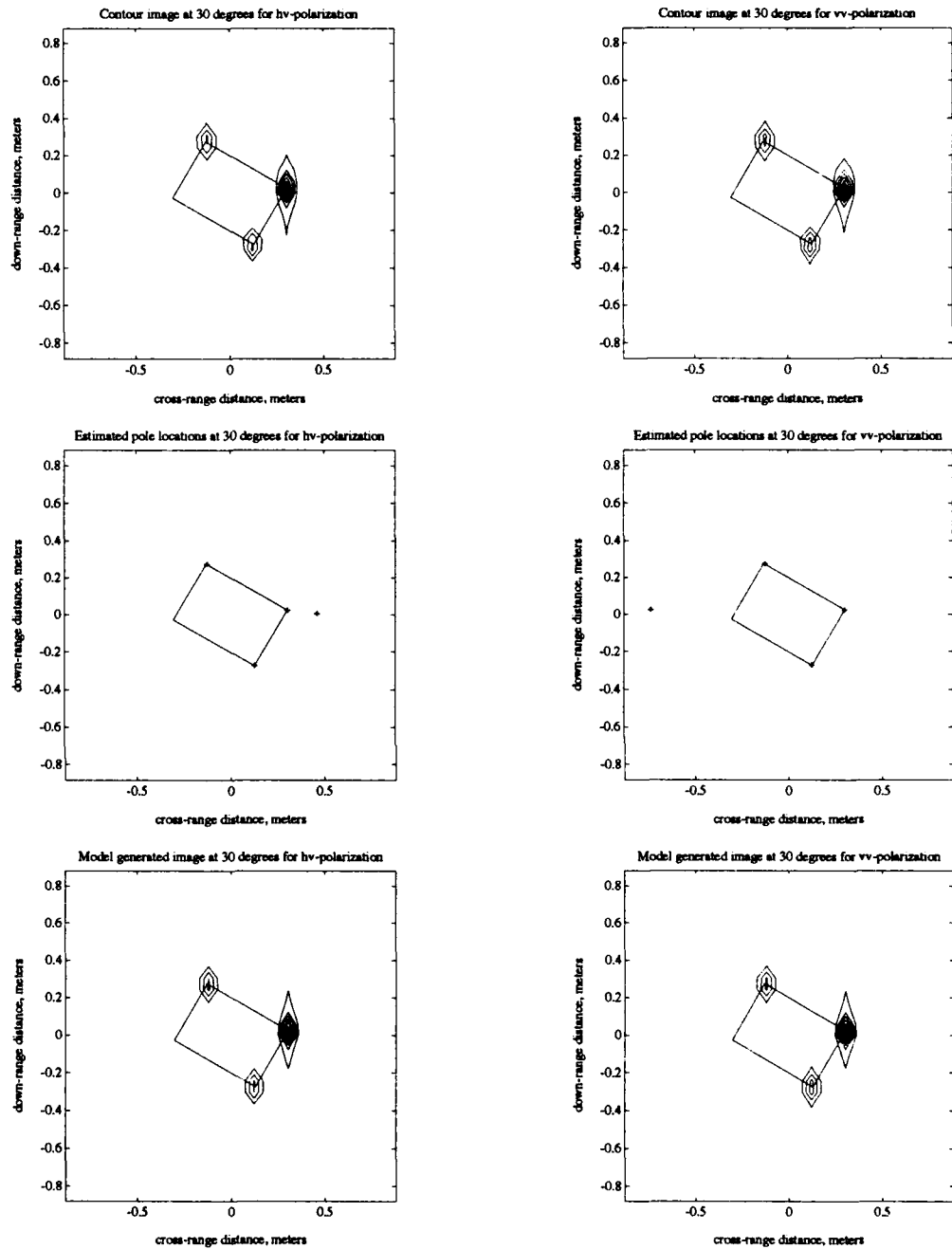


Figure 93: Single polarization inclined plate example for a square grid (from 15° polar) of data centered around 30°. Contour images, estimated pole locations and model generated images are shown for hh and hv -polarizations. Pole locations were estimated by Algorithm Two. Model orders were $Q, K, R, L = 10, 4, 10, 1$.

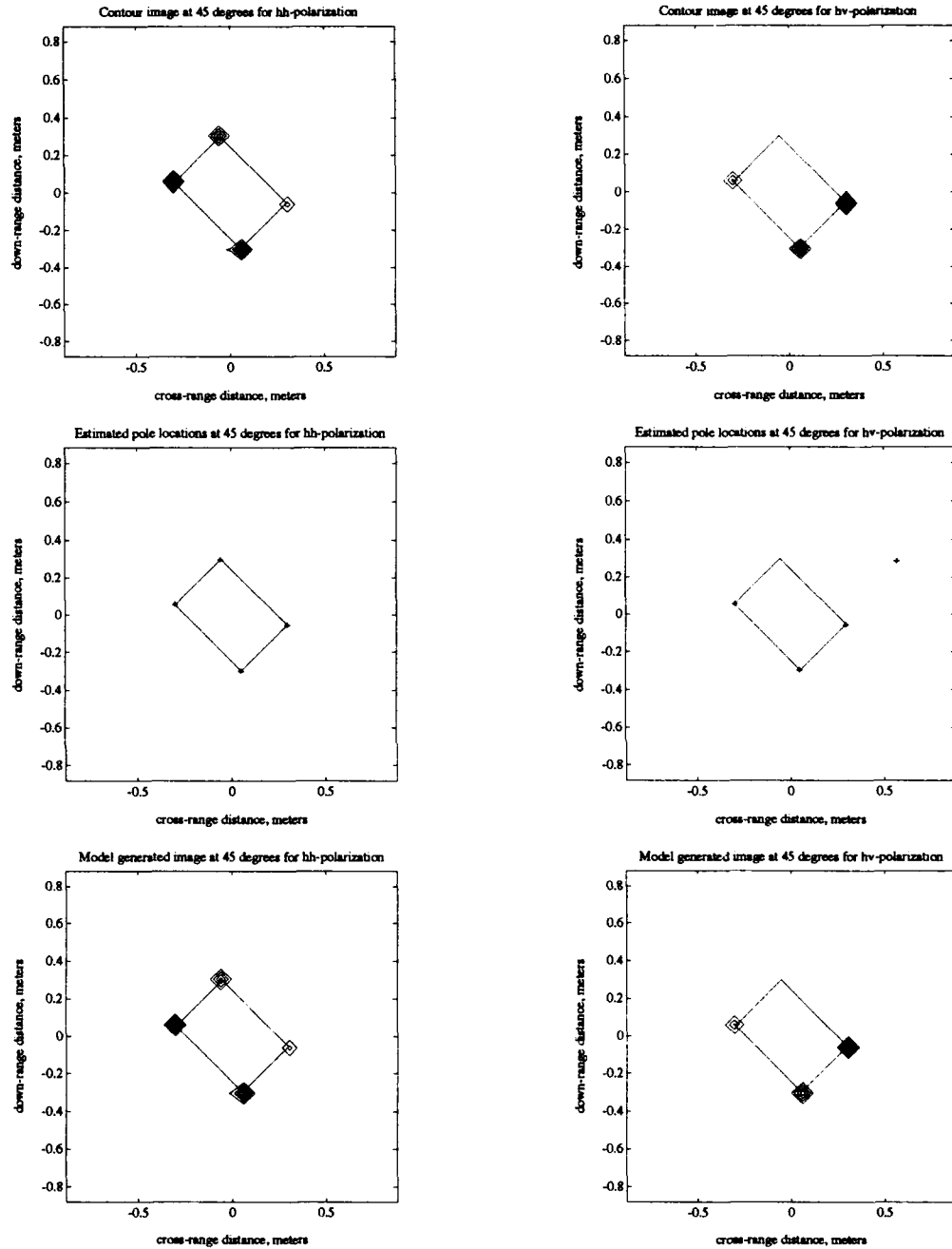


Figure 94: Single polarization inclined plate example for a square grid (from 15° polar) of data centered around 45°. Contour images, estimated pole locations and model generated images are shown for hh and vv -polarizations. Pole locations were estimated by Algorithm Two. Model orders were $Q, K, R, L = 10, 4, 10, 1$.

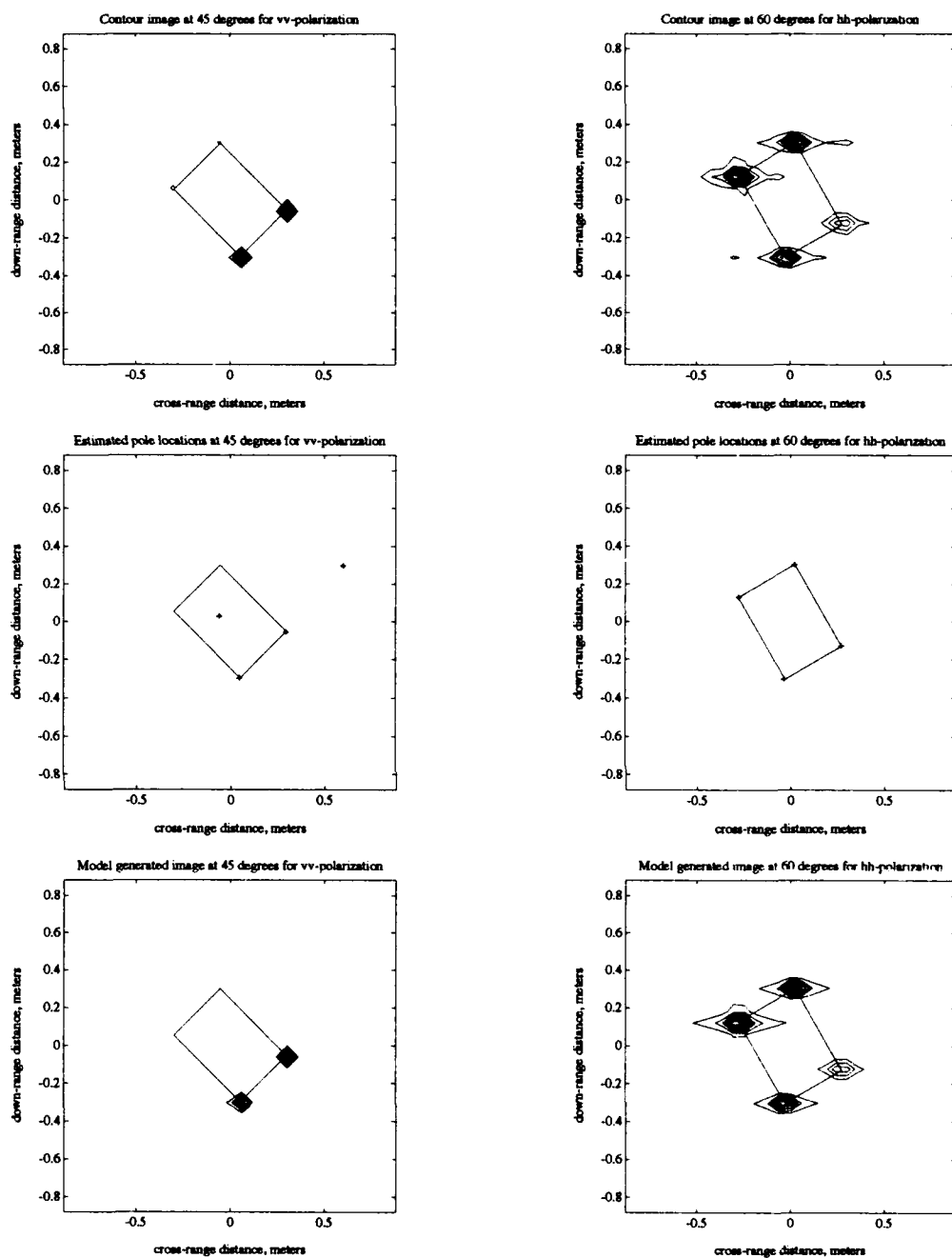


Figure 95: Single polarization inclined plate example for a square grid (from 15° polar) of data centered around 45° and 60° . Contour images, estimated pole locations and model generated contour images of the plate are shown for vv -polarization at 45° and hh polarization at 60° . Pole locations were estimated by Algorithm Two. Model orders were $Q, K, R, L = 10, 4, 10, 1$ for 45° and 60° .

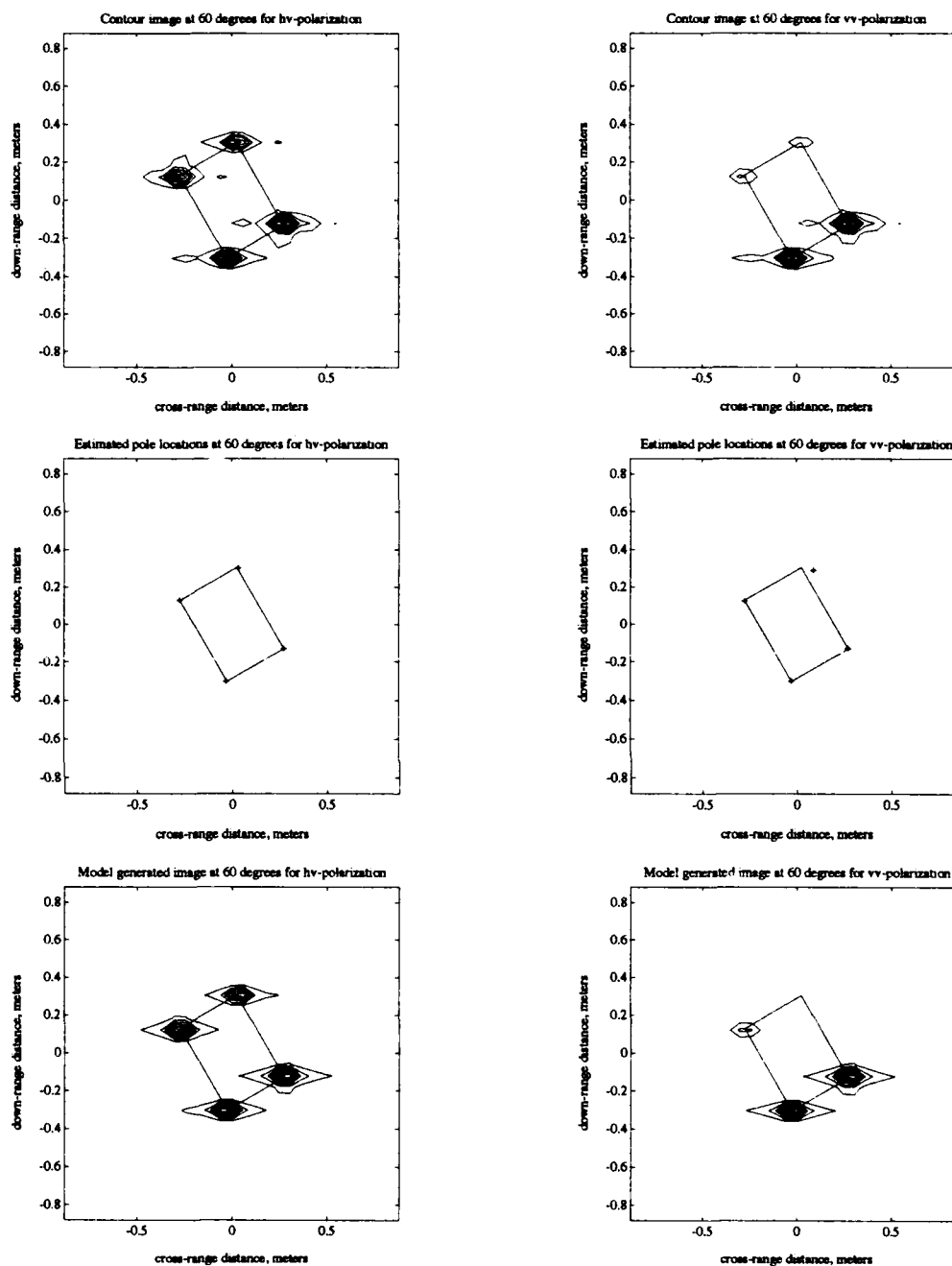


Figure 96: Single polarization inclined plate example for a square grid (from 15° polar) of data centered around 60° . Contour images, estimated pole locations and model generated images are shown for hh and vv -polarizations. Pole locations were estimated by Algorithm Two. Model orders were $Q, K, R, L = 10, 4, 10, 1$.

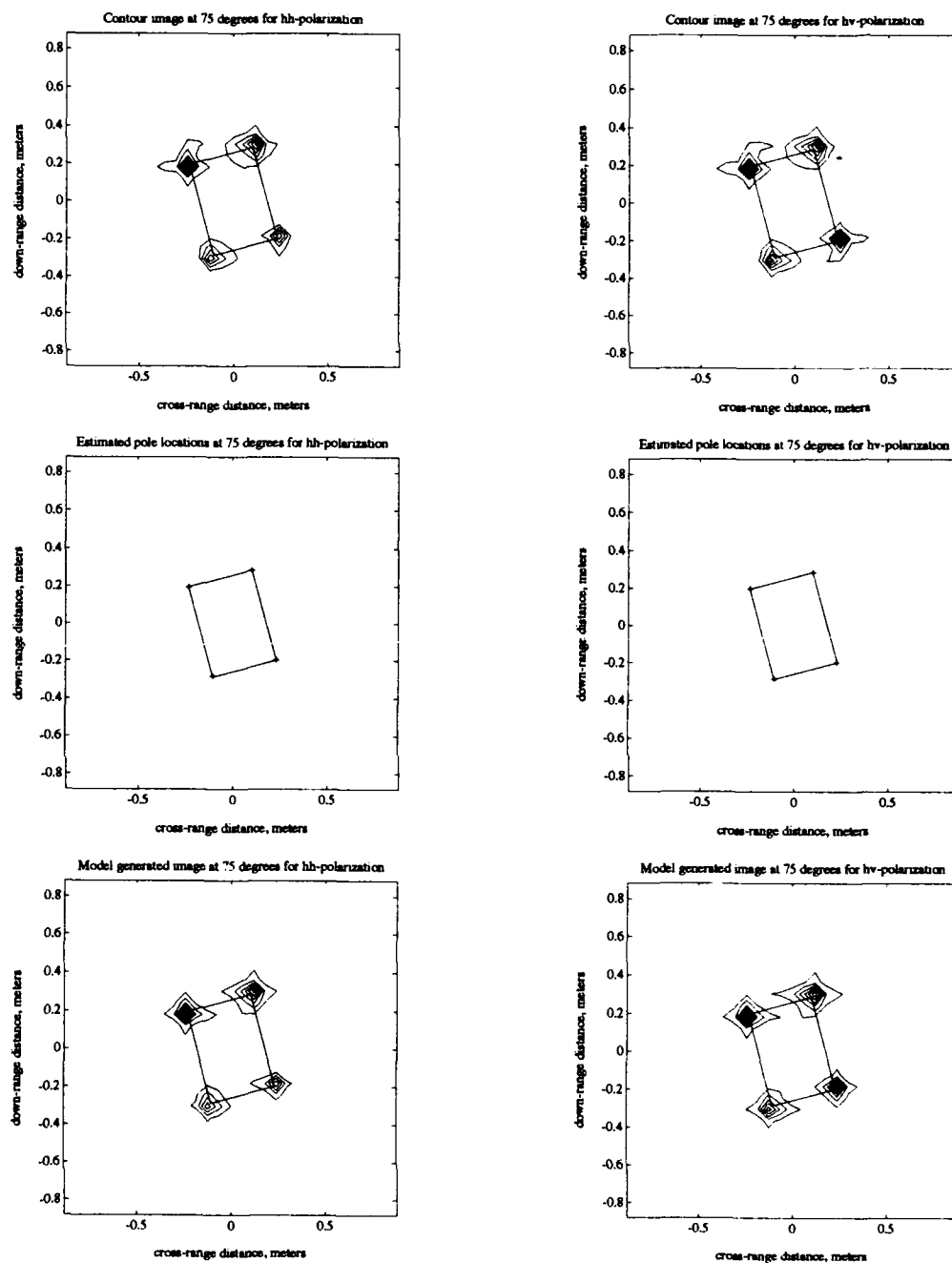


Figure 97: Single polarization inclined plate example for a square grid (from 15° polar) of data centered around 75° . Contour images, estimated pole locations and model generated images are shown for hh and hv -polarizations. Pole locations were estimated by Algorithm Two. Model orders were $Q, K, R, L = 10, 4, 10, 1$.

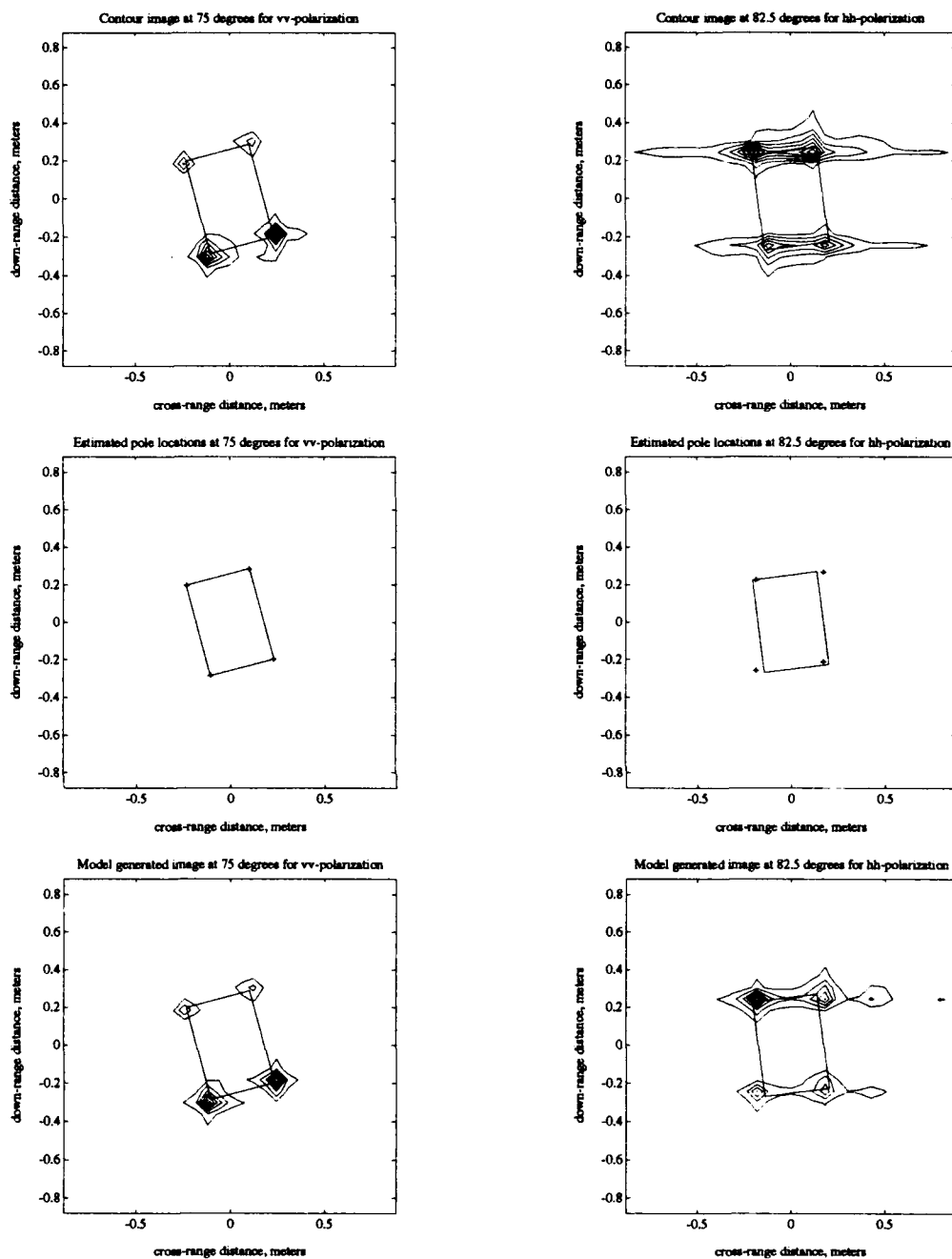


Figure 98: Single polarization inclined plate example for a square grid (from 15° polar) of data centered around 75° and 82.5° . Contour images, estimated pole locations and model generated contour images of the plate are shown for vv -polarization at 75° and hh polarization at 82.5° . Pole locations were estimated by Algorithm Two. Model orders were $Q, K, R, L = 10, 4, 10, 1$ for 75° and $Q, K, R, L = 10, 4, 10, 2$ for 82.5° .

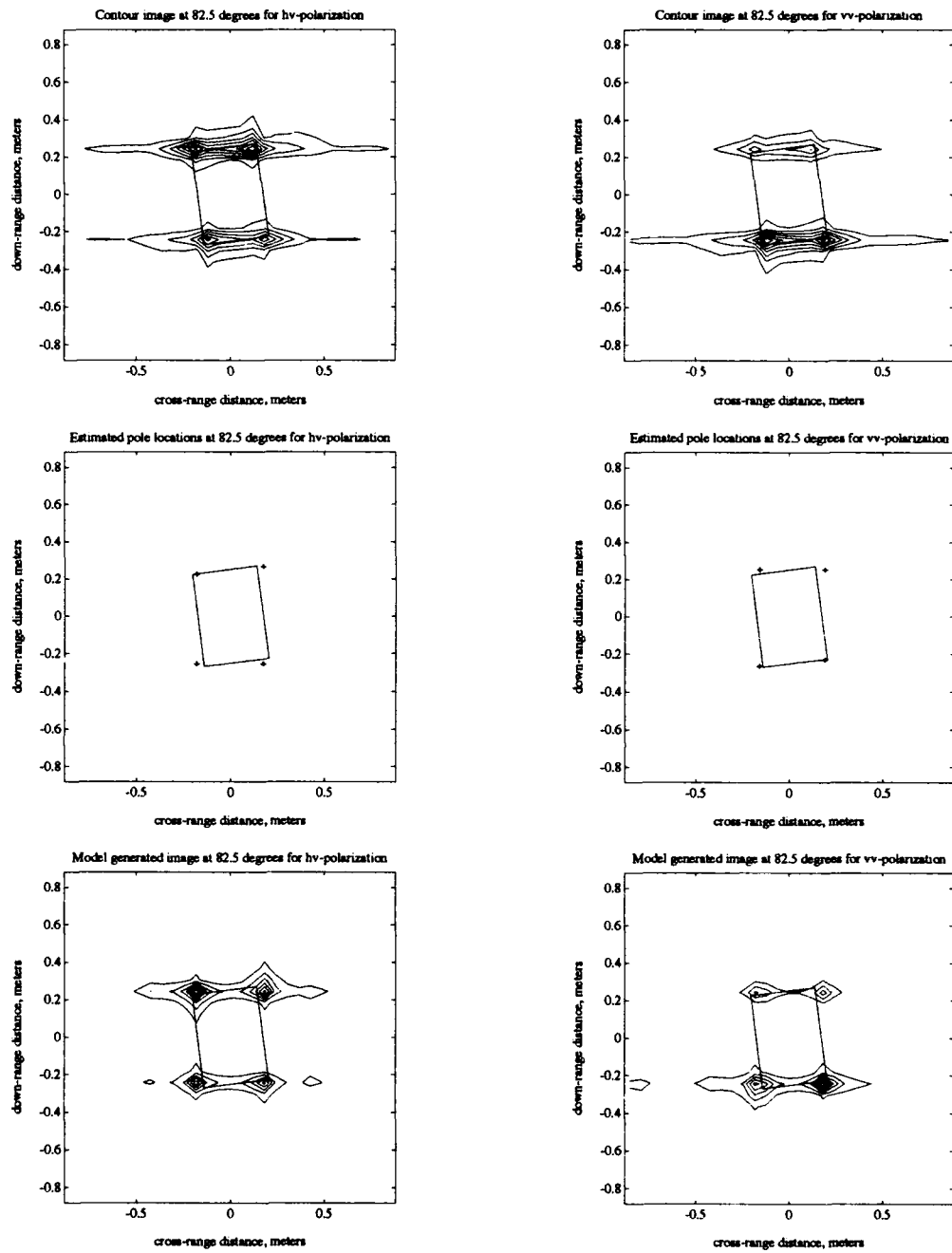


Figure 99: Single polarization inclined plate example for a square grid (from 15° polar) of data centered around 82.5° . Contour images, estimated pole locations and model generated images are shown for hh and hv -polarizations. Pole locations were estimated by Algorithm Two. Model orders were $Q, K, R, L = 10, 4, 10, 2$.

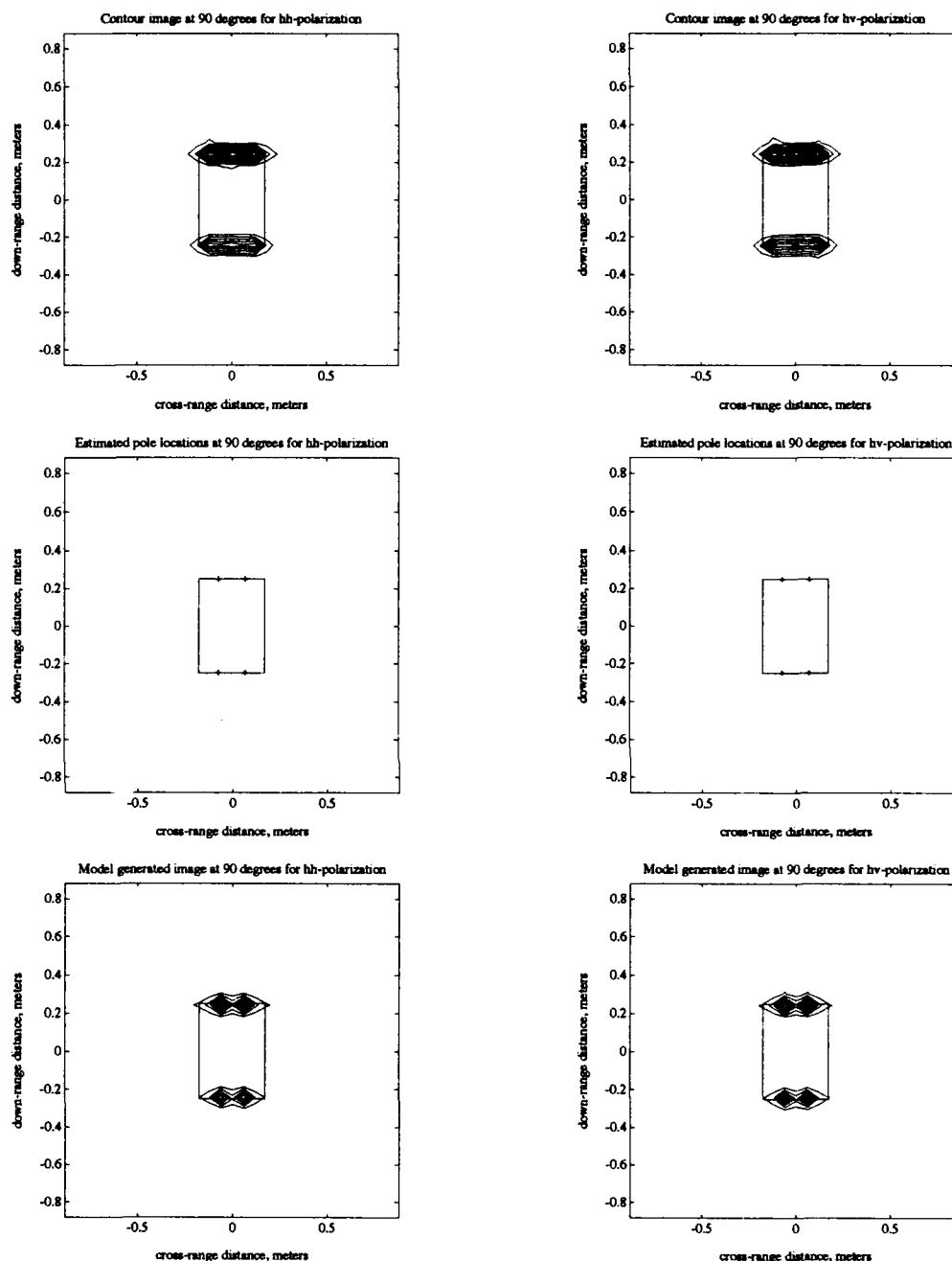


Figure 100: Single polarization inclined plate example for a square grid (from 15° polar) of data centered around 90° . Contour images, estimated pole locations and model generated images are shown for hh and hv -polarizations. Pole locations were estimated by Algorithm Two. Model orders were $Q, K, R, L = 10, 2, 10, 2$.

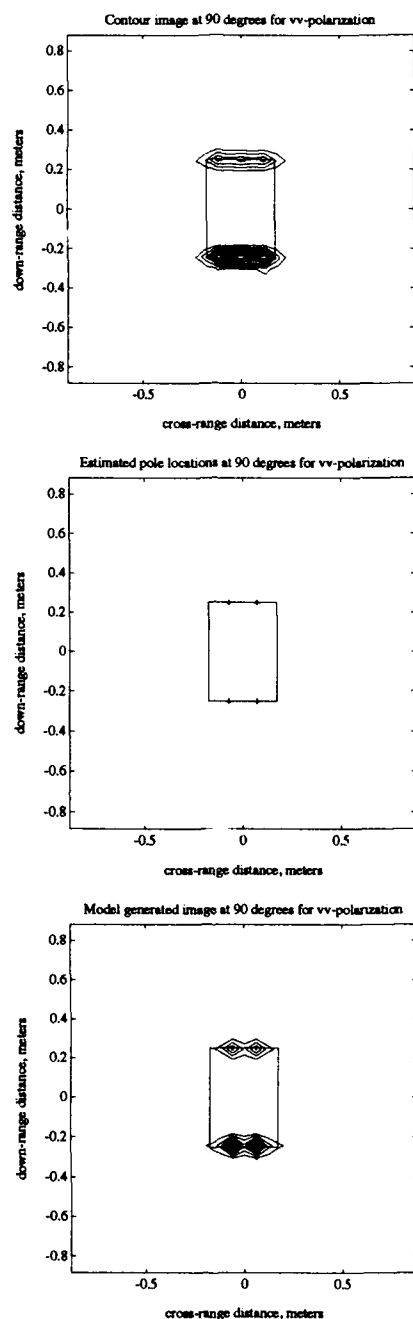


Figure 101: Single polarization inclined plate example for a square grid (from 15° polar) of data centered around 90° . Contour images, estimated pole locations and model generated images are shown for vv -polarization. Pole locations were estimated by Algorithm Two. Model orders were $Q, K, R, L = 10, 2, 10, 2$.

Table 11: Model orders and relative errors for single polarization results for the scattering from an inclined plate. The data lies on a square grid (from 15° polar swath).

Angle	Model Order; Q, K, R, L	RE (hh)	RE (hv)	RE (vv)
0	10,2,10,2	0.9722	0.5494	0.9722
7.5	10,4,10,2	0.7381	0.3531	0.7189
15	10,4,10,1	0.3805	0.3204	0.3593
30	10,4,10,1	0.3452	0.3206	0.3217
45	10,4,10,1	0.3147	0.3286	0.3620
60	10,4,10,1	0.3163	0.3164	0.3308
75	10,4,10,1	0.3091	0.3219	0.3210
82.5	10,4,10,2	0.6126	0.7008	0.6794
90	10,2,10,2	0.9084	0.9090	0.9130

than the corresponding estimated pole locations for the 15° polar grid data.

As before, noise was added to the data, and the RE versus total SNR is shown in Figure 102. As with the polar data scenarios, the REs (and the parameter estimates) are not very dependent upon SNR for SNRs over 10 dB.

From the results in Table 11 it can be seen that interpolating the data to a square grid, in general, reduces the RE. Part of the remaining RE can be attributed to interpolation error while other factors which add to the RE include estimation error and modeling error as discussed in Chapter III. An alternate interpolation method, given in Equation 4.26, was implemented on several of the scenarios, with no significant change in results. The 2-D TLS-Prony Technique was developed assuming the data lies on a rectangular grid. Thus, it is appropriate to interpolate polar data to a rectangular grid before applying the 2-D TLS Prony Technique. If

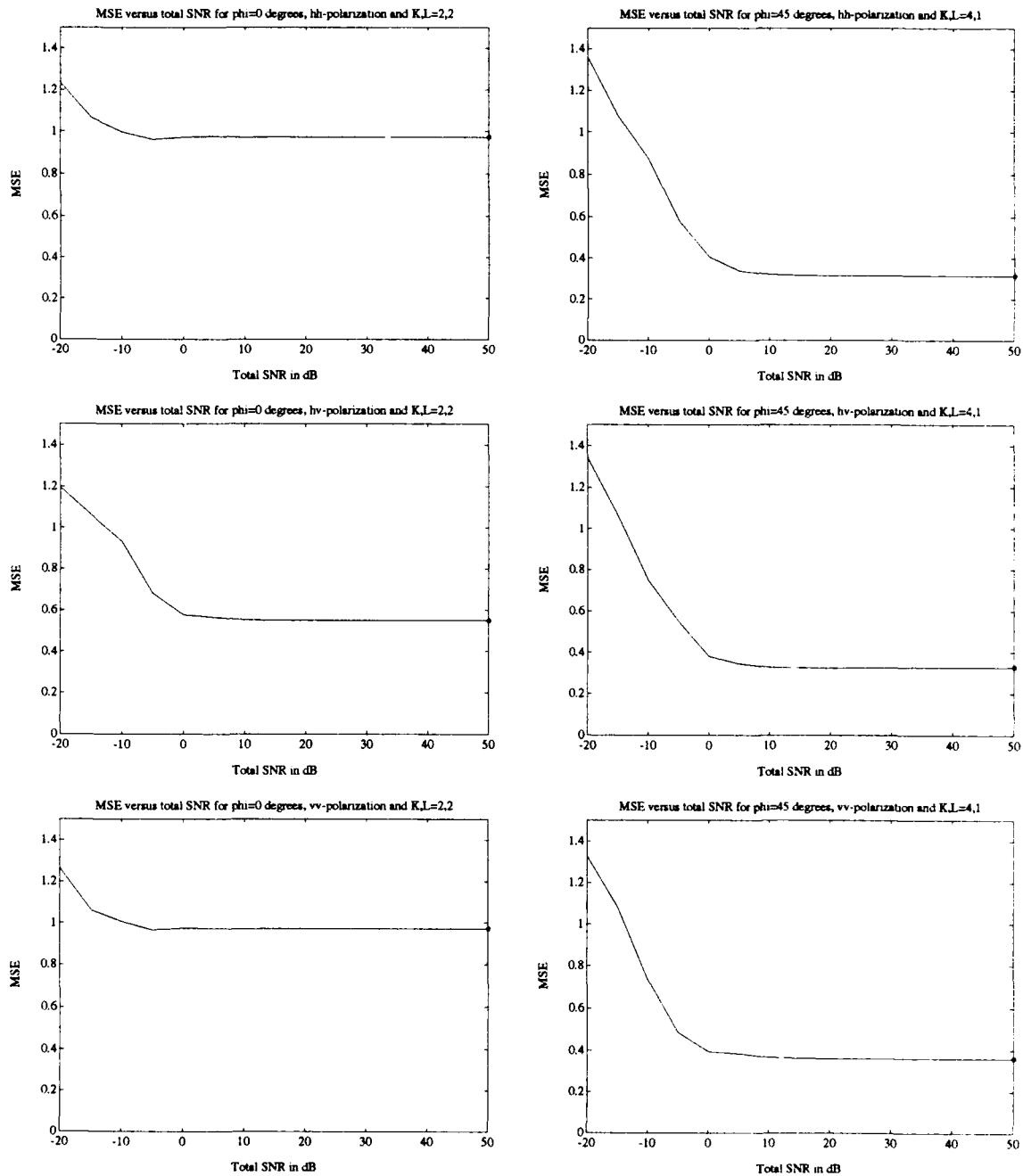


Figure 102: RE versus SNR for noise added to the GTD data of the plate. All three polarizations are shown for $\phi = 0^\circ$ and $\phi = 45^\circ$. The model orders were $Q, K, R, L = 10, 2, 10, 2$ for the $\phi = 0^\circ$ plots and $Q, K, R, L = 10, 4, 10, 1$ for the $\phi = 45^\circ$ plots. The 'o' at 50 dB in each plot is the RE for no noise added to the data for that scenario. The data lies on a square grid interpolated from a 15° swath of polar data.

the angular swath of the polar data is small, this step may not be necessary, and interpolation error can be avoided. The next data set, analyzed in Section 6.3.4, confirms this assumption for a 3° swath of polar data.

6.3.4 Single Polarization Analysis of Three Degree Polar Swaths of Data

In order to determine if the angular extent of the data set has a significant effect on the RE and the parameter estimates, a new data set was generated. This data set is also 31×31 , but the angular extent is only 3° with samples every 0.1° , while the frequency range is from 9.0 GHz to 9.48 GHz in 0.016 GHz steps. Figures 103 through 116 show the simulation results for this scenario. Shown for each angle are three contour images of the plate, each image corresponding to one of the three polarizations, found by directly using the polar data in the 2-D IFFT. Also shown are three sets of pole locations, each set corresponding to one of the three polarizations, estimated by Algorithm Two with no noise added to the original data. In the cases where there are more than four poles, only the four highest energy poles are shown in these plots. Along with these plots contour images are shown which were generated from all of the estimated parameters (not just the four highest energy poles). The parameters estimated by Algorithm Two are used in the 2-D model in Equation 5.2 to generate data in the 2-D frequency domain. The unambiguous range, R_u , is 9.3684 meters in each direction for this data set. Only one-fifth of this range is shown in each direction in the figures which follow. The model orders were chosen to reflect the expected number of scattering centers on the plate for the corner dominated

scenarios for the given center angle, and in the edge scenario cases, the model orders were chosen slightly larger than the expected number of scattering centers to allow the 2-D TLS-Prony Technique to more accurately model the data.

Examining Figures 103 through 116, it can be seen that the resolution of the contour images is lower than it was for the 15° polar swaths of data. This is due to the smaller 2-D angular and frequency bandwidths on the 2-D frequency plane for the 3° polar swaths of data. Even with this lower resolution data, the estimated pole locations are still, in general, located on the scattering centers (corners and edges) of the plate. These examples demonstrate the resolution capabilities of the 2-D TLS-Prony Technique. For many of the contour images, the locations of the peaks are not directly on the corners of the plate, but the estimated pole locations lie on the corners.

For the $\phi = 0^\circ$ case, shown in Figures 103 and 104, the distance (in the down-range direction) between the front edge and the rear edge is 1.1493 Fourier Bins. For the $\phi = 45^\circ$ case, shown in Figures 109 and 110, the down-range distance between corners C2 and C4 is 0.3574 Fourier Bins, and thus the 2-D TLS-Prony Technique is superresolving these scattering centers in the down-range direction (x -direction).

As before, noise was added to the data, and the RE versus total SNR results are shown in Figures 117 and 118. From Figure 117, it can be seen that for $\phi = 0^\circ$ the REs are not very dependent on SNR for SNRs over 20 dB. However, the REs for $\phi = 45^\circ$ are dependent on SNR for SNRs up to and over 50 dB. This is understandable since the 2-D TLS Prony technique is superresolving two of the down-range

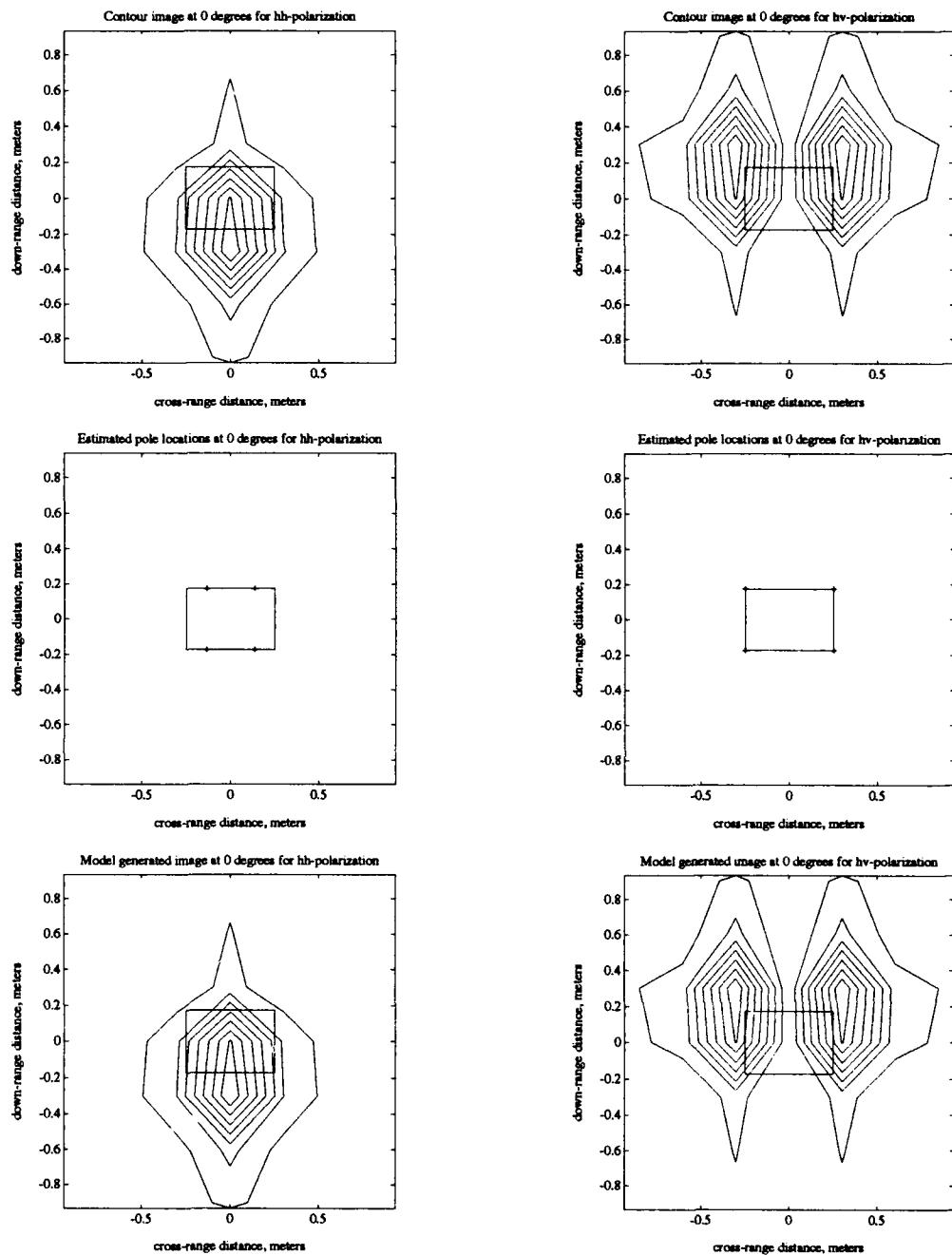


Figure 103: Single polarization inclined plate example for a 3° polar swath of data centered around 0° . Contour images, estimated pole locations and model generated images are shown for hh and hv -polarizations. Pole locations were estimated by Algorithm Two. Model orders were $Q, K, R, L = 10, 2, 10, 2$.

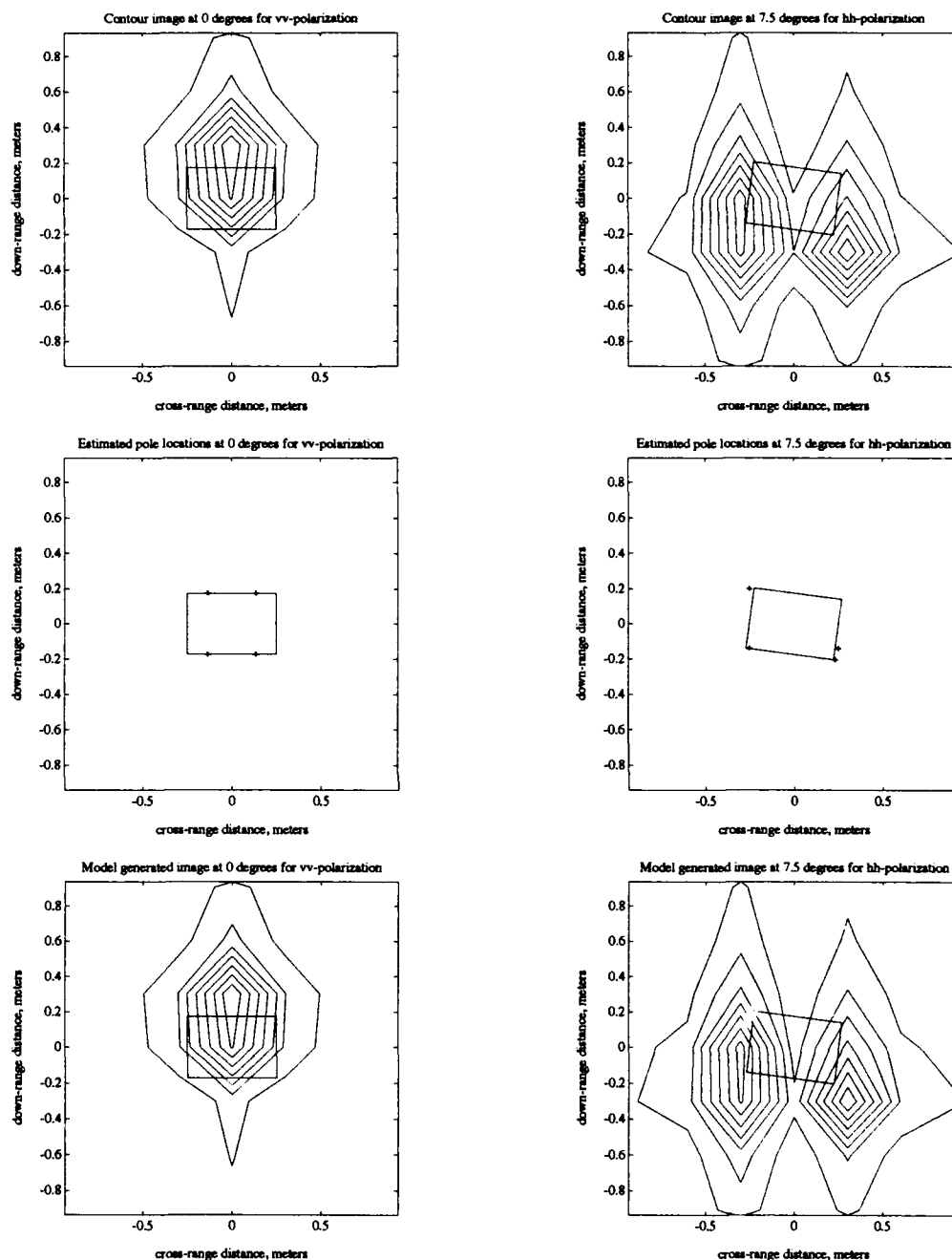


Figure 104: Single polarization inclined plate example for a 3° polar swath of data centered around 0° and 7.5° . Contour images, estimated pole locations and model generated contour images of the plate are shown for vv polarization at 0° and hh -polarization at 7.5° . Pole locations were estimated by Algorithm Two. Model orders were $Q, K, R, L = 10, 2, 10, 2$ for 0° and $Q, K, R, L = 10, 4, 10, 2$ for 7.5° .

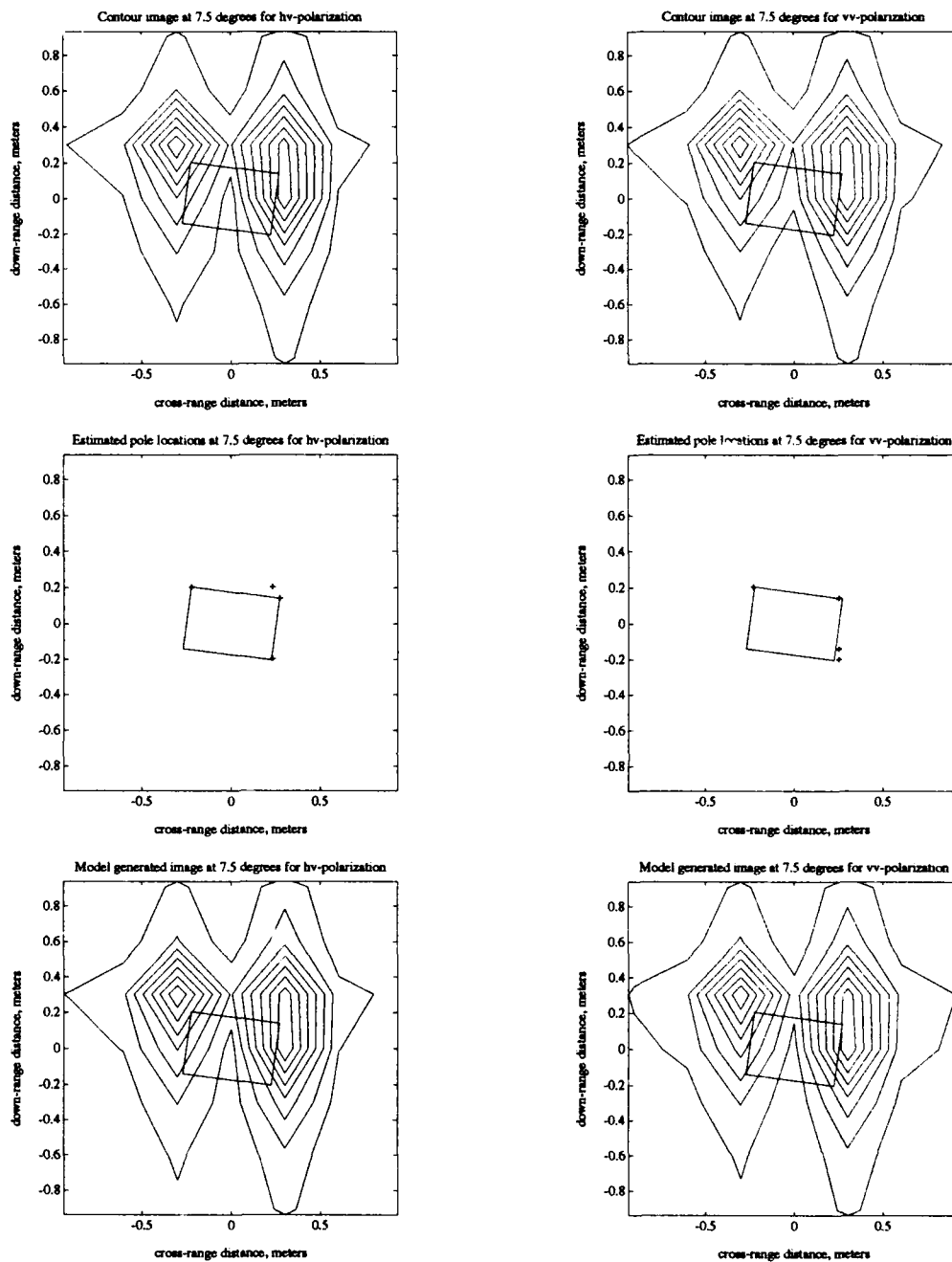


Figure 105: Single polarization inclined plate example for a 3° polar swath of data centered around 7.5° . Contour images, estimated pole locations and model generated images are shown for hh and vv -polarizations. Pole locations were estimated by Algorithm Two. Model orders were $Q, K, R, L = 10, 4, 10, 2$.

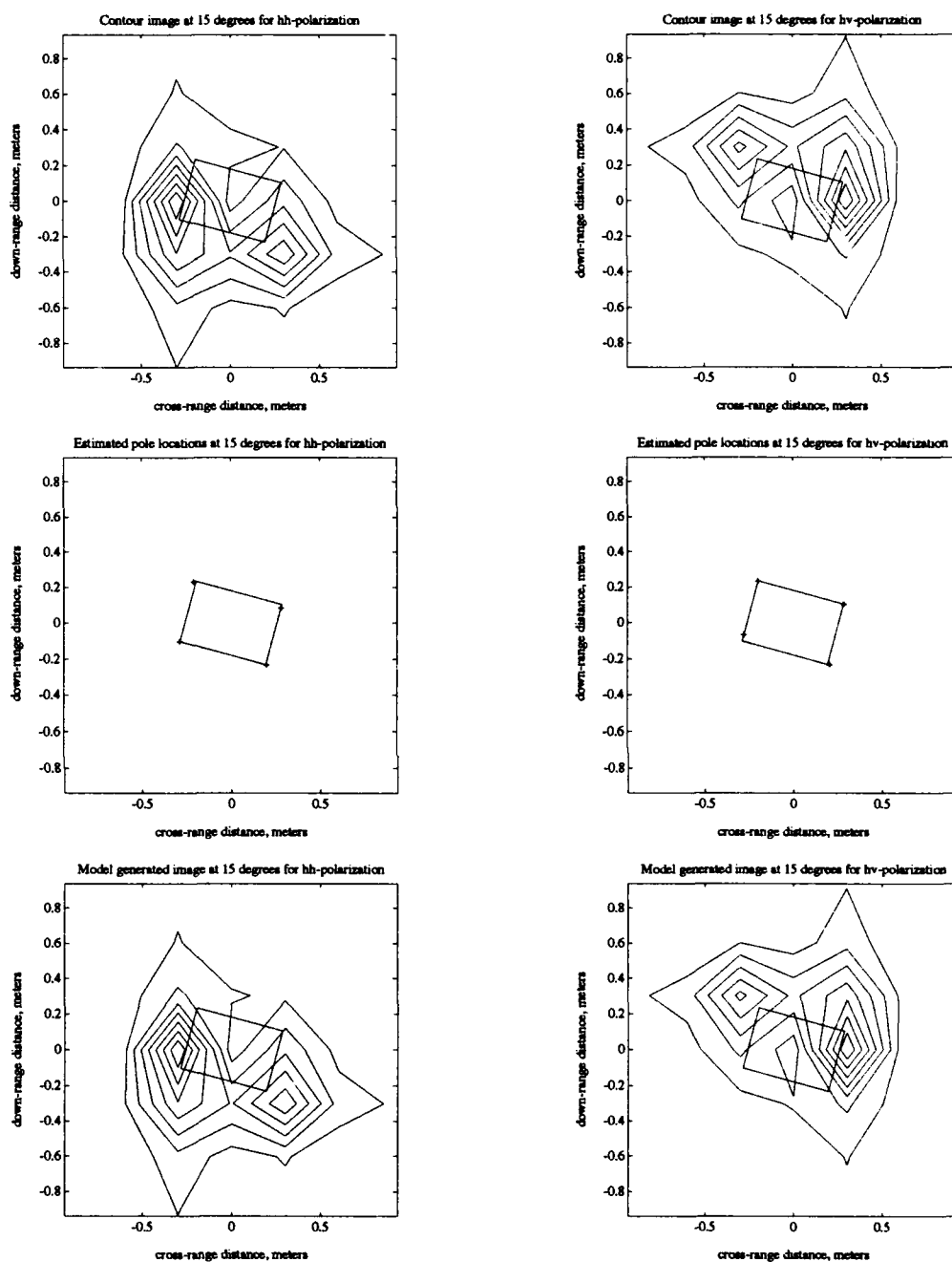


Figure 106: Single polarization inclined plate example for a 3° polar swath of data centered around 15° . Contour images, estimated pole locations and model generated images are shown for hh and hv -polarizations. Pole locations were estimated by Algorithm Two. Model orders were $Q, K, R, L = 10, 4, 10, 1$.

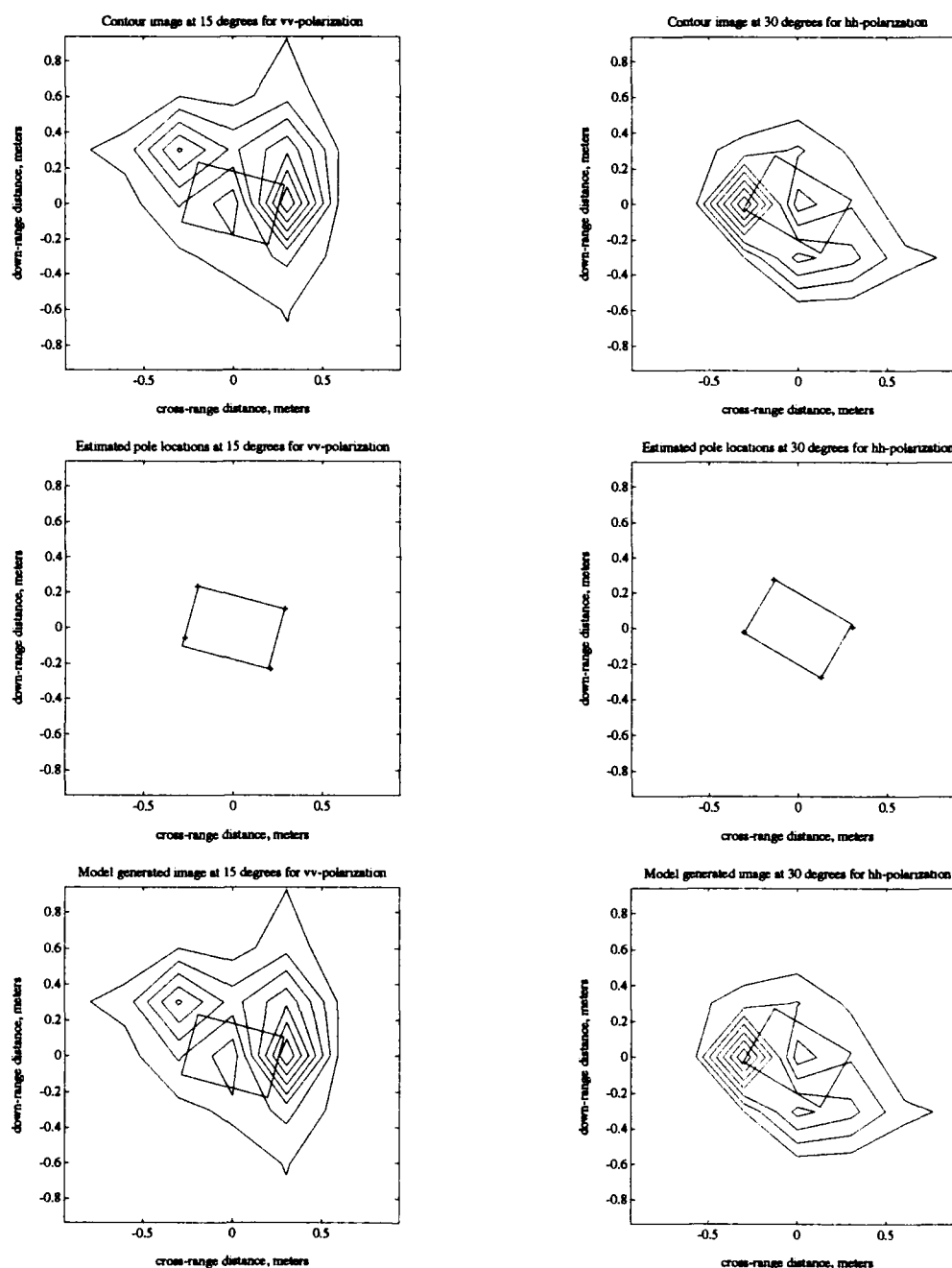


Figure 107: Single polarization inclined plate example for a 3° polar swath of data centered around 15° and 30°. Contour images, estimated pole locations and model generated contour images of the plate are shown for vv polarization at 15° and hh -polarization at 30°. Pole locations were estimated by Algorithm Two. Model orders were $Q, K, R, L = 10, 4, 10, 1$ for 15° and 30°.

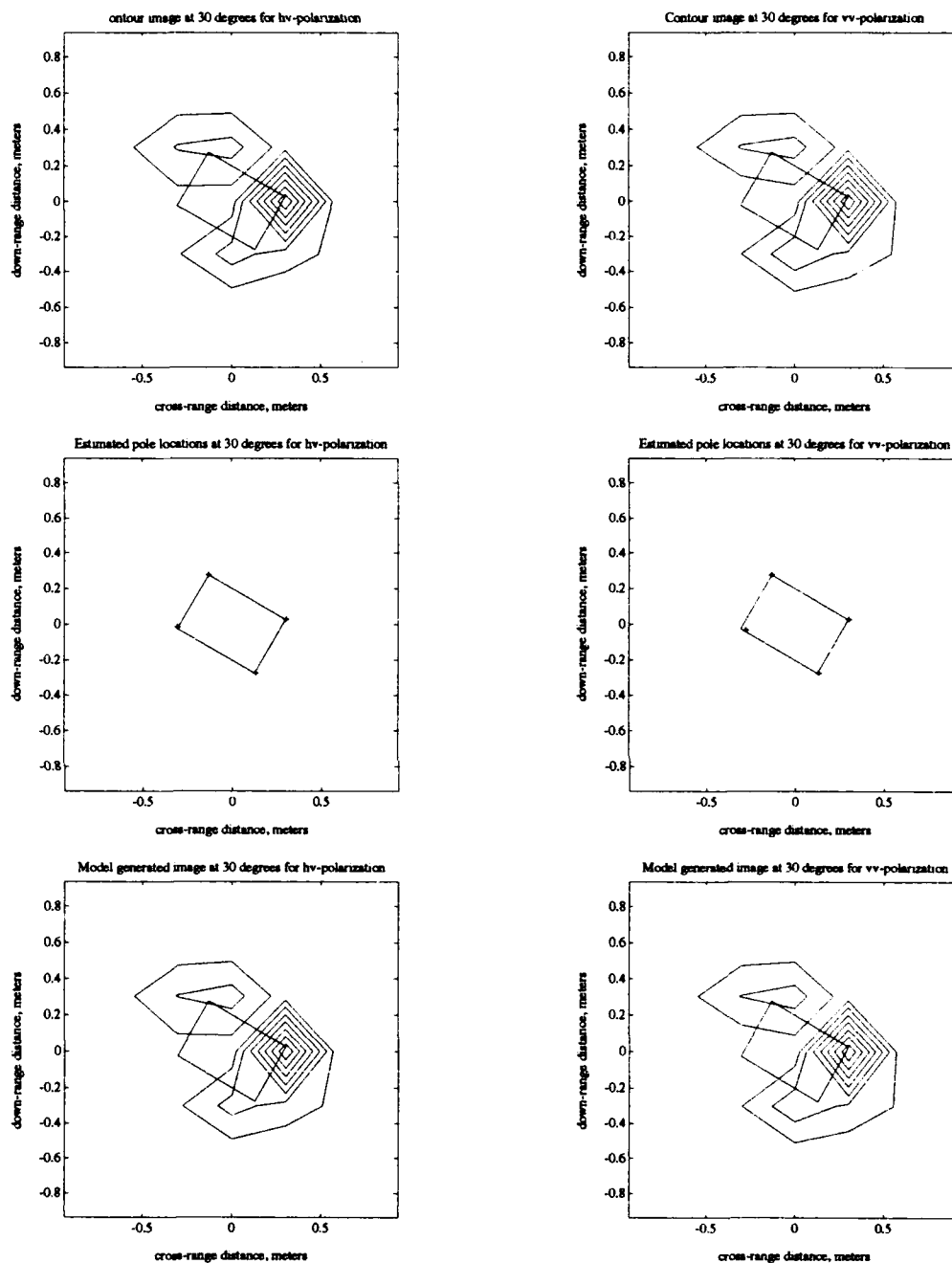


Figure 108: Single polarization inclined plate example for a 3° polar swath of data centered around 30° . Contour images, estimated pole locations and model generated images are shown for hh and hv -polarizations. Pole locations were estimated by Algorithm Two. Model orders were $Q, K, R, L = 10, 4, 10, 1$.

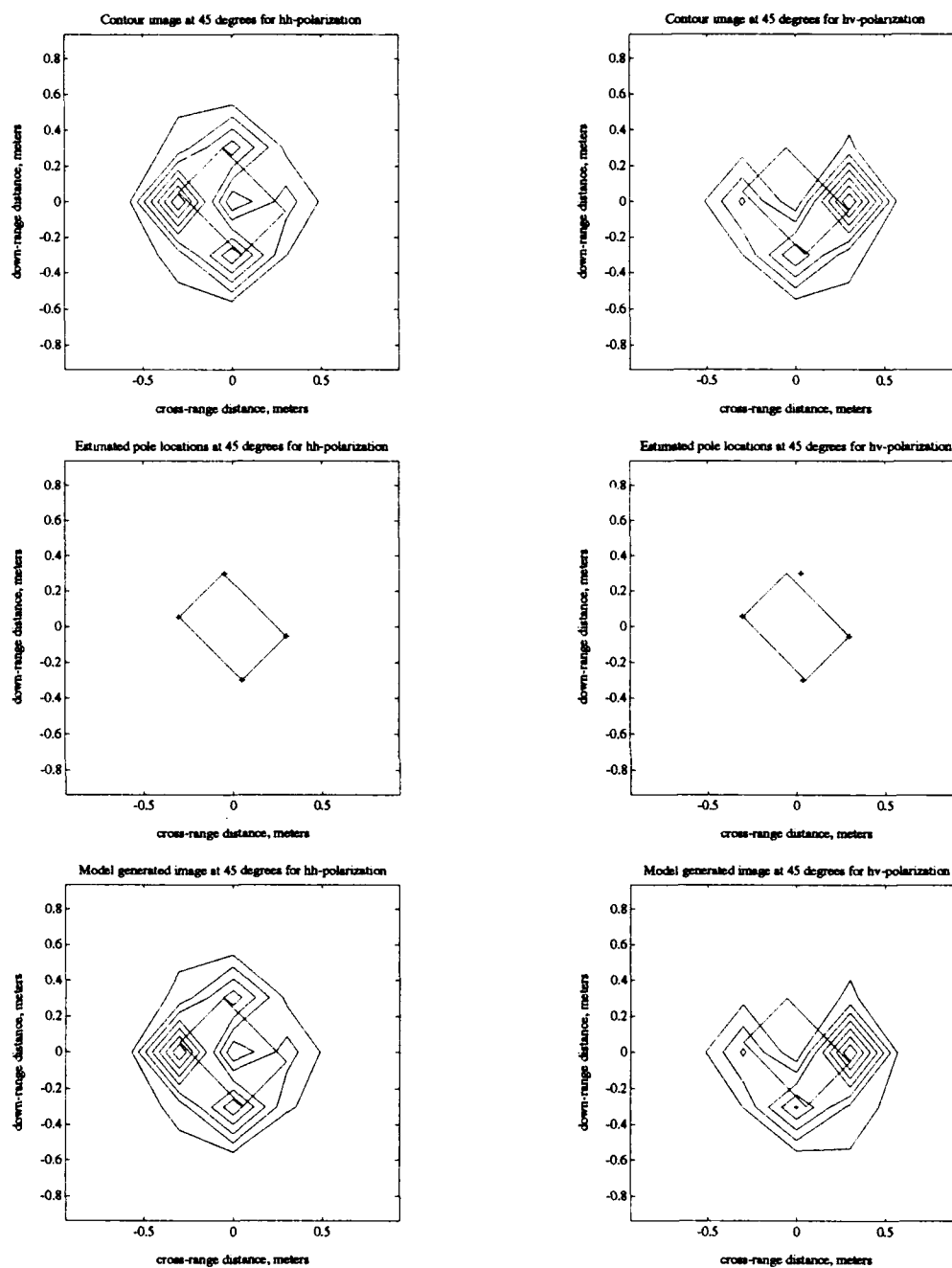


Figure 109: Single polarization inclined plate example for a 3° polar swath of data centered around 45° . Contour images, estimated pole locations and model generated images are shown for hh and vv -polarizations. Pole locations were estimated by Algorithm Two. Model orders were $Q, K, R, L = 10, 4, 10, 1$.

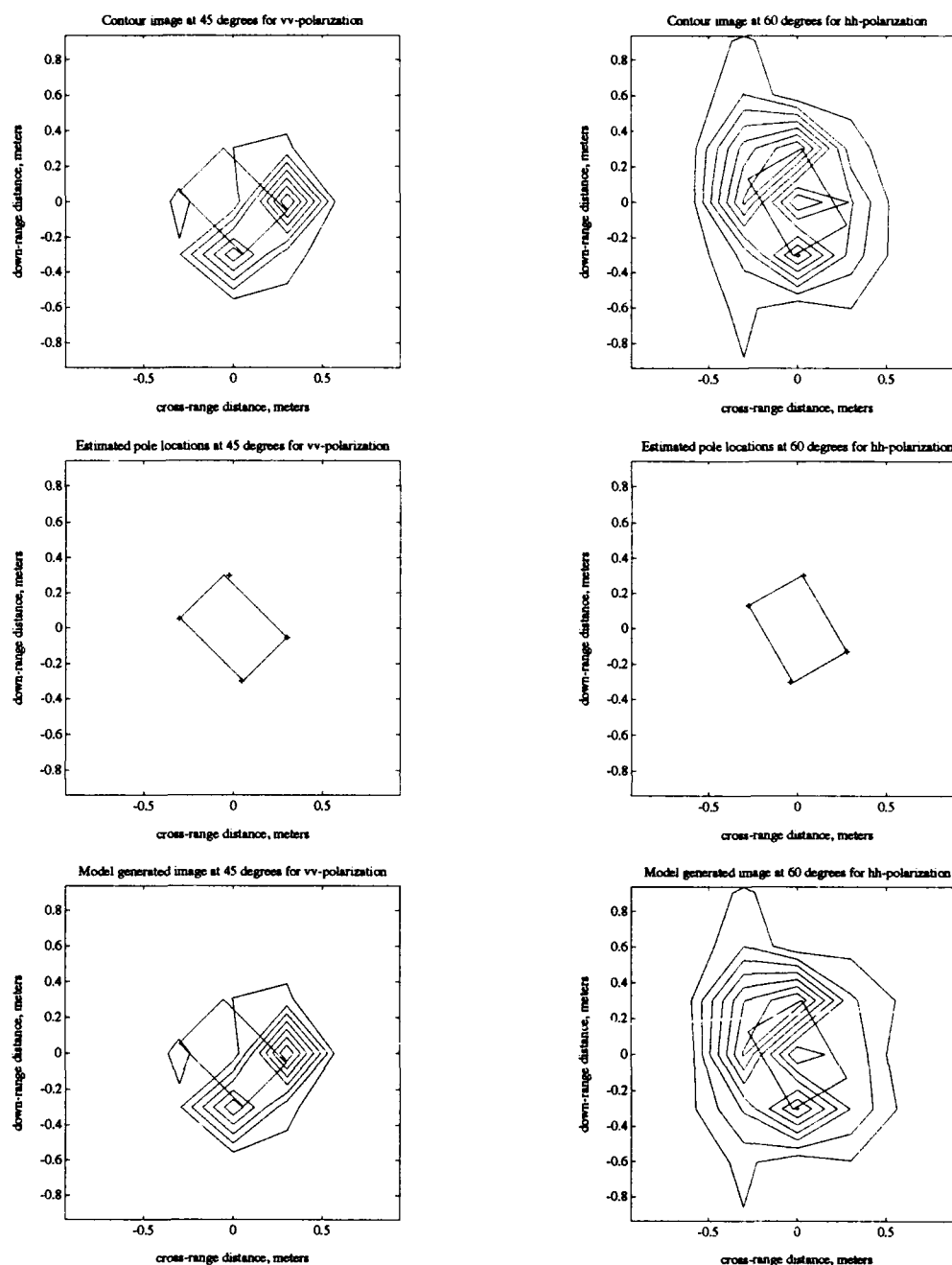


Figure 110: Single polarization inclined plate example for a 3° polar swath of data centered around 45° and 60° . Contour images, estimated pole locations and model generated contour images of the plate are shown for vv polarization at 45° and hh -polarization at 60° . Pole locations were estimated by Algorithm Two. Model orders were $Q, K, R, L = 10, 4, 10, 1$ for 45° and 60° .

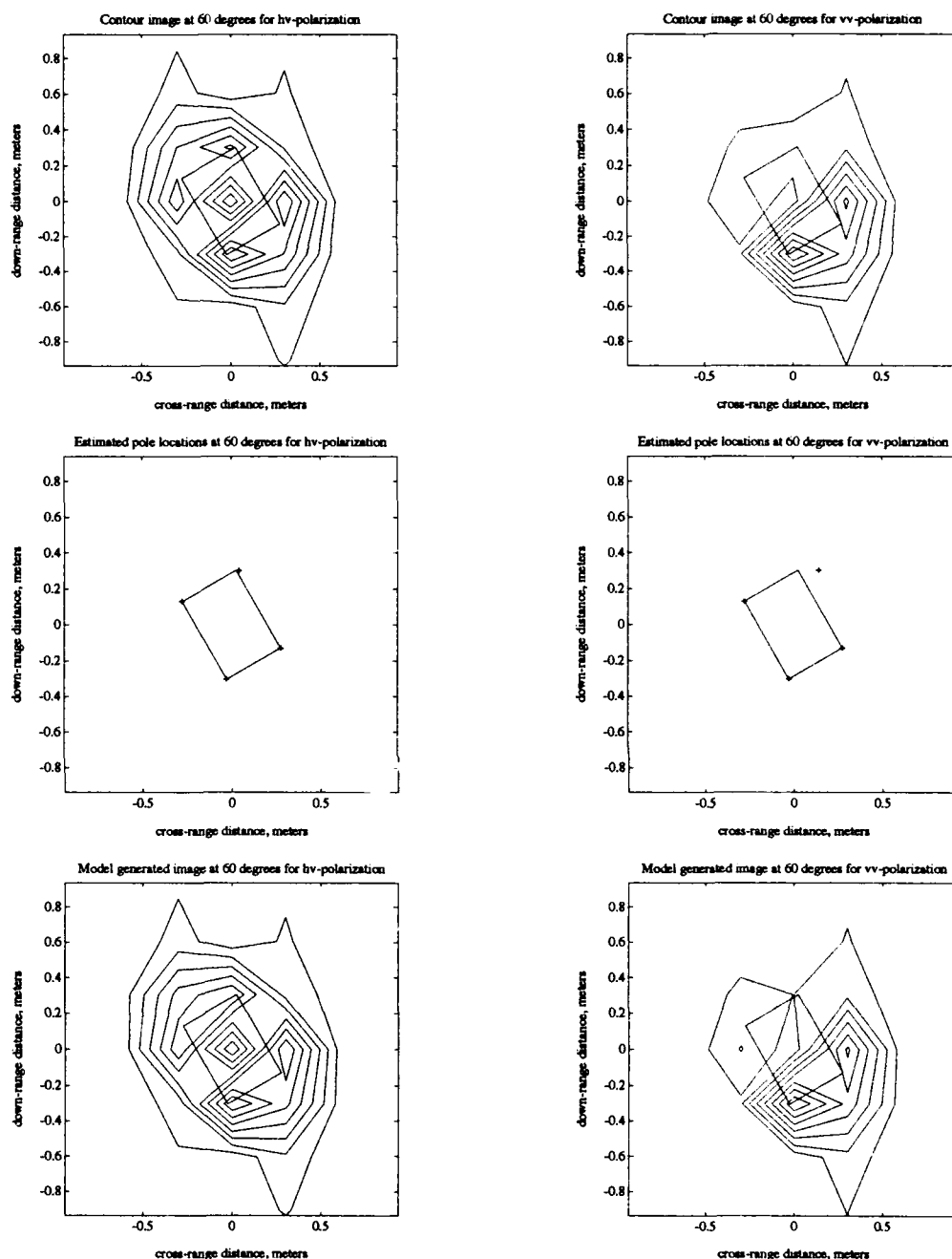


Figure 111: Single polarization inclined plate example for a 3° polar swath of data centered around 60° . Contour images, estimated pole locations and model generated images are shown for hh and vv -polarizations. Pole locations were estimated by Algorithm Two. Model orders were $Q, K, R, L = 10, 4, 10, 1$.

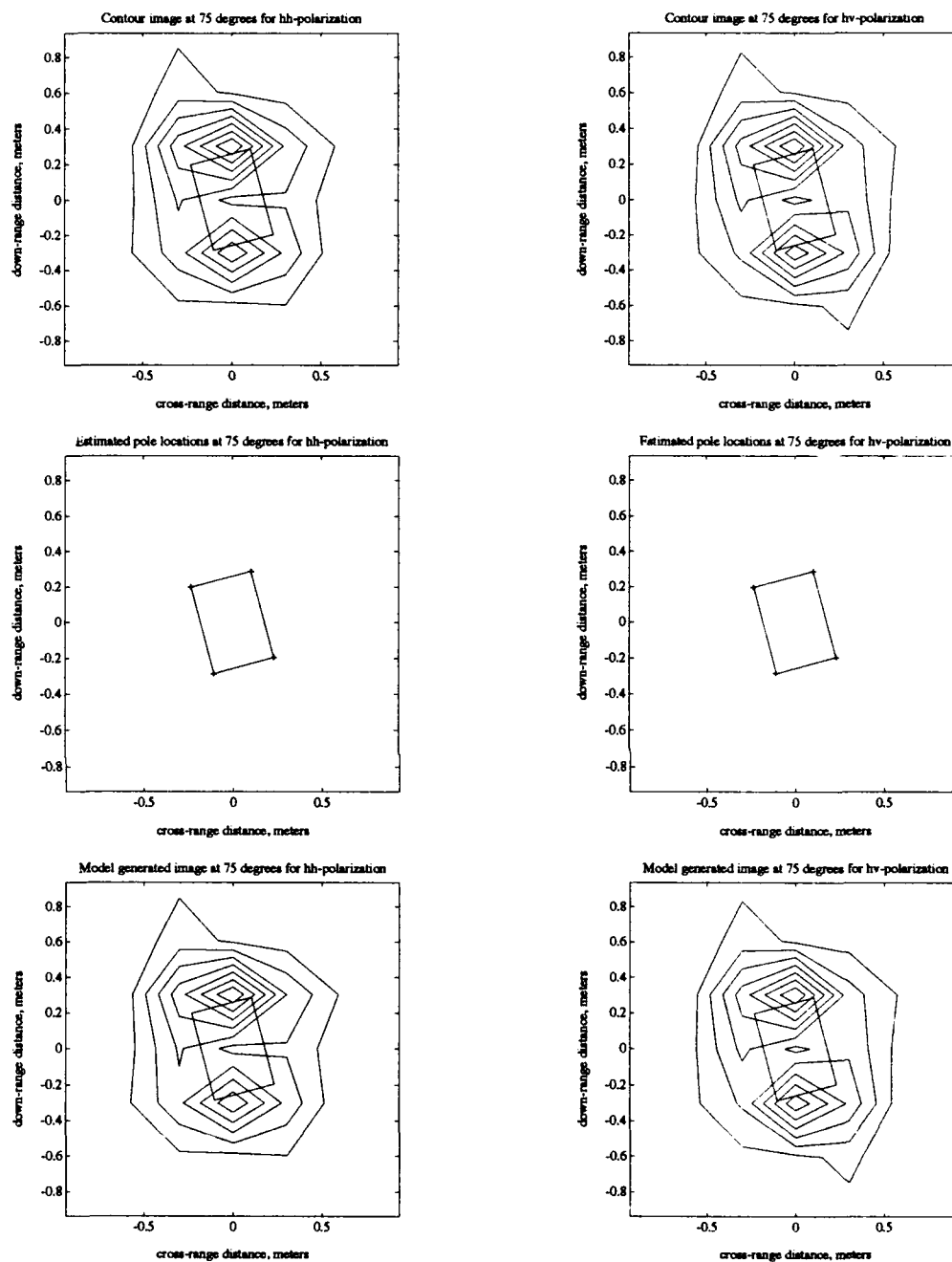


Figure 112: Single polarization inclined plate example for a 3° polar swath of data centered around 75° . Contour images, estimated pole locations and model generated images are shown for hh and hv -polarizations. Pole locations were estimated by Algorithm Two. Model orders were $Q, K, R, L = 10, 4, 10, 1$.

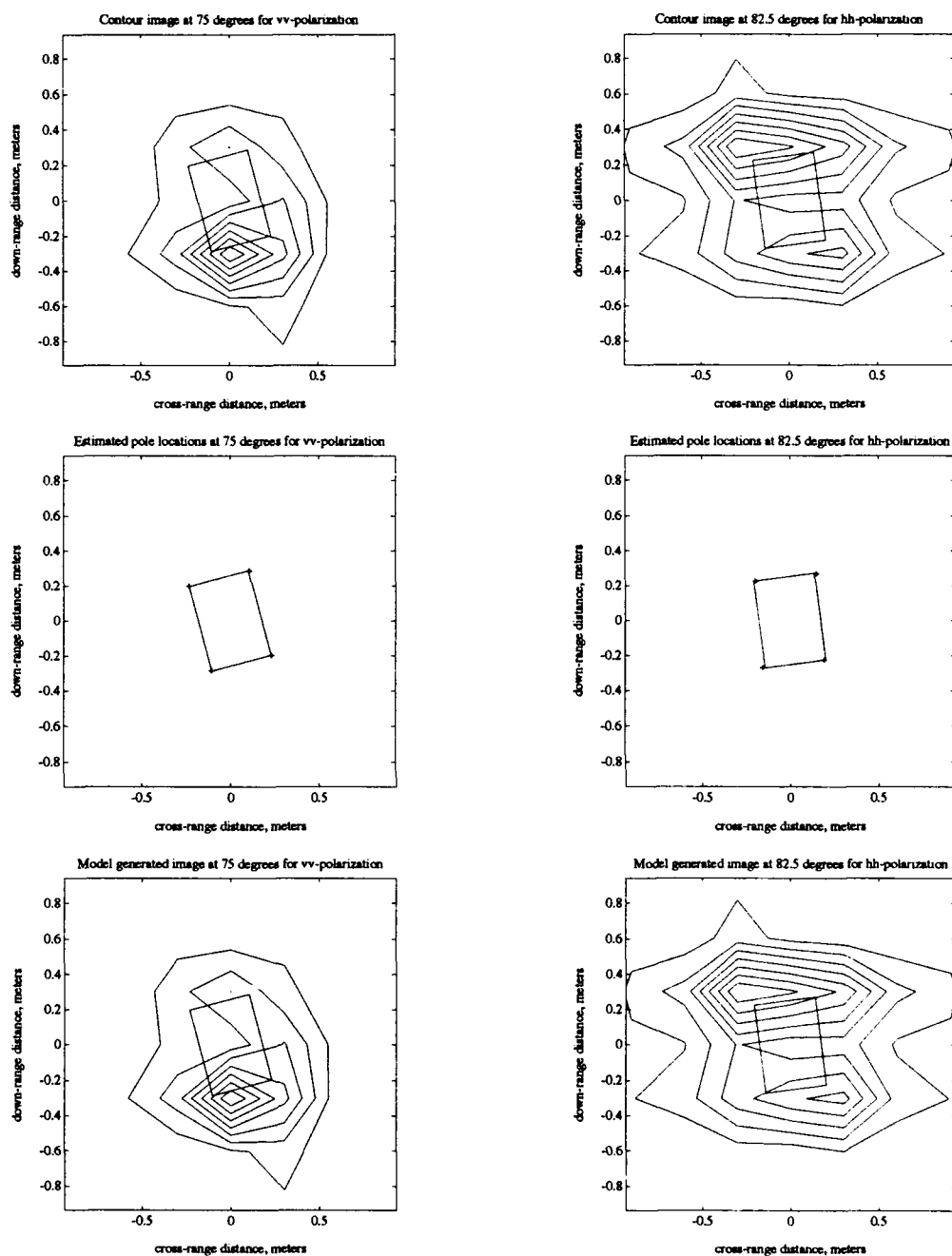


Figure 113: Single polarization inclined plate example for a 3° polar swath of data centered around 75° and 82.5° . Contour images, estimated pole locations and model generated contour images of the plate are shown for vv -polarization at 75° and hh -polarization at 82.5° . Pole locations were estimated by Algorithm Two. Model orders were $Q, K, R, L = 10, 4, 10, 1$ for 75° and $Q, K, R, L = 10, 4, 10, 2$ for 82.5° .

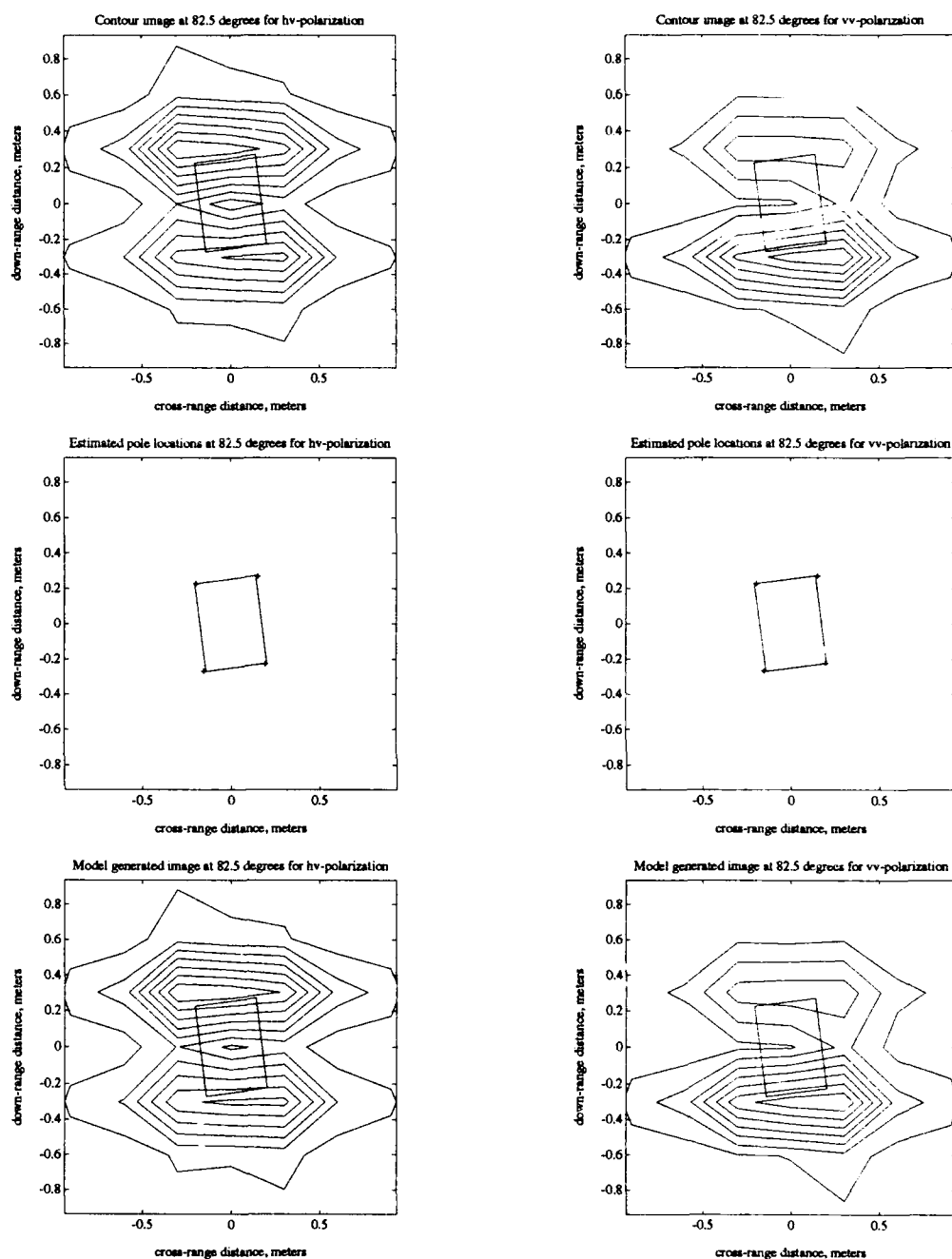


Figure 114: Single polarization inclined plate example for a 3° polar swath of data centered around 82.5° . Contour images, estimated pole locations and model generated images are shown for hh and hv -polarizations. Pole locations were estimated by Algorithm Two. Model orders were $Q, K, R, L = 10, 4, 10, 2$.

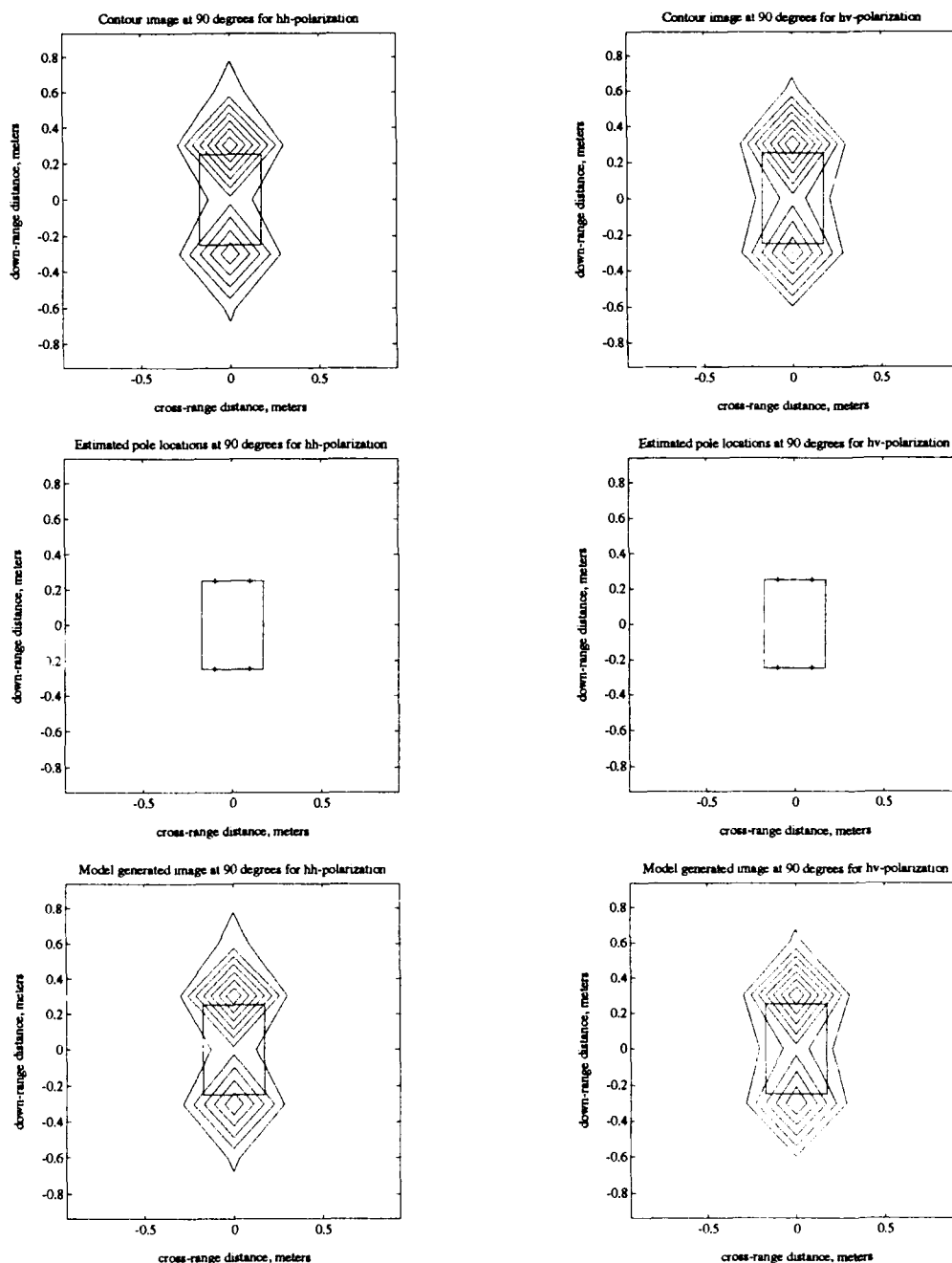


Figure 115: Single polarization inclined plate example for a 3° polar swath of data centered around 90° . Contour images, estimated pole locations and model generated images are shown for hh and hv -polarizations. Pole locations were estimated by Algorithm Two. Model orders were $Q, K, R, L = 10, 2, 10, 2$.

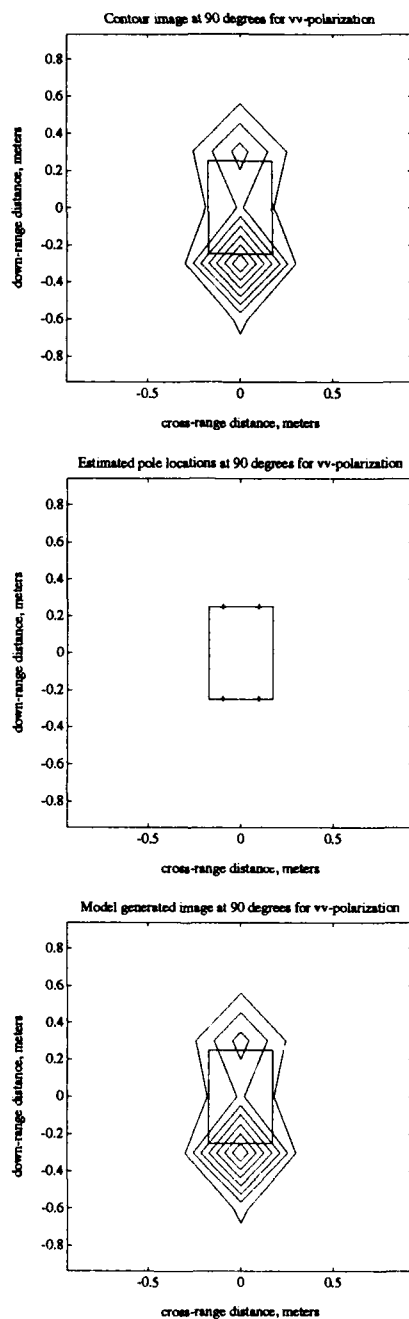


Figure 116: Single polarization inclined plate example for a 3° polar swath of data centered around 90° . Contour images, estimated pole locations and model generated images are shown for vv -polarization. Pole locations were estimated by Algorithm Two. Model orders were $Q, K, R, L = 10, 2, 10, 2$.

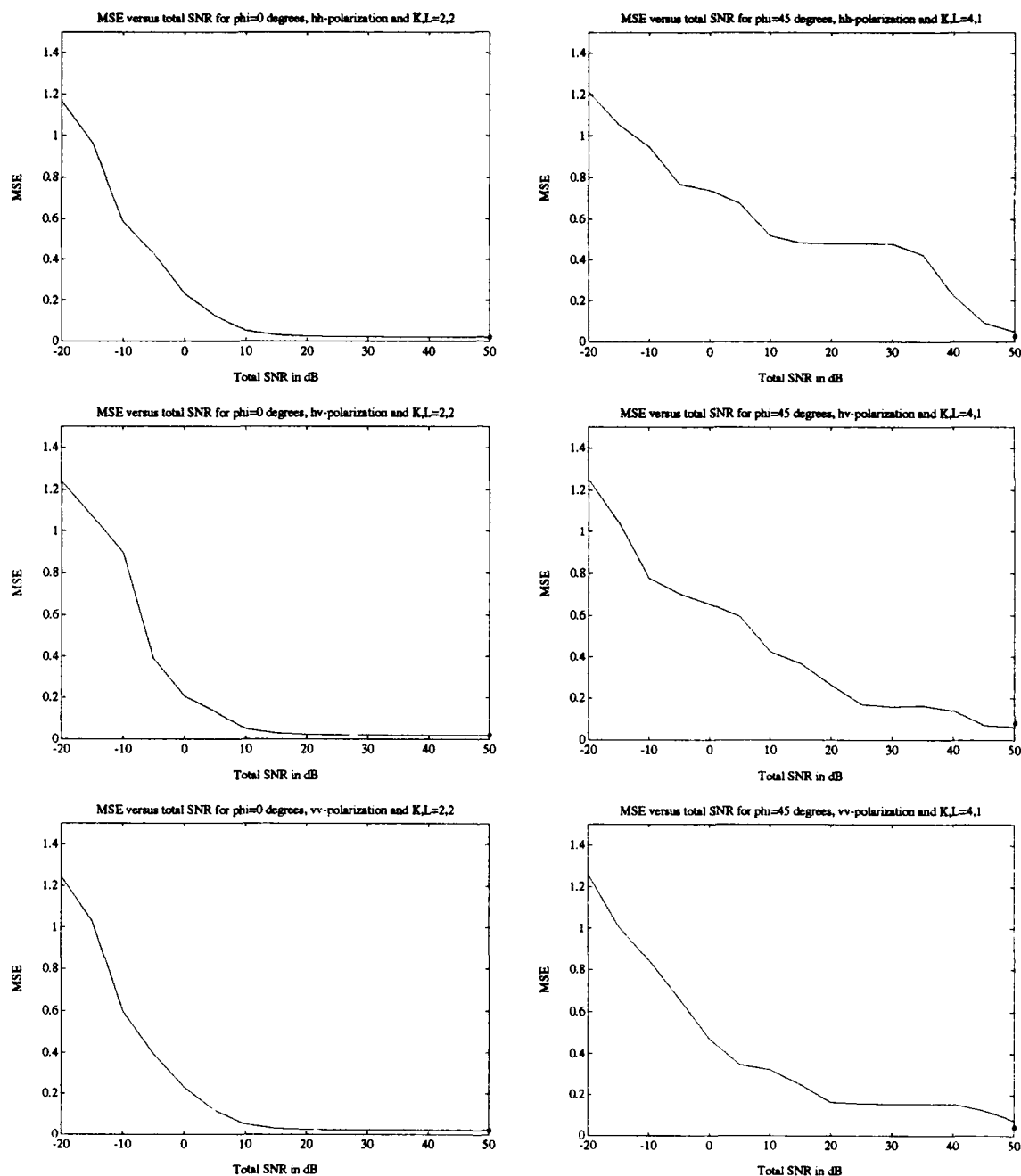


Figure 117: RE versus SNR for noise added to the GTD data of the plate. All three polarizations are shown for $\phi = 0^\circ$ and $\phi = 45^\circ$. The model orders are $Q, K, R, L = 10, 2, 10, 2$ for the $\phi = 0^\circ$ plots and $Q, K, R, L = 10, 4, 10, 1$ for the $\phi = 45^\circ$ plots. The 'o' at 50 dB in each plot is the RE for no noise added to the data for that scenario. The data is a 3° swath of polar data.

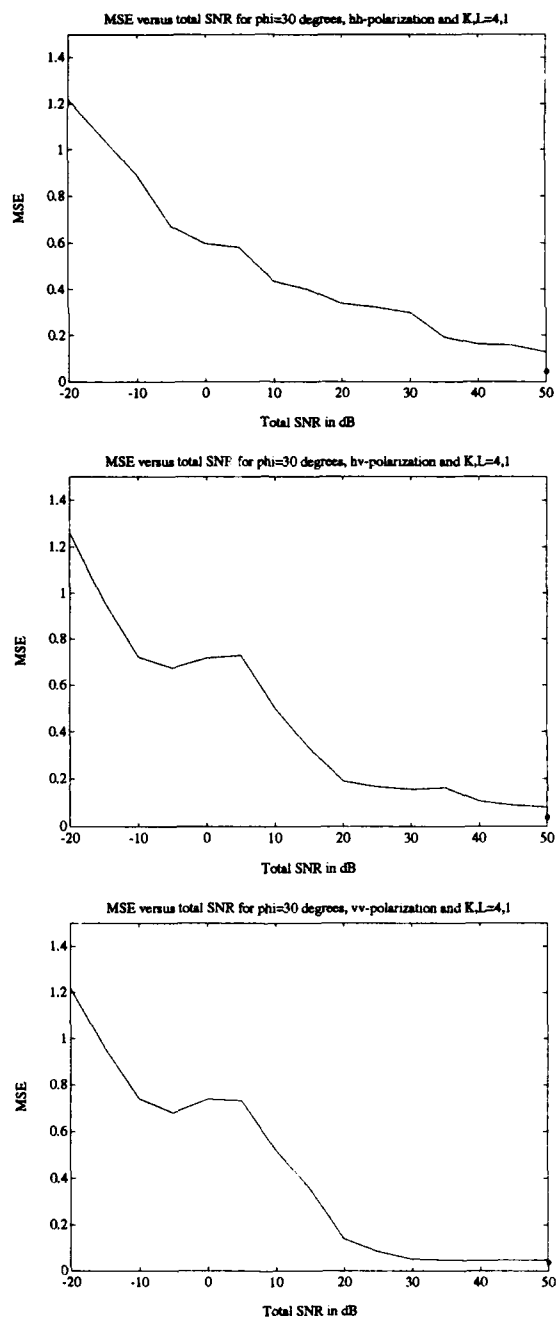


Figure 118: RE versus SNR for noise added to the GTD data of the plate. All three polarizations are shown for $\phi = 30^\circ$. The model orders were $Q, K, R, L = 10, 4, 10, 1$. The 'o' at 50 dB in each plot is the RE for no noise added to the data for that scenario. The data is a 3° swath of polar data.

Table 12: Model orders and relative errors for single polarization results for the scattering from an inclined plate. The data is a 3° polar swath.

Angle	Model Order; Q, K, R, L	RE (hh)	RE (hv)	RE (vv)
0	10,2,10,2	0.0214	0.0192	0.0216
7.5	10,4,10,2	0.1016	0.0463	0.0955
15	10,4,10,1	0.0466	0.0470	0.0506
30	10,4,10,1	0.0450	0.0370	0.0366
45	10,4,10,1	0.0273	0.0834	0.0421
60	10,4,10,1	0.1251	0.0965	0.0911
75	10,4,10,1	0.0553	0.0559	0.0503
82.5	10,4,10,2	0.0552	0.0485	0.0509
90	10,2,10,2	0.0417	0.0438	0.1085

corners (C2 and C4). As stated before, the parameter estimates associated with parametric techniques which are superresolving modes are, in general, sensitive to noise [10]. Thus, for the 2-D TLS-Prony Technique, for a fixed data set size (31×31 in this case), as the angular and frequency bandwidths are decreased (and subsequently the samples on the 2-D frequency plane become closer), the effects of noise become more detrimental to the ability of the algorithm to accurately model the data. Figure 118 shows the RE versus total SNR results for $\phi = 30^\circ$. As with the $\phi = 45^\circ$ results, these results show that the RE is more sensitive to SNR than it was for the data taken over a larger angular swath.

In order to show how the scattering center locations are affected by noise, several scatter plots are shown in Figure 119. These plots correspond to the scenario for hh -polarization and $\phi = 45^\circ$. Ten overlaid realizations are shown for each plot. The pole locations estimated from the noise corrupted GTD data are designated by

‘+’s while the pole locations estimated directly from the GTD data are designated by ‘o’s. Six plots are shown, each for a specific SNR between 0 and 50 dB. From these plots, it can be seen that the location of the corner with the largest scattering return, which is the left-most corner in the plots (C4), is accurately estimated for total SNRs as low as 20 dB. As the SNR decreases, the locations of the other corners are not estimated as accurately. Note that the model orders chosen for this example were $Q, K, R, L=10,4,10,1$. These model orders were chosen to reflect the expected number of scattering centers. The plots corresponding to total SNRs of 20 and 30 dB show that the locations of corners C1 and C2 are not estimated at all. This is probably due to the closeness of corner C2 to corner C4 in down-range and corner C1 to corner C3 in cross-range.

This estimation inaccuracy can be corrected for by choosing a larger model order and retaining the four highest energy poles. This is done, and the results are shown in Figure 120. The model orders for these plots are $Q, K, R, L=10,4,10,2$. Only the four highest energy poles are shown in these plots. From these plots, it can be seen that the locations of corners C1 and C2 are now estimated by Algorithm Two, but these locations are not directly on the corners. There is some bias present in their estimated locations possibly due to the scattering from the other two dominant corners (C3 and C4) on the plate. However, this example shows that it is appropriate to overmodel the number of scattering centers when noise is added to data when the data set chosen requires superresolution to estimate the locations of the scattering centers.

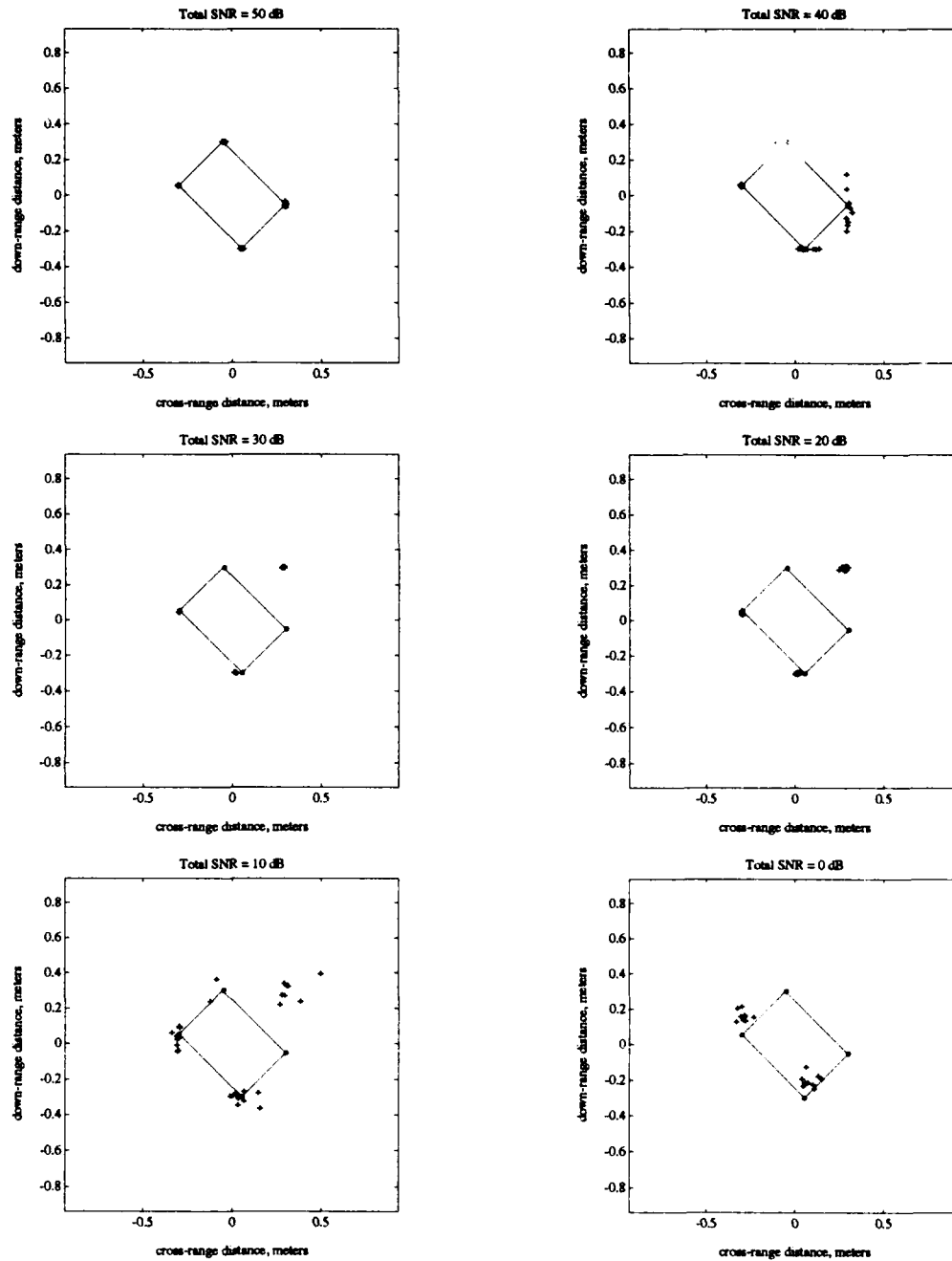


Figure 119: Estimated pole locations for noise corrupted GTD data. The GTD data is a 3° polar swath with hh -polarization centered around $\phi = 45^\circ$. Each plot contains ten overlaid realizations, where the estimated pole locations for the noise corrupted GTD data are designated by '+'s and the pole locations estimated directly from the GTD data are designated by 'o's. The model orders were $Q, K, R, L = 10, 4, 10, 1$ for all of the plots.

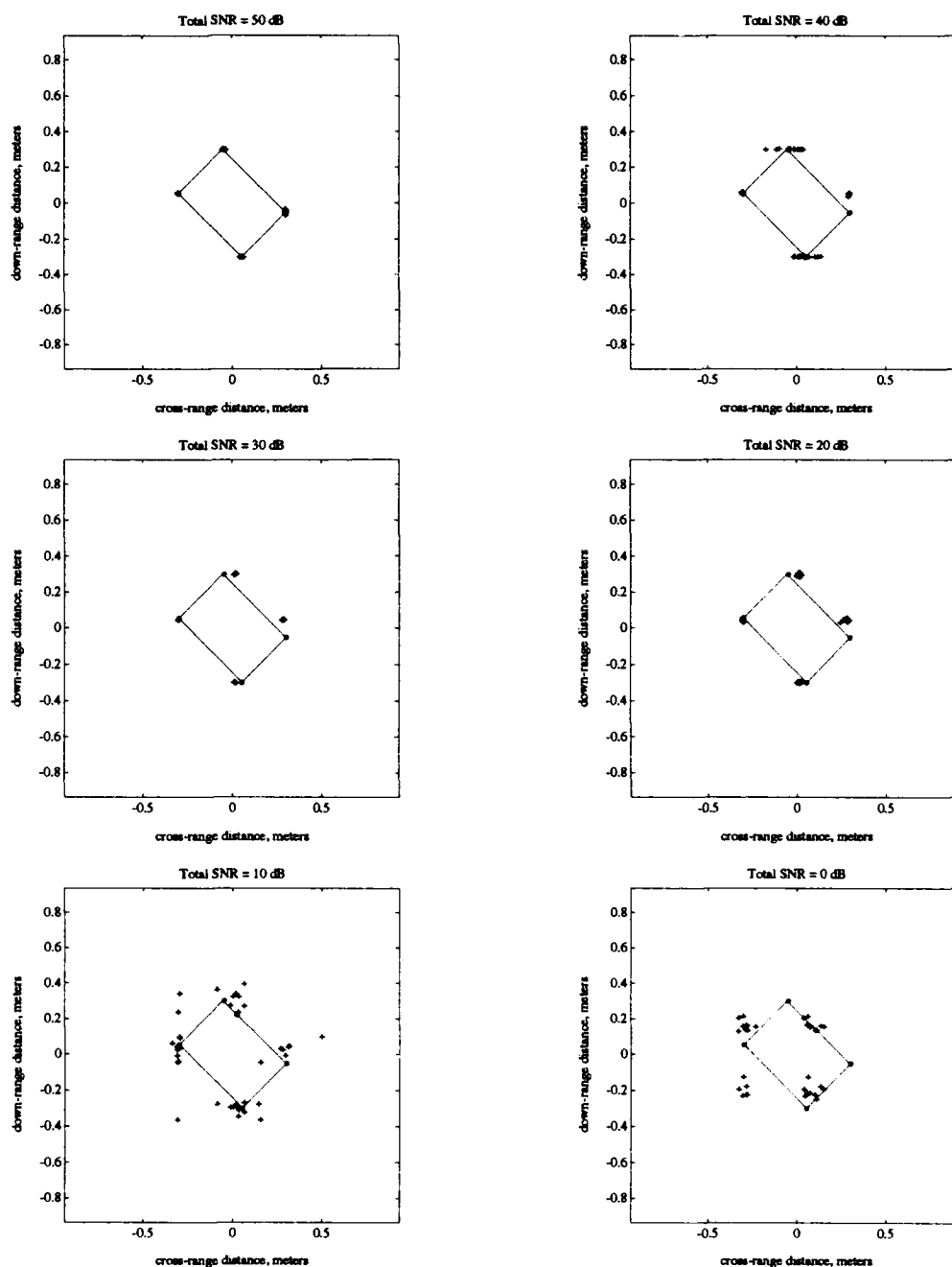


Figure 120: Estimated pole locations for noise corrupted GTD data. The GTD data is a 3° polar swath with hh -polarization centered around $\phi = 45^\circ$. Each plot contains ten overlaid realizations, where the four highest energy pole locations for each realization for the noise corrupted GTD data are designated by '+'s and the pole locations estimated directly from the GTD data are designated by 'o's. The model orders were $Q, K, R, L = 10, 4, 10, 2$ for all of the plots.

From the REs in Table 12 it can be concluded that the 2-D damped exponential better models the polar data, with no noise added, for data taken over smaller angular swaths. Even with noise added to the data, for SNRs over 20 dB, the REs corresponding to the 3° angular swath data are lower than the REs corresponding to the 15° polar swath data with no noise added. From Figures 103 through 116 it can be seen that the resolution of the images for a 3° polar swath is less than it was for the data corresponding to a 15° polar swath. However, the estimated pole locations are, in general, located on the scattering centers of the plate. This demonstrates the superresolution capabilities of the 2-D TLS-Prony Technique. This is very useful since the bandwidth and angular requirements of a SAR are reduced when utilizing the 2-D TLS-Prony Technique. The angular swath of 3° and frequency bandwidth of 480 MHz are reasonable numbers for SARs available today. Also, the lower REs confirm the damped exponential as a valid model for corners away from grazing angles (see Chapter III).

Several of the 3° polar swaths of data were interpolated onto a rectangular grid and Algorithm Two was applied to the data (these simulations are not shown here). In each case, the RE was greater than the REs in Table 12. This larger RE is most probably due to interpolation error. A drawback to gathering data over a smaller angular and frequency bandwidth is that the parameters estimated from this data are more sensitive to noise, as is demonstrated in Figures 117 and 119, than when parameters are estimated from data gathered over larger angular and frequency bandwidths. This same characteristic is seen in the full-polarization simulations

which follow.

6.4 Full-Polarization Analysis of Plate

The full-polarization data set is now used in FPA2 to better estimate the scattering center locations and to examine the polarimetric properties of the scattering centers on the inclined flat plate. As in the single-polarization case, several data sets are analyzed. First, 15° polar sections of the data are analyzed. Note that as the angle of incidence changes, the incident polarization changes. Over 15° this may be a factor. This data is then interpolated onto a square grid and the full-polarization data is analyzed. Finally, 3° polar sections of the data are analyzed.

The polarimetric characteristics of the scattering centers are represented by polarization ellipses calculated from the pole and amplitude coefficient estimates as discussed in Chapter V. The plotting of the ellipses on the image plane requires a quantity called the ellipse factor. The units of the amplitude coefficients (which have the same units of the scattering coefficients, which are the data) are in meters. This is a result of the definition of the scattering matrix given in Equation 2.19. Since the coordinates of the image plane are in meters, it is appropriate to place the ellipses directly on these plots. However, due to the small magnitude of the scattering coefficients (nominally around 10^{-3} meters), the size of the ellipses must be scaled-up in order to view them on these plots. Thus, the ellipse factor is the dimensionless ratio between the size of the ellipses as viewed on the plots which follow to the actual size of the ellipses.

Note that in Section 3.4 it was stated that separating the angular dependence

from the scattering matrix was a poor assumption for canonical scattering centers such as the corner and the edge. The angular scattering response for the corner and the edge does vary with polarization, but the impulsive and constant behaviors do occur at the same aspect angles for the various polarizations. The full-polarization model in Equation 5.54 is still an accurate representation to the full-polarization scattering response of a corner or an edge since each polarization has an amplitude coefficient associated with it. Only the poles, which determine the scattering center locations, are estimated from multiple polarization data, and each set of amplitude coefficients is determined from the data set with the polarization corresponding to that amplitude coefficient. Thus, the full-polarization version of the 2-D TLS-Prony Technique is a valid full-polarization model for the scattering from canonical scattering centers such as the corner and edge, and using the full-polarization data simultaneously to determine the scattering center locations and polarimetric characteristics is valid, as demonstrated in this section.

6.4.1 Full-Polarization Analysis of Fifteen Degree Polar Swaths of Data

First, nine 15° polar swaths data are analyzed using FPA2. As in the single polarization analysis for the 15° polar swaths of data the polar data is used directly by FPA2. The results are shown in Figures 121 through 123. The model orders chosen reflect the expected number of scattering centers on the plate for the corner dominated scenarios and for the edge dominated scenarios, the model orders are chosen slightly larger than the expected number of scattering centers. The model orders

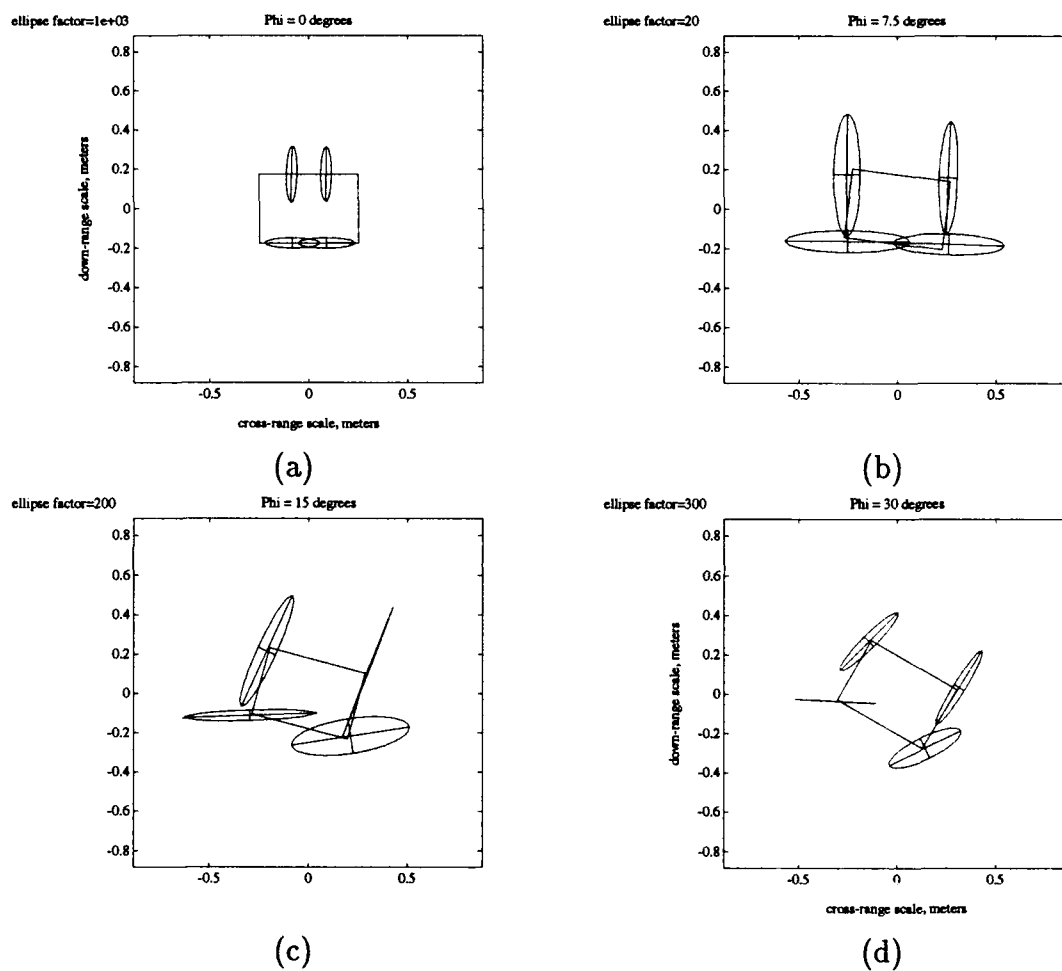


Figure 121: Full polarization flat plate example. Pole locations estimated by FPA2 are located at the centers of the ellipses. The data is a 15° polar swath of centered around (a) 0° , (b) 7.5° , (c) 15° and (d) 30° . The model orders used are given in Table 13.

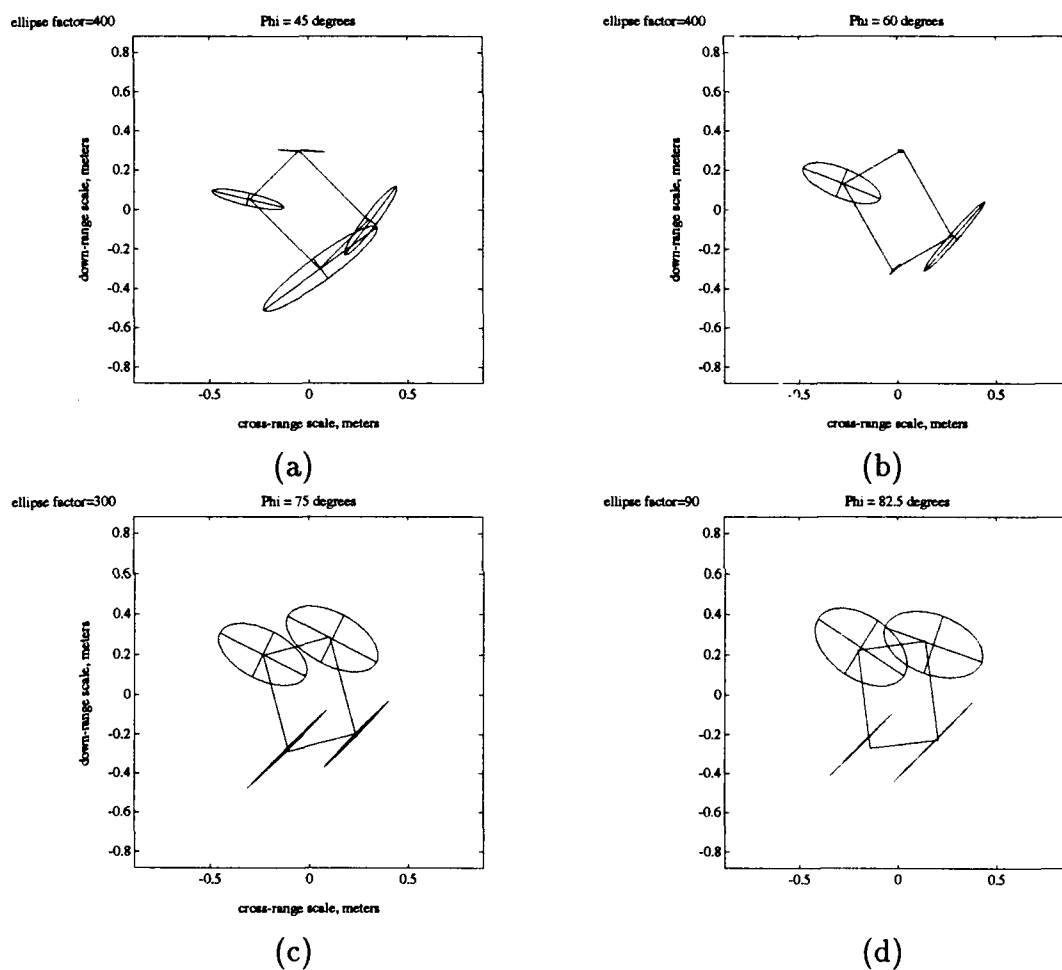


Figure 122: Full polarization flat plate example. Pole locations estimated by FPA2 are located at the centers of the ellipses. The data is a 15° polar swath centered around (a) 45° , (b) 60° , (c) 75° and (d) 82.5° . The model orders used are given in Table 13.

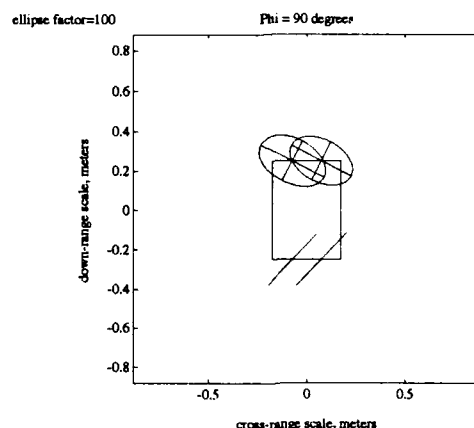


Figure 123: Full polarization flat plate example. Pole locations estimated by FPA2 are located at the centers of the ellipses. The data is a 15° polar swath centered around 90° . The model orders used are given in Table 13.

used and the relative errors (REs) for the FPA2 generated estimates are given in Table 13. The RE for the full-polarization case is defined as

$$\text{RE}_{\text{fp}} = \frac{\| [D'_h \ D'_v] - [D_h \ D_v] \|}{\| [D_h \ D_v] \|} \quad (6.3)$$

where $[D'_h \ D'_v]$ is the data matrix generated by the parameter estimates and $[D_h \ D_v]$ is the actual data matrix. As with the single polarization cases, noise was added to two full-polarization scenarios and the results are shown in Figure 124. From this figure, it can be seen that for a 15° polar swath of data, the REs (and the parameter estimates) are relatively constant for total SNRs over 10 dB.

In examining the figures, the locations where the ellipses are centered are the pole locations. In general, the poles are located on the scattering centers of the plate, as expected. The pole locations in the full-polarization cases, are, in general, located on the scattering centers more frequently than in the single polarization cases. In

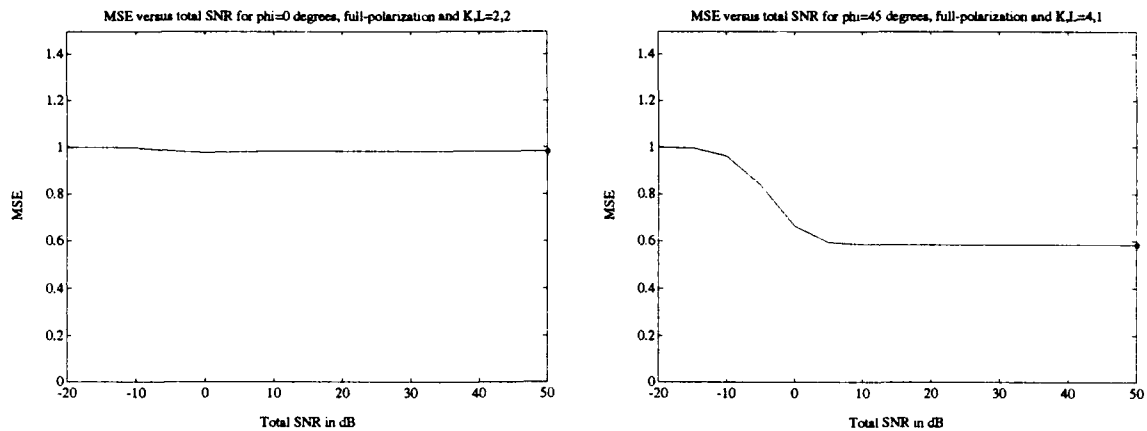


Figure 124: RE versus SNR for noise added to the GTD data of the plate. Full polarization results are shown for $\phi = 0^\circ$ and $\phi = 45^\circ$. The model orders are $Q, K, R, L = 10, 2, 10, 2$ for the $\phi = 0^\circ$ plot and $Q, K, R, L = 10, 4, 10, 1$ for the $\phi = 45^\circ$ plot. The 'o' at 50 dB in each plot is the RE for no noise added to the data for that scenario. The data is a 15° swath of polar data.

the single polarization examples, there are many cases where there are extraneous poles not associated with any scattering centers. This is due to low (or zero) energy scattering centers which exist for some of the single polarization data sets. When all of the full-polarization data is used simultaneously to estimate the poles, one of the polarizations may have no energy associated with a scattering center, but the other polarization, in general, does. Thus, using all of the full-polarization data simultaneously to estimate the poles allow for more accurate parameter estimates.

The ellipses show the polarimetric characteristics of the scattering centers on the plate as viewed from the radar. The polarimetric characteristics of each scattering center are directly related to the polarization of the electric field scattered from that scattering center [43]. For example, consider Figure 121(d), which shows the

Table 13: Model orders and relative errors for full-polarization results for the scattering from an inclined plate. The data is a 15° angular swath of polar data.

Angle	Model Order, Q, K, R, L	RE_{fp}
0	10,2,10,2	0.9820
7.5	10,4,10,2	0.7469
15	10,4,10,1	0.5970
30	10,4,10,1	0.6170
45	10,4,10,1	0.5827
60	10,4,10,1	0.6604
75	10,4,10,1	0.4516
82.5	10,4,10,2	0.6418
90	10,2,10,2	0.9225

response at $\phi = 30^\circ$. The response of the left-most corner of the plate, which is corner C4, is horizontally dominated. This corresponds with Figures 67 and 68, which contain the single polarization responses of the plate for $\phi = 30^\circ$. The images for vv and hv -polarizations show little or no response for C4, while the hh -polarization response shows a large response for C4.

The ellipses associated with some of the corners correspond to a polarization that is nearly linear (linear implies that the ellipse has collapsed to a line) which is aligned with one of the edges that defines the corner. For example, consider corner C2 (upper right corner) for $\phi = 30^\circ$ shown in Figure 121(d). The polarization ellipse associated with this corner is nearly linear and is aligned with the edge defined from corner C2 to corner C3. This same phenomena is seen for several other corners in the plots.

The ellipses on the leading edge of the plate for $\phi = 90^\circ$ are shown in Figure 123.

The polarimetric characteristics of the leading edge of the plate in this scenario is that of linear polarization tilted at approximately 45° . This correlates well with the physical situation. At this aspect angle, the plate is viewed as an edge tilted at approximately 45° . Electromagnetically, the front edge of this type of structure supports a linear scattered field with this polarization [49].

6.4.2 Full-Polarization Analysis of Fifteen Degree Polar Swaths of Data with Higher Model Orders

Next, the same nine 15° polar swaths of the data are analyzed using FPA2. The model orders were chosen to be larger to determine their effect on the REs and the ellipse locations and form. The results are shown in Figures 125 through 127. In these figures, only the six highest energy pole locations are shown in each case.

The model orders used and the relative error for the FPA2 generated estimates are given in Table 14. The REs were determined from all of the parameters estimated by FPA2 (not just the six highest energy modes). As in the single polarization cases, the REs are lower when the larger model orders are chosen.

For the corner dominated scenarios ($15^\circ \leq \phi \leq 75^\circ$), the predominant scattering ellipses are, in general, the same as the ellipses for the lower model orders. The remaining two ellipses for each angle are smaller in size than the predominant ellipses, and usually placed near one of the corners. For the edge dominated scenarios, the additional ellipses help the 2-D TLS-Prony Technique more completely model the data.

As with the single polarization cases, noise was added to two full-polarization

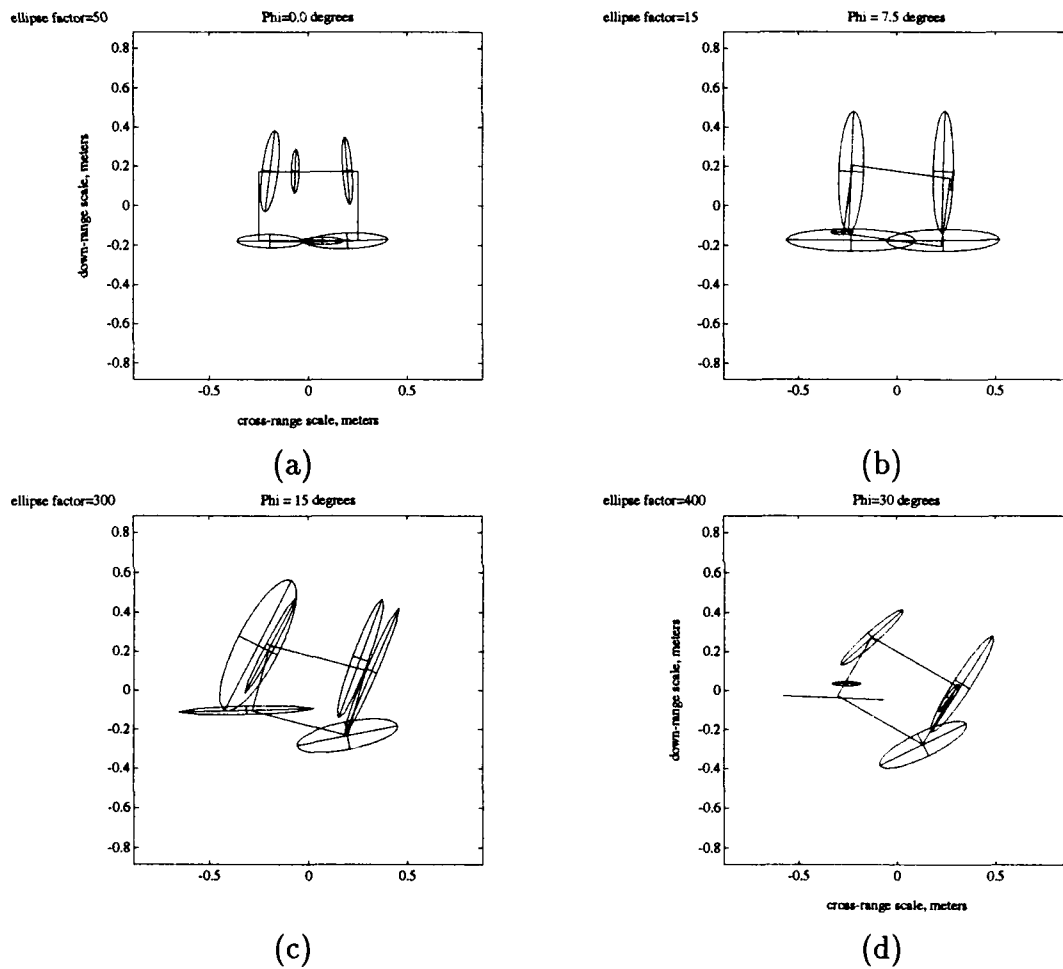


Figure 125: Full polarization flat plate example. Pole locations estimated by FPA2 are located at the centers of the ellipses. The data is a 15° polar swath centered around (a) 0° , (b) 7.5° , (c) 15° and (d) 30° . The model orders used are given in Table 14.

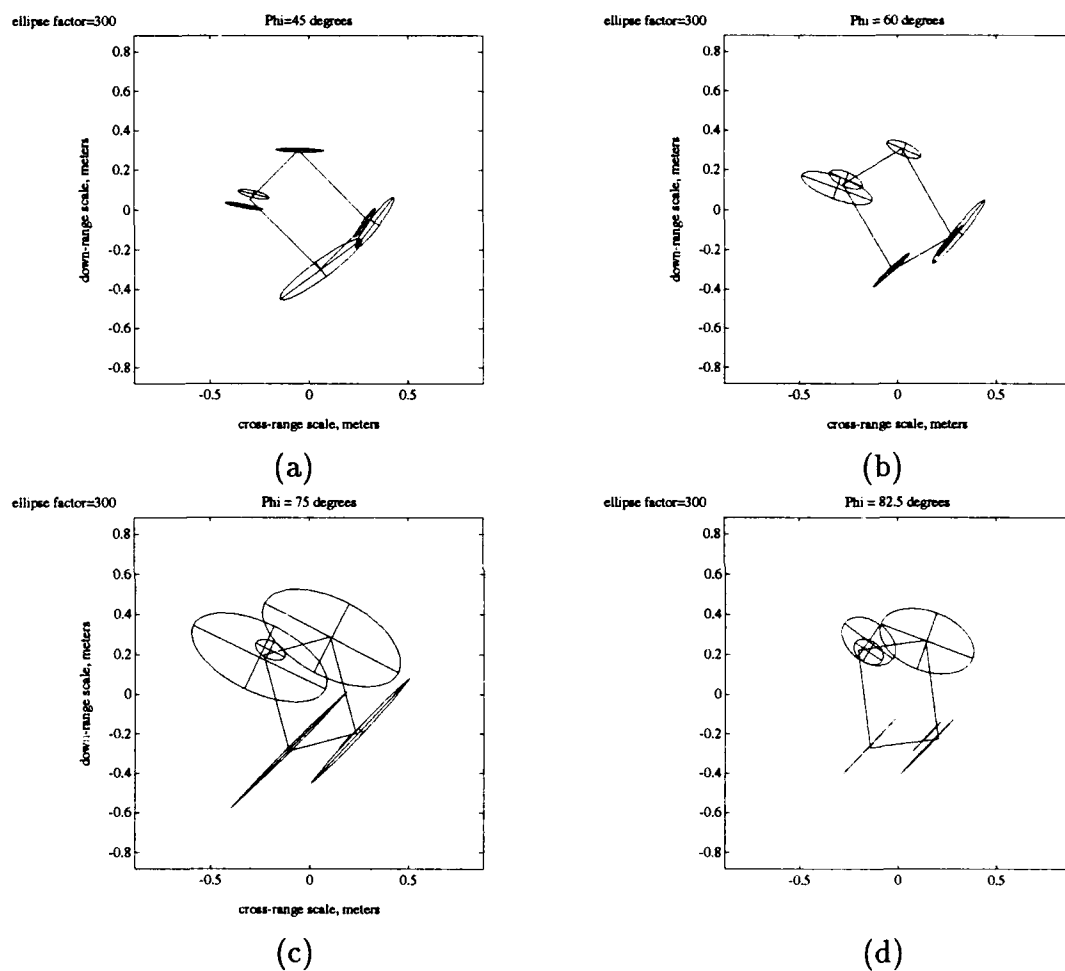


Figure 126: Full polarization flat plate example. Pole locations estimated by FPA2 are located at the centers of the ellipses. The data is a 15° polar swath centered around (a) 45° , (b) 60° , (c) 75° and (d) 82.5° . The model orders used are given in Table 14.

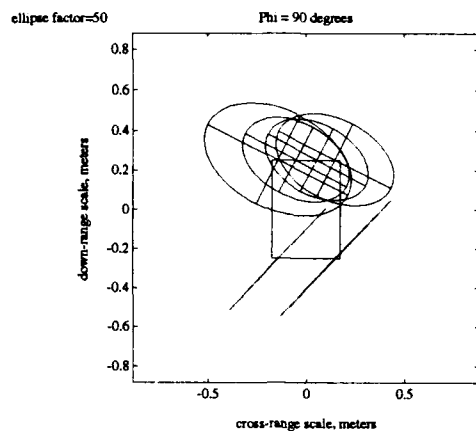


Figure 127: Full polarization flat plate example. Pole locations estimated by FPA2 are located at the centers of the ellipses. The data is a 15° polar swath centered around 90° . The model orders used are given in Table 14.

scenarios and the results are shown in Figure 128. From this figure, it can be seen that for a 15° polar swath of data with larger model orders, the REs (and the parameter estimates) are slightly more sensitive to total SNR than they are for the scenarios depicted in Figure 124.

6.4.3 Full-Polarization Analysis of Square Grids of Data Interpolated from Fifteen Degree Polar Swaths of Data

Next, the 15° polar swaths of data are interpolated onto a square grid as in the single polarization case. The 29×29 data set on the square grid is analyzed using FPA2. The results are shown in Figures 129 through 131. The effects of interpolating the polar data onto a square grid on the polarization ellipses is examined here.

The model orders chosen reflect the expected number of scattering centers on

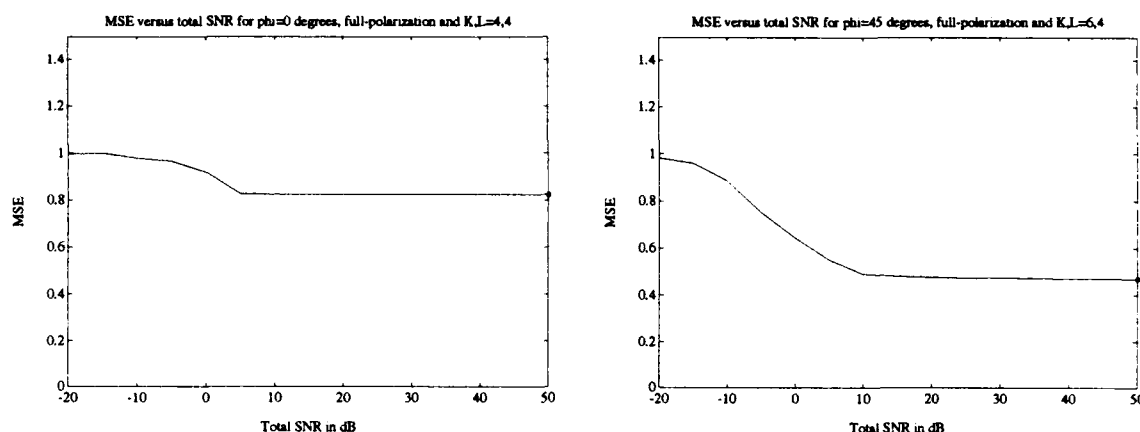


Figure 128: RE versus SNR for noise added to the GTD data of the plate. Full polarization results are shown for $\phi = 0^\circ$ and $\phi = 45^\circ$. The model orders are $Q, K, R, L = 10, 4, 10, 4$ for the $\phi = 0^\circ$ plot and $Q, K, R, L = 10, 6, 10, 4$ for the $\phi = 45^\circ$ plot. The 'o' at 50 dB in each plot is the RE for no noise added to the data for that scenario. The data is a 15° swath of polar data.

the plate for the corner dominated scenarios and for the edge dominated scenarios, the model orders are chosen slightly larger than the expected number of scattering centers. The relative error for the FPA2 generated estimates are given in Table 15. The REs in Table 15 are lower than the REs from Table 13 as expected. The pole locations are, in general, the same as the pole locations for the polar data examples. As with the single polarization cases, noise was added to two full-polarization scenarios and the results are shown in Figure 132. From this figure, it can be seen that for a square grid of data which was interpolated from a 15° polar swath of data, the REs (and the parameter estimates) are relatively constant for total SNRs over 10 dB.

The polarization ellipses estimated from the square grid data are nearly identical

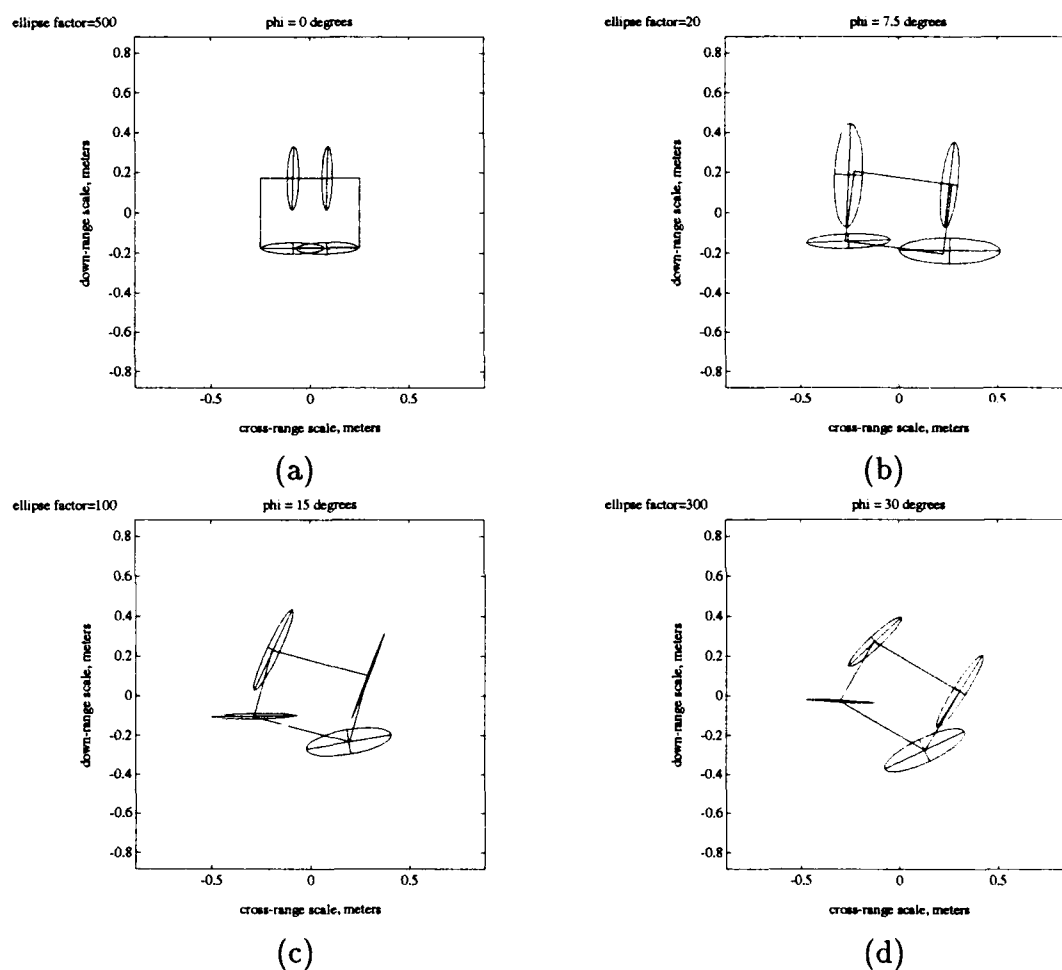


Figure 129: Full polarization flat plate example. Pole locations estimated by FPA2 are located at the centers of the ellipses. The data is a square grid interpolated from a 15° polar swath of data centered around (a) 0° , (b) 7.5° , (c) 15° and (d) 30° . The model orders used are given in Table 15.

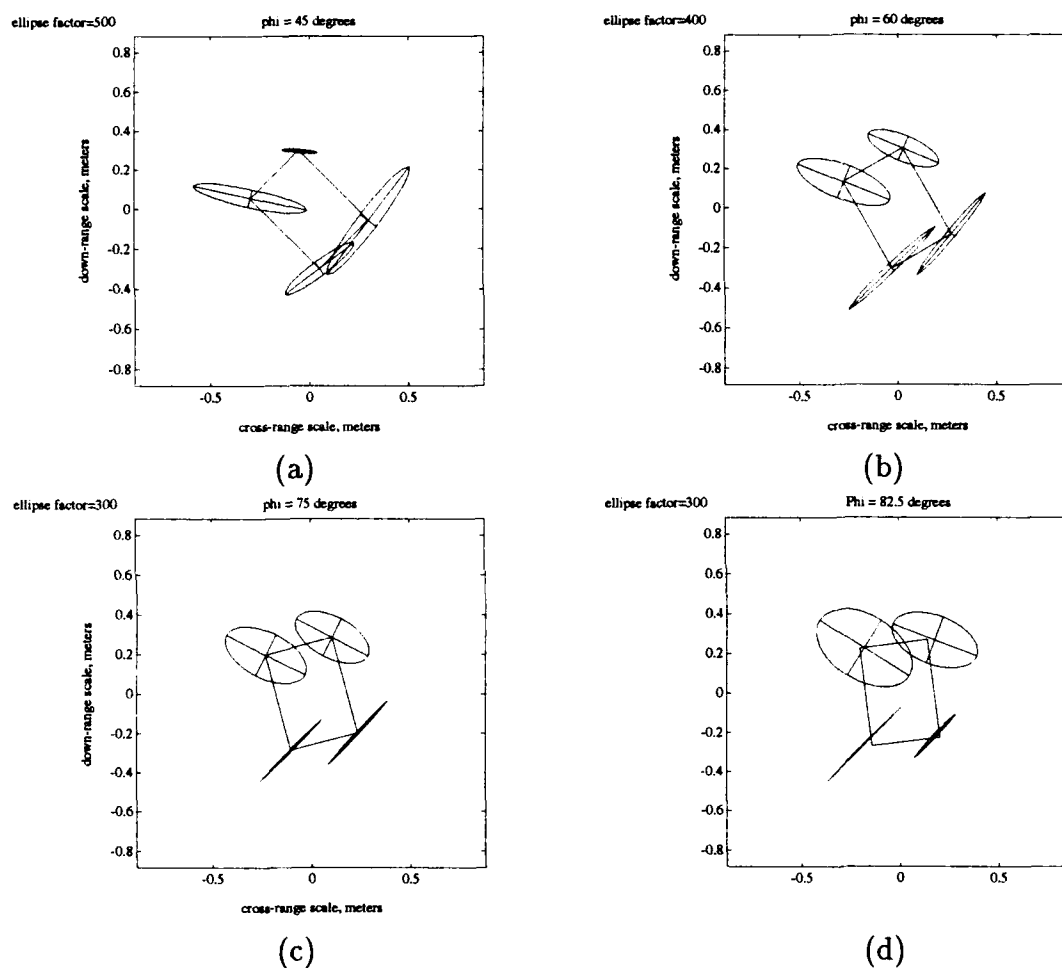


Figure 130: Full polarization flat plate example. Pole locations estimated by FPA2 are located at the centers of the ellipses. The data is a square grid interpolated from a 15° polar swath of data centered around (a) 45° , (b) 60° , (c) 75° and (d) 82.5° . The model orders used are given in Table 15.

Table 14: Model orders and relative errors for full-polarization results for the scattering from an inclined plate. The model orders for these examples were chosen higher than the model orders in Table 13. The data is a 15° angular swath of polar data.

Angle	Model Order, Q, K, R, L	RE_{fp}
0	10,4,10,4	0.8247
7.5	10,6,10,4	0.5926
15	10,6,10,4	0.5083
30	10,6,10,4	0.6072
45	10,6,10,4	0.4703
60	10,6,10,4	0.2332
75	10,6,10,4	0.3247
82.5	10,6,10,4	0.4185
90	10,4,10,4	0.3814

to the polarization ellipses found by using the polar data directly in FPA2. The REs for the square grid data estimates are lower than the REs for the polar grid data. Thus, even though the REs are larger when the polar data is used directly in FPA2, the parameter estimates are nearly identical to the parameter estimates obtained when square grid data is used.

6.4.4 Full-Polarization Analysis of Three Degree Polar Swaths of Data

Next, nine 3° polar swaths of the data are analyzed using FPA2. The results are shown in Figures 133 through 135. The model orders chosen reflect the expected number of scattering centers on the plate for the corner dominated scenarios and for the edge dominated scenarios, the model orders are chosen slightly larger than the

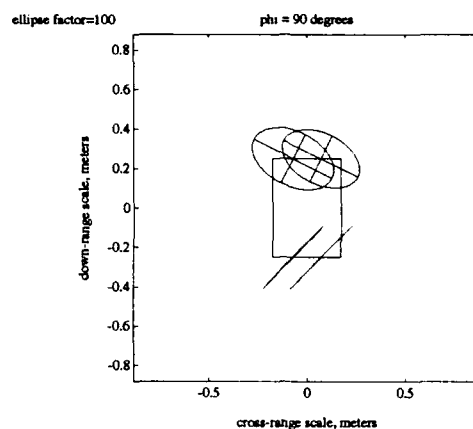


Figure 131: Full polarization flat plate example. Pole locations estimated by FPA2 are located at the centers of the ellipses. The data is a square grid interpolated from a square grid of data interpolated from a 15° polar swath of data centered around 90° . The model orders used are given in Table 15.

expected number of scattering centers. The polarization ellipses for these 3° data sets are nearly identical to the polarization ellipses for the 15° polar and square data sets. Thus the polarimetric characteristics of the plate are well estimated (it is assumed since the estimates are nearly identical for the various data sets, and since they correlate to the known physical characteristics of the plate, that the estimates are accurate) for the various 2-D angular and frequency bandwidths.

The relative errors for the FPA2 generated estimates are given in Table 16. As with the single polarization cases, noise was added to two full-polarization scenarios and the results are shown in Figure 136. From this figure, it can be seen that for the 3° polar swath of data, the RE for the $\phi = 0^\circ$ scenario is not very dependent upon SNR for SNRs over 15 dB. However, for the $\phi = 30^\circ$ and $\phi = 45^\circ$ scenarios, the REs are dependent upon SNR for SNRs up to 50 dB. This same phenomena was

Table 15: Model orders and relative errors for full-polarization results for the scattering from an inclined plate. The data lies on a square grid and was interpolated from a 15° polar swath of data.

Angle	Model Order, Q, K, R, L	RE_{fp}
0	10,2,10,2	0.9719
7.5	10,4,10,2	0.7102
15	10,4,10,1	0.3517
30	10,4,10,1	0.3326
45	10,4,10,1	0.3282
60	10,4,10,1	0.3133
75	10,4,10,1	0.3218
82.5	10,4,10,2	0.6766
90	10,2,10,2	0.9105

seen in the single polarization case as depicted in Figures 117 and 118 and is due to the fact that FPA2 is superresolving scattering centers.

In order to show how the scattering center locations and polarimetric characteristics are affected by noise, several ellipse plots are shown in Figure 137. These plots correspond to the scenario for full-polarization and $\phi = 45^\circ$ with model orders $Q, K, R, L=10,4,10,1$. Ten overlaid realizations are shown for each plot. The ellipses estimated from the noise corrupted GTD data are overlaid on one another. Recall that the estimated scattering center location is located at the center of the ellipse. The pole locations estimated directly from the GTD data, with no noise added, are designated by 'o's. Six plots are shown, each for a specific SNR between 0 and 50 dB. From these plots, it can be seen that the polarimetric characteristics and the locations the two largest scattering centers (corners C2 and C3) are well

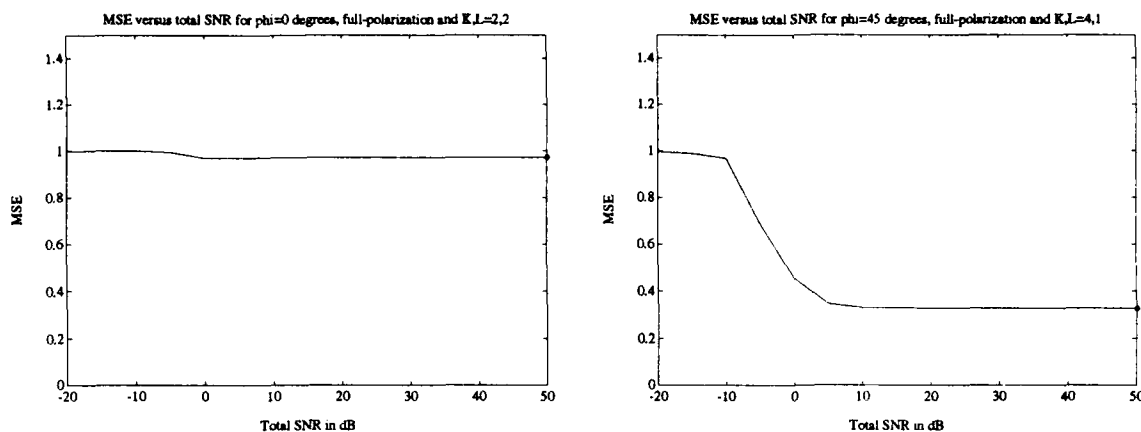


Figure 132: RE versus SNR for noise added to the GTD data of the plate. Full polarization results are shown for $\phi = 0^\circ$ and $\phi = 45^\circ$. The model orders were $Q, K, R, L = 10, 2, 10, 2$ for the $\phi = 0^\circ$ plot and $Q, K, R, L = 10, 4, 10, 1$ for the $\phi = 45^\circ$ plot. The 'o' at 50 dB in each plot is the RE for no noise added to the data for that scenario. The data lies on a square grid which was interpolated from a 15° swath of polar data.

estimated for SNRs as low as 10 dB. However, the other two corners are not well estimated below 40 dB. As in the single polarization case, the model orders are raised to $Q, K, R, L = 10, 4, 10, 2$ in an attempt to allow FPA2 to better estimate the four scattering centers. The results are shown in Figure 137. These plots show ten overlaid realizations, where the four ellipses that correspond to the four highest energy modes are shown. As can be seen from these plots, the four corners are well estimated for total SNRs as low as 20 dB. Thus, as in the single polarization case, raising the model order allows FPA2 to better estimate the scattering centers.

The REs in Table 16 are the lowest for all of the full-polarization examples. As with the single polarization examples, the smaller angular bandwidth allows the scattering centers to be more accurately modeled. This is due to several factors.

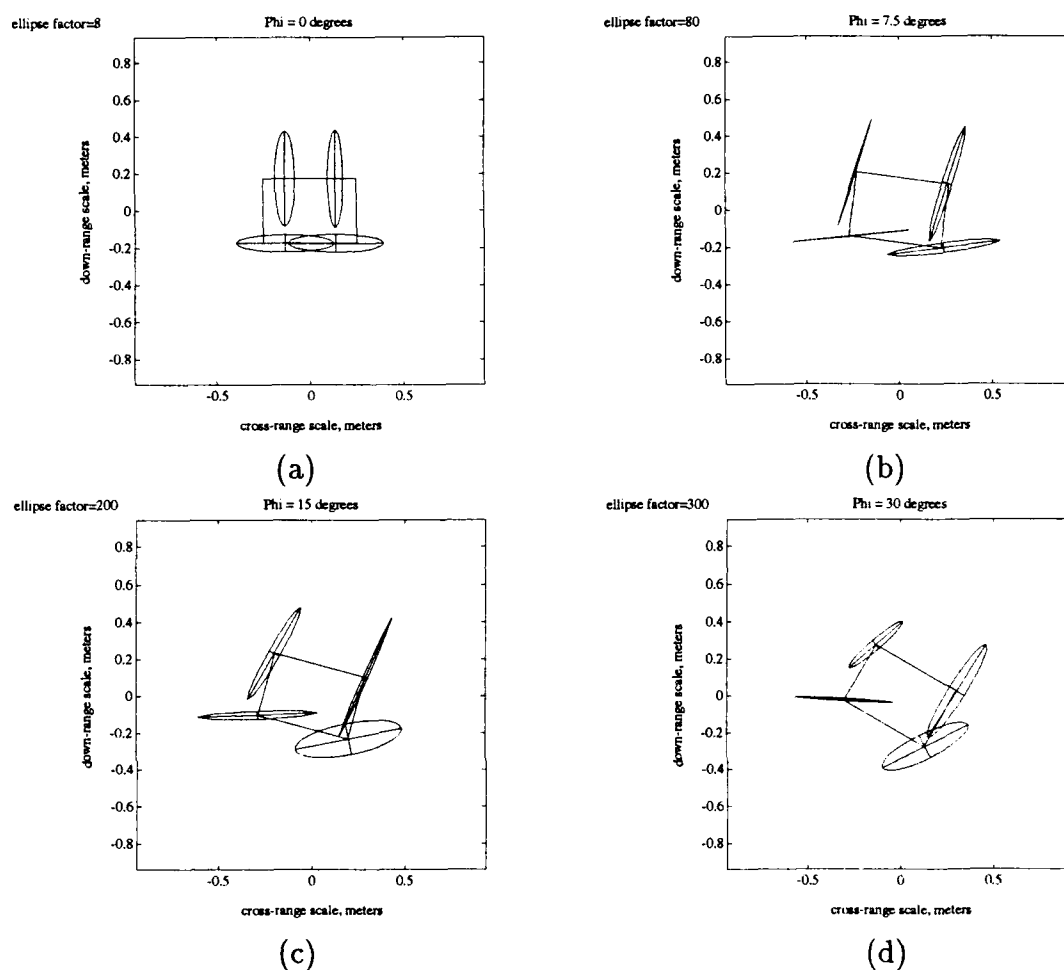


Figure 133: Full polarization flat plate example. Pole locations estimated by FPA2 are located at the centers of the ellipses. The data is a 3° polar swath centered around (a) 0° , (b) 7.5° , (c) 15° and (d) 30° . The model orders used are given in Table 16.

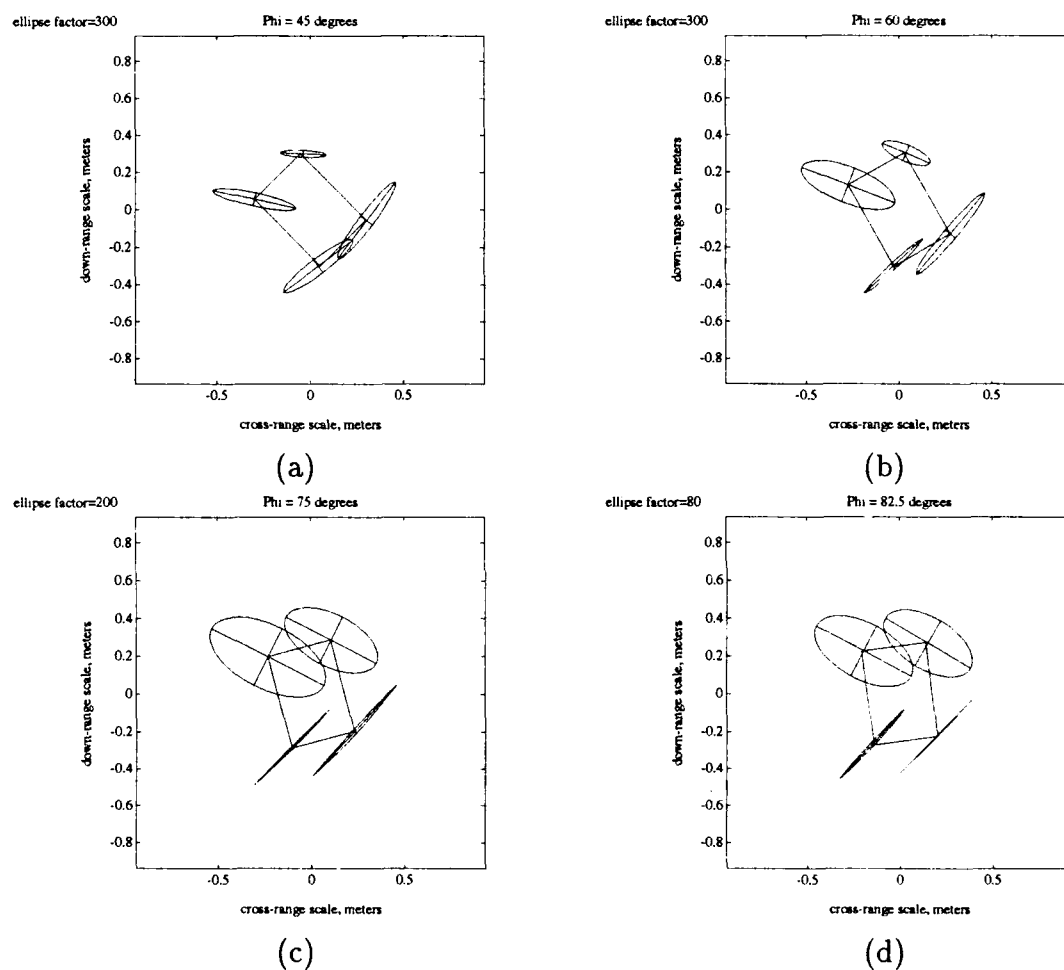


Figure 134: Full polarization flat plate example. Pole locations estimated by FPA2 are located at the centers of the ellipses. The data is a 3° polar swath centered around (a) 45° , (b) 60° , (c) 75° and (d) 82.5° . The model orders used are given in Table 16.

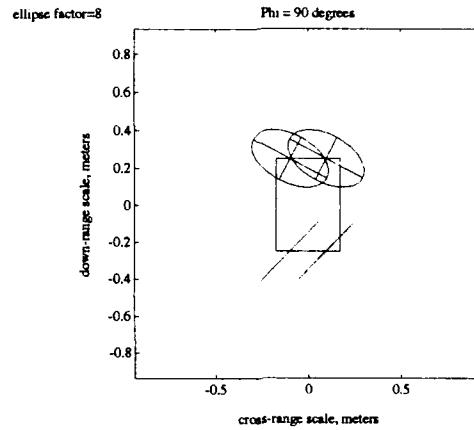


Figure 135: Full polarization flat plate example. Pole locations estimated by FPA2 are located at the centers of the ellipses. The data is a 3° polar swath centered around 90° . The model orders used are given in Table 16.

First, over larger angular bandwidths, the scattering centers appear to “move” to the 2-D TLS-Prony algorithm over the various angular cuts, since the data is expected to lie on a rectangular grid but was actually measured on a polar grid in the 2-D frequency plane. Also, when the data is interpolated onto a square grid, the scattering centers no longer move, but interpolation error is introduced. When the data is taken over a smaller angular bandwidth, the movement of the scattering centers is small enough to keep the RE small and there is no need to interpolate the data to a square grid. However, as was also seen in the single polarization examples, the estimation of parameters from the data over a smaller angular and frequency bandwidth is more sensitive to noise.

From all of the RE versus total SNR plots, with the exception of the $\phi = 45^\circ$ and $\phi = 30^\circ$ scenarios for 3° polar swaths of data, it is apparent that for Total

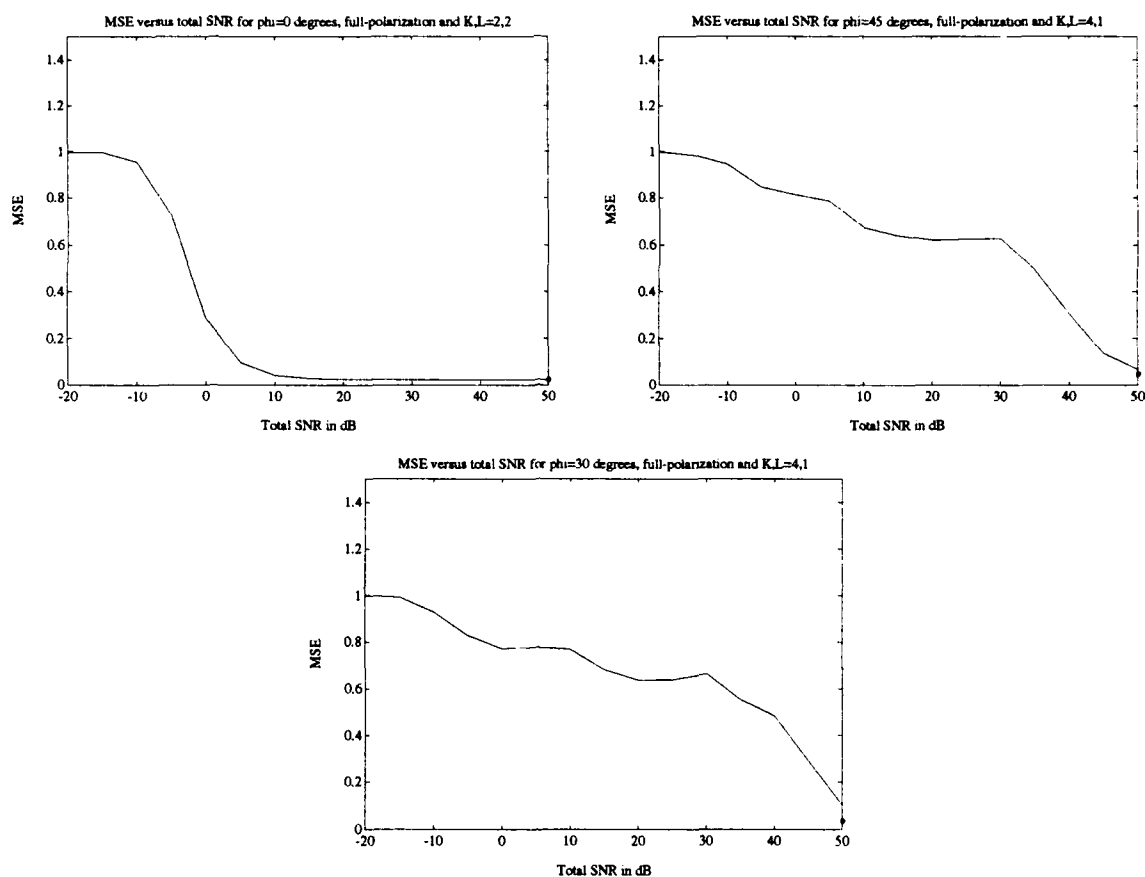


Figure 136: RE versus SNR for noise added to the GTD data of the plate. Full polarization results are shown for $\phi = 0^\circ$, $\phi = 30^\circ$, and $\phi = 45^\circ$. The model orders are $Q, K, R, L = 10, 2, 10, 2$ for the $\phi = 0^\circ$ plot and $Q, K, R, L = 10, 4, 10, 1$ for the $\phi = 30^\circ$ and $\phi = 45^\circ$ plots. The 'o' at 50 dB in each plot is the RE for no noise added to the data for that scenario. The data is a 3° swath of polar data.

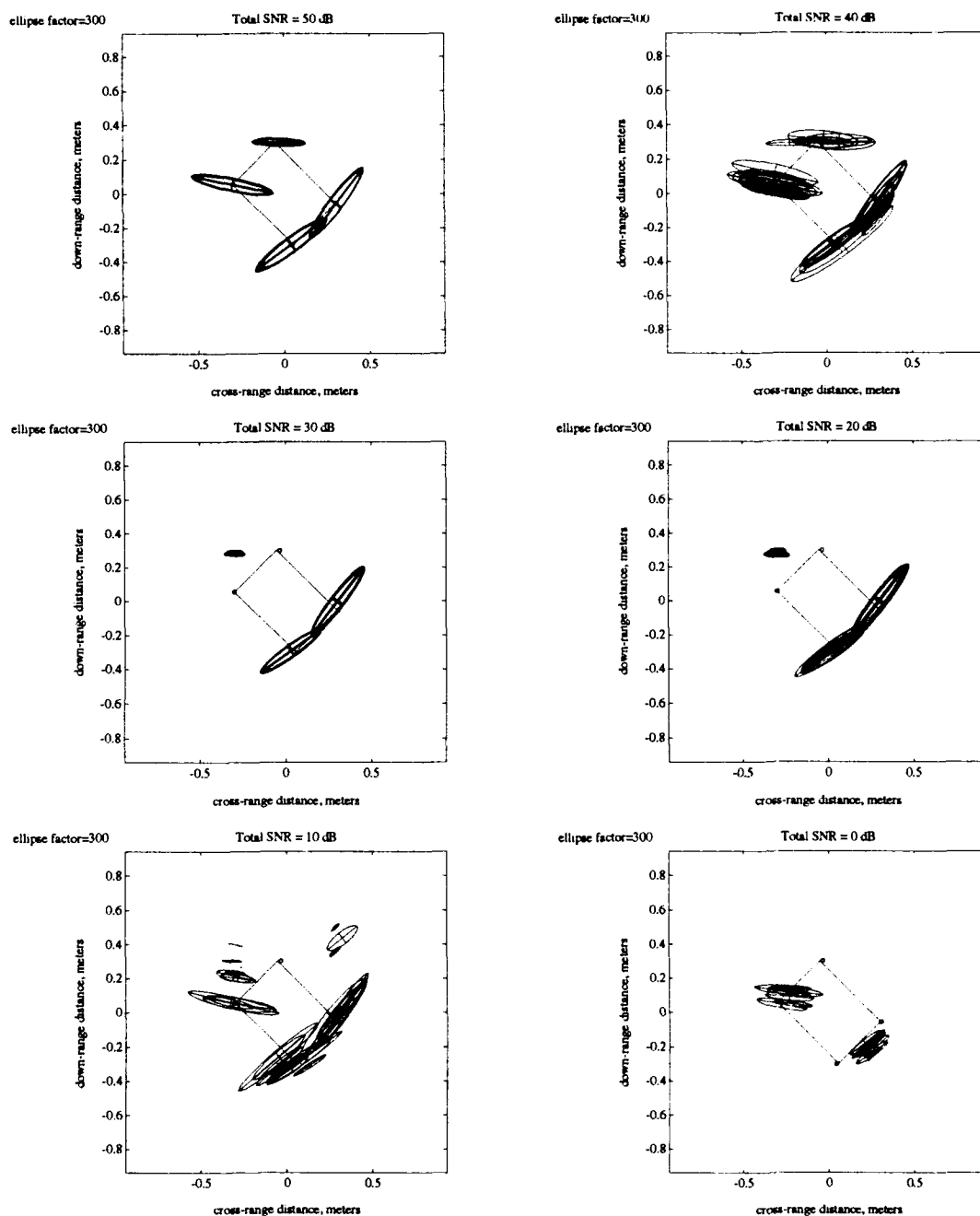


Figure 137: Estimated ellipses for noise corrupted GTD data. The GTD data is a full-polarization 3° polar swath. Each plot contains ten overlaid realizations, where all ten of the estimated ellipses for the noise corrupted GTD data are shown and the pole locations estimated directly from the GTD data are designated by 'o's. The model orders were $Q, K, R, L = 10, 4, 10, 1$ for all of the plots.

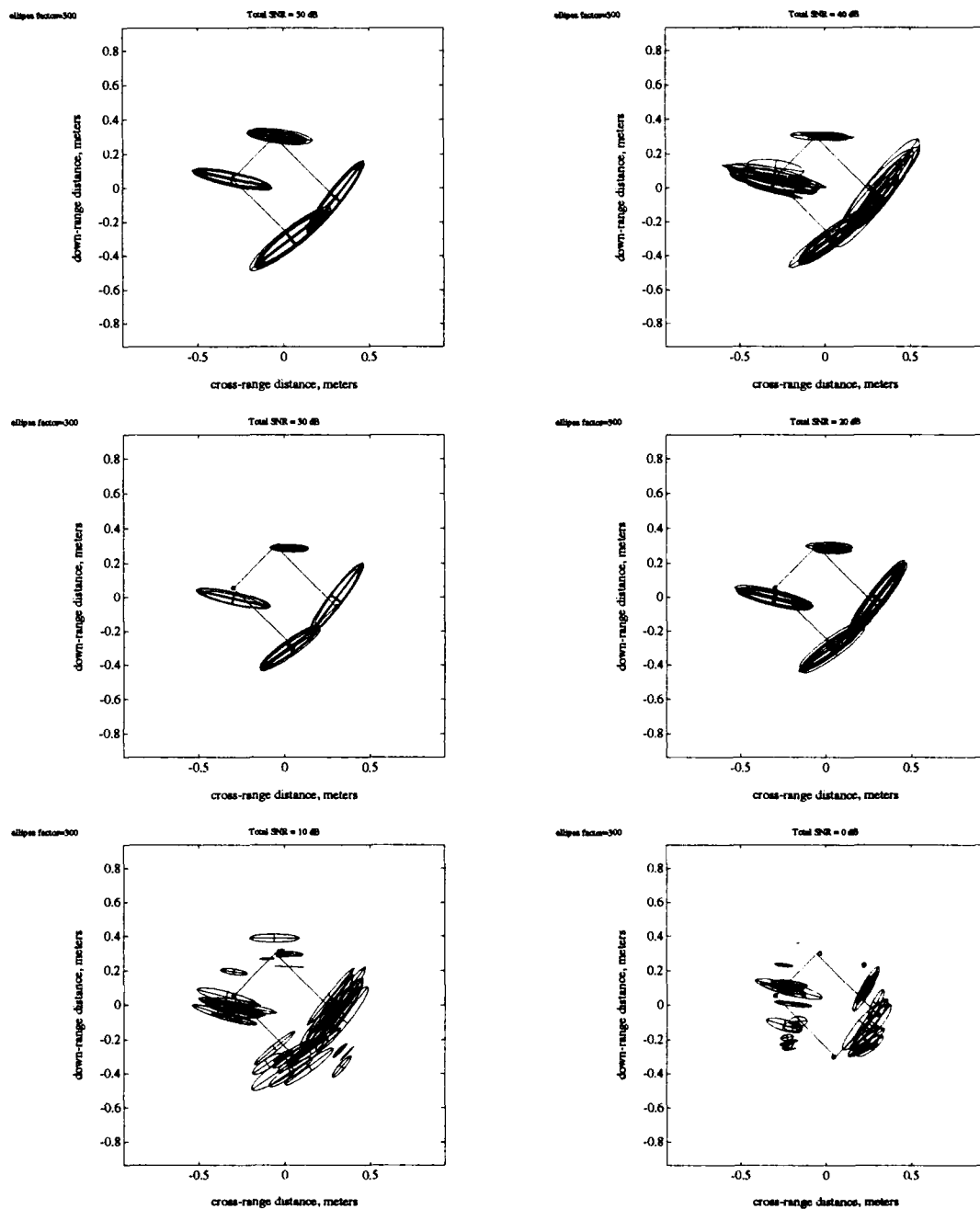


Figure 138: Estimated ellipses for noise corrupted GTD data. The GTD data is a full-polarization 3° polar swath. Each plot contains ten overlaid realizations, where all ten of the estimated ellipses for the noise corrupted GTD data are shown and the pole locations estimated directly from the GTD data are designated by 'o's'. The model orders were $Q, K, R, L = 10, 4, 10, 2$ for all of the plots. Only the four ellipses corresponding to the four highest energy modes are shown in the plots.

Table 16: Model orders and relative errors for full-polarization results for the scattering from an inclined plate. The data is a 3° angular swath of polar data.

Angle	Model Order, Q, K, R, L	RE_{fp}
0	10,2,10,2	0.0232
7.5	10,4,10,2	0.0772
15	10,4,10,1	0.0413
30	10,4,10,1	0.0351
45	10,4,10,1	0.0479
60	10,4,10,1	0.1077
75	10,4,10,1	0.0561
82.5	10,4,10,2	0.0531
90	10,2,10,2	0.0589

SNRs over 15 dB, the RE is very near the RE for no noise added to the GTD data. This demonstrates the noise cleaning ability of the estimation techniques which were discussed in detail in Chapter V. This also implies that the parameter estimates are not effected by noise for the scenarios where the REs are not effected by noise.

There is a trade-off between the size of the 2-D angular and frequency bandwidths of the data gathered and the noise tolerance of the estimation technique. One method to decrease the effects of noise on the smaller 2-D frequency and angular bandwidth data (3° polar data set) is to take a larger data set over the same angular and frequency bandwidths. This larger data set should allow the 2-D TLS-Prony algorithms to better estimate the scattering center locations, damping factors and amplitudes. Another method to decrease the effects of noise on the parameter estimates for the 3° data set is to take the data over a 2-D angular and frequency bandwidth which is larger than the 3° polar data examined here, but not larger than

the 15° data set (thus, somewhere around 6° may be appropriate).

The results for the 15° polar swaths of data (both on the original polar grid and the square grid) had REs which can be considered high, but they still estimated the scattering center locations and damping factors well, as can be seen by comparing the results for these cases with the results for the 3° polar swaths of data. It is not necessarily true that if a given model models the data with a larger RE, that the parameter estimates are not representative of the modes which exist in the data. For the 15° polar swaths of data, it is assumed that the parameter estimates are accurate, since they match the parameter estimates for the 3° polar swaths of data, with no noise added to the data. The 3° polar swaths of data, with no noise added to the data, are considered accurate since the REs associated with these data sets are relatively low.

6.5 Analysis of Individual Scattering Centers on Plate

Recall from Chapter III that the response of a corner as a function of frequency is $\frac{1}{\omega}$ and as a function of angle is a constant (for non-grazing situations). In Chapter III, the ability of a damped exponential to model the frequency behavior of a corner was demonstrated. Here, the frequency and angle responses of the estimates for the individual corners on the plate are compared to the $\frac{1}{\omega}$ and constant behaviors of a corner. Consider the single polarization plate simulation for hh -polarization and $\phi = 45^\circ$. Two data sets are examined, the square grid of data interpolated from the 15° swath of polar data, and the 3° swath of polar data. For both data sets, eight plots are shown over two figures.

The GTD code described in [49] has the capability to predict the scattering due to an individual corner on the plate. This capability is used here. The 2-D TLS-Prony Technique is used to estimate the parameters from a data set which contains the scattering response of a single corner on the plate. The model orders are set at $Q, K, R, L = 10, 1, 10, 1$ for the scenarios where the data contains the scattering response for a single corner on the plate. For the 2-D Prony Model in Equation 5.2, recall that the x -poles correspond to the frequency portion of the 2-D frequency domain data while the y -poles correspond to the angle portion of 2-D frequency domain data.

For each data set, the first four plots contain frequency response data, one plot for each corner of the plate. Shown are the frequency responses at 45° as taken from the data (solid line) and as estimated by the model. Two model estimates are shown in each plot; the first (dashed line) corresponds to the estimates from the data set generated for only one corner of the plate while the second (dash-dotted line) corresponds to the estimates from the complete data set for the plate. Also shown in each plot is the model assumed $\frac{1}{\omega}$ behavior for the corner (dotted line, this plot is difficult to see since it nearly overlaps the solid line).

The second four plots for each data set contain angular response data, one for each corner of the plate. As with the frequency response plots, shown are the angular responses at 45° as taken from the data (solid line) and as estimated by the model. Two model estimates are shown in each plot, the first (dashed line) corresponds to the estimates from the data set generated for only one corner of the plate while the

second (dash-dotted line) corresponds to the estimates from the complete data set for the plate. The model assumed constant behavior of the corner is not shown in the angular plots.

From the results shown in Figures 139 through 142, it is observed that the damped exponential model is appropriate for the scattering from the corners of the plate around $\phi = 45^\circ$, as was also concluded in Chapter III. Several full-polarization scenarios were run (but not shown here) and the results are similar to the results shown for the single-polarization case. In the figures corresponding to the angular dependencies of the scattering centers, it is seen that the data shown is not constant as a function of angle, but a smooth function which is close to a constant. A more appropriate model for the angular behavior of a corner (in non-grazing situations) might be a damped exponential, which, of course, is what is used in the 2-D TLS-Prony Technique. A constant was chosen in Table 1 since it was the simplest model which was close to the actual scattering behavior of a corner in non-grazing situations.

6.6 Summary

In this chapter several radar target modeling examples, involving simulated radar data, were discussed. The scattering from an inclined thin metal plate was generated using the GTD. This data was then used by both the single-polarization and the full-polarization 2-D TLS Prony Techniques to estimate the locations, damping factors and polarimetric characteristics of the scattering centers on the plate. Issues involving 2-D angular and frequency bandwidths, model order selection, ef-

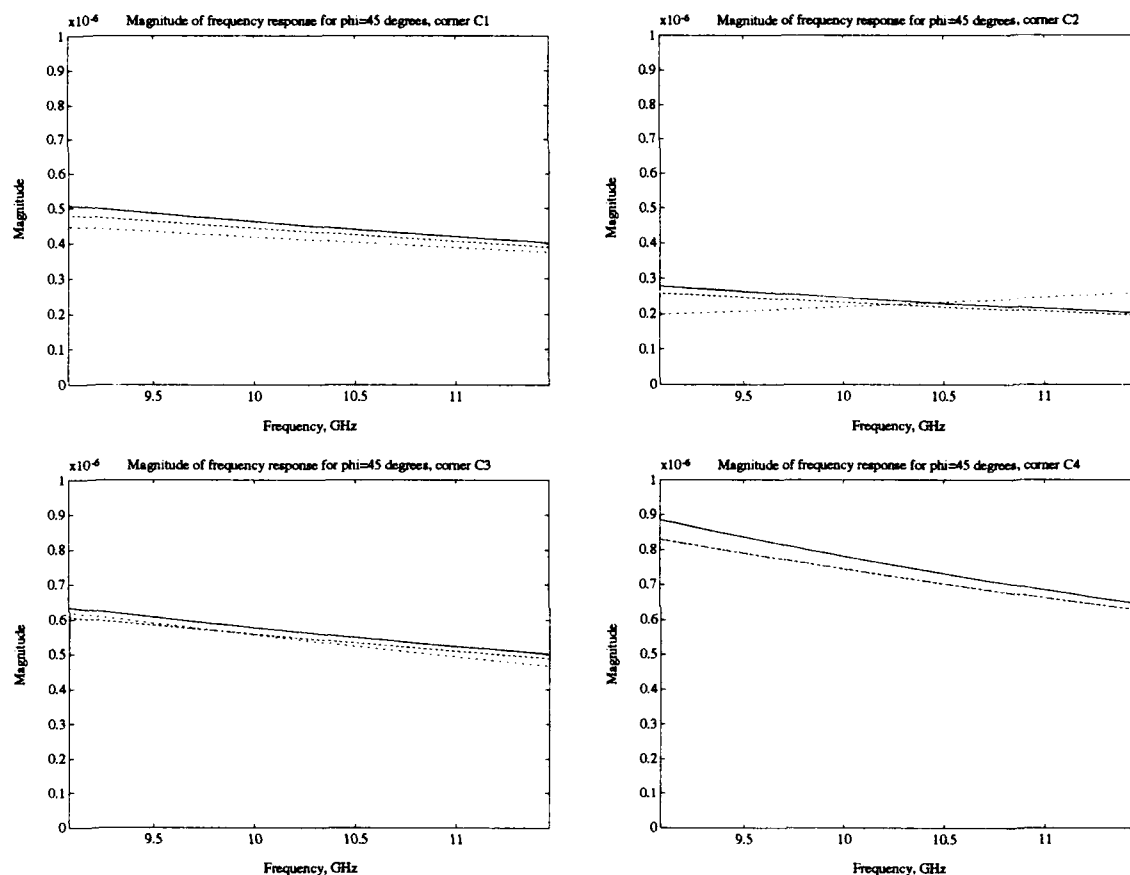


Figure 139: Frequency response comparisons for parameter estimates from a square grid of data generated from a 15° polar swath of data centered around $\phi = 45^\circ$. Each plot corresponds to a corner of the plate. The solid line is the magnitude of the actual scattering data at 45° . The dashed line is the magnitude of the frequency data generated by the parameters estimates from the single corner data set at 45° . The dash-dotted line is the magnitude of the frequency data generated by the parameters estimates from the full plate data set at 45° . The dotted line is the ideal $\frac{1}{\omega}$ frequency behavior of the corner.

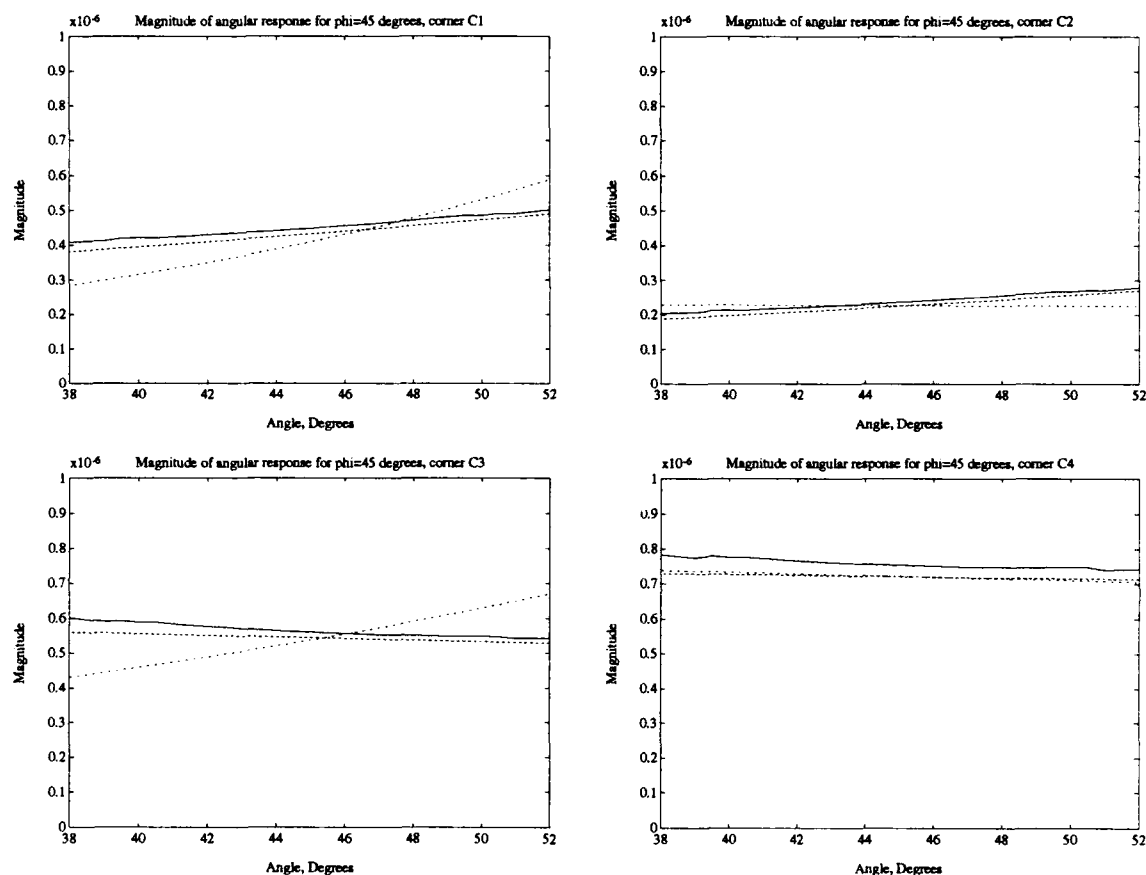


Figure 140: Angular response comparisons for parameter estimates from a square grid of data generated from a 15° polar swath of data centered around $\phi = 45^\circ$. Each plot corresponds to a corner of the plate. The solid line is the magnitude of the actual scattering data at 9.24 GHz. The dashed line is the magnitude of the angular data generated by the parameters estimates from the single corner data set at 9.24 GHz. The dash-dotted line is the magnitude of the angular data generated by the parameters estimates from the full plate data set at 9.24 GHz.

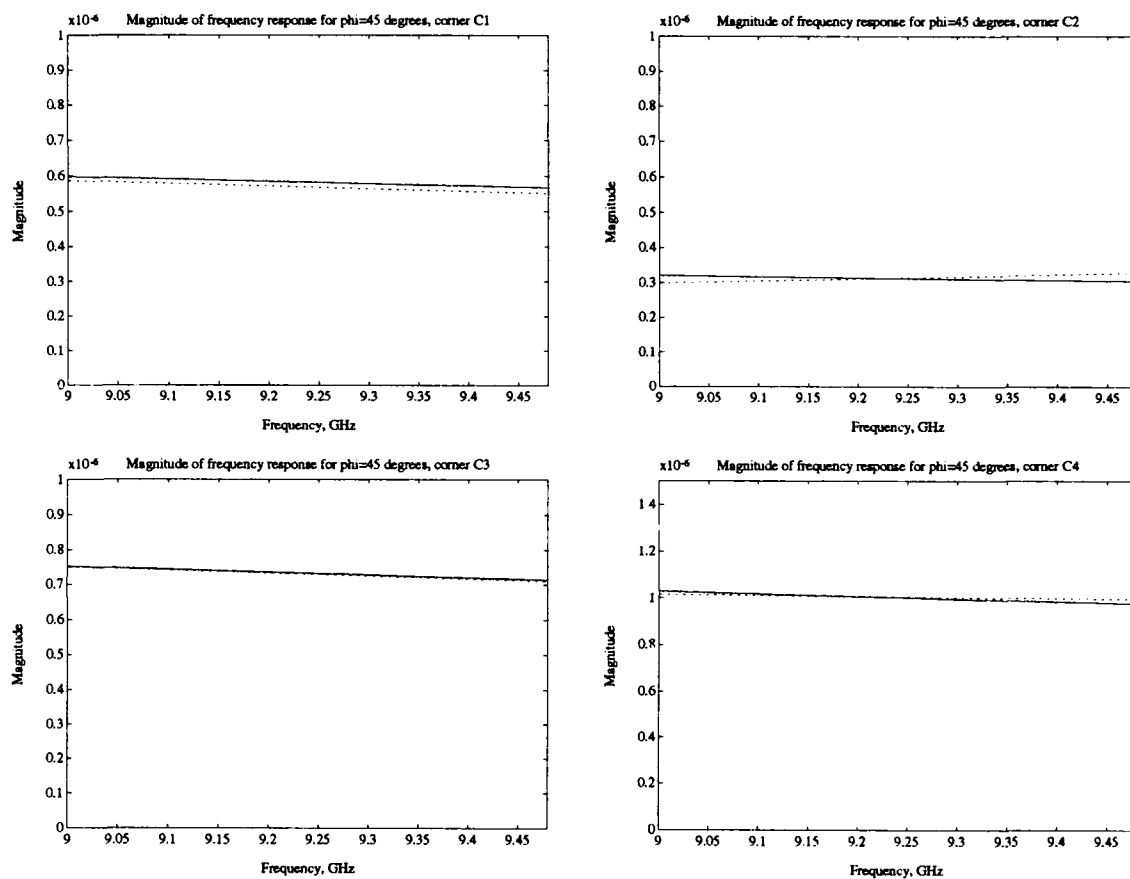


Figure 141: Frequency response comparisons for parameter estimates from a 3° polar swath of data centered around $\phi = 45^\circ$. Each plot corresponds to a corner of the plate. The solid line is the magnitude of the actual scattering data at 45° . The dashed line is the magnitude of the frequency data generated by the parameters estimates from the single corner data set at 45° . The dash-dotted line is the magnitude of the frequency data generated by the parameters estimates from the full plate data set at 45° . The dotted line is the ideal $\frac{1}{\epsilon}$ frequency behavior of the corner.

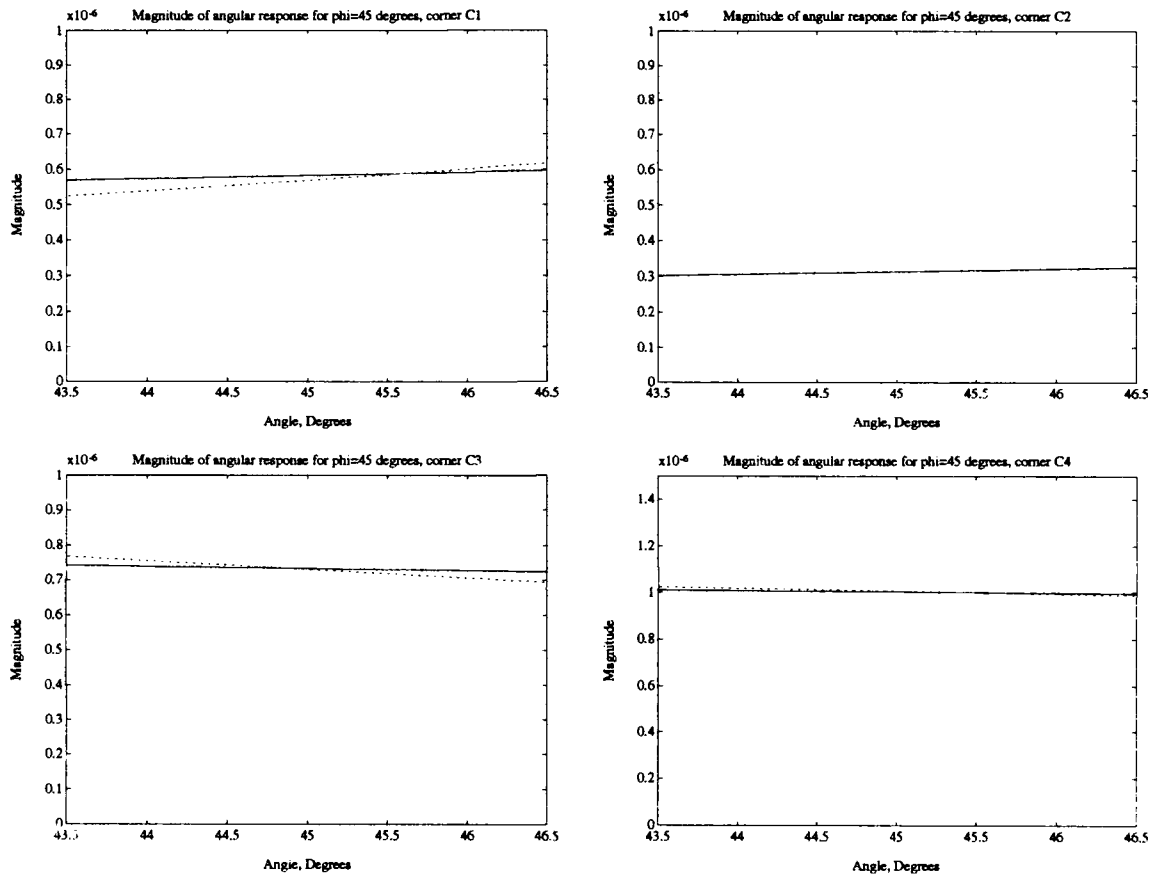


Figure 142: Angular response comparisons for parameter estimates from a 3° polar swath of data centered around $\phi = 45^\circ$. Each plot corresponds to a corner of the plate. The solid line is the magnitude of the actual scattering data at 9.24 GHz. The dashed line is the magnitude of the angular data generated by the parameters estimates from the single corner data set at 9.24 GHz. The dash-dotted line is the magnitude of the angular data generated by the parameters estimates from the full plate data set at 9.24 GHz.

fects of noise on parameter estimates, and the form (polar grid or square grid) of the data set on the 2-D frequency plane were addressed. Also, the validity of the damped exponential to model the scattering from the canonical scattering centers was addressed.

CHAPTER VII

Summary and Conclusions

7.1 Summary of Work and Conclusions

This focus of this work has been to develop signal processing algorithms and models for the scattering from radar targets. The models, which are summarized in Table 1, are based upon the high-frequency electromagnetic scattering characteristics of the canonical scattering centers analyzed. The algorithms developed can be used to reduce the raw radar data of a complicated radar target to a set of estimated descriptive parameters which can be used by a classification algorithm to identify the target. As stated before, a basic assumption of this work is that the scattering from radar targets can be comprised as the sum of the scattering from a finite number of canonical scattering centers in the high-frequency case. This is a valid assumption if the scattering centers are electrically isolated. This is also a reasonable assumption even if two scattering centers are electrically close, since their combined response can be treated as the response from a new type of canonical scattering center. Recall that the high-frequency case implies that the overall target size is at least one wavelength.

The electromagnetic modeling of the canonical scattering centers used exact and

approximate methods of scattering prediction. Exact methods were used where possible. The sphere for all aspect angles has an exact scattering solution for plane wave incidence. The right-circular cylinder also has an exact scattering solution, but only for limited aspect angles. The remainder of the canonical scattering centers analyzed do not have exact scattering solutions, and approximate techniques such as the Method of Moments (MM) and the Geometrical Theory of Diffraction (GTD) were used to estimate their scattering characteristics. The MM and the GTD were both used to predict the scattering from canonical scattering centers such as the corner, edge, flat plate, dihedral, and trihedral. Once the scattering characteristics of all of the canonical scattering centers were investigated, models were developed and are summarized in Table 1. These models characterize the scattering from the canonical scattering centers as functions of frequency and angle. These exact models are not contained in the 2-D damped exponential Prony model in Equation 5.2, but the damped exponential model can accurately approximate most of the electromagnetically based models in Table 1. All of the frequency models and one of the angular models are well approximated by damped exponentials. Two of the angular models, however, are not well modeled using damped exponentials, as discussed in Chapter III.

The reason that a damped exponential model was chosen as the model for the 2-D TLS-Prony Technique over the electromagnetically based models is that the estimation algorithm developed for the 2-D TLS-Prony Technique required a damped exponential model. Recall that the 2-D TLS-Prony Technique is an extension of

the 1-D TLS-Prony Technique developed in [29]. It may be possible to develop a 2-D estimation algorithm based on a model which directly uses the electromagnetic models, but that is beyond the scope of this work. This type of estimation algorithm has been developed in 1-D by Carrière and Moses [61].

It must also be noted that even though the damped exponential does not model all of the scattering centers well, it is still an improvement in the modeling of radar scattering. Much of the previous work in RTI assumed a point scatterer model for the scattering from all types of canonical scattering centers [34], [35], [39]. The extension to a 2-D damped exponential model is an improvement over the point scatterer model.

The 2-D TLS-Prony Technique is not limited to the analysis of radar signals. As demonstrated in Chapter V, the technique is capable of solving the general 2-D frequency estimation problem. This technique can be applied to other areas such as tomography, sonar, radio astronomy, and medical imaging to name a few. The use of damped exponentials allows the poles in transform domain spectra (range-domain in the radar problem) to have a dispersion. This is useful in modeling radar targets. The execution time of this algorithm can be optimized since several of the steps require a number of independent calculations which can be done in parallel.

The statistics of the 2-D TLS-Prony Technique algorithms are estimated and compared to their respective Cramér-Rao Bounds (CRBs) in Chapter V for some undamped and damped exponentials in noise examples utilizing a number of Monte-Carlo simulations. The x and y -pole estimates had different statistics, the x -pole

estimates being more accurate than the y -pole estimates, when Algorithm One and FPA1 were used since the y -pole estimates were based on the x -amplitude coefficients as the input data. Thus, a propagation of error caused the y -poles estimates to have variances which were farther away from their respective CRBs than the x -pole variances were away from their respective CRBs. This difference in estimates was removed in Algorithm Two and FPA2 by utilizing the original algorithms twice. First, the x -poles are estimated and then the y -poles are estimated. Then the y -poles are estimated first followed by the x -poles. These two sets of pole pairs are combined and the more accurate estimates from each set are retained. This method achieves y -pole estimates which are as accurate as the x -poles. Asymptotic expressions (asymptotic in SNR) for the actual statistics of the 1-D TLS-Prony estimation algorithm have been developed by Ying [62]. In future work, these results can be extended to achieve asymptotic expressions for the variance of the pole locations and amplitude coefficients for the 2-D TLS-Prony Technique.

The simulations described in Chapter VI demonstrate some of the capabilities and limitations of the 2-D TLS-Prony Technique. The ability of the 2-D TLS-Prony Technique to determine the scattering center locations for various angular and frequency bandwidths is well demonstrated. Comparing the single-polarization results and the full-polarization results, it is apparent that the full-polarization ellipses give an excellent representation of the polarimetric characteristics of each scattering center on a target. There is a trade-off involving the angular and frequency bandwidths on the 2-D frequency plane when the polar data is directly used by the algorithms.

For larger angular and frequency bandwidths (15° for this work), the effects of noise on the parameter estimates and the relative error (RE) are insignificant for SNRs over 15 dB; however, the RE is relatively high. For smaller angular and frequency bandwidths (3° for this work), the effects of noise are more severe than they are for the larger bandwidths, but the RE between the model and the original data is relatively small for high SNRs when compared to the larger angular and frequency bandwidths. The effects of noise on the parameter estimates for the smaller angular and frequency bandwidths are demonstrated in the scatter plots shown for the 3° polar data cases. For low SNR, the parameter estimates are degraded and this is reflected in the larger RE. Thus, for low SNR and smaller angular bandwidths it is appropriate to use a larger model order as discussed and demonstrated in Chapter VI.

The superresolution capabilities of the 2-D TLS-Prony Technique is demonstrated in two sets of simulations. First, the simulations in Chapter V involve sinusoids in noise which are only 0.4 Fourier Bins apart. The 2-D TLS-Prony Technique easily resolves the sinusoids for SNRs as low as 10 dB. Second, the flat plate examples in Chapter VI for the 3° polar swaths of data also demonstrate superresolution capabilities. The contour images of the plate generated using the 2-D IFFT show peaks in the range domain which are not located on the corners of the plate, but the estimated scattering center locations do lie almost exactly (much closer than the peaks in the contour image) on the corners of the plate, as they should.

For the data which was interpolated onto a square grid, the REs were lower than

the REs for the equivalent data on a polar grid, but the estimated pole locations were, in general, the same for either polar or square data over the same 2-D bandwidths. The REs may be reduced for the square grid data by developing a more appropriate interpolation method. The one used is a linear function to estimate the data values on the square grid from the surrounding polar values. An interpolation algorithm which takes the nature of the data into account may be more appropriate.

The analysis of the single scattering centers at the end of Chapter VI demonstrates the accuracy of the models in Table 1 and the abilities and limitations of the damped exponentials to model the data. The examples at $\phi = 45^\circ$ examined the responses from the corners in non-grazing situations, thus, their behavior is well modeled by damped exponentials.

One item of note should be mentioned concerning the difference between data taken on a polar grid and that taken on a rectangular grid. Recall in Section 3.5 that a correspondence between the angular model for the canonical scattering centers and the y -poles was made. The angular model for the canonical scattering centers assumed that the frequency is held constant and the response of the scattering center is modeled as the angle is varied. Thus, this corresponds to data on a polar grid. In Chapters V and VI, it is stated that the 2-D TLS-Prony Technique requires data on a rectangular grid, not a polar grid. Thus, there is a discrepancy since the estimation technique requires data on a rectangular grid and the model in Table 1 corresponds to data on a polar grid. For the scattering centers in Table 1, this is not a problem, since any of the angular responses can be modeled by a damped exponential equally

(as good as or as poorly as) on a rectangular grid or on a polar grid if the angular swath is of a reasonable size (15° is reasonable, as shown previously in the preceding simulations). Obviously, as the angular swath of the data gathered decreases, the polar and rectangular data will become more alike.

7.2 Areas for Future Research

The list of canonical scattering centers in Table 1 is not all inclusive for all types of radar targets. As new types of canonical scattering centers are examined, they can be added to this group. Also, new and improved scattering prediction techniques for the various types of canonical scattering centers are continuously being developed which can give more insight into the physical phenomena which cause the scattering from the various canonical scattering centers.

The development of a model and estimation algorithm based on the entries in Table 1 would be useful. As mentioned previously, a 1-D version has already been developed [61]. This version only used the frequency models in Table 1 and does not use the angular models in the table. The results of this 1-D version are equivalent to the results for the 1-D TLS-Prony Technique in terms of their ability to determine the scattering center locations for the scenarios shown in [61]. This is probably due to the fact that the scenarios investigated consisted of flat plate scattering examples away from grazing conditions, where the damped exponential gives an excellent approximation to the $\frac{1}{\omega}$ frequency response for the corner. The development of the 2-D estimation algorithm which can use both the frequency and angular models (especially the $U(\varphi)$ and $\delta(\varphi)$ angular models) should reduce the RE significantly.

A detailed statistical analysis of the 2-D TLS-Prony Technique is possible by extending the work of Ying [62]. By statistics, it is meant that the probability density function of the parameter estimates is determined. Ying developed the asymptotic (in SNR) statistics for the 1-D TLS-Prony Technique. These results give the asymptotic statistics for the x -poles and the x -amplitude coefficients. From Ying's analysis, the asymptotic statistics are very close to the actual statistics for SNR reasonable total SNR values (~ 10 dB per mode yields an error within 1 dB). This was confirmed by comparing the asymptotic statistics results with Monte-Carlo simulations. Recall that the x -amplitude coefficients serve as the input data to the second 1-D Prony model. Since the statistics of this "data" are known, Ying's approach can be used again to determine the statistics of the y -poles and the amplitude coefficients. Thus, the asymptotic statistics for all of the parameters estimated by Algorithm One can be determined. From this, the statistics of the parameters estimated by Algorithm Two can also be determined.

The effects of the 2-D angular and frequency bandwidths on the parameter estimates can be investigated further. The effects of the 2-D bandwidths are investigated to some extent here. It is shown that utilizing the polar data directly in the estimation algorithms gives accurate parameter estimates for both large angular swaths (15°) and small angular swaths (3°) even though the RE is very different for the two cases. Recall that even though the RE is relatively large, that does not necessarily mean that the parameter estimates are inaccurate. The development of an interpolation scheme that better fits the data should provide lower REs, but even

the square grid data analyzed here provided accurate parameter estimates.

For this work, the determination of model order was based upon knowledge of how many scattering centers are present on a target (*e.g.* four corners on a plate). When the number of scattering centers on a given target is unknown, a guess must be made. There is an upper bound on the guess. Recall that the initial orders of prediction for the x and y -poles were Q and R respectively. From a previous result [59], it is best to choose these two prediction orders to be one-third of the data length in the x and y -directions, respectively (*e.g.* $Q \approx \frac{M}{3}$ and $R \approx \frac{N}{3}$, where M and N are the data lengths as defined in Chapter V). It is also well known that choosing the model orders, K and L , less than their corresponding prediction orders, Q and R , leads to more accurate parameter estimates [53]–[55]. Thus the prediction orders, which are one-third of the data lengths, serve as the upper bounds on the model orders. Of course, if there are more scattering centers on the target than this upper bound, one of two solutions exist. The prediction orders can be chosen larger than one-third of the data lengths and thus the model orders can be chosen larger or, if possible, more data can be collected.

Even though the model orders have upper bounds, an accurate method for determining the correct model orders for a data set, with an unknown number of 2-D modes, does not exist for the 2-D TLS-Prony Technique. Several methods of model order selection for Auto-Regressive Moving-Average (ARMA) models are discussed in [10]. They include Final Prediction Error (FPE) and Minimum Description Length (MDL). These techniques involve varying the model order over a range and

choosing the "best" model order based upon a function which involves the model order and the RE between the estimated data and the original data. Techniques along these lines can possibly be extended to the 2-D TLS-Prony Technique.

REFERENCES

- [1] E. M. Kennaugh and D. L. Moffatt, "Transient and impulse response approximations," in *Proc. IEEE*, vol. 53, pp. 893-901, Aug. 1965.
- [2] W. L. Stutzman and G. A. Thiele, *Antenna Theory and Design*. New York, NY: John Wiley & Sons, 1981.
- [3] N. Akhter and R. J. Marhefka, "Far zone scattering from rectangular and triangular dihedrals in the principal plane," Tech. Rep. 721198-1, The Ohio State University, Department of Electrical Engineering, ElectroScience Laboratory, Feb. 1989.
- [4] C. F. Chen and C. H. Hsiao, "Stability tests for singular cases of discrete systems," *Circuits, Systems, and Signal Processing*, vol. 8, no. 2, pp. 123-132, 1989.
- [5] A. K. Jordan and W. W. Boerner, "Inverse methods in electromagnetic imaging," *ASI*, pp. 33-42, Jan. 1985.
- [6] E. M. Kennaugh and R. L. Cosgriff, "The use of impulse response in electromagnetic scattering problems," in *1958 IRE National Convention Record*, pp. 72-77, 1958.
- [7] D. L. Moffatt *et al.*, "Transient response characteristics in identification and imaging," *IEEE Transactions on Antennas and Propagation*, vol. AP-29, pp. 192-205, Mar. 1981.
- [8] R. Carrière and R. L. Moses, "Autoregressive moving average modeling of radar target signatures," tech. rep., in Proceedings of the IEEE 1988 National Radar Conference, pp. 225-229, Ann Arbor, MI April 20-21, 1988.
- [9] R. Carrière and R. L. Moses, "High resolution radar target modeling using ARMA models," tech. rep., The Ohio State University, Department of Electrical Engineering, ElectroScience Laboratory, May 1989.
- [10] S. M. Kay, *Modern Spectral Estimation, Theory and Application*. Englewood Cliffs, NJ: Prentice-Hall, 1988.
- [11] R. L. Moses and R. Carrière, "Parametric modeling of radar targets using canonical scattering centers," Tech. Rep. 719267-13, The Ohio State University, Department of Electrical Engineering, ElectroScience Laboratory, Dec. 1988.

- [12] P. M. Joseph and R. D. Spital, "The exponential edge-gradient effect in X-ray computed tomography," *Phys. Med. Biol.*, pp. 473-487, 1981.
- [13] R. M. Lewitt, "Reconstruction algorithms: Transform methods," in *Proc. IEEE*, vol. 71, pp. 390-408, Mar. 1983.
- [14] Y. Censor, "Finite series-expansion reconstruction methods," *Proceedings of the IEEE*, vol. 71, pp. 409-419, Mar. 1983.
- [15] D. J. Rossi and A. S. Willsky, "Reconstruction from projections based on detection and estimation of objects—parts i and ii: Performance analysis and robustness analysis," *IEEE Transactions on Acoustics, Speech, and Signal Processing*, vol. SP-32, Aug. 1984.
- [16] G. M. Dural, *Polarimetric ISAR Imaging to Identify Basic Scattering Mechanisms using Transient Signatures*. PhD thesis, The Ohio State University, Dec. 1988. Also: ElectroScience Laboratory Report 312884-9.
- [17] S. M. Scarborough, "Ultrawideband radar imaging and the diagnosis of scattering centers," Master's thesis, The Ohio State University, 1990.
- [18] L. M. Novak, "A comparison of 1-D and 2-D algorithms for radar target classification," in *The IEEE International Conference on Systems Engineering*, (Dayton, Ohio), pp. 6-12, August 1-3 1991.
- [19] J. Capon, "High resolution frequency-wavenumber spectrum analysis," in *Proc. IEEE*, vol. 57, pp. 1408-1418, Aug. 1969.
- [20] J. A. Cadzow and K. Ogino, "Two-dimensional spectral estimation," *IEEE Transactions on Acoustics, Speech, and Signal Processing*, vol. ASSP-29, pp. 396-401, June 1981.
- [21] J. S. Lim and N. A. Malik, "A new algorithm for two-dimensional maximum entropy power spectrum estimation," *IEEE Transactions on Acoustics, Speech, and Signal Processing*, vol. ASSP-29, pp. 401-413, June 1981.
- [22] J. H. McClellan, "Multidimensional spectral estimation," in *Proc. IEEE*, vol. 70, pp. 1029-1039, Sept. 1982.
- [23] B. F. McGuffin and B. Liu, "An efficient algorithm for two-dimensional autoregressive spectrum estimation," *IEEE Transactions on Acoustics, Speech, and Signal Processing*, vol. ASSP-37, pp. 106-117, Jan. 1989.
- [24] A. J. Devaney and G. A. Tsihrintzis, "Maximum likelihood estimation of object location in diffraction tomography," *IEEE Transactions on Acoustics, Speech, and Signal Processing*, vol. ASSP-39, pp. 2004-2005, Mar. 1991.
- [25] N. J. Dusaussoy and I. E. Abdou, "The extended MENT algorithm: A maximum entropy type algorithm using prior knowledge for computerized tomography," *IEEE Transactions on Acoustics, Speech, and Signal Processing*, vol. SP-39, pp. 1164-1180, May 1991.

- [26] S. W. Lang and J. H. McClellan, "Multidimensional mem spectral estimation," *IEEE Transactions on Acoustics, Speech, and Signal Processing*, vol. ASSP-30, pp. 880–887, Dec. 1982.
- [27] S. Y. Kung, K. S. Arun, and D. V. B. Rao, "State-space and singular-value decomposition-based approximation methods for the harmonic retrieval problem," *J. Opt. Soc. Am.*, vol. 73, pp. 1799–1811, Dec. 1983.
- [28] Y. Hua, "Estimating two-dimensional frequencies by matrix enhancement and matrix pencil," in *Proceedings of the International Conference on Acoustics, Speech, and Signal Processing*, (Toronto, Ontario), pp. 3073–3076, May 14–17 1991.
- [29] M. A. Rahman and K.-B. Yu, "Total least squares approach for frequency estimation using linear prediction," *IEEE Transactions on Acoustics, Speech, and Signal Processing*, vol. ASSP-35, pp. 1440–1454, Oct. 1987.
- [30] E. M. Kennaugh, "Effects of type of polarization on echo characteristics," Tech. Rep. 389-1 – 389-14, The Ohio State University, Department of Electrical Engineering, Antenna Laboratory, 1949–1952.
- [31] J. R. Huynen, *Phenomenological Theory of Radar Targets*. PhD thesis, Technical University Delft, Druckerij Bronder-Offset N.V. Rotterdam, Netherlands, 1970.
- [32] J. R. Huynen, "Towards a theory of perception for radar targets," in *Inverse Methods in EM Imaging: Part 2* (W. M. Boerner, ed.), Dordrecht, Holland: Reidel, 1985.
- [33] W. M. Boerner, A. C. Manson, and J. R. Huynen, "Radar target classification using polarimetric target slant range signatures," Tech. Rep. Final Report EMID-CL-83-06-15, University of Illinois at Chicago Communications Laboratory, Chicago, Illinois, June 1983.
- [34] W. L. Cameroon and L. K. Leung, "Feature motivated polarization scattering matrix decomposition," in *1990 IEEE International Radar Conference Record*, (Washington, DC), May 1990.
- [35] F. D. Garber, N. F. Chamberlin, and Ö. Snorrason, "Time-domain and frequency-domain feature selection for reliable radar target identification," in *Proceeding of the IEEE 1988 National Radar Conference*, (Arlington, VA), pp. 78–94, IEEE, April 1988.
- [36] N. F. Chamberlain, E. K. Walton, and F. D. Garber, "Radar target identification of aircraft using polarization-diverse features," *IEEE Transactions on Aerospace and Electronic Systems*, vol. AES-26, Sept. 1990. (to appear).
- [37] W. M. Steedly and R. L. Moses, "The Cramér-Rao bound for pole and amplitude estimates of damped exponential signals in noise," in *Proceedings of the International Conference on Acoustics, Speech, and Signal Processing*, (Toronto, Ontario), pp. 3569–3572, May 14–17, 1991.

- [38] W. M. Steedly, "High resolution exponential modeling of fully polarized radar returns," Master's thesis, The Ohio State University, Oct. 1989. also: ElectroScience Laboratory Report 717220-3.
- [39] O. S. Sands, *Transitive, Anti-Symmetric Relational Attributes in Structural Description Matching with Applications to Radar Target Identification*. PhD thesis, The Ohio State University, Columbus, OH, 1990.
- [40] O. Snorrason, *Topics in Pattern Recognition: Applications to RTI Systems*. PhD thesis, The Ohio State University, Columbus, OH, 1990.
- [41] R. F. Harrington, *Time-Harmonic Electromagnetic Fields*. New-York, NY: McGraw-Hill, 1961.
- [42] M. I. Skolnik, *Introduction to Radar Systems*. New York: McGraw-Hill, 1980.
- [43] N. F. Chamberlain, *Recognition and Analysis of Aircraft Targets by Radar, using Structural Pattern Representations Derived from Polarimetric Signatures*. PhD thesis, The Ohio State University, June 1989. Also: ElectroScience Laboratory Report 719710-3.
- [44] P. L. Uslenghi and J. R. Huynen, *Electromagnetic Scattering*. New York, NY: Academic Press, 1 ed., 1978.
- [45] J. J. Bowman and T. B. A. Senior, *Electromagnetic and Acoustic Scattering by Simple Shapes*. New York, NY: Hemisphere Publishing Co., 1 ed., 1987.
- [46] R. F. Harrington, "Matrix methods for field problems," in *Proc. IEEE*, vol. 55, Feb. 1967.
- [47] E. H. Newman, "A user's manual for the electromagnetic surface patch code: Esp version iv," Tech. Rep. 716199-11, The Ohio State University, Department of Electrical Engineering, ElectroScience Laboratory, Aug. 1988.
- [48] J. B. Keller, "Geometrical theory of diffraction," *J. Opt. Society of America*, pp. 116-130, Jan. 1962.
- [49] R. J. Marhefka, "Radar cross section - basic scattering code rcs-bsc (version 2.0) user's manual," Tech. Rep. 718295-15, The Ohio State University, Department of Electrical Engineering, ElectroScience Laboratory, Feb. 1990.
- [50] R. L. Bracewell, *The Fourier Transform and Its Applications*. New York, NY: McGraw-Hill, 2 ed., 1986.
- [51] W. Leeper, "Identification of scattering mechanisms from measured impulse response signatures of several conducting objects," Master's thesis, The Ohio State University, 1988.
- [52] J. V. Krogmeier, *Rational Modeling and Linear Prediction of Random Fields*. PhD thesis, The University of Illinois, Champaign-Urbana, IL, 1990.

- [53] Y. T. Chan and R. P. Langford, "Spectral estimation via the high-order Yule-Walker equations," *IEEE Transactions on Acoustics, Speech, and Signal Processing*, vol. ASSP-30, pp. 689-698, Oct. 1982.
- [54] J. A. Cadzow, "Spectrum estimation: An overdetermined rational model equation approach," *Proceedings of the IEEE*, vol. 70, pp. 907-939, Sept. 1982.
- [55] P. Stoica, T. Söderström, and F. Ti, "Asymptotic properties of the high-order Yule-Walker estimates of sinusoidal frequencies," *IEEE Transactions on Acoustics, Speech, and Signal Processing*, vol. ASSP-37, pp. 1721-1734, Nov. 1989.
- [56] G. H. Golub and C. F. VanLoan, *Matrix Computations*. Baltimore, MD: Johns Hopkins, 2 ed., 1989.
- [57] D. L. Mensa, *High Resolution Radar Cross-Section Imaging*. Norwood, MA: Artech House, 1 ed., 1991.
- [58] D. E. Dudgeon and R. M. Mersereau, *Multidimensional Digital Signal Processing*. Englewood Cliffs, NJ: Prentice-Hall, 1 ed., 1984.
- [59] Y. Hua and T. K. Sarkar, "A perturbation property of the TLS-LP method," *IEEE Transactions on Acoustics, Speech, and Signal Processing*, vol. ASSP-38, pp. 2004-2005, Nov. 1990.
- [60] J. D. Kraus and K. R. Carver, *Electromagnetics*. New-York, NY: McGraw-Hill, 1 ed., 1973.
- [61] R. Carrière and R. L. Moses, "High resolution parametric modeling of canonical radar scatterers with application to radar target identification," in *Proceeding of the International Conference on Systems Engineering*, pp. 13-16, IEEE, 1991.
- [62] W. M. S. C. Ying and R. L. Moses, "Statistical analysis of svd-based prony techniques," in *Proceeding of the Twenty-Fifth Asilomar Conference on Signals, Systems, and Computers*, (Pacific Grove, CA), IEEE, November 4-6 1991.